Fall 12-18-2015

# Biodegradable Hybrid Nanogels for Combination Chemotherapy

Swapnil Desale
*University of Nebraska Medical Center*

**BIODEGRADABLE HYBRID NANOGELS FOR COMBINATION CHEMOTHERAPY**

By

Swapnil S. Desale

A DISSERTATION

Presented to the Faculty of

The Graduate College in the University of Nebraska

In Partial Fulfillment of the Requirements

For the Degree of Doctor of Philosophy

Department of Pharmaceutical Sciences

Under the Supervision of Professor Tatiana K. Bronich

Medical Center

Omaha, Nebraska

October 2015

# TABLE OF CONTENTS

## CHAPTER I. INTRODUCTION

## CHAPTER II. BIODEGRADABLE HYBRID NANOGELS FOR COMBINATION DRUG THERAPY IN OVARIAN CANCER

## CHAPTER III. TARGETED DELIVERY OF PLATINUM-TAXANE COMBINATION THERAPY IN OVARIAN CANCER

**CHAPTER IV. HSP90-INHIBITION ENHANCES THE LYSOSOMAL TARGETING AND EFFICACY OF ErbB2-TARGETED DRUG DELIVERY**

**CHAPTER V. POLYPEPTIDE-BASED NANOGELS CO-ENCAPSULATING A SYNERGISTIC COMBINATION OF DOXORUBICIN WITH 17-AAG SHOW POTENT ANTI-TUMOR ACTIVITY IN ErbB2-DRIVEN BREAST CANCER MODELS**

**CHAPTER VI.**

**ACKNOWLEDGEMENT**

It gives me enormous amount of pleasure knowing that the bumpiest ride of my life is coming to an end. This past 5 years has tested many sides of my personal and professional life to the extreme. There are several ups and downs that occurred in this phase of my life but I am glad that I was able to survive it. This would not have been possible without the contributions of many people who help me to shape my graduation. At this special moment, I would sincerely like to appreciate all of them for priceless support.

The acknowledgment begins with my mentor Dr. Tatiana Bronich. If it wouldn't be her, I don't know how the end product of my Ph.D. would be. Right from my first day in the lab, she was extremely supportive and was constantly pushing me to be productive. With her as a mentor, I have learned many things not only professionally but also personally. There were the times when I was under extreme pressure but later I realized that it happened for my own good and hence I don't regret any of these unpleasant situations. Now I feel that I have achieved significant success as a graduate student with her guidance. I would sincerely thank her for letting me explore the industry side of my field by allowing me to go for an internship. This experience indeed turns out to be a very critical thing for my future career.  Overall it was pleasant ride with her and I hope to stay in touch even after my graduation.

Another two individuals who also deserve a large share of my appreciation are Dr. Srikumar Raja and Dr. Hamid band. My experience as a collaborator with them was extremely satisfying. Since the project we shared was more of a biology-based, they were

to be a great scientist and will have very bright future ahead. Dr. Svetlana Romanova was a great help for me especially during polymer synthesis. The polymers she synthesized for me were successfully translated into ideal drug delivery systems. Another person who helped me at the later stage of my Ph.D. was Dr. Bhopal Mohapatra. He was the one who salvage many predicaments of our animal studies with his experience and expertise.

I also would like to thank other members (previous and present) of our Nanomedicine group including Dr. Hardeep Singh Oberoi, Dr. Jong Oh Kim, Dr. Natasha Nukolova, Hangting Hu, Dr. Fan Lei, Tong Liu, Xinyuan Xi, Anya Brynskikh Boyum, Dr. Shaheen Ahmed, Dr. Chantey Morris, and many others for the kind help, friendship, and the opportunity to work with them. Many thanks to the administrative staff (Christine Allmon, Jamie Arbaugh, Keith Sutton, and Katina Winters) for their administration support. I would like to acknowledge the technical assistance from UNMC core facilities in my research and financial support from NIH and UNMC Graduate Assistantship.

This acknowledgement would be incomplete without thanking my dear friends Aditya Bade and Dr. Nilesh Wagh. They were the emotional pillars who help me climb till the end of graduation. They neutralized many of my unpleasant situations over the weekend with their encouragement, camaraderie, entertainment and support. I have made many friends during past 5 years on and off campus. I would like to thank all of them especially Hemant, Vivek, Prathamesh, Shrey and Rajesh for their contribution and I wish them all the best to achieve their desired goals.

My family has been a backbone of my entire career. Even though they are 1000s of miles away from me, but they have supported me every day. It's because of their countless prayers; I have been able to reach to the position where I am right now.  In spite

of being reluctant to send me to United States, they encourage me to follow my dreams and pursue my Ph.D. degree. Special thanks to my brother Jayesh, my Sister-in-law Geeta and my wonderful niece Swara. I love all of them so much and blessed to have them in my life.

Swapnil Desale

October, 2015

# BIODEGRADABLE HYBRID NANOGELS FOR COMBINATION CHEMOTHERAPY

Swapnil Desale, Ph.D.

University of Nebraska Medical Center, 2015

Advisor: Tatiana K. Bronich, Ph.D.

Combination chemotherapy is commonly used to treat cancer, because such a therapy regimens usually involve sequential administration of multiple drugs and allow targeting different cell signaling pathway. The co-delivery of drug combination at a controlled ratio via the same vehicle is offering the advantages such as spatial-temporal synchronization of drug exposure, synergistic therapeutic effects and suppression of drug resistance. Undoubtedly, there are several molecular and pharmacological factors that determine the effectiveness of drug combinations. A rationally designed drug combination is required since certain drug ratios and the definitive exposure to the targets of interest can only be synergistic while others are additive or even antagonistic. Cisplatin (CDDP) and paclitaxel (PTX) combination has resulted in improvement in the ovarian cancer treatment compare to individual drug with limited side effects. Multiple clinical trials studied the overall efficacy of CDDP and PTX and found significant benefit over the pre-existing treatments. Since then, this combination has been the treatment of choice for both early stage as well as advanced cases of ovarian cancer. However, administration of two different agents comes with the inconvenience of repeated or extended duration of drug infusion in patients. Moreover, the most extensively used conventional formulation of paclitaxel, Taxol®, utilizes Cremophor EL (polyethoxylated castor oil) that has been

linked to significant toxicities including allergic, hypersensitivity and anaphylactic reactions during infusion that require premedication and prolonged peripheral neuropathy. Combining such drugs in one delivery carrier is therefore a well-suited and convenient strategy for controlling the pharmacokinetics and co-delivery of the desired drug ratio in vivo, to maximize the therapeutic potency and minimize drug-associated toxicities. In an attempt to develop such multidrug vehicle, we designed a functional biodegradable and biocompatible polypeptide-based polymeric nanogels. Triblock copolymers containing the blocks of ethylene glycol, glutamic acid and phenylalanine (PEG–PGlu–PPhe) were successfully synthesized via NCA-based ring-opening copolymerization and their composition was confirmed by $^1$H NMR. Self-assembly behavior of PEG–PGlu$_{90}$–PPhe$_{25}$ was utilized for the synthesis of hybrid micelles with PPhe hydrophobic core, cross-linked ionic PGlu intermediate shell layer, and PEG corona. Cross-linked micelles (nanogels, NG) were about 90 nm in diameter ($\xi$-potential $= -20$ mV), uniform (narrow size distribution), and exhibited nanogels-like behavior. Degradation of NG was observed in the presence of proteolytic enzymes (cathepsin B). The resulting NG can incorporate the combination of drugs with very different physical properties such as CDDP (15 w/w% loading) and PTX (9 w/w% loading). Binary drug combination in NG exhibited synergistic cytotoxicity against human ovarian A2780 cancer cells and exerted a superior antitumor activity by comparison to individual drug-loaded NGs or free cisplatin in cancer xenograft model in vivo. However, this system relies solely on the enhanced permeation and retention (EPR) effect to facilitate the delivery of the drug combination to the tumor site. Regardless of the importance and popularity of EPR effect-based drug delivery, this strategy has some limitations related to

the inter- and intra-tumor heterogeneity, variations in the density as well as permeability of the tumor vasculature that can affect the accumulation of nanocarriers. One of the popular approaches to circumvent these problems is by surface-functionalization of the drug carrier with ligands that can target receptors with differential expression on the cancer cell surface, which helps in increasing the mean residence time of the delivery system at the tumor site and improving target cell uptake.

One such receptor of interest is the folate receptor (FR). Its natural ligand, FA, comes with the advantages of high binding affinity, stability and a simple chemical structure together with ease of availability, making it a suitable targeting ligand for ovarian cancer therapy. FA can thus be successfully conjugated to macromolecular systems without loss of binding affinity to its receptor. Our group has previously demonstrated a tumor-specific delivery and improved anti-cancer effect in vivo of CDDP-loaded NGs decorated with FA targeting groups. In the next part of our study, we designed FA-linked NGs incorporating platinum-taxane combination, and examined whether FR-targeted concurrent delivery of synergistic combination of CDDP and PTX can lead to enhanced therapeutic efficacy compared to nontargeted NG system. FA-decorated NGs significantly suppressed the growth of intraperitoneal ovarian tumor xenografts outperforming their nontargeted counterparts without extending their cytotoxicity to the normal tissues. We also confirmed that synchronized co-delivery of the platinum-taxane drug combination via single carrier to the same targeted cells is more advantageous than a combination of targeted single drug formulations administered at the same drug ratio. Lastly, we demonstrated that the same platform can also be used for localized chemotherapy. Our data indicate that intraperitoneal administration can be more effective

in the context of targeted combination therapy. Our findings suggest that multifunctional NGs are promising drug delivery carriers for improvement of current treatment for ovarian cancer.

Combination chemotherapy is also very common in the treatment of breast cancer. Trastuzumab (Herceptin™), in combination with chemotherapy is currently used for treatment of ErbB2-overexpressing breast cancers, following surgical removal of the primary tumor. However, patients either do not respond to Trastuzumab based therapies or relapse during the course of the treatment, necessitating the development of newer therapeutics. ErbB2 depends on heat shock protein 90 (HSP90) association for stability and, among client proteins of the chaperone, ErbB2 is perhaps the most sensitive to HSP90 inhibition. HSP90 inhibitors (such as the ansamycin antibiotic, Geldanamycin and related molecules like 17-AAG) have shown significant promise in pre-clinical models of ErbB2-driven breast cancer as well as initial phase I/II clinical trials. The mechanism involves attenuation of oncogenic signaling via degradation of ErbB2 as well as other critical downstream signaling mediators in the pathway, which include phospho-Akt and c-Raf. In a cancer cell, these signaling molecules are strongly dependent on HSP90 to maintain their stability. In a recently completed phase II study of 17-AAG and trastuzumab, an overall clinical benefit (including stable disease) was seen in 57% of the patients with ErbB2-positive metastatic breast cancer progressing on trastuzumab. We therefore hypothesized that HSP90-inhibition will enhance ErbB2-targeted drug delivery by promoting the endocytic uptake of ErbB2-bound nano-encapsulated cargo and facilitating its re-routing from a recycling pathway to the lysosomes. Using Trastuzumab-conjugated NGs (Trast-NG) encapsulating the DNA-damaging drug Doxorubicin (DOX)

as a model chemotherapeutic, we demonstrate through both in vitro and in vivo studies that HSP90-inhibition can indeed lead to an enhancement of targeted delivery of DOX specifically into ErbB2-overexpressing breast cancer cells. As a consequence, a sub-therapeutic and non-toxic dose of the HSP90 inhibitor 17AAG markedly improves the efficacy of ErbB2-targetd nanogels in vivo. In a follow up study, we attempted to co-encapsulate DOX and 17-AAG since combining drugs in one delivery carrier is a well-suited strategy for controlling the pharmacokinetics and co-delivery of the desired drug ratio in vivo. However, co-incorporation of drug molecules with different physicochemical properties, such as hydrophilic DOX and hydrophobic 17-AAG, has been challenging. We have recently described biodegradable polymeric nanogels (NGs) based on poly(ethylene glycol)-b-poly(L-glutamic acid) (PEG-b-PGA) with pendant phenylalnine functionalities [23]. Such NGs have multiple hydrophobic domains formed by phenylalanine moieties within the cross-linked PGA polyion cores surrounded by a hydrophilic PEG shell. Herein, we explored these novel NGs for co-encapsulation of 17-AAG and DOX. The potency of this co-delivery system was evaluated in a panel of human breast cancer lines and in an ErbB2-driven orthotopic xenograft model. We demonstrate that NGs-based co-delivery of synergistic combination of 17-AAG and DOX exhibited superior antitumor efficacy compared to a combination of free drugs. The implications of our results may support a new platform for delivery of combinations of HSP90 inhibitors with cytotoxic agents for treatment of various types of cancers.

# LIST OF FIGURES

# LIST OF TABLES

**LIST OF ABBREVIATIONS**

| | |
|---|---|
| 17-AAG | 17-N-allylamino-17-demethoxygeldanamycin |
| $^1$H-NMR | Proton Nuclear Magnetic Resonance |
| ABS | Acetate Buffered Saline |
| AAALAC | American Association for Accreditation of Laboratory Animal Care |
| ADC | Antibody-Drug-Conjugates |
| ANP | Antibody-Nanoparticle |
| AFM | Atomic Force Microscopy |
| ANOVA | One-way Analysis of Variance |
| ALT | Alanine Aminotransferase |
| AST | Aspartate Aminotransferase |
| BGlu | L-glutamic Acid γ-benzyl Ester |
| BLI | Bioluminescence Imaging |
| CA-125 | Cancer Antigen 125 |
| CI | Combination Index |
| CD | Circular Dichroism |
| CDDP | cis-dichlorodiamminoplatinum (II) |
| *cl* | Cross-linked |
| CMC | Critical Micellar Concentration |
| $D_{eff}$ | Effective Hydrodynamic Diameter |
| D*av* | Number-average Particle Diameter |
| DAPI | 4′,6-diamidino-2-phenylindole |
| DAB+ | 3,3'-Diaminobenzidine |
| DOX | Doxorubicin |

| | |
|---|---|
| DLS | Dynamic Light Scattering |
| DMEM | Dulbecco's Modified Eagle's Medium |
| DMSO | Dimethyl Sulfoxide |
| ED | 1,2-ethylenediamine |
| EDC | 1-(3-dimethylaminopropyl)-3-ethylcarbodiimide hydrochloride |
| EDTA | Ethylenediaminetetraacetic Acid |
| ESCRT | Endosomal Sorting Complex Required for Transport |
| EGFR | Epidermal Growth Factor Receptor |
| EPR | Enhanced Permeability and Retention |
| ELISA | Enzyme-linked Immunosorbent Assay |
| FACS | Fluorescence-activated Cell Sorting |
| FDA | Food and Drug Administration |
| FPLC | Fast Protein Liquid Chromatography |
| FA | Folic Acid |
| FBS | Fetal Bovine Serum |
| FR | Folate Receptor |
| FD | Folate Deficient |
| FTIR | Fourier Transform Infrared Spectroscopy |
| GPC | Gel Permeation Chromatography |
| Fmoc | 9-Fluorenylmethyloxycarbonyl |
| H$av$ | Number-average Particle Height |
| HLB | Hydrophilic-lipophilic Balance |
| H&E | Hematoxylin and Eosin |
| HSP90 | Heat Shock Protein 90 |
| HPLC | High Pressure Liquid Chromatography |

| | |
|---|---|
| IP | Intraperitoneal |
| IV | Intravenous |
| IACUC | Institutional Animal Care and Use Committee |
| ICP-MS | Inductively Coupled Plasma-Mass Spectrometer |
| IHC | Immunohistochemistry |
| $IC_{50}$ | Half Maximal Inhibitory Concentration |
| MTT | (3-(4,5-dimethylthiazol-2-yl)-2,5-diphenyltetrazolium bromide |
| mPEG | Methoxy Polyethylene Glycol |
| MW | Molecular Weight |
| MWCO | Molecular Weight Cut-off |
| mAb | Monoclonal Antibody |
| NG | Nanogels |
| NCA | N-carboxyanhydride |
| NHS | N-Hydroxysuccinimide |
| PTX | Paclitaxel |
| Pt | Platinum |
| PDI | Polydispersity index |
| PEG | Polyethylene Glycol |
| PGlu | Poly(L-glutamic acid) |
| PPhe | Poly(L-phenylalanine) |
| PEG-*b*-PGlu | Polyethylene Glycol-block-poly(L-glutamic acid) |
| PEG-b-PGlu-b-PPhe | Polyethylene Glycol-*block*-poly(L-glutamic acid)-*block*-poly(L-phenylalanine) |
| PME | L-phenylalanine Methyl Ester |
| PBS | Phosphate Buffered Saline |

| | |
|---|---|
| PMA | Poly(sodium methacrylic acid) |
| RBC | Red Blood Cells |
| RI | Refractive Index |
| RPMI | Roswell Park Memorial Institute medium |
| RP-HPLC | Reverse Phase-high Pressure Liquid Chromatography |
| ROIs | Regions of Interest |
| SD | Standard Deviation |
| SEC | Size Exclusion Chromatography |
| SEM | Standard Error of the Mean |
| TEM | Transmission Electron Microscopy |
| THF | Tetrahydrofuran |
| T/C | $(V_t - V_o)$ treated tumor/ $(V_t - V_o)$ control tumor, where $V_t$ and $V_o$ represent the mean tumor volume on the evaluation day and at the start of the treatment, respectively. |
| TBME | tert-butyl Methyl Ether |
| Trast-NG | Trastuzumab-conjugated Nanogels |
| UV | Ultraviolet–visible Spectroscopy |

## LIST OF CONTRIBUTIONS

1. Chapter II – Dr. Svetlana Romanova assisted in the monomer and polymer synthesis. Dr. Luda S. Shlyakhtenko helped with AFM imaging of the nanogels. Dr. Yi Zhao assisted in the animal studies. Dr. Larisa Poluektova and Edward Makarov assisted in immunohistochemistry. Dr. Samuel Cohen performed the histopathological analysis of tissue samples. Platinum measurements were done at core facility of University of Nebraska Medical Center. Jaclyn Hollinger assisted in blood chemistry studies.

2. Chapter III – Dr. Svetlana Romanova performed the synthesis and characterization the polymer for this study. Dr. Jinjin Zhang assisted with FPLC for estimation of purify of targeted nanogels. Kruti Soni helped in the animal studies. Platinum measurements were performed at core facility of University of Nebraska Medical Center by Dr. Chantey Morris. Dr. Samuel Cohen performed the histopathological analysis of tissue samples.

3. Chapter IV – Dr. Jinjin Zhang assisted with the purification of trastuzumab-nanogel conjugates. The synthesis of nanogels was initially described by Dr. Bronich and Sirisha Bontha. Further work on this system was performed by Drs. Nataliya Nukolova and Jong Oh Kim. Dr. Srikumar raja and Haitao Luan assisted in flow cytometry and confocal immunofluorescence microscopy. Haitao Luan performed the cell cycle analysis. Dr. Bhopal Mohapatra, Kruti soni, Dr. Jinjin Zhang, Dr. Dan Feng and Timothy Bielecki assisted in the animal studies. Dr. Bhopal Mohapatra performed western blot and also assisted in Ki-67-caspase-3

staining. Dr. Samuel Cohen performed the histopathological analysis of tissue samples

4. Chapter V – Dr. Jong Oh Kim synthesized the polymer for this study. Kruti Soni helped in release study. Confocal immunofluorescence analysis and western blot were performed by Dr. Srikumar Raja and his colleagues. Dr. Bhopal Mohapatra, Kruti soni, Dr. Jinjin Zhang, Dr. Dan Feng and Timothy Bielecki assisted in the animal studies. Dr. Bhopal Mohapatra assisted in Ki-67-caspase-3 staining. Dr. Samuel Cohen performed the histopathological analysis of tissue samples

5. Major contributions in all chapters were made by Swapnil Desale. The overall project was designed under the guidance of Dr. Tatiana K. Bronich. Dr. Hamid Band and Dr. Srikumar Raja provided valuable direction to Chapter IV and V; and important contributions in the preparation of the manuscripts.

6. This work was supported by National Institute of Health grant CA116590 (Dr. Tatiana Bronich). We acknowledge the assistance of the Nanomaterials Core facility of the Center for Biomedical Research Excellence (CoBRE) Nebraska Center for Nanomedicine supported by the Institutional Development Award (IDeA) from the National Institute of General Medical Sciences of the National Institutes of Health under grant number P20GM103480. Work for chapter IV and V was supported by: the NIH (Grants CA116552, CA99163, CA87986 and CA105489 to Dr. Hamid Band, and CA96844 to Dr. Vimla Band; P20GM103480 to Dr. Tatiana Bronich); DOD Breast Cancer Research Grants (DAMD W81XWH-07-1-0351 to VB; DOD-IDEA W81WH-11-1-0167 to HB and TKB); Nebraska Department of Health and Human Services (LB-506 grant to Dr.

## CHAPTER 1

## INTRODUCTION

### 1.1. Cancer

Cancer is a major health problem and the second leading cause of illness-related death. The six essential changes in cell physiology suggested to collectively contribute to the malignant growth are self-sufficiency in growth signals, insensitivity to anti-growth signals, tissue invasion and metastasis, limitless replicative potential, sustained angiogenesis and evading apoptosis [1]. Currently available chemotherapeutic agents have played a significant role in reducing mortality/morbidity and in increasing patient's overall lifespan [2]. Most of the chemotherapeutic agents have relatively narrow therapeutic index; develop resistance and leads to off-target biodistribution upon intravenous administration leading to severe side effects to healthy tissues. These limitations of conventional chemotherapeutic strategies frequently result in suboptimal dosing, treatment delay or discontinuance and reduced patient compliance to therapy [3]. Despite the recent advances in early diagnosis and cancer treatment, the development of chemotherapeutic agents which can effectively deliver on efficacy, safety and convenience for the patient remains a great challenge [3].

### 1.2. Combination chemotherapy

Combination chemotherapy is medicine's best attempt to address aforementioned issues. In combination chemotherapy, cancer cells are attacked by drugs with synergistic cytotoxicity by disrupting different stages of the cell reproduction cycle. Majority of chemotherapeutic drugs act on a specific phase of the cell cycle, so it is logical to attack multiple phases of the cell replication cycle to prevent mutation and resistance. The

primary goals of drug combination in anticancer treatment are to overcome tumor heterogeneity, reduce chemo-resistance and achieve additive or more desirable synergistic anticancer efficacy without overlapping toxicity. Frei et al. proved in 1965 that a combination therapy consisting of two cytotoxic agents was therapeutically more effective than monotherapy in children with acute leukemia [4]. Since then, clinically effective drug combinations, that would improve the efficacy of oncology treatment, have been widely researched. The fundamentals of combination chemotherapy development have remained mostly unchanged over the last few decades. The general principles have been to: i) use drugs with non-overlapping toxicities so that each drug can be administered at near-maximal dose; ii) combine agents with different mechanisms of action and minimal cross-resistance in order to inhibit the emergence of broad spectrum drug resistance; iii) preferentially use drugs with proven activity as single drugs and iv) administer the combination at early stage disease and at a schedule with a minimal treatment-free period between cycles but still allowing the recovery of sensitive target tissues [5-7]. In combination therapy the overall therapeutic benefit of the drugs in combination were found to be greater than the sum of the effects of the drugs individually. The best drug combination with maximal antitumor efficacy can be calculated by combination index (CI) analysis, an effective way to demonstrate that drugs are working synergistically [8]. Unlike single agent therapy, synergistic combinations of two or more agents proved to overcome toxicity and other side-effects associated with high doses of single drugs [9, 10]. The use of combination therapy for cancer treatment has been well established in recent years and is depicted in figure 1.1.
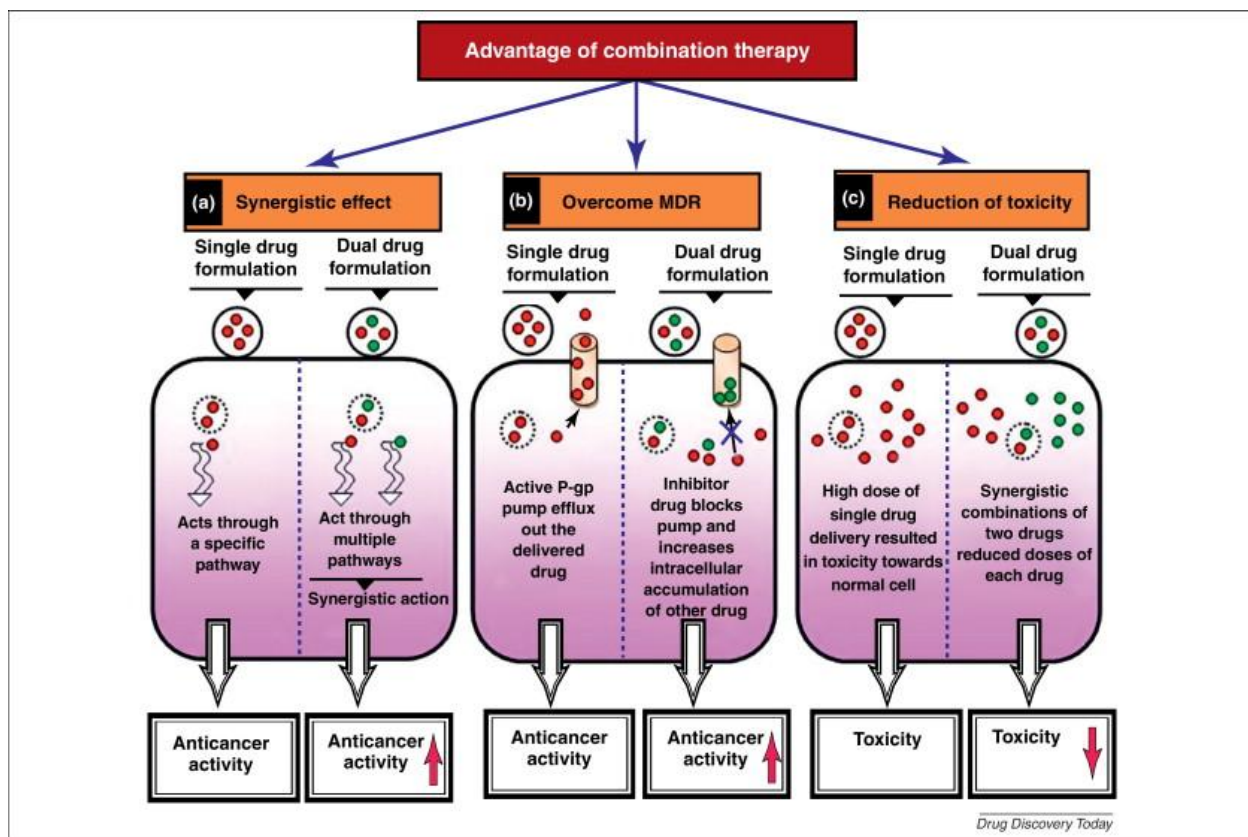
**Figure 1.1.** Schematic representation depicting various advantages shown by combination drug delivery for cancer therapy. Adapted from [11].

The widely investigated drug combinations for effective cancer treatment are the combination of multiple chemotherapeutic agents, chemotherapy with radiotherapy, chemotherapy with hormone therapy and immunotherapy with chemotherapy [11]. Hormone therapy which involves administration of specific steroid hormones or drugs is often given to patients with early stages of breast cancer and it act by blocking/downregulating the estrogen receptor or by reducing the estrogen concentration around or within the cancer cell [12, 13]. Combination of chemotherapy and radiotherapy is one of the most promising strategies for current cancer therapeutics. It has been shown to improve patient survival and the locoregional control of various cancers when compared with radiotherapy alone [14-16]. Cancer treatment using different monoclonal

antibodies is another practiced strategy for the current treatment of cancer. Antibodies have the unique capacity to target and kill tumor cells while simultaneously activating immune effectors to kill tumor cells through the complement cascade or antibody-dependent cellular cytotoxicity. This multifaceted antibody-mediated killing mechanism combined with chemotherapy has been taken up by various investigators to achieve enhanced antitumor activity [17-19]. Among different combination therapies the most practiced and well researched therapy method is co-treatment with multiple chemotherapeutic drugs. Therefore, current trends in anticancer research have progressively concentrated on the development of new combinations of anticancer drugs with a view to overcoming the limitations frequently associated with conventional chemotherapy. Considering the scope of this work, we have focused on combination chemotherapy in leading gynecologic cancers which are ovarian and breast cancer.

## 1.3.    Combination chemotherapy in ovarian cancer

Ovarian cancer is the most lethal gynecologic malignancy in women and it is the leading cause of death from gynecologic cancer. Approximately 60% of patients will experience a relapse after the standard first-line treatment including cytoreductive surgery and adjuvant chemotherapy [20]. At this time, when relapse occurs, the chance of cure decreases drastically and treatment is solely palliative. Surgery is not sufficiently validated due to the lack of phase III clinical trials, and there are no approved targeted therapies in relapsed ovarian cancer. Therefore, chemotherapy is the only option to achieve these objectives. Management of ovarian cancer has evolved from single agent to combination chemotherapy. Clinical trials performed in the late 1970s demonstrated that cisplatin (CDDP) is an active chemotherapy in advanced or recurrent ovarian cancer with

a response rate in the range of 13–30% [21]. Subsequently, CDDP became the primary choice for many clinical trials in ovarian cancer. Early trials also identified the toxicity profile of this platinum agent including the risk of myelosupression and nephrotoxicity. The next generation of ovarian cancer treatment regimens included the combination therapy of CDDP plus other chemotherapeutic drug. One of such a research study evaluating combination chemotherapy with CDDP plus cyclophosphamide revealed that the tumor progression and survival were markedly improved compared with CDDP only [22]. As a result, the standard combination chemotherapy in the late 1980s and early 1990s was CDDP plus cyclophosphamide. Discovery of paclitaxel (PTX) changed the standard of care in ovarian cancer yet again. Clinical trials comparing cyclophosphamide and CDDP with PTX and CDDP demonstrated that the platinum/taxane treatment regimens had an improved outcome compared with standard combination of cyclophosphamide and CDDP [23, 24]. After decades of clinical trials, intravenous treatment regimens were accepted in the 1990s as the standard of care for advanced ovarian cancer [25]. Till today, this combination is considered as standard chemotherapy regimen in advanced ovarian cancer and suggested that a plateau has been reached for IV chemotherapy. The typical course of platinum/taxane regimen for epithelial ovarian cancer involves 3 to 6 cycles. A cycle is a schedule of regular doses of a drug, followed by a rest period. In patients with advanced ovarian cancer (stages III–IV), six cycles of chemotherapy are recommended [26]. In an attempt to deliver increased concentrations of drugs to the ovarian tumors, intraperitoneal (IP) route of administration of chemotherapy has been investigated which involves administration of drugs through surgically placed

IP catheters (Fig. 1.2). The IP administration allows very large concentrations of active agents to reach the tumor while attempting to minimize systemic toxicity.
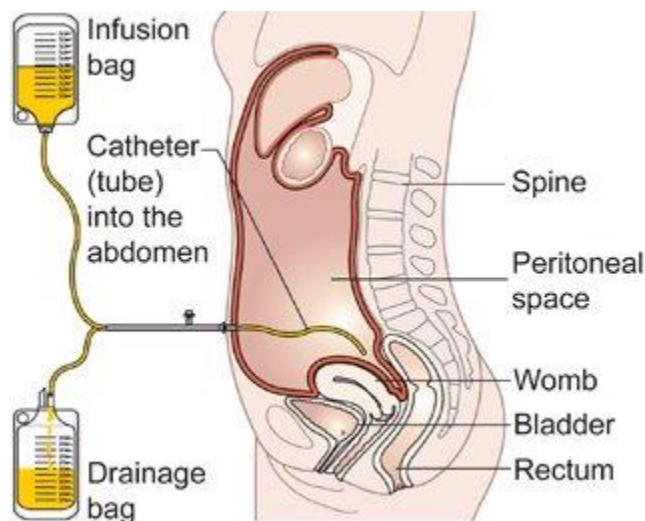


**Figure 1.2** IP administration of chemotherapy in ovarian cancer

The IP administration of CDDP resulted in a 10–20 fold greater concentration in the tumor space compared with IV [27-29], while for paclitaxel the IP pharmacokinetics demonstrate a 1000-fold greater IP versus IV concentration [30, 31]. Three randomized phase III trials have demonstrated a major improvement in the treatment of advanced ovarian cancer through the utilization of IP chemotherapy [32-34]. A phase III study reported by Markman and colleagues in 2001 in stage III ovarian cancer patients who had undergone optimal debulking surgery to less than 1 cm residual tumor [33]. The standard chemotherapy arm used IV PTX and CDDP. The investigational arm utilized IV paclitaxel followed by IP CDDP (100 mg/m$^2$ versus 75 mg/m$^2$ in the IV arm). This study demonstrated an improvement in progressive free survival (22 versus 28 months, $p = 0.01$) and a borderline improvement in overall survival (52 versus 63 months, $p = 0.05$) in the investigational arm. The increased toxicity associated with the IP arm prevented the routine use of this regimen despite its proven efficacy. Later a phase III

study reported by Armstrong and colleagues in 2006 in optimally debulked stage III ovarian cancer patients with less than 1 cm residual tumor [32], established a new standard of care. This study randomized patients to IV PTX (135 mg/m$^2$) over 24 h on day 1 followed by IV CDDP (75 mg/m$^2$) on day 2 versus IP CDDP (100 mg/m$^2$) on day 2 and IP paclitaxel (60 mg/m$^2$) on day 8. This study demonstrated a significant improvement in overall survival (49.7 versus 65.6 months, p = 0.03). Significant neurotoxicity was also observed in this study (19% in IP versus 9% in the IV group) (Fig. 1.3).
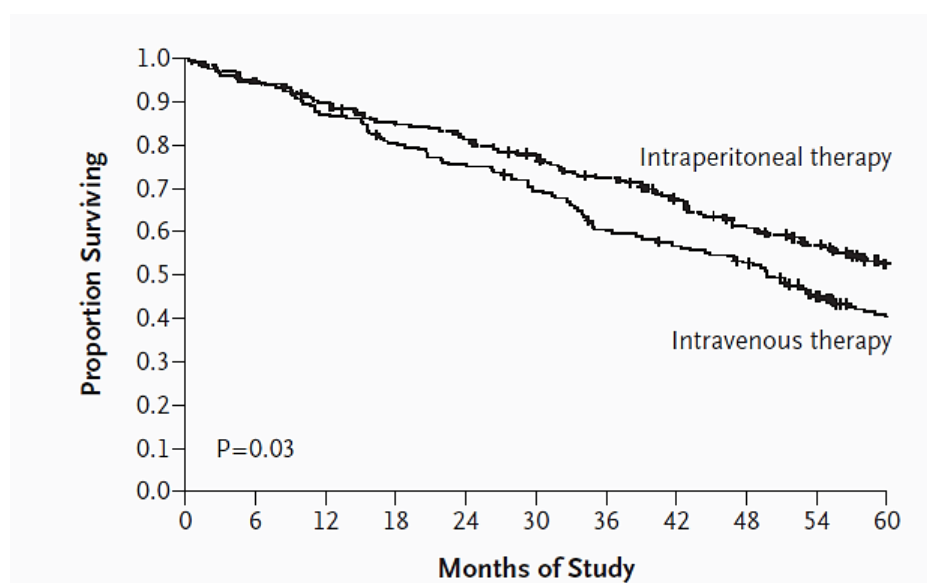


**Figure 1.3.** Overall survival among the 415 patients with stage III ovarian cancer who were randomly assigned to treatment with intravenous PTX and CDDP or to treatment with intravenous PTX, intraperitoneal CDDP, and intraperitoneal PTX. Adapted from [32].

Although increased toxicity was noted during and following IP chemotherapy in this study, the quality-of-life measurements returned to baseline 1 year following treatment. Despite these phase III trials demonstrating a significant survival advantage with IP compared with IV chemotherapy and a National Cancer Institute clinical alert supporting IP chemotherapy, controversies regarding the use of IP chemotherapy still exist and this

route of administration has not gained overwhelming support by the gynecologic and medical oncology community [35]. Some of the barriers to utilizing IP therapy include IP therapy-related side effects, complexity of IP administration, and controversies still related to the clinical survival advantage of IP therapy.

## 1.4. Combination chemotherapy in breast cancer

Breast cancer is the most frequently diagnosed cancer and the leading cause of cancer-related death among females worldwide. The latest world cancer statistics available from the International Agency for Research on Cancer showed that 1,677,000 women were diagnosed with breast cancer and 577,000 women died in 2012 [36]. Despite the success in early detection, up to five percent of women diagnosed with breast cancer in the United States have metastatic disease at the time of first presentation. In addition, up to 30 percent of women with early-stage, non-metastatic breast cancer at diagnosis will develop distant metastatic disease [12]. Advancement in chemotherapy, surgery, lymph node evaluation and hormone receptor blocking therapy have improved the survival of breast cancer patients [37]. Genetic and molecular profiling of breast cancer has revealed its profound complexity and heterogeneity [38, 39]. Such complexity makes it challenging for clinicians to find the optimal treatment regimen in the treatment of breast cancer. The cell surface receptors of the ErbB family including EGFR, ErbB2 (also known as Her2/neu) and ErbB3 (Her3) are over-expressed or deregulated in many types of cancers, including breast cancers. The past two decades have seen an explosion of activity in the development of ErbB-receptor targeted therapeutics. EGFR and ErbB2 have been the primary targets for therapeutic development. For example, the humanized monoclonal antibodies Trastuzumab (Herceptin™; Genentech; against ErbB2) or

Cetuximab (Erbitux™; Eli Lilly and Company; against EGFR) and the tyrosine kinase inhibitors, Lapatinib (Tykerb; Glaxo Smithkline; dual EGFR/Her2 inhibitors) or Erlotinib (Tarceva; Genentech; against ErbB2) are currently used clinically. However, de novo and acquired resistance to treatment necessitate continued exploration of novel strategies. One emerging approach is the use of antibody-drug conjugates, such as Trastuzumab-DM1 (also developed by Genentech), which is an anti-mitotic fungal toxin chemically conjugated to anti-ErbB2 monoclonal antibody. An alternative strategy involves targeted delivery of conventional chemotherapeutic drugs (such as Doxorubicin, Paclitaxel or Campothecin) encapsulated in anti-ErbB2 or anti-EGFR antibodies or ligands conjugated liposomal or polymer micelle based nanoparticles are being explored at a laboratory and pre-clinical stage. Both approaches use the overexpression of EGFR and ErbB2 as addresses to specifically deliver cytotoxic cargo. This may be particularly useful as a strategy for overcoming resistance to currently approved ErbB-directed targeted therapies. However, for both antibody-drug conjugates as well as targeted nanoparticulate drug-delivery systems, the extent of endocytosis of the receptor and its distribution between recycling versus lysosomal pathways can limit successful delivery of the chemotherapeutic payload into ErbB2 or EGFR overexpressing breast cancers. Considering a scope of thesis, this section is intended to focus on use of clinical combination therapy for the treatment of ErbB2-driven breast cancer. Although, Trastuzumab in combination with chemotherapy has shown effectiveness in many patients, challenges due to intrinsic or acquired therapeutic resistance have prompted the development of Trastuzumab-MCC-DM1 (T-DM1; Genentech), which is an antibody-

drug conjugate (ADC). DM1 is a Maytansanoid (a derivative of Maytansine; a Vinca alkaloid), which functions as an antimitotic drug (Fig. 1.4) [40].
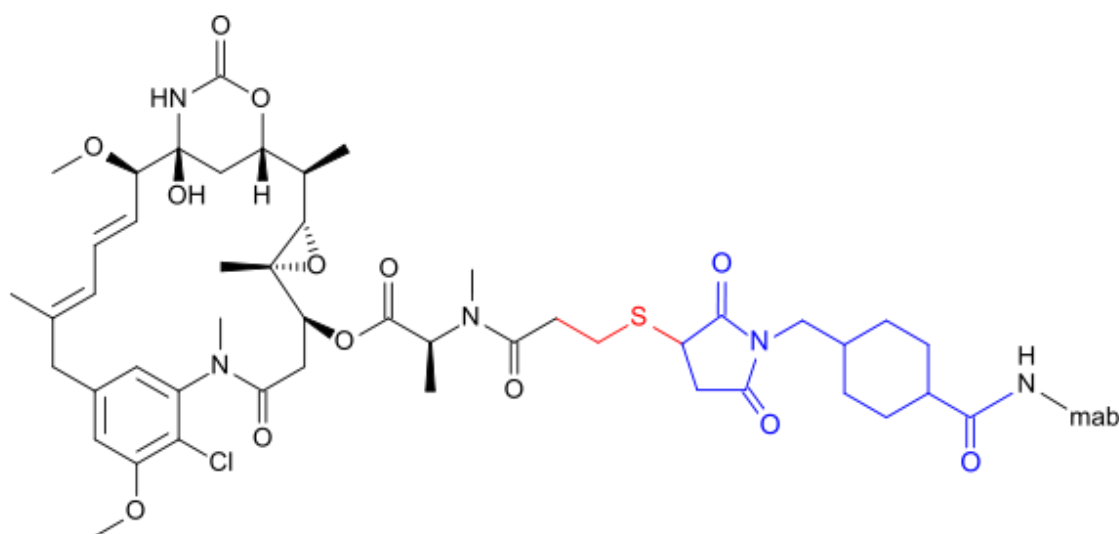


**Figure 1.4.** Schematic representation of T-DM1. The maytansine skeleton is shown in black at left. The thioether group that makes mertansine is shown in red. The linker group that makes emtansine is shown in blue at right, bound to the amino group (NH–) of a lysine residue in the trastuzumab molecule (–mab).

DM1 is chemically conjugated to Trastuzumab via a non-reducible Succinimidyl-4-(N-maleimidomethyl) cyclohexane-1-carboxylate (MCC) crosslinker, which was optimized based on a systematic comparison of various reducible and non-reducible crosslinkers in in vitro studies (intracellular drug release) and in vivo pharmacokinetics and toxicity studies [41-43]. While the mechanism(s) of Trastuzumab resistance remains unclear, several studies indicate that it is not due to loss of ErbB2 overexpression [44, 45]; consequently the rationale for T-DM1 design was to use ErbB2 as an address to deliver the cytotoxic drug specifically to ErbB2-overexpressing breast cancers. T-DM1 demonstrated potent and selective activity against a panel of ErbB2 overexpressing breast cancer cell lines (including several Trastuzumab-resistant model cell lines) as compared to normal or ErbB2-low cancer cell lines [46, 47]. Most importantly, the drug exhibited

favorable pharmacokinetics, low toxicity in mice and also inhibited growth of Trastuzumab-sensitive as well as resistant ErbB2-overexpressing human breast cancer cell xenografts in mice [46]. Although it was presumed that the cytotoxicity was a result of internalization of the ADC direct data demonstrating internalization of the ADC was lacking. The importance of this is underscored by recent studies that have shown that ErbB2 receptor is not efficiently internalized [48, 49]. Given the numerous studies, which suggest that ErbB2 receptor is either internalization resistant or rapidly recycles back to the cell surface [48], data on the site of action of T-DM1 is critical in order to improve designs for optimizing the intracellular delivery of the Maytansanoid. This will especially become important in cases where patient-specific mutations or alterations in the activities of regulators of endocytic trafficking (discussed above) could potentially cause refractoriness or reduce the efficacy of T-DM1. For example, one factor that is hypothesized to contribute to the low rate of endocytosis is the constitutive association of ErbB2 with Heat Shock Protein 90 (HSP90) [49]. It has been demonstrated that HSP90 ATPase inhibitors such as 17-allylaminodemethoxy geldanamycin (17-AAG) induced rapid downregulation of cell surface ErbB2 which is mediated by ubiquitin modification of ErbB2 [50, 51]. Subsequent work has shown that 17-AAG indeed promotes the delivery of surface ErbB2 to the lysosome [52, 53], an organelle where molecules such as T-DM1 are intended to go. Several HSP90 inhibitors are currently in phase I and II clinical trials and could potentially be combined with T-DM1.

## 1.5. Nanocarrier-based approach for combination chemotherapy

Despite the fact that combination chemotherapeutic strategies have helped toward the better treatment of cancer, their clinical success is largely hindered as a result of the

inadequate accessibility of chemotherapeutic agents to tumor tissue, requiring high doses, rapid abolition, poor solubility and inconsistent bioavailability. While in vitro cellular studies have generated many leads for combinatorial regimens, their clinical results are often met with little improvement in efficacy and at times higher toxicity [54-56]. One major factor that separates *in vitro* success from *in vivo* clinical outcomes is the varying pharmacokinetics among different drugs. Controlling the therapeutic cocktail that reach the diseased cells and tissues therefore become a major clinical challenge. One strategy toward more effective combination therapies thus is devising a better scheme for precise and control delivery of multiple therapeutic agents. Thus, to mitigate the limitations associated with conventional combination chemotherapy, there is an urgent need for developing a drug delivery system that could enhance the delivery of drugs to the tumor site while reducing toxic side effects.

Advances in nanotechnology have opened up infinite opportunities in controlled drug delivery and novel combination strategies. Nano-formulated drugs have now come of age in the clinic and are inspiring innovative investigations in drug delivery [57]. Nanoparticle therapies provide improved drug solubility, reduced systemic toxicity, longer circulation times in the blood, controllable release profiles, and the potential to target specific cells and tissues [58-60]. Recently, nanocarriers are gaining increasing attention for their ability to co-encapsulate multiple therapeutic agents and to synchronize their delivery to the diseased cells. Various nanoparticle platforms such as liposomes, dendrimers, micelles, carbon nanotubes (CNTs), polymer–drug conjugates and nanogels have been used to carry broad classes of therapeutics including cytotoxic agents, chemosensitizers, small interference RNA (siRNA), and antiangiogenic agents.

### 1.5.1. Liposomes

Liposomes are spherical vesicles consisting of amphiphilic phospholipid bilayers. Phosphatidylcholine and phosphatidylethanolamine are the common building blocks for liposomal preparation whereas cholesterol is a frequent additive that serves to modify the rigidity of the lipid membranes. Liposomes have been pharmaceutical carriers of choice for drug delivery applications and several liposomal drug formulations have already been approved, and many more are under clinical evaluation [61]. One major advantage of liposomes as a drug carrier is its ability to work with both hydrophobic and hydrophilic drugs; hydrophobic drugs can be enclosed within the phospholipid bilayers, while hydrophilic can drugs reside in the aqueous cavity [62]. Liposomes are typically prepared by rehydrating lipid films to form multilamellar vesicles, which subsequently undergo mechanical extrusions to form unilamellar vesicles [63]. Multidrug-loaded liposomes can be prepared using either active extrusion or passive diffusion followed by filtration of unloaded drugs. CPX-351 (cytarabine/daunorubicin liposome injection) is a liposomal formulation of cytarabine and daunorubicin for intravenous infusion. [64]. In preparing CPX-351, cytarabine was hydrated and extruded with the lipid components yielding cytarabine-loaded liposomes. These liposomes were then incubated with daunorubicin to achieve dual-drug encapsulation. The two drugs contained within the liposome in a 5:1 molar ratio, showed synergistic cytotoxicity in vitro and in murine models of hematological malignancies Liposome-encapsulated curcumin and resveratrol were prepared by film hydration method. Systemic administration of this formulation inhibited prostate cancer by increasing their bioavailability synergistically and enhanced the anticancer effects. Combination therapy of liposomal paclitaxel and cisplatin as

neoadjuvant chemotherapy in locally advanced cervical cancer was evaluated by Li et al [65]. Patients were administered with intravenous dose of 175 mg/m$^2$ PTX and 75 mg/m$^2$ CDDP. The total response rate was 86.1% (62/72) including a complete response and partial response rate of 27.8% (20/72) and 58.3% (42/72). The study showed that liposomal paclitaxel with cisplatin as an additional chemotherapy regimen is efficacious and tolerable in the NACT of cervical cancer. Transferrin-conjugated liposome co-encapsulating doxorubicin and varapamil proved to be effective in doxorubicin-resistant K562 cells and showed enhanced cytotoxicity caused by overcoming P-gp-mediated multidrug resistance [66]. A Phase I study was performed by taking a liposomal formulation entrapped with irinotecan and floxuridine in the ratio of 1:1 and the maximum tolerated dose and pharmacokinetic parameters of the liposomal formulation were determined in patients with advanced solid tumors. The results demonstrated the dual-drug-loaded liposomal formulation was well tolerated showing enhanced anticancer activity in patients [67]. Co-delivery of the P-gp inhibitor, tariquidar, and cytotoxic drug, paclitaxel, into tumor cells to reverse the multi-drug resistance using long-circulating liposomes [68]. Anticancer drug combinations can act synergistically or antagonistically *in vivo* against tumor cells depending on the ratios of the individual agents comprising the combination. Mayer et al examined the liposomes for loading of various drug combinations (irinotecan/floxuridine, cytarabine/daunorubicin, and cisplatin/daunorubicin) at different ratios (1:1, 5:1, and 10:1) [69]. The liposomes not only maintained drug ratios in the plasma after injection, but also delivered the formulated drug ratio directly to tumor tissue. Apart from small molecule therapeutic combination, liposomes have been also reported to encapsulate combination of small

molecule and oligodeoxynucleotides/siRNAs. Cationic liposomes targeted with a monoclonal antibody against the disialoganglioside GD2 co-encapsulating c-myc antisense oligodeoxynucleotides and doxorubicin led to the most pronounced delay in tumor growth when administered in a sequential manner. As a result, their combination translates into a statistically significant suppression of blood vessel density and an enhanced apoptosis, compared to all treatments given separately. Saad et al showed an efficient encapsulation of doxorubicin and siRNA targeted to MRP1 and BCL2 mRNA (suppressors of pump and non-pump cellular-resistance, respectively) into the cationic liposomes which led to enhanced cell-death induction and suppression of cellular resistance in multi-drug resistant lung cancer cells.

Two liposomal drug combinations have entered clinical trials. First is small molecules combinations in Phase II clinical trials, CPX-351 (cytarabine and daunorubicin) in patients with newly diagnosed acute myeloid leukemia [70], and CPX-1 (irinotecan HCI:floxuridine) in patients with colorectal cancer (http://www.celatorpharma.com/new/products.html).

### 1.5.2. Polymer-dug conjugates

Covalently attaching therapeutic agents to water-soluble polymers is another approach that improves the drugs systemic circulation lifetime and reduces their exposure to normal tissues. The advantages of polymer–drug conjugates include passive tumor targeting by EPR effect due to its leaky vasculature which allows selective extravasation of the conjugate in tumor tissue and retained for longer period due to its poor lymphatic drainage [54]. Polyethylene glycol, poly (l-glutamic acid) (PGA), and N-(2-hydroxypropyl)methacrylamide (HPMA) are examples of polymers that have been

accepted into clinical practice [71]. Currently, more than fourteen polymer–drug conjugates have undergone clinical evaluation and a polyglutamic acid (PGA)-paclitaxel conjugate (CT-2103, OPAXIO®, previously known as Xyotax®) is expected to enter the market in the near future [71, 72]. Since these polymers have the multivalent functional groups, recent research efforts have synthesized conjugates with a combination of drugs to the polymer chains and demonstrated synergistic efficacy. HPMA copolymer carrying the combination of the aromatase inhibitor aminoglutethimide and doxorubicin was the first report of these types of conjugates [73]. Drugs were linked through a biodegradable linker and a loading capacity was approximately 5% w/w for aminoglutethimide and 7% w/w for doxorubicin. The data suggested that the conjugate carrying both drugs was more active than the combination of two polymer conjugates each carrying a single drug [73]. A follow on study investigated the mechanism of synergy and suggested that such increased activity could be due to a variety of factors, including drug release rate, conjugate conformation in solution and possibly, activation of certain molecular pathways (induction of apoptosis)[74]. Santucci et al used PEG to conjugate the chemotherapeutic agent epirubicin (EPI) and the diffusible messenger nitric oxide (NO). Authors build a dendronised structure to one terminus of the PEG chain since unmodified PEG has a maximum loading capacity of two drug molecules per polymer chain [75]. This strategy also allowed to obtain two chemically distinct termini i.e. a carboxylic acid used for NO conjugation and a hydroxyl group to conjugate EPI.
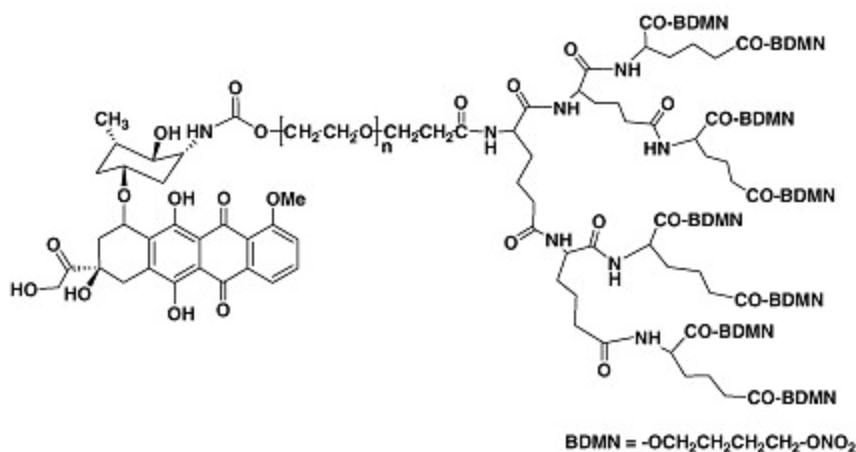
**EPI-PEG-(NO)8 conjugate**

**Figure 1.5.** Structure of dendronized EPI-PEG-(NO)$_8$ conjugate [75].

In cancer cells, EPI and NO act synergistically, conversely, in cardiomyocytes NO counterbalances EPI induced cardio-toxicity. In vivo studies confirmed that this conjugate displayed anticancer activity but was less cardio-toxic [75, 76].

Minko group synthesized a six-branched luteinizing hormone secreting hormone-targeted conjugate containing equimolecular amounts of camptothecin and BH$_3$. In vitro studies showed that such multicomponent conjugate was almost 100 times more cytotoxic than the single conjugates and displayed enhanced antitumour activity in vivo when compared with monotherapy [77].

Segal et al. developed an HPMA copolymer containing antiangiogenic agent, TNP-470 (Caplostatin) and the aminobiisphosphonate alendronate [78]. In this combination, alendronate has the double function of targeting moiety (to promote bone targeting) and of pharmacologically active agent. In vitro evaluation of this combination conjugate confirmed its synergy and in vivo results showed almost complete tumour regression observed in a human osteosarcoma model [78]. In another study, the same group

developed HPMA conjugate of alendronate and paclitaxel. Prostate and breast cancer cells showed anticancer and antiangiogenic activity in in vitro experiments and suggest promising applications in bone metastasis.

Lammers et al synthesized and evaluated an HPMA-based polymer–drug conjugate carrying 6.4 wt% of gemcitabine and 5.7 wt% of doxorubicin [79]. The resulting construct had able to effectively kill cancer cells in vitro, to circulate for prolonged period of time, to localize to tumors relatively selectively, and to inhibit tumor growth. As compared to free drug, polymer-dug conjugate increased the efficacy of the combination of gemcitabine and doxorubicin without increasing its toxicity, and it more strongly inhibited angiogenesis and induced apoptosis [79]. Another HPMA-conjugate carrying the doxorubicin and the anti-inflammatory agent dexamethasone was reported [80]. The conjugate with a combination of two drugs showed better therapeutic activity that the individual drug conjugates. Doxorubicin and a phosphatidylinositol-3 kinase inhibitor wortmannin were conjugated alone or combination onto poly(ethylene glycol)-poly(aspartate hydrazide) block copolymers through a hydrazone bond [81]. Polymer–drug conjugates assembled into a unimodal micelle structure with a < 100 nm particle size. Wortmannin enhanced the efficacy of doxorubicin through an efficient combination delivery accompanied by synergistic drug action.

### 1.5.3. Polymeric micelles

Amphiphilic block or graft copolymers comprised of two or more chains with different hydrophobicity have been used extensively in pharmaceutical applications ranging from sustained-release technologies to gene delivery. These copolymers are known to spontaneously self-assemble in an aqueous solution into nanoscopic polymeric

micelles (10 to 100 nm) having fairly narrow size distribution. The nature of the self-assembly process allows for significant versatility in the chemical composition of the polymeric micelles and thus permits fine tuning of the material properties, morphology and sizes. These micelles have unique core-shell architectures with hydrophobic polymer chains segregating into a micelle core surrounded by a shell of hydrophilic chains. Hydrophobic drugs can be entrapped into the micelle core non-specifically through hydrophobic interactions or specifically by chemical conjugation to the core-forming block of the copolymer via a carefully designed pH- or enzyme-sensitive linker that can be cleaved to release a drug in its active form. A variety of drugs with diverse physicochemical properties can be incorporated into the core by engineering the structure of the core-forming segment of the copolymer to attain sufficiently strong interaction with drug molecules. These polymeric micelle systems can also be used for co-delivery of two or more drugs with similar or different properties for combination therapy, or to combine multiple modalities within a single carrier (Fig. 1.6).
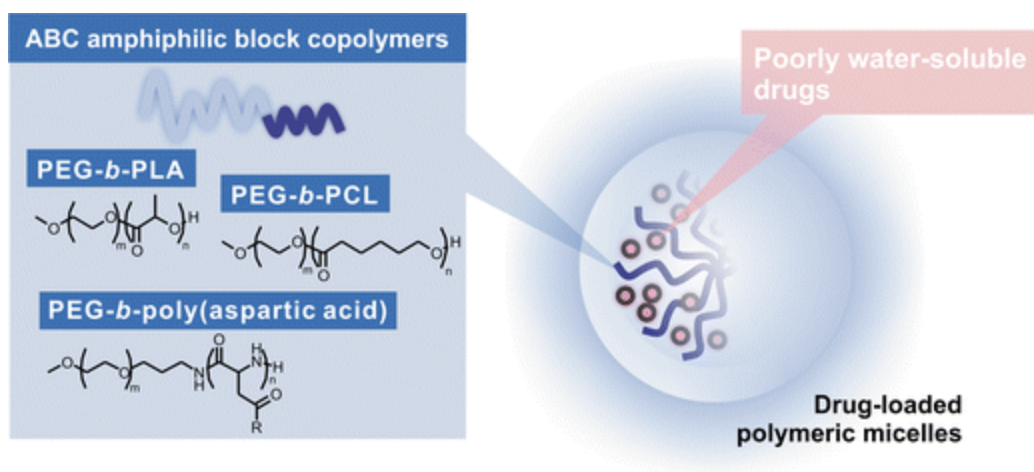


**Figure 1.6.** Multi-drug polymeric micelles for drug delivery. Adapted from [82].

Simultaneous delivery of chemotherapeutic drugs by polymeric micelles improves safety, and may permit anticancer agents to act at solid tumors at the same time, aiming for

synergistic drug interaction [83-85]. Multi-drug delivery is very often realized by the step-wise physical loading of an anticancer agents in a polymeric micelle. Multi-drug polymeric micelles may release physically loaded drug(s) by disassembly of polymeric micelles in blood and/or by diffusion. Drug release tends to be rapid in vivo, and in vitro results must be interpreted with caution due to poor in vitro/in vivo correlation. Thus, while EPR targeting of solid tumors is feasible with physically loaded drug, it is regarded as challenging, and research on multidrug polymeric micelles for tumor targeting deserves more attention. Another way for multi-drug loading is via chemical conjugation, a reversible covalent linkage is required between an anticancer agent and a block copolymer. Drug release from multi-prodrug polymeric micelles may occur by simple hydrolysis or stimuli- /environment dependent release and may be tuned by choice of chemical linkage, e.g., esters, and spacer groups [54, 86]. Shin et al attempted to physically co-incorporate three hydrophobic drugs, PTX, rapamycin, and 17-AAG in Poly(ethylene glycol)-block-poly(d,l-lactic acid) (PEG-*b*-PLA) micelles using a simple solvent evaporation method in various drug(s)-in-micelle combinations (Fig. 1.7) [87].
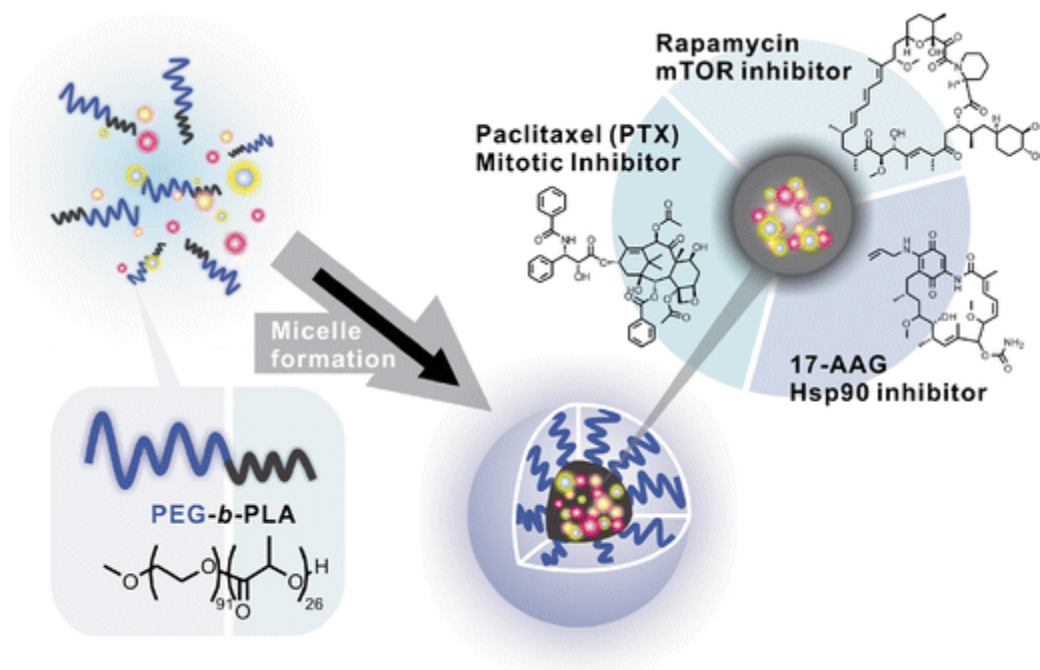
**Figure 1.7.** PEG-*b*-PLA micelles for the delivery of PTX, rapamycin, and 17-AAG. Adapted from [87].

Three drug-loaded PEG-b-PLA micelles had a 10–10,000-fold increase in aqueous solubility of PTX, rapamycin, and 17-AAG (up to 7.2, 3.3, and 7.3 mg/mL, respectively). PEG-b-PLA micelles delayed release of three drugs compared to single drug-loaded micelles in vitro. Simultaneous delivery of PTX, rapamycin, and 17-AAG via 3-in-1 PEG-b-PLA micelles (particle size of ca. 30–40 nm) at 60, 30, and 60 mg/kg, respectively IV injection caused durable antitumor responses in A549 human non-small cell lung cancer and MDA-MB-231 human breast cancer xenograft models with acceptable acute toxicity [84]. Na et al studied the antitumor effects of 5-fluorouracil, CDDP, CPT-11, oxaliplatin, etoposide, mitomycin-C, doxorubicin and PTX by determination of in vitro cytotoxicity to CT-26 colorectal tumor cells or in vivo following a subcutaneous transplant in BALB/c mice [88]. Single agent and combination in vivo studies were performed using drug-loaded polymeric micelles composed of poly(γ-benzyl

l-glutamate) and poly(ethylene oxide) (GEG) or poly(l-lactide)/poly(ethylene glycol) (LE) diblock copolymer. When tumor cells were exposed to doxorubicin concurrently with etoposide or paclitaxel, evidence of synergy was observed in CT-26 cells in vitro. Doxorubicin and paclitaxel loaded into GEG or LE copolymers at a high concentration (19.5 and 16.7 wt%, respectively) were almost completely released (83.2% and 93.7%, respectively) by day 3. When tumor-bearing mice were treated in combination with doxorubicin–paclitaxel or doxorubicin–etoposide, substantial antitumor activity was evident compared with single therapy. These data suggest that chemotherapy using micelle-loaded anticancer drugs represents a promising potential as a carrier system in modulating drug delivery. In another study, wang at al reported core-shell-type micelles that were doubly emulsified from an amphiphilic copolymer methoxy poly(ethylene glycol)-poly(lactide-co-glycolide) (mPEG-PLGA) [89]. These micelles offered advantages over other nanocarriers, as they were easy to fabricate by improved double emulsion method, biocompatible, and showed high loading efficacy. More importantly, these micelles could co-deliver hydrophilic doxorubicin and hydrophobic PTX. The drug-loaded micelles possessed a better polydispersity, indicating that they are more readily subject to controlled size distribution. Co-delivery nanocarrier suppressed tumor cells growth more efficiently than the delivery of either doxorubicin or PTX at the same concentrations, indicating a synergistic effect. Moreover, the drug-loaded micelles with a DOX/PTX concentration ratio of 2:1 showed the highest anti-tumor activity to three different types of tumor cells. Kabanov and collaborators reported amphiphilic poly(2-oxazoline)s (POx)-based micelles as a promising high capacity delivery platform for multidrug cancer chemotherapy [85]. A variety of binary and ternary drugs combinations

of PTX, docetaxel, 17-AAG, etoposide and bortezomib were solubilized in defined polymeric micelles achieving unprecedented high total loading capacities of up to 50 wt % drug per final formulation. Multi-drug loaded POx micelles showed enhanced stability in comparison to single-drug loaded micelles. Drug ratio dependent synergistic cytotoxicity of micellar etoposide /17-AAG was observed in MCF-7 cancer cells and of micellar bortezomib /17-AAG in MCF-7, PC3, MDA-MB-231 and HepG2 cells.

Katragadda et al developed a micellar nanocarriers for concomitant delivery of PTX and 17-AAG for cancer therapy [90]. PTX and 17-AAG were simultaneously loaded into polymeric micelles by a solvent evaporation method. Two candidate nanocarrier constructs, PEG–PLA-based micelles and PEG-distearoylphosphatidylethanolamine/tocopheryl polyethylene glycol 1000 (PEG-DSPE/TPGS)-based mixed micelles, were assessed for the release kinetics of the loaded drugs. Compared to PEG–PLA micelles, entrapment of paclitaxel and 17-AAG into PEG-DSPE/TPGS mixed micelles resulted in significantly prolonged release half-lives. Paclitaxel/17-AAG-loaded PEG-DSPE/TPGS mixed micelles were as effective in blocking the proliferation of human ovarian cancer SKOV-3 cells as the combined free drugs. There are plenty of other examples of use of micelles a carrier of drug combinations. This section only covers the most relevant examples. For detailed information about the application of polymeric micelles as a multi-drug vehicles, please see the review by cho et al [82].

### 1.5.4. Nanogels

Nanogels are three-dimensional hydrogel materials in the nanoscale size range formed by crosslinked swellable polymer networks with a high capacity to hold water,

without actually dissolving into the aqueous medium. Nanogels can be composed of a variety of naturally occurring polymers, synthetic polymers or a combination thereof. Their characteristics such as size, charge, porosity, amphiphilicity, softness, and degradability can be fine-tuned by varying the chemical composition of the nanogels. They are mostly spherical particles but the current advancement in synthetic strategies allow for the fabrication of nanogels of different shapes [91, 92]. They can be also designed to have either a core-shell or a core-shell-corona structure, with at least one of the layers crosslinked for structural integrity. Being mostly hydrophilic in nature, nanogels are highly biocompatible with a high loading capacity for guest molecules and their unique physical properties offer them distinct advantages over other types of nanomaterials for biomedical applications. Nanogels not only protect the cargo from degradation and elimination but also participate actively in the delivery process due to their characteristic properties like stimuli-responsive behavior, softness and swelling to help achieve a controlled, triggered response at the target site [93-95]. The versatility of their architecture allows for incorporation of a plethora of guest molecules ranging from inorganic nanoparticles to biomacromolecules like proteins and DNA with suitable modifications of the materials used for their construction, without compromising their gel-like behavior [96-99]. This multifunctionality and stability is hard to find in other types of nanoparticulate systems [100, 101]; especially the ability to incorporate entities with very different physical properties within the same carrier. Inorganic nanomaterials have distinct material properties like optical activity, electrical conductivity and magnetic properties that make them suitable for in vivo diagnostic and imaging applications, but they suffer from limitations of poor colloidal stability, low aqueous solubility and rapid

elimination by the mononuclear phagocytic system (MPS). Polymeric nanogels can be used as carriers for such imaging probes by imparting stability and increasing their utility. This lead to the evolution of a new class of agents termed 'nanohybrids' which are nanogels incorporating inorganic materials [102, 103]. Such nanohybrids can contain a wide variety of diagnostic and imaging agents for different types of medical conditions. Nanogels prevent biomolecules like enzymes and genetic material from degradation while their own macromolecular properties help increase the circulation half-lives of small molecules, and serve as a highly convenient platform for combination delivery of therapeutic molecules. They can be targeted specifically to the site of interest by conjugation with a targeting ligand or due to the passive targeting that is a characteristic feature of their nanoscale size. Despite such diversity in their applications, nanogels are not yet a part of clinical use. Many comprehensive and more specialized review articles on synthesis and application of nanogels were recently published.

### 1.5.4.1.    Synthesis of nanogels

Nanogels can be synthesized by a number of techniques. Since an in-depth discussion of all the available techniques is beyond the scope of this review, a brief overview of the techniques is given, along with reference to more detailed sources. Traditionally, nanogels have been classified based on the method of crosslinking as either physically or chemically (covalently) crosslinked nanogels. Chemical crosslinking involves formation of covalent bonds between the polymer chains during polymerization of low molecular weight monomers or crosslinking of polymer precursors. The most extensively employed methods for preparing chemically crosslinked nanogels utilize heterogeneous polymerization reactions in the presence of either bifunctional or multifunctional

crosslinkers [104, 105]. Conventional and controlled/living radical polymerization techniques allow for preparation of nanogels with different composition, dimensions, and architectures including core-shell and hollow nanogel particles [106, 107]. The use of functional initiators and macroinitiators further allows the incorporation of functionalities in the interior or on the surface of nanogels, which facilitate multivalent bioconjugation [108]. A variety of other crosslinking approaches including click chemistry, Schiff-base reactions, thiol-disulfide exchange, amide crosslinking, photo-induced crosslinking, enzyme-mediated crosslinking etc., have been developed for the synthesis of nanogels from the polymer precursors. In addition, the crosslinking reactions carried out on preformed core-shell self-assemblies such as polymer micelles allow introducing a high degree of spatial organization into the nanogels [109]. For a comprehensive look into crosslinking strategies, the reader is directed to excellent review written by Haag and colleagues [110]. Recent advances in nanoscale fabrication methods provided further unique opportunities to fabricate well-defined nanogels with precise control over size, shape, deformability and surface chemistry in a high-throughput manner [111-113]. Physically crosslinked systems though formed under the mild conditions, tend to be more fragile than their covalently crosslinked counterparts since they are stabilized by relatively weak interactions between polymer chains such as hydrogen bonding, hydrophobic interactions or ionic interactions. The use of hydrophobically-modified polymers and other associating polymers for preparing functional nanogels has recently been reviewed by Sasaki and Akiyoshi [114]. One of the challenges in the formation of nanogels by such polymers is a control over the particle size, which requires fine-tuning of the polymer concentrations or environmental parameters such as temperature, pH, and

ionic strength. A study by Nielsen and co-workers has demonstrated that these challenges can be addressed by utilizing a microfluidics-based approach [115]. Overall, the advances in polymer chemistry led to the exceptional diversity and control over the composition, architecture and functionality of crosslinked nanogels, which in turn provide more flexibility to tune their properties to comply with targeted biomedical applications.

### 1.5.4.2.  Stimuli-responsive behavior

Stimuli-responsive behavior of nanogels is a sequence of events initiated by an external cue that comes either from the specific environment within the body like change in pH, temperature, redox conditions or enzyme concentration, or a stimulus that can be applied externally such as light, magnetic field, etc. This stimulus then causes a conformational or structural change in the nanogel, which is mediated by various factors including, but not limited to, transition in the temperature below or above its lower critical solution temperature (LCST) or the ionization of acidic or basic functional groups on the polymer chains. These changes also alter the hydrophilicity and/or hydrophobicity of the nanogels or, in other words, the extent of interaction of the system with water molecules [116-118] and is mostly manifested in the form of swelling or deswelling of the nanogel network, which in turn causes responses like release of the entrapped cargo [119, 120]. One of the considerable advantages of nanogels over the macroscopic gels is their very rapid response to a change in environmental conditions [121]. The responsiveness of nanogels to the external physical or chemical signals can be tightly regulated by controlling the structure of the materials used for preparation of the nanogels [93, 122]. For example, in the case of polyelectrolyte nanogels pH-dependent ionization of functional groups results in an increase of osmotic pressure inside the nanogel due to

entrapped counterions and ultimately results in the swelling of the nanogels [122-124]. It is well recognized that a balance between the osmotic pressure and the polymer elasticity sets the physical dimensions of a hydrogel particle [125]. Thus, the extent of swelling also depends on structural characteristics of the nanogel like the chemical composition, hydrophilicity of crosslinkers, and the degree of crosslinking of the nanogel network, which controls the freedom of conformational mobility of the polymer chains [126, 127]. Tan et al. studied pH-responsive polyampholyte nanogels with different fractions of methacrylic acid (MAA) and 2-diethylaminoethyl methacrylate (DEAM) units in the crosslinked polymer cores that were sterically stabilized by poly(ethylene glycol), PEG, shell [128] The MAA segment in this nanogel is a weak acid and DEAM is a weak base (pKa = 5.4 for MAA and pKa = 7.3 for DEAM). The DEAM segments could be protonated at low pH, imparting a positive charge to this segment, whereas the MAA units are negatively charged at high pH. As a result, these nanogels exhibited marked swelling at both high and low pH values, but shrunk in the vicinity of isoelectric point due to overall charge neutralization. It was demonstrated that swelling-deswelling transition can be tuned by varying the composition of MAA and DEAM in the nanogels. The unique charge-switching properties of amphoteric nanogels based on poly(N-isopropylacrylamide) functionalized with aminophenylboronic acid (PBA) were explored by Hoare and Pelton to regulate the release of preloaded insulin in glucose-dependent manner [129]. The binding of glucose to the PBA residues shifts the boronic acid ionization equilibrium, increases the anionic charge density on the gel and drives a gel swelling response. These nanogels were designed to both swell and deswell in response to glucose according to the pH of the medium, the concentration of PBA groups grafted

to the nanogel, and the relative concentrations of the cationic and anionic functional groups in the platform nanogel. Such PBA-nanogels had a high capacity for insulin uptake and selectively released insulin under physiological conditions in an "on-off" manner with fluctuating glucose level. Similar approach was adapted by Wu et al. for the design of a nanogel-based glucose sensor, which comprised of a core of Ag nanoparticle encapsulated within a glucose-recognizing crosslinked shell containing PBA residues. The swelling of the gel in response to glucose binding causes a change in the refractive index of the medium around Ag nanoparticle that leads to change in its fluorescence properties. The response rate is reported to be on the order of 100 ns, and the detection sensitivity for change in glucose concentration was reported to be $\pm$ 0.1 mM [130]. Thus, both sensitivity and rate of response of the nanogels can be programmed and fine-tuned by alterations in the structure of the building blocks [93, 122]. Accordingly, the cargo (mostly drugs) can either be conjugated chemically to the nanogels or merely entrapped physically into its core [15], depending on the stimulus that is most feasible for utilization at the targeted site of disease. Often multifunctional nanogels, which respond to a combination of more than one external signal, can also be fabricated for more site-specific response [131-133]. These stimuli are frequently disease- or organ-specific, since different pathological conditions are associated with changes in pH, temperature and redox balance or expression levels of certain biomolecules as compared to the normal physiological conditions [134]. The reversible crosslinks containing disulfide bonds that are stable in extracellular milieu but are cleaved in the reductive intracellular environments due to the differences in the reductive potential between the extracellular and intracellular compartments, are successfully utilized in design of redox-responsive

nanogels [132, 135, 136]. The nanogels with disulfide links are stable during circulation in the blood but labile while internalized in cells, thus, facilitating the release of the drug. Matyjaszewski et al. have prepared biodegradable nanogels with disulfide-functionalized dimethacrylate crosslinkers that degraded into individual polymeric chains in the presence of glutathione and enabled both the release of encapsulated cargos and the removal of the carriers [137]. Thayumanavan and coworkers reported the preparation of redox-sensitive nanogels based on random amphiphilic copolymer that contains hydrophilic oligoethyleneglycol (OEG) and hydrophobic pyridyldisulfide (PDS) units as side-chain functionalities [138]. Self-assembled nanostructures formed by this polymer were crosslinked by initiating a thiol-disulfide exchange reaction among the PDS groups using dithiothreitol (DTT). The size of the resulting nanogels can be tuned by varying the copolymer molecular weight, composition and concentration, while the extent of crosslinking can be controlled by the amount of added DTT. The release of the encapsulated doxorubicin (DOX) was triggered by glutathione treatment and the release rate can be tuned by adjusting the crosslinking density.

### 1.5.4.3.    Nanogels as a therapeutic drug carrier

Nanogels are highly swollen and can incorporate 30% wt. or more of biological molecules and drugs through electrostatic, van der Waals and/or hydrophobic interactions or covalent bonding with the polymer chains. These loading capacities are unusually high and exceed those of liposomes and polymeric micelles. As a result of drug loading, the nanogels collapse forming stable nanoparticles, in which biological agent becomes entrapped. Introducing dispersing hydrophilic polymers (e.g., PEG) in a nanogel structure can prevent their aggregation. During the collapse of the drug-nanogel complex hydrophilic polymer chains become exposed at the surface and form a protective layer

around the nanogel. The control and versatility of polymer chemistry allows designing a broad range of drug formulations and inclusion of multiple therapeutic cargos within the same nanogel carrier. Stimuli-responsive drug release via temperature or pH-induced volume collapse can also be very attractive for drug delivery applications. The functionalization of the nanogel surface can further facilitate their selective accumulation in the target tissue or cells. Development of nanogels that can carry, protect, target and release therapeutic agents in spatially and temporally controlled manner is actively ongoing and their rational design can provide a platform for multiple applications. The group of Wang took advantage of the activity of bacterial lipases, which are abundant in microbial flora, to construct a nanogel for the on-demand release of antibiotics [134]. In this approach, the triple-layered nanogel contains a hydrophobic lipase-sensitive poly(ε-caprolactone) (PCL) interlayer between the crosslinked polyphosphoester core and the PEG shell. Prior to reaching sites of bacterial infection, the antibiotics are protected inside the polyphosphoester core and are not released due to the compacted PCL molecular fence. However, rapid drug release was observed in the presence of lipase or lipase-secreting bacteria.

### 1.5.4.3.1. Nanogels for small therapeutic molecule delivery

Over the past few years, significant progress has been achieved in application of nanogels as a delivery carrier for small biologically active molecules. Nanogels can be a versatile platform for the incorporation of various small drug molecules through the combination of electrostatic and hydrophobic interactions as well as hydrogen-bond formation [139]. The swelling of nanogels in an aqueous environment allows for easy permeation of the cargos. The rational design of the nanogels might be an effective tool

to tune the drug release rates, to affect carrier-cell interactions, and achieve desirable therapeutic effect of the drugs. One of the most important features of weakly-crosslinked polyelectrolyte nanogels is their ability to incorporate molecules of the opposite charge. For example, cationic crosslinked PEG-polyethyleneimine (PEG-PEI) nanogels were explored for immobilization of negatively charged biologically active compounds such as retinoic acid, indomethacin or valproic acid [139, 140]. These drug formulations formed stable colloidal dispersions at physiological pH and ionic strength, could be lyophilized and then redispersed. Similar nanogels and complexation strategy has been successfully utilized for incorporation of various nucleoside analog 5′-triphosphates [141, 142]. It was reported that these drug-loaded nanogels could improve the delivery of the active triphosphates of therapeutic nucleoside analogs into cancer cells and inhibited tumor growth in the mammary carcinoma animal model [142]. Recently, the same group demonstrated the significant advantage of active 5′-triphosphates of nucleoside reverse transcriptase inhibitors encapsulated in cationic nanogels over free drugs in the antiviral therapy of HIV-1 infection in the central nervous system (CNS) [143]. Our group utilized a controlled template synthesis of nanogels by polyion complexation and crosslinking of doubly hydrophilic block ionomers, such as PEG-b-poly(methacrylic acid) (PEG-b-PMA) [123, 144]. The resulting nanogels have swollen cores of a crosslinked PMA network surrounded by a shell composed of PEG chains. This synthetic approach allows versatile control of the macroscopic properties of nanogels (size, degree of swelling, drug loading) by changing the number and the chemical structure of the crosslinks [144]. Notably, in contrast to many nanoparticles these anionic nanogels exhibited very low nonspecific adhesion to nontargeted surfaces, which can minimize their off target effect

and facilitate target-specific delivery [145]. Such core-shell nanogels can incorporate very large amounts (up to 50% wt.) of weakly basic drug DOX through electrostatic coupling with carboxylic groups in the cores. DOX-loaded nanogels were stable for a prolonged period of time, exhibited noticeable pH-sensitive behavior with accelerated release of DOX in acidic environment due to the protonation and swelling of the nanogel crosslinked cores, and demonstrated cytotoxic activities in cancer cell lines [146]. Introduction of reversible crosslinks with disulfide bonds in the PMA ionic cores (cystamine was used as a biodegradable crosslinker) allowed developing nanogels that are degradable in the presence of the reducing agent (glutathione, cysteine), which in turn facilitated the release of the incorporated DOX [146]. This difference in the release kinetics led to considerable increase of cytotoxicity: degradable DOX-loaded nanogels displayed nearly six-fold higher cytotoxic activity than non-degradable nanogels. Shi et al. used PEG-poly(L-glutamic acid-co-L-cystine) copolymers to prepare nanogels stabilized by disulfide bridges and also demonstrated that DOX release was accelerated in intracellular reductive and acidic conditions [147]. DOX was loaded into these polypeptide-based nanogels, and an accelerated release was observed in glutathione monoester pretreated HeLa cells. Anionic PEG-b-PMA nanogels were further used to encapsulate hydrophilic drug cisplatin through coordination interactions with COOH functionalities [123]. Cisplatin-loaded nanogels displayed pH-sensitive release of Pt species in sustained manner that can be effectively controlled by adjusting the degree of crosslinking of the crosslinked cores. The released platinum species retained their activity and were able to form Pt adducts with nuclear DNA in the cancer cells [123]. It was shown that loading of cisplatin into the nanogels greatly improved drug therapeutic index

by improving PK, enhancing tumor delivery, increasing antitumor efficacy, and mitigating the cisplatin-mediated nephrotoxicity in a mouse model of ovarian cancer [148]. When the same cispaltin-loaded nanogels were also decorated with targeting ligands (e.g. folate or LHRH peptide), tumor growth inhibition could be even further enhanced [149, 150]. Peng et al. described dual pH- and temperature-responsive nanogels based on N-isopropylacrylamide, MAA, and PEG methylether methacrylate (NIPAAm-MAA-PEGMA) for the entrapment and release of cisplatin. It was shown that cisplatin release can be accelerated at acidic pH, and could be additionally controlled by the temperature change due to the deswelling behavior of these nanogels at the body temperature [151]. Small molecules usually contain only limited number of ionic groups, which are able to interact with oppositely charged nanogels, and complementary hydrophobic, hydrogen or coordination bonding between drug molecules and nanogels can further stabilize the electrostatic pairing [139]. Recently, our laboratory demonstrated that microenvironment formed by the hydrophobic domains in the nanogel ionic cores influences solubilization capacity and release characteristics of the nanogels [152]. Diblock copolymer, PEG-b-poly(L-glutamic acid), hydrophobically-modified with L-phenylalanine methyl ester moieties was used for the synthesis of nanogels with small size (ca. 70nm in diameter) and narrow particle size distribution. Stable DOX-loaded hybrid nanogels were prepared at high DOX capacity (30% wt.). It was shown that the release rates of DOX from hydrophobically-modified carriers were substantially less compared to nonmodified nanogels: a burst release of over 85% of the incorporated drug within 8h for nonmodified nanogels was observed while only ~20% of the incorporated DOX was released from hydrophobically-modified nanogels during the same period of

time. These results suggested that intermolecular interactions in combination with more compact crosslinked core could account for the delayed and controlled release of DOX from hydrophobically-modified polyelectrolyte nanogels. It was also found that these DOX-loaded nanogels exhibited an improved antitumor efficacy compared to free DOX in an ovarian tumor xenograft mouse model.

Nanogels have also been explored as a carrier for poorly water-soluble drugs. Wang et al. introduced thermoresponsive nanogels based on chitosan–poly(NIPAAm-co-acrylamide) for the delivery of paclitaxel (PTX) [153]. Loading capacity of these nanogels for PTX was around 9% wt. and drug-nanogel formulation showed very good colloidal stability. This nanogel released PTX in a temperature-dependent manner wherein significantly faster drug release was achieved at higher temperature. Moreover, PTX-loaded nanogels demonstrated improved antitumor efficacy in mice bearing HT-29 colon carcinoma tumors after intravenous administration. In another study by Gref and coworkers, hydrophobic molecule benzophenone (widely used as sunscreen agent) was solubilized into nanogels formed spontaneously upon the association of a lauryl-modified dextran and a β-cyclodextrin polymer in aqueous media [154]. The highest benzophenone loadings (about 2.5 % wt.) were obtained by solubilizing it in both polymer solutions before mixing them to form nanogels. Such nanogel-based formulations present a compelling future opportunity for the application in the cosmetic field as sun screen carriers prepared by a simple "green" technology. The use of nanogels for the development of long-lasting formulations of local anesthetics has recently been reviewed by Tan et al [155]. Eckmann and colleagues explored biocompatible physically crosslinked hybrid nanogels consisting of a partially denatured lysozyme cores and

dextran shells for the local delivery of dexamethasone to alleviate acute pulmonary inflammation [156]. To target the pulmonary vasculature, nanogels were coated with antibodies directed to endothelial determinant, Intercellular Adhesion Molecule-1 (ICAM). The synthesized ICAM- targeted nanogels were loaded with dexamethasone at 5% wt. In vivo studies in animal model of LPS-induced lung injury showed that nanogels targeted to lungs succeeded in delivering encapsulated dexamethasone, as was indicated by drastic reduction in pulmonary vasculature inflammation to levels found in naïve mice. In other work, similar dextran-lysozyme nanogels were utilized as scaffolds for the in situ synthesis of silver nanoparticles [157, 158]. Such hybrid nanogels exhibited bactericidal properties towards E. coli and bacteriostatic properties towards S. aureus, and their antibacterial activity can be tuned by varying lysozyme content. The tunability of the hybrid nanogels makes it possible to optimize release of the bactericidal agent for specific clinical use and type of infection. Nagasaki's group used the protonated crosslinked poly(2-[N,N-diethylamino]ethyl methacrylate) (PEAMA) cores of the stimuli-responsive PEGylated nanogels for the synthesis of gold nanoparticles without any reducing agents ("gold nanogels") [159]. It was shown that the tertiary amino groups in the PEAMA gel core play a crucial role in the reduction of the Au(III) ions (nanoreactor) as well as the immobilization of the resulting gold nanoparticles (nanomatrix) to attain large payloads of gold nanoparticles. The resulting gold-containing nanogels showed a remarkable photothermal efficacy in response to laser-irradiation resulting in selective cytotoxicity in cancer cells. In other studies, a potential of the similar constructs to enhance cancer cell radiosensitivity was reported [160].

### 1.5.4.3.1.1. Nanogels for combination drug delivery

Drug combinations directed simultaneously at multiple pharmacological targets have the potential to dramatically improve the response to treatment and are already a standard clinical practice in the treatment of cancer and infectious diseases [161]. However, the difference in pharmacokinetic and pharmacodynamic profiles among diverse drug molecules makes dosing and scheduling optimization very challenging. Combining drugs in one delivery carrier is a well-suited strategy for controlling the pharmacokinetics and co-delivery of the desired drug ratio in vivo, and a variety of nanoscale carriers, including nanogels, have been investigated in terms of their ability to deliver multiple drugs [162, 163]. As highlighted in previous sections, the nanogel structure can be readily adjusted to integrate features of different materials and, thus, offer advantages for combinatorial encapsulation of drugs with varying physicochemical properties such as small molecules, proteins and nucleic acids. Fahmy and coworkers developed liposomal nanogels of drug-complexed cyclodextrins and cytokine-encapsulating biodegradable polymers that can deliver small hydrophobic molecular TGF-$\beta$ inhibitor and water-soluble protein cytokine (IL-2) in a sustained fashion to the tumor microenvironment [164]. They demonstrated that synergistic effects of simultaneously delivered IL-2 and TGF-$\beta$ inhibitor on activation of the innate arm of the immune system led to delayed tumor growth and enhanced survival of melanoma tumor-bearing mice after systemic administration. Akiyoshi and colleagues evaluated nanogels based on acrylate group–modified CHP for co-delivery of prostaglandin E2 receptor–specific agonist EP4A (small molecule) in combination with bone morphogenic proteins (BMP-2) for bone regeneration [165]. In this study, EP4A-containing nanogels and BMP-2-containing nanogels were crosslinked

with thiol-bearing PEG to obtain disc-like scaffolds for the implantation into large bone defects. Combination treatment with EP4A and low-dose BMP-2 efficiently activated bone cells to regenerate calvarial bone by forming both outer and inner cortical plates as well as bone marrow tissue and resulted in the formation of enough bone to cover the defects in calvarial bone. In another study, cationic physically-crosslinked nanogels composed of a hexadecyl group-bearing cycloamylose and spermine-modified cycloamylose to complex and co-deliver plasmid DNA along with phospholipaseA2 (PLA2) [166]. As a lipolytic enzyme, PLA2 catalyzes hydrolysis of a variety of different phospholipids. Thus, being delivered into endosomes by nanogel it could disrupt the lipid membrane and subsequently trigger the release of the co-encapsulated DNA into the cytoplasm. Transfection experiments confirmed that DNA expression level was enhanced when complexed with PLA2. Similarly, pDNA and proteins were successfully co-encapsulated using pH- and temperature-sensitive carbohydrate-based nanogels [167]. The nanogels had a core-shell structure with a crosslinked hydrophobic core that could be loaded with proteins and the shell contained carbohydrate residues that allowed for the complexation of DNA. These nanogels were capable of loading larger-than-normal amounts of cargo by using a heating and cooling cycle. Altogether, these studies may open new avenues for the development of the carrier-mediated combination therapies.

## 1.6. Conclusion

Combination chemotherapy is preferred over treatment with single agents to combat most cancers as it targets multiple cell-survival pathways at the same time and delays the onset of resistance. This helps in achieving long-term tumor remission and increases median survival. Cisplatin (CDDP)-based therapy has been the standard treatment for

ovarian cancer since its discovery. After paclitaxel (PTX) was shown to be effective in ovarian cancer, multiple clinical trials studied the overall efficacy of CDDP and PTX and found significant benefit over the pre-existing treatments. Since then, this combination has been the treatment of choice for both early stage as well as advanced cases of ovarian cancer. However, administration of two different agents comes with the inconvenience of repeated or extended duration of drug infusion in patients. Moreover, the most extensively used conventional formulation of paclitaxel, Taxol®, utilizes Cremophor EL (polyethoxylated castor oil) that has been linked to significant toxicities including allergic, hypersensitivity and anaphylactic reactions during infusion that require premedication and prolonged peripheral neuropathy. Combining such drugs in one delivery carrier is therefore a well-suited and convenient strategy for controlling the pharmacokinetics and co-delivery of the desired drug ratio in vivo, to maximize the therapeutic potency and minimize drug-associated toxicities.

Cross-linked nanogels have been found to be promising drug carriers to achieve this goal. Being mostly hydrophilic in nature, nanogels are highly biocompatible with a high loading capacity for guest molecules. The nanogel structure can be readily adjusted to integrate features of different materials and, thus, offer advantages for combinatorial encapsulation of drugs with varying physicochemical properties. One of the widespread synthetic techniques for the synthesis of nanogels is the crosslinking of preformed core-shell self-assemblies such as polymer micelles that allows introducing a high degree of spatial organization into the nanogels. Cross-linking is known to impart control over the swelling behavior of the nanogels and thus helps in achieving controlled release of the incorporated cargo, which is an added advantage over the structural integrity imparted to

the carrier system upon in vivo administration. The enhanced stability also makes the prolonged circulation of the nanogels possible, which in turn allows for increased drug accumulation at the target site by enhanced permeability and retention effect (EPR). We report a design of multi-compartment cross-linked nanogels based on hybrid triblock copolymers, poly(ethylene glycol)-block-poly(L-glutamic acid)-block-poly(L-phenylalanine) (PEG-b-PGlu-b-PPhe) for simultaneous loading and delivery of binary CDDP and PTX combination. Such nanogels have 1) a hydrophobic core formed by PPhe chains, which serves as a reservoir for PTX solubilization, 2) an anionic layer, which incorporates CDDP through coordination with the carboxylic groups of PGlu, and 3) an outer PEG shell stabilized, which stabilizes micelles in aqueous dispersion. The crosslinks incorporated into PGlu block layer ensure that the PEG-b-PGlu-b-PPhe micelles remain stable until they encounter proteases, which degrade the micelles by cleaving the polypeptide chains of the block copolymers. This work demonstrates that such biodegradable hybrid micelles carrying CDDP and PTX drug combination exert superior antitumor efficacy in treatment of ovarian cancer in xenograft mouse tumor model. However, our system relied solely on the EPR effect to facilitate the delivery of the drug combination to the tumor site. Regardless of the importance and popularity of EPR effect-based drug delivery, this strategy has some limitations related to the inter- and intra-tumor heterogeneity, variations in the density as well as permeability of the tumor vasculature that can affect the accumulation of nanocarriers. One of the popular approaches to circumvent these problems is by surface-functionalization of the drug carrier with ligands that can target receptors with differential expression on the cancer cell surface, which helps in increasing the mean residence time of the delivery system at

the tumor site and improving target cell uptake. One such receptor of interest is the folate receptor (FR). Malignant cells, due to their high rate of cell division, have an increased requirement of folic acid (FA), since it is essential component of cell metabolism and DNA synthesis and repair. To fulfill this higher need of FA, FR is known to be over-expressed in a large number of malignant tissues, including ovarian cancer, compared to normal tissues with the exception of the kidney and choroid plexus. Furthermore, this receptor becomes accessible via the plasma compartment only after the cells lose their polarity owing to malignant transformation which makes it a differential target for cancer tissue that is easily accessible for intravenously administered FA conjugated systems. Its natural ligand, FA, comes with the advantages of high binding affinity, stability and a simple chemical structure together with ease of availability, making it a suitable targeting ligand for ovarian cancer therapy. FA can thus be successfully conjugated to macromolecular systems without loss of binding affinity to its receptor. Many different agents targeting the folate pathway are currently in clinical development. To date, FA-targeted agents showed significant promise in phase II clinical trials but it has not been confirmed in phase III studies. Accordingly, there is a need for further identification of new therapeutic combinations and refinement of patient selection. To this end, FA-conjugated imaging agents could be used for pre-selection of patients based on the expression of FR and several methods have been already developed for this purpose.

Our group has previously demonstrated a tumor-specific delivery and improved anti-cancer effect in vivo of CDDP-loaded nanogels decorated with FA targeting groups. In our further study, we designed FA-linked nanogels incorporating platinum-taxane combination, and examined whether FR-targeted concurrent delivery of synergistic

combination of CDDP and PTX can lead to enhanced therapeutic efficacy compared to

nontargeted NG system.

## 1.7. References

[1] D. Hanahan, R.A. Weinberg, The hallmarks of cancer, cell, 100 (2000) 57-70.
[2] M. Suggitt, M.C. Bibby, 50 years of preclinical anticancer drug screening: empirical to target-driven approaches, Clin Cancer Res, 11 (2005) 971-981.
[3] G.F. Ismael, D.D. Rosa, M.S. Mano, A. Awada, Novel cytotoxic drugs: old challenges, new solutions, Cancer Treat Rev, 34 (2008) 81-91.
[4] E. Frei 3rd, M. Karon, R.H. Levin, E.J. Freireich, R.J. Taylor, J. Hananian, O. Selawry, J.F. Holland, B. Hoogstraten, I.J. Wolman, The effectiveness of combinations of antileukemic agents in inducing and maintaining remission in children with acute leukemia, Blood, 26 (1965) 642.
[5] L.D. Mayer, A.S. Janoff, Optimizing combination chemotherapy by controlling drug ratios, Mol Interventions, 7 (2007) 216.
[6] T.O. Harasym, P.G. Tardi, N.L. Harasym, P. Harvie, S.A. Johnstone, L.D. Mayer, Increased preclinical efficacy of irinotecan and floxuridine coencapsulated inside liposomes is associated with tumor delivery of synergistic drug ratios, Oncology Research Featuring Preclinical and Clinical Cancer Therapeutics, 16 (2006) 361-374.
[7] W. Zoli, L. Ricotti, A. Tesei, F. Barzanti, D. Amadori, In vitro preclinical models for a rational design of chemotherapy combinations in human tumors, Crit Rev Oncol Hematol, 37 (2001) 69-82.
[8] T.-C. Chou, Drug combination studies and their synergy quantification using the Chou-Talalay method, Cancer Res, 70 (2010) 440-446.
[9] C.A. Dasanu, T.J. Herzog, D.T. Alexandrescu, Carboplatin—gemcitabine in the therapy of advanced ovarian cancer: dose reduction consideration, J Oncol Pharm Pract, 16 (2010) 63-66.
[10] S.V. Bava, V.T. Puliappadamba, A. Deepti, A. Nair, D. Karunagaran, R.J. Anto, Sensitization of taxol-induced apoptosis by curcumin involves down-regulation of nuclear factor-κB and the serine/threonine kinase Akt and is independent of tubulin polymerization, J Biol Chem, 280 (2005) 6301-6308.
[11] P. Parhi, C. Mohanty, S.K. Sahoo, Nanotechnology-based combinational drug delivery: an emerging approach for cancer therapy, Drug Discov Today, 17 (2012) 1044-1052.
[12] E.B.C.T.C. Group, Effects of chemotherapy and hormonal therapy for early breast cancer on recurrence and 15-year survival: an overview of the randomised trials, Lancet, 365 (2005) 1687-1717.
[13] E.B.C.T.C. GROUP, Systemic treatment of early breast cancer by hormonal, cytotoxic, or immune therapy: 133 randomised trials involving 31 000 recurrences and 24 000 deaths among 75 000 women, Lancet, 339 (1992) 1-15.
[14] B. Pauwels, A.E. Korst, F. Lardon, J.B. Vermorken, Combined modality therapy of gemcitabine and radiation, Oncologist, 10 (2005) 34-51.
[15] N.D. Nigro, V. Vaitkevicius, B. Considine, Combined therapy for cancer of the anal canal: a preliminary report, Dis Colon Rectum, 36 (1993) 709-711.

[16] L.M. DeAngelis, W. Seiferheld, S.C. Schold, B. Fisher, C.J. Schultz, Combination chemotherapy and radiotherapy for primary central nervous system lymphoma: Radiation Therapy Oncology Group Study 93-10, J Clin Oncol, 20 (2002) 4643-4648.

[17] D.J. Slamon, B. Leyland-Jones, S. Shak, H. Fuchs, V. Paton, A. Bajamonde, T. Fleming, W. Eiermann, J. Wolter, M. Pegram, Use of chemotherapy plus a monoclonal antibody against HER2 for metastatic breast cancer that overexpresses HER2, N Engl J Med, 344 (2001) 783-792.

[18] M. Czuczman, A. Grillo-Lopez, C. White, M. Saleh, L. Gordon, A. LoBuglio, C. Jonas, D. Klippenstein, B. Dallaire, C. Varns, Treatment of patients with low-grade B-cell lymphoma with the combination of chimeric anti-CD20 monoclonal antibody and CHOP chemotherapy, J Clin Oncol, 17 (1999) 268-268.

[19] K. Margolin, M. Gordon, E. Holmgren, J. Gaudreault, W. Novotny, G. Fyfe, D. Adelman, S. Stalter, J. Breed, Phase Ib trial of intravenous recombinant humanized monoclonal antibody to vascular endothelial growth factor in combination with chemotherapy in patients with advanced cancer: pharmacologic and long-term safety data, J Clin Oncol, 19 (2001) 851-856.

[20] T.P. Díaz-Montes, R.E. Bristow, Secondary cytoreduction for patients with recurrent ovarian cancer, Curr Oncol Rep, 7 (2005) 451-458.

[21] A. Rossof, R. Talley, R. Stephens, T. Thigpen, M. Samson, C. Groppe Jr, H. Eyre, R. Fisher, Phase II evaluation of cis-dichlorodiammineplatinum (II) in advanced malignancies of the genitourinary and gynecologic organs: a Southwest Oncology Group Study, Cancer Treat Reports, 63 (1978) 1557-1564.

[22] D.G. Decker, T.R. Fleming, G.D. Malkasian Jr, M.J. Webb, J.A. Jefferies, J.H. Edmonson, Cyclophosphamide plus cis-platinum in combination: treatment program for stage III or IV ovarian carcinoma, Obstetrics & Gynecology, 60 (1982) 481-487.

[23] M.J. Piccart, K. Bertelsen, K. James, J. Cassidy, C. Mangioni, E. Simonsen, G. Stuart, S. Kaye, I. Vergote, R. Blom, Randomized intergroup trial of cisplatin–paclitaxel versus cisplatin–cyclophosphamide in women with advanced epithelial ovarian cancer: three-year results, J Natl Cancer Inst, 92 (2000) 699-708.

[24] W.P. McGuire, W.J. Hoskins, M.F. Brady, P.R. Kucera, E.E. Partridge, K.Y. Look, D.L. Clarke-Pearson, M. Davidson, Cyclophosphamide and cisplatin compared with paclitaxel and cisplatin in patients with stage III and stage IV ovarian cancer, N Engl J Med, 334 (1996) 1-6.

[25] M. Cristea, E. Han, L. Salmon, R.J. Morgan, Review: Practical considerations in ovarian cancer chemotherapy, Ther Adv Med Oncol, 2 (2010) 175-187.

[26] K. Bertelsen, S. Grenman, G. Rustin, How long should first-line chemotherapy continue?, Ann Oncol, 10 (1999) 17-20.

[27] J.G. Schneider, Intraperitoneal chemotherapy, Obstet Gynecol Clin North Am, 21 (1994) 195-212.

[28] R. Pretorius, N. Hacker, J. Berek, L. Ford, J. Hoeschele, T. Butler, L.a. Lagasse, Pharmacokinetics of Ip cisplatin in refractory ovarian carcinoma, Cancer Treat Reports, 67 (1983) 1085-1092.

[29] E. Casper, D. Kelsen, N. Alcock, J. Lewis Jr, Ip cisplatin in patients with malignant ascites: pharmacokinetic evaluation and comparison with the iv route, Cancer Treat Reports, 67 (1983) 235-238.

[30] P. Francis, E. Rowinsky, J. Schneider, T. Hakes, W. Hoskins, M. Markman, Phase I feasibility and pharmacologic study of weekly intraperitoneal paclitaxel: a Gynecologic Oncology Group pilot Study, J Clin Oncol, 13 (1995) 2961-2967.

[31] M. Markman, E. Rowinsky, T. Hakes, B. Reichman, W. Jones, J. Lewis, S. Rubin, J. Curtin, R. Barakat, M. Phillips, Phase I trial of intraperitoneal taxol: a Gynecoloic Oncology Group study, J Clin Oncol, 10 (1992) 1485-1491.

[32] D.K. Armstrong, B. Bundy, L. Wenzel, H.Q. Huang, R. Baergen, S. Lele, L.J. Copeland, J.L. Walker, R.A. Burger, Intraperitoneal cisplatin and paclitaxel in ovarian cancer, N Engl J Med, 354 (2006) 34-43.

[33] M. Markman, B.N. Bundy, D.S. Alberts, J.M. Fowler, D.L. Clark-Pearson, L.F. Carson, S. Wadler, J. Sickel, Phase III trial of standard-dose intravenous cisplatin plus paclitaxel versus moderately high-dose carboplatin followed by intravenous paclitaxel and intraperitoneal cisplatin in small-volume stage III ovarian carcinoma: an intergroup study of the Gynecologic Oncology Group, Southwestern Oncology Group, and Eastern Cooperative Oncology Group, J Clin Oncol, 19 (2001) 1001-1007.

[34] D.S. Alberts, P. Liu, E.V. Hannigan, R. O'Toole, S.D. Williams, J.A. Young, E.W. Franklin, D.L. Clarke-Pearson, V.K. Malviya, B. DuBeshter, Intraperitoneal cisplatin plus intravenous cyclophosphamide versus intravenous cisplatin plus intravenous cyclophosphamide for stage III ovarian cancer, N Engl J Med, 335 (1996) 1950-1955.

[35] R.F. Ozols, M.A. Bookman, A. du Bois, J. Pfisterer, A. Reuss, R.C. Young, Intraperitoneal cisplatin therapy in ovarian cancer: comparison with standard intravenous carboplatin and paclitaxel, Gynecologic Oncol, 103 (2006) 1-6.

[36] I.A.f.R.o. Cancer, W.H. Organization, GLOBOCAN: Estimated Cancer Incidence, Mortality, and Prevalence Worldwide in 2012, IARC, 2014.

[37] E. Bilal, J. Dutkowski, J. Guinney, I.S. Jang, B.A. Logsdon, G. Pandey, B.A. Sauerwine, Y. Shimoni, H.K.M. Vollan, B.H. Mecham, Improving breast cancer survival analysis through competition-based multidimensional modeling, (2013).

[38] B.D. Lehmann, J.A. Bauer, X. Chen, M.E. Sanders, A.B. Chakravarthy, Y. Shyr, J.A. Pietenpol, Identification of human triple-negative breast cancer subtypes and preclinical models for selection of targeted therapies, J Clin Invest 121 (2011) 2750.

[39] M.J. Van De Vijver, Y.D. He, L.J. van't Veer, H. Dai, A.A. Hart, D.W. Voskuil, G.J. Schreiber, J.L. Peterse, C. Roberts, M.J. Marton, A gene-expression signature as a predictor of survival in breast cancer, N Engl J Med, 347 (2002) 1999-2009.

[40] S. Remillard, L.I. Rebhun, G.A. Howie, S.M. Kupchan, Antimitotic activity of the potent tumor inhibitor maytansine, Science, 189 (1975) 1002-1005.

[41] A.A. Wakankar, M.B. Feeney, J. Rivera, Y. Chen, M. Kim, V.K. Sharma, Y.J. Wang, Physicochemical Stability of the Antibody− Drug Conjugate Trastuzumab-DM1: Changes due to Modification and Conjugation Processes, Bioconjug Chem, 21 (2010) 1588-1595.

[42] N.L. Jumbe, Y. Xin, D.D. Leipold, L. Crocker, D. Dugger, E. Mai, M.X. Sliwkowski, P.J. Fielder, J. Tibbitts, Modeling the efficacy of trastuzumab-DM1, an antibody drug conjugate, in mice, J Pharmacokinet Pharmacodyn, 37 (2010) 221-242.

[43] J.R. Junutula, K.M. Flagella, R.A. Graham, K.L. Parsons, E. Ha, H. Raab, S. Bhakta, T. Nguyen, D.L. Dugger, G. Li, Engineered thio-trastuzumab-DM1 conjugate with an improved therapeutic index to target human epidermal growth factor receptor 2–positive breast cancer, Clin Cancer Res, 16 (2010) 4769-4778.

[44] R. Nahta, L.X. Yuan, B. Zhang, R. Kobayashi, F.J. Esteva, Insulin-like growth factor-I receptor/human epidermal growth factor receptor 2 heterodimerization contributes to trastuzumab resistance of breast cancer cells, Cancer Res, 65 (2005) 11118-11128.

[45] C.A. Ritter, M. Perez-Torres, C. Rinehart, M. Guix, T. Dugger, J.A. Engelman, C.L. Arteaga, Human breast cancer cells selected for resistance to trastuzumab in vivo overexpress epidermal growth factor receptor and ErbB ligands and remain dependent on the ErbB receptor network, Clin Cancer Res, 13 (2007) 4909-4919.

[46] G.D.L. Phillips, G. Li, D.L. Dugger, L.M. Crocker, K.L. Parsons, E. Mai, W.A. Blättler, J.M. Lambert, R.V. Chari, R.J. Lutz, Targeting HER2-positive breast cancer with trastuzumab-DM1, an antibody–cytotoxic drug conjugate, Cancer Res, 68 (2008) 9280-9290.

[47] T.T. Junttila, G. Li, K. Parsons, G.L. Phillips, M.X. Sliwkowski, Trastuzumab-DM1 (T-DM1) retains all the mechanisms of action of trastuzumab and efficiently inhibits growth of lapatinib insensitive breast cancer, Breast Cancer Res Treat, 128 (2011) 347-356.

[48] A.M. Hommelgaard, M. Lerdrup, B. van Deurs, Association with membrane protrusions makes ErbB2 an internalization-resistant receptor, Mol Biol Cell, 15 (2004) 1557-1567.

[49] M. Lerdrup, S. Bruun, M.V. Grandal, K. Roepstorff, M.M. Kristensen, A.M. Hommelgaard, B. van Deurs, Endocytic down-regulation of ErbB2 is stimulated by cleavage of its C-terminus, Mol Biol Cell, 18 (2007) 3656-3666.

[50] P. Zhou, N. Fernandes, I.L. Dodge, A.L. Reddi, N. Rao, H. Safran, T.A. DiPetrillo, D.E. Wazer, V. Band, H. Band, ErbB2 degradation mediated by the co-chaperone protein CHIP, J Biol Chem, 278 (2003) 13829-13837.

[51] W. Xu, M. Marcu, X. Yuan, E. Mimnaugh, C. Patterson, L. Neckers, Chaperone-dependent E3 ubiquitin ligase CHIP mediates a degradative pathway for c-ErbB2/Neu, Proc Natl Acad Sci, 99 (2002) 12847-12852.

[52] S.M. Raja, R.J. Clubb, M. Bhattacharyya, M. Dimri, H. Cheng, W. Pan, C. Ortega-Cava, A. Lakku-Reddi, M. Naramura, V. Band, A combination of trastuzumab and 17-AAG induces enhanced ubiquitinylation and lysosomal pathway-dependent ErbB2 degradation and cytotoxicity in ErbB2-overexpressing breast cancer cells, Cancer Biol Ther, 7 (2008) 1630-1640.

[53] M. Lerdrup, A.M. Hommelgaard, M. Grandal, B. van Deurs, Geldanamycin stimulates internalization of ErbB2 in a proteasome-dependent way, J Cell Sci, 119 (2006) 85-95.

[54] F. Greco, M.J. Vicent, Combination therapy: opportunities and challenges for polymer–drug conjugates as anticancer nanomedicines, Adv Drug Deliv Rev, 61 (2009) 1203-1213.

[55] C. Delbaldo, S. Michiels, N. Syz, J.-C. Soria, T. Le Chevalier, J.-P. Pignon, Benefits of adding a drug to a single-agent or a 2-agent chemotherapy regimen in advanced non–small-cell lung cancer: a meta-analysis, Jama, 292 (2004) 470-484.

[56] T.C. Krivak, K.M. Darcy, C. Tian, D. Armstrong, B.E. Baysal, H. Gallion, C.B. Ambrosone, J.A. DeLoia, Relationship between ERCC1 polymorphisms, disease progression, and survival in the Gynecologic Oncology Group Phase III Trial of

intraperitoneal versus intravenous cisplatin and paclitaxel for stage III epithelial ovarian cancer, J Clin Oncol, 26 (2008) 3598-3606.

[57] D. Peer, J.M. Karp, S. Hong, O.C. Farokhzad, R. Margalit, R. Langer, Nanocarriers as an emerging platform for cancer therapy, Nature nanotechnology, 2 (2007) 751-760.

[58] A.Z. Wang, R. Langer, O.C. Farokhzad, Nanoparticle delivery of cancer drugs, Annu Rev Med, 63 (2012) 185-198.

[59] L. Zhang, F. Gu, J. Chan, A. Wang, R. Langer, O. Farokhzad, Nanoparticles in medicine: therapeutic applications and developments, Clin Pharmacol Ther, 83 (2008) 761-769.

[60] C.-M.J. Hu, L. Zhang, Therapeutic nanoparticles to combat cancer drug resistance, Curr Drug Metab, 10 (2009) 836-841.

[61] B.S. Pattni, V.V. Chupin, V.P. Torchilin, New Developments in Liposomal Drug Delivery, Chem Rev, (2015).

[62] M.C. Branco, J.P. Schneider, Self-assembling materials for therapeutic delivery, Acta biomaterialia, 5 (2009) 817-831.

[63] A. Bangham, M.M. Standish, J. Watkins, Diffusion of univalent ions across the lamellae of swollen phospholipids, Journal of molecular biology, 13 (1965) 238-IN227.

[64] W.F. Bayne, L.D. Mayer, C.E. Swenson, Pharmacokinetics of CPX-351 (cytarabine/daunorubicin HCl) liposome injection in the mouse, J Pharm Sci, 98 (2009) 2540-2548.

[65] Y. Li, X. Wang, J. Li, W. Ding, Combination therapy of liposomal paclitaxel and cisplatin as neoadjuvant chemotherapy in locally advanced cervical cancer, Eur J Gynaecol Oncol, 36 (2014) 54-58.

[66] J. Wu, Y. Lu, A. Lee, X. Pan, X. Yang, X. Zhao, R.J. Lee, Reversal of multidrug resistance by transferrin-conjugated liposomes co-encapsulating doxorubicin and verapamil, J Pharm Sci, 10 (2007) 350-357.

[67] G. Batist, K.A. Gelmon, K.N. Chi, W.H. Miller, S.K. Chia, L.D. Mayer, C.E. Swenson, A.S. Janoff, A.C. Louie, Safety, pharmacokinetics, and efficacy of CPX-1 liposome injection in patients with advanced solid tumors, Clin Cancer Res, 15 (2009) 692-700.

[68] N.R. Patel, A. Rathi, D. Mongayt, V.P. Torchilin, Reversal of multidrug resistance by co-delivery of tariquidar (XR9576) and paclitaxel using long-circulating liposomes, Int J Pharm, 416 (2011) 296-299.

[69] L.D. Mayer, T.O. Harasym, P.G. Tardi, N.L. Harasym, C.R. Shew, S.A. Johnstone, E.C. Ramsay, M.B. Bally, A.S. Janoff, Ratiometric dosing of anticancer drug combinations: controlling drug ratios after systemic administration regulates therapeutic activity in tumor-bearing mice, Mol Cancer Ther, 5 (2006) 1854-1863.

[70] E.J. Feldman, J.E. Lancet, J.E. Kolitz, E.K. Ritchie, G.J. Roboz, A.F. List, S.L. Allen, E. Asatiani, L.D. Mayer, C. Swenson, First-in-man study of CPX-351: a liposomal carrier containing cytarabine and daunorubicin in a fixed 5: 1 molar ratio for the treatment of relapsed and refractory acute myeloid leukemia, J Clin Oncol, 29 (2011) 979-985.

[71] F. Greco, M.J. Vicent, Polymer-drug conjugates: current status and future trends, Front Biosci, (2008) 2744-2756.

[72] J.W. Singer, Paclitaxel poliglumex (XYOTAX™, CT-2103): a macromolecular taxane, J Control Release, 109 (2005) 120-126.

[73] M.J. Vicent, F. Greco, R.I. Nicholson, A. Paul, P.C. Griffiths, R. Duncan, Polymer Therapeutics Designed for a Combination Therapy of Hormone-Dependent Cancer, Angew Chem Int Ed Engl, 117 (2005) 4129-4134.

[74] F. Greco, M.J. Vicent, S. Gee, A.T. Jones, J. Gee, R.I. Nicholson, R. Duncan, Investigating the mechanism of enhanced cytotoxicity of HPMA copolymer–Dox–AGM in breast cancer cells, J Control Release, 117 (2007) 28-39.

[75] L. Santucci, A. Mencarelli, B. Renga, G. Pasut, F. Veronese, A. Zacheo, A. Germani, S. Fiorucci, Nitric oxide modulates proapoptotic and antiapoptotic properties of chemotherapy agents: the case of NO-pegylated epirubicin, FASEB J, 20 (2006) 765-767.

[76] L. Santucci, A. Mencarelli, B. Renga, D. Ceccobelli, G. Pasut, F.M. Veronese, E. Distrutti, S. Fiorucci, Cardiac safety and antitumoral activity of a new nitric oxide derivative of pegylated epirubicin in mice, Anti-cancer drugs, 18 (2007) 1081-1091.

[77] J.J. Khandare, P. Chandna, Y. Wang, V.P. Pozharov, T. Minko, Novel polymeric prodrug with multivalent components for cancer therapy, J Pharmacol Exp Ther, 317 (2006) 929-937.

[78] E. Segal, H. Pan, P. Ofek, T. Udagawa, P. Kopecková, J. Kopecek, R. Satchi-Fainaro, Targeting angiogenesis-dependent calcified neoplasms using combined polymer therapeutics, PLoS One, 4 (2009) e5233.

[79] T. Lammers, V. Subr, K. Ulbrich, P. Peschke, P.E. Huber, W.E. Hennink, G. Storm, Simultaneous delivery of doxorubicin and gemcitabine to tumors in vivo using prototypic polymeric drug carriers, Biomaterials, 30 (2009) 3466-3475.

[80] H. Krakovičová, T. Etrych, K. Ulbrich, HPMA-based polymer conjugates with drug combination, Eur J Pharm Sci, 37 (2009) 405-412.

[81] Y. Bae, T.A. Diezi, A. Zhao, G.S. Kwon, Mixed polymeric micelles for combination cancer chemotherapy through the concurrent delivery of multiple chemotherapeutic agents, J Control Release, 122 (2007) 324-330.

[82] H. Cho, T.C. Lai, K. Tomoda, G.S. Kwon, Polymeric Micelles for Multi-Drug Delivery in Cancer, AAPS PharmSciTech, 16 (2015) 10-20.

[83] H. Cho, T.C. Lai, G.S. Kwon, Poly (ethylene glycol)-block-poly (ε-caprolactone) micelles for combination drug delivery: evaluation of paclitaxel, cyclopamine and gossypol in intraperitoneal xenograft models of ovarian cancer, J Control Release, 166 (2013) 1-9.

[84] J.R. Hasenstein, H.-C. Shin, K. Kasmerchak, D. Buehler, G.S. Kwon, K.R. Kozak, Antitumor activity of Triolimus: a novel multidrug-loaded micelle containing Paclitaxel, Rapamycin, and 17-AAG, Mol Cancer Ther, 11 (2012) 2233-2242.

[85] Y. Han, Z. He, A. Schulz, T.K. Bronich, R. Jordan, R. Luxenhofer, A.V. Kabanov, Synergistic Combinations of Multiple Chemotherapeutic Agents in High Capacity Poly (2-oxazoline) Micelles, Mol Pharm, 9 (2012) 2302-2313.

[86] R. Duncan, Polymer conjugates as anticancer nanomedicines, Nat Rev Cancer, 6 (2006) 688-701.

[87] H.-C. Shin, A.W. Alani, H. Cho, Y. Bae, J.M. Kolesar, G.S. Kwon, A 3-in-1 polymeric micelle nanocontainer for poorly water-soluble drugs, Mol Pharm, 8 (2011) 1257-1265.

[88] H.S. Na, Y.K. Lim, Y.-I. Jeong, H.S. Lee, Y.J. Lim, M.S. Kang, C.-S. Cho, H.C. Lee, Combination antitumor effects of micelle-loaded anticancer drugs in a CT-26 murine colorectal carcinoma model, Int J Pharm, 383 (2010) 192-200.

[89] H. Wang, Y. Zhao, Y. Wu, Y.-l. Hu, K. Nan, G. Nie, H. Chen, Enhanced anti-tumor efficacy by co-delivery of doxorubicin and paclitaxel with amphiphilic methoxy PEG-PLGA copolymer nanoparticles, Biomaterials, 32 (2011) 8281-8290.

[90] U. Katragadda, Q. Teng, B.M. Rayaprolu, T. Chandran, C. Tan, Multi-drug delivery to tumor cells via micellar nanocarriers, Int J Pharm, 419 (2011) 281-286.

[91] J.P. Rolland, B.W. Maynor, L.E. Euliss, A.E. Exner, G.M. Denison, J.M. DeSimone, Direct fabrication and harvesting of monodisperse, shape-specific nanobiomaterials, J Am Chem Soc, 127 (2005) 10096-10100.

[92] F.R. Kersey, T.J. Merkel, J.L. Perry, M.E. Napier, J.M. DeSimone, Effect of aspect ratio and deformability on nanoparticle extravasation through nanopores, Langmuir, 28 (2012) 8773-8781.

[93] A.V. Kabanov, S.V. Vinogradov, Nanogels as pharmaceutical carriers: finite networks of infinite capabilities, Angew Chem Int Ed, 48 (2009) 5418-5429.

[94] V.P. Torchilin, Multifunctional, stimuli-sensitive nanoparticulate systems for drug delivery, Nat Rev Drug Discov, 13 (2014) 813-827.

[95] L. Zha, B. Banik, F. Alexis, Stimulus responsive nanogels for drug delivery, Soft Matter, 7 (2011) 5908-5916.

[96] H. Ayame, N. Morimoto, K. Akiyoshi, Self-assembled cationic nanogels for intracellular protein delivery, Bioconjug Chem, 19 (2008) 882-890.

[97] K. Raemdonck, J. Demeester, S. De Smedt, Advanced nanogel engineering for drug delivery, Soft Matter, 5 (2009) 707-715.

[98] J.K. Oh, D.I. Lee, J.M. Park, Biopolymer-based microgels/nanogels for drug delivery applications, Prog Polym Sci, 34 (2009) 1261-1282.

[99] R.T. Chacko, J. Ventura, J. Zhuang, S. Thayumanavan, Polymer nanogels: a versatile nanoscopic drug delivery platform, Adv Drug Deliv Rev, 64 (2012) 836-851.

[100] M. Malmsten, Soft drug delivery systems, Soft Matter, 2 (2006) 760-769.

[101] M.E. Napier, J.M. DeSimone, Nanoparticle drug delivery platform, J. Macromol. Sci., Polym. Rev., 47 (2007) 321-327.

[102] M. Beija, J.-D. Marty, M. Destarac, RAFT/MADIX polymers for the preparation of polymer/inorganic nanohybrids, Prog Polym Sci, 36 (2011) 845-886.

[103] D.J. Siegwart, J.K. Oh, K. Matyjaszewski, ATRP in the design of functional materials for biomedical applications, Prog Polym Sci, 37 (2012) 18-37.

[104] T.K. Bronich, P.A. Keifer, L.S. Shlyakhtenko, A.V. Kabanov, Polymer micelle with cross-linked ionic core, J Am Chem Soc, 127 (2005) 8236-8237.

[105] R.K. O'Reilly, C.J. Hawker, K.L. Wooley, Cross-linked block copolymer micelles: functional nanostructures of great potential and versatility, Chem Soc Rev, 35 (2006) 1068-1083.

[106] M. Oishi, Y. Nagasaki, Stimuli-responsive smart nanogels for cancer diagnostics and therapy, Nanomedicine, 5 (2010) 451-468.

[107] W.-H. Chiang, V.T. Ho, W.-C. Huang, Y.-F. Huang, C.-S. Chern, H.-C. Chiu, Dual stimuli-responsive polymeric hollow nanogels designed as carriers for intracellular triggered drug release, Langmuir, 28 (2012) 15056-15064.

[108] N. Sanson, J. Rieger, Synthesis of nanogels/microgels by conventional and controlled radical crosslinking copolymerization, Polym Chem, 1 (2010) 965-977.

[109] M. Elsabahy, G.S. Heo, S.-M. Lim, G. Sun, K.L. Wooley, Polymeric Nanostructures for Imaging and Therapy, Chem Rev, (2015).

[110] X. Zhang, S. Malhotra, M. Molina, R. Haag, Micro-and nanogels with labile crosslinks–from synthesis to biomedical applications, Chem Soc Rev, 44 (2015) 1948-1973.

[111] S.E. Gratton, P.D. Pohlhaus, J. Lee, J. Guo, M.J. Cho, J.M. DeSimone, Nanofabricated particles for engineered drug therapies: A preliminary biodistribution study of PRINT™ nanoparticles, J Control Release, 121 (2007) 10-18.

[112] J.L. Perry, K.P. Herlihy, M.E. Napier, J.M. DeSimone, PRINT: a novel platform toward shape and size specific nanoparticle theranostics, Acc Chem Res, 44 (2011) 990-998.

[113] L.C. Glangchai, M. Caldorera-Moore, L. Shi, K. Roy, Nanoimprint lithography based fabrication of shape-specific, enzymatically-triggered smart nanoparticles, J Control Release, 125 (2008) 263-272.

[114] Y. Sasaki, K. Akiyoshi, Nanogel engineering for new nanobiomaterials: from chaperoning engineering to biomedical applications, Chem Rec, 10 (2010) 366-376.

[115] J.J. Water, Y. Kim, M.J. Maltesen, H. Franzyk, C. Foged, H.M. Nielsen, Hyaluronic acid-based nanogels produced by microfluidics-facilitated self-assembly improves the safety profile of the cationic host defense peptide novicidin, Pharm Res, (2015) 1-9.

[116] H. Lai, P. Wu, A infrared spectroscopic study on the mechanism of temperature-induced phase transition of concentrated aqueous solutions of poly (N-isopropylacrylamide) and N-isopropylpropionamide, Polymer, 51 (2010) 1404-1412.

[117] F.D. Jochum, P. Theato, Temperature-and light-responsive smart polymer materials, Chem Soc Revi, 42 (2013) 7468-7483.

[118] H. Mok, H. Jeong, S.-J. Kim, B.H. Chung, Indocyanine green encapsulated nanogels for hyaluronidase activatable and selective near infrared imaging of tumors and lymph nodes, Cheml Commun, 48 (2012) 8628-8630.

[119] T. Canal, N.A. Peppas, Correlation between mesh size and equilibrium degree of swelling of polymeric networks, J Biomed Mater Res, 23 (1989) 1183-1193.

[120] S.R. Lustig, N.A. Peppas, Solute diffusion in swollen membranes. IX. Scaling laws for solute diffusion in gels, J Appl Polym Sci, 36 (1988) 735-747.

[121] G.M. Eichenbaum, P.F. Kiser, S.A. Simon, D. Needham, pH and ion-triggered volume response of anionic hydrogel microspheres, Macromolecules, 31 (1998) 5084-5093.

[122] M. Motornov, Y. Roiter, I. Tokarev, S. Minko, Stimuli-responsive nanoparticles, nanogels and capsules for integrated multifunctional intelligent systems, Prog Polym Sci, 35 (2010) 174-211.

[123] H.S. Oberoi, F.C. Laquer, L.A. Marky, A.V. Kabanov, T.K. Bronich, Core cross-linked block ionomer micelles as pH-responsive carriers for cis-diamminedichloroplatinum (II), J Control Release, 153 (2011) 64-72.

[124] G. Tamura, Y. Shinohara, A. Tamura, Y. Sanada, M. Oishi, I. Akiba, Y. Nagasaki, K. Sakurai, Y. Amemiya, Dependence of the swelling behavior of a pH-responsive PEG-modified nanogel on the cross-link density, Polym J, 44 (2012) 240-244.

[125] J. Ricka, T. Tanaka, Swelling of ionic gels: quantitative performance of the Donnan theory, Macromolecules, 17 (1984) 2916-2921.

[126] A. Pikabea, G. Aguirre, J.I. Miranda, J. Ramos, J. Forcada, Understanding of nanogels swelling behavior through a deep insight into their morphology, J Polym Sci Polym Chem, (2015).

[127] G.M. Eichenbaum, P.F. Kiser, A.V. Dobrynin, S.A. Simon, D. Needham, Investigation of the swelling response and loading of ionic microgels with drugs and proteins: The dependence on cross-link density, Macromolecules, 32 (1999) 4867-4878.

[128] B.H. Tan, P. Ravi, K.C. Tam, Synthesis and Characterization of Novel pH-Responsive Polyampholyte Microgels, Macromol Rapid Commun, 27 (2006) 522-528.

[129] T. Hoare, R. Pelton, Charge-switching, amphoteric glucose-responsive microgels with physiological swelling activity, Biomacromolecules, 9 (2008) 733-740.

[130] W. Wu, N. Mitra, E.C. Yan, S. Zhou, Multifunctional hybrid nanogel for integration of optical glucose sensing and self-regulated insulin release at physiological pH, ACS Nano, 4 (2010) 4831-4839.

[131] R. Cheng, F. Meng, C. Deng, H.-A. Klok, Z. Zhong, Dual and multi-stimuli responsive polymeric nanoparticles for programmed site-specific drug delivery, Biomaterials, 34 (2013) 3647-3657.

[132] N. Morimoto, X.-P. Qiu, F.M. Winnik, K. Akiyoshi, Dual stimuli-responsive nanogels by self-assembly of polysaccharides lightly grafted with thiol-terminated poly (N-isopropylacrylamide) chains, Macromolecules, 41 (2008) 5985-5987.

[133] Y.-J. Pan, Y.-Y. Chen, D.-R. Wang, C. Wei, J. Guo, D.-R. Lu, C.-C. Chu, C.-C. Wang, Redox/pH dual stimuli-responsive biodegradable nanohydrogels with varying responses to dithiothreitol and glutathione for controlled drug release, Biomaterials, 33 (2012) 6570-6579.

[134] M.-H. Xiong, Y. Bao, X.-Z. Yang, Y.-C. Wang, B. Sun, J. Wang, Lipase-sensitive polymeric triple-layered nanogel for "on-demand" drug delivery, J Am Chem Soc, 134 (2012) 4355-4362.

[135] Z.-Y. Qiao, R. Zhang, F.-S. Du, D.-H. Liang, Z.-C. Li, Multi-responsive nanogels containing motifs of ortho ester, oligo (ethylene glycol) and disulfide linkage as carriers of hydrophobic anti-cancer drugs, J Control Release, 152 (2011) 57-66.

[136] D. Maciel, P. Figueira, S. Xiao, D. Hu, X. Shi, J.o. Rodrigues, H. Tomás, Y. Li, Redox-responsive alginate nanogels with enhanced anticancer cytotoxicity, Biomacromolecules, 14 (2013) 3140-3146.

[137] J.K. Oh, D.J. Siegwart, H.-i. Lee, G. Sherwood, L. Peteanu, J.O. Hollinger, K. Kataoka, K. Matyjaszewski, Biodegradable nanogels prepared by atom transfer radical polymerization as potential drug delivery carriers: synthesis, biodegradation, in vitro release, and bioconjugation, J Am Chem Soc, 129 (2007) 5939-5945.

[138] J.-H. Ryu, R.T. Chacko, S. Jiwpanich, S. Bickerton, R.P. Babu, S. Thayumanavan, Self-cross-linked polymer nanogels: a versatile nanoscopic drug delivery platform, J Am Chem Soc, 132 (2010) 17227-17235.

[139] S.V. Vinogradov, Colloidal microgels in drug delivery applications, Curr Pharm Des, 12 (2006) 4703.

[140] T.K. Bronich, S.V. Vinogradov, A.V. Kabanov, Interaction of nanosized copolymer networks with oppositely charged amphiphilic molecules, Nano Lett, 1 (2001) 535-540.

[141] E. Kohli, H.-Y. Han, A.D. Zeman, S.V. Vinogradov, Formulations of biodegradable Nanogel carriers with 5′-triphosphates of nucleoside analogs that display a reduced cytotoxicity and enhanced drug activity, J Control Release, 121 (2007) 19-27.

[142] C.M. Galmarini, G. Warren, E. Kohli, A. Zeman, A. Mitin, S.V. Vinogradov, Polymeric nanogels containing the triphosphate form of cytotoxic nucleoside analogues show antitumor activity against breast and colorectal cancer cell lines, Mol Cancer Ther, 7 (2008) 3373-3380.

[143] T. Gerson, E. Makarov, T.H. Senanayake, S. Gorantla, L.Y. Poluektova, S.V. Vinogradov, Nano-NRTIs demonstrate low neurotoxicity and high antiviral activity against HIV infection in the brain, Nanomed Nanotech Biol Med, 10 (2014) 177-185.

[144] J.O. Kim, N.V. Nukolova, H.S. Oberoi, A.V. Kabanov, T.K. Bronich, Block ionomer complex micelles with cross-linked cores for drug delivery, Polym Sci Ser A, 51 (2009) 708-718.

[145] G. Sahay, J.O. Kim, A.V. Kabanov, T.K. Bronich, The exploitation of differential endocytic pathways in normal and tumor cells in the selective targeting of nanoparticulate chemotherapeutic agents, Biomaterials, 31 (2010) 923-933.

[146] J.O. Kim, G. Sahay, A.V. Kabanov, T.K. Bronich, Polymeric micelles with ionic cores containing biodegradable cross-links for delivery of chemotherapeutic agents, Biomacromolecules, 11 (2010) 919-926.

[147] F. Shi, J. Ding, C. Xiao, X. Zhuang, C. He, L. Chen, X. Chen, Intracellular microenvironment responsive PEGylated polypeptide nanogels with ionizable cores for efficient doxorubicin loading and triggered release, J Mater Chem, 22 (2012) 14168-14179.

[148] H.S. Oberoi, N.V. Nukolova, F.C. Laquer, L.Y. Poluektova, J. Huang, Y. Alnouti, M. Yokohira, L.L. Arnold, A.V. Kabanov, S.M. Cohen, Cisplatin-loaded core cross-linked micelles: comparative pharmacokinetics, antitumor activity, and toxicity in mice, Int J Nanomedicine, 7 (2012) 2557.

[149] N.V. Nukolova, H.S. Oberoi, S.M. Cohen, A.V. Kabanov, T.K. Bronich, Folate-decorated nanogels for targeted therapy of ovarian cancer, Biomaterials, 32 (2011) 5417-5426.

[150] N.V. Nukolova, H.S. Oberoi, Y. Zhao, V.P. Chekhonin, A.V. Kabanov, T.K. Bronich, LHRH-targeted nanogels as a delivery system for cisplatin to ovarian cancer, Mol Pharm, 10 (2013) 3913-3921.

[151] J. Peng, T. Qi, J. Liao, B. Chu, Q. Yang, W. Li, Y. Qu, F. Luo, Z. Qian, Controlled release of cisplatin from pH-thermal dual responsive nanogels, Biomaterials, 34 (2013) 8726-8740.

[152] H.S.O. Jong Oh Kim, Swapnil Desale, Alexander V. Kabanov, and Tatiana K. Bronich, Polypeptide nanogels with hydrophobic moieties in the cross-linked ionic cores: synthesis, characterization and implications for anticancer drug delivery, J Drug Taget, (2013).

[153] Y. Wang, H. Xu, J. Wang, L. Ge, J. Zhu, Development of a Thermally Responsive Nanogel Based on Chitosan–Poly (N-Isopropylacrylamide-co-Acrylamide) for Paclitaxel Delivery, J Pharm Sci, 103 (2014) 2012-2021.

[154] S. Daoud-Mahammed, P. Couvreur, K. Bouchemal, M. Chéron, G. Lebas, C. Amiel, R. Gref, Cyclodextrin and polysaccharide-based nanogels: entrapment of two

hydrophobic molecules, benzophenone and tamoxifen, Biomacromolecules, 10 (2009) 547-554.

[155] J.P. Tan, M.B. Tan, M.K. Tam, Application of nanogel systems in the administration of local anesthetics, Local Reg Anesth 3 (2010) 93.

[156] M.C.C. Ferrer, V.V. Shuvaev, B.J. Zern, R.J. Composto, V.R. Muzykantov, D.M. Eckmann, Icam-1 targeted nanogels loaded with dexamethasone alleviate pulmonary inflammation, Plos One (2014) e102329.

[157] M.C.C. Ferrer, R.C. Ferrier Jr, D.M. Eckmann, R.J. Composto, A facile route to synthesize nanogels doped with silver nanoparticles, Journal of nanoparticle research, 15 (2013) 1-7.

[158] M.C.C. Ferrer, S. Dastgheyb, N.J. Hickok, D.M. Eckmann, R.J. Composto, Designing nanogel carriers for antibacterial applications, Acta biomaterialia, 10 (2014) 2105-2111.

[159] T. Nakamura, A. Tamura, H. Murotani, M. Oishi, Y. Jinji, K. Matsuishi, Y. Nagasaki, Large payloads of gold nanoparticles into the polyamine network core of stimuli-responsive PEGylated nanogels for selective and noninvasive cancer photothermal therapy, Nanoscale, 2 (2010) 739-746.

[160] H. Yasui, R. Takeuchi, M. Nagane, S. Meike, Y. Nakamura, T. Yamamori, Y. Ikenaka, Y. Kon, H. Murotani, M. Oishi, Radiosensitization of tumor cells through endoplasmic reticulum stress induced by PEGylated nanogel containing gold nanoparticles, Cancer Lett, 347 (2014) 151-158.

[161] J. Woodcock, J.P. Griffin, R.E. Behrman, Development of novel combination therapies, N Engl J Med, 364 (2011) 985-987.

[162] S.S. Desale, S.M. Raja, J.O. Kim, B. Mohapatra, K.S. Soni, H. Luan, S.H. Williams, T.A. Bielecki, D. Feng, M. Storck, Polypeptide-based nanogels co-encapsulating a synergistic combination of doxorubicin with 17-AAG show potent anti-tumor activity in ErbB2-driven breast cancer models, J Control Release, 208 (2015) 59-66.

[163] S.S. Desale, S.M. Cohen, Y. Zhao, A.V. Kabanov, T.K. Bronich, Biodegradable hybrid polymer micelles for combination drug therapy in ovarian cancer, J Control Release, (2013).

[164] J. Park, S.H. Wrzesinski, E. Stern, M. Look, J. Criscione, R. Ragheb, S.M. Jay, S.L. Demento, A. Agawu, P.L. Limon, Combination delivery of TGF-β inhibitor and IL-2 by nanoscale liposomal polymeric gels enhances tumour immunotherapy, Nat Mater, 11 (2012) 895-905.

[165] P. Kamolratanakul, T. Hayata, Y. Ezura, A. Kawamata, C. Hayashi, Y. Yamamoto, H. Hemmi, M. Nagao, R. Hanyu, T. Notomi, Nanogel-based scaffold delivery of prostaglandin E2 receptor–specific agonist in combination with a low dose of growth factor heals critical-size bone defects in mice, Arthritis Rheumatol, 63 (2011) 1021-1033.

[166] S. Toita, S.-i. Sawada, K. Akiyoshi, Polysaccharide nanogel gene delivery system with endosome-escaping function: co-delivery of plasmid DNA and phospholipase A 2, J Control Release, 155 (2011) 54-59.

[167] M. Ahmed, R. Narain, Intracellular delivery of DNA and enzyme in active form using degradable carbohydrate-based nanogels, Mol Pharm, 9 (2012) 3160-3170.

**CHAPTER II**

**BIODEGRADABLE HYBRID NANOGELS FOR COMBINATION DRUG**

**THERAPY IN OVARIAN CANCER[1]**

**2.1 Introduction.**

Ovarian cancer is the most lethal gynecologic malignancy in women, which causes nearly 15,000 deaths in the United States every year. Its high death rate is a result of the fact that most patients (>75%) are diagnosed at an advanced stage of disease at which point the 5-year survival rate is less than 30% [1, 2]. The vast majority of ovarian cancers are epithelial in origin and characterized by the rapid growth and spread of solid intraperitoneal tumors and formation of large volumes of ascitic fluid. The standard treatment for patients with advanced ovarian cancer is maximal surgical cytoreduction followed by systemic platinum-based chemotherapy [2]. Cytotoxic action of platinum compounds such as cisplatin (*cis*-dichlorodiamminoplatinum (II), CDDP) is mediated through the formation of platinum-DNA adducts, which in turn inhibits DNA replication and/or transcription and results in apoptosis and necrosis [3, 4]. Despite its success, use of CDDP is greatly limited by severe dose limiting side effects, rapid elimination, and development of acquired drug resistance. No new small molecule platinum drug have gained international marketing approval since 1999 indicating a shift in focus in the last decade away from drug design and towards drug delivery [5]. Among drug delivery systems, those based on self-assembled block copolymer micelles have great potential for delivery of anticancer drugs [6]. The advantages of polymer micelles include their small

---

[1] Reproduced with permission from Desale SS, Cohen SM, Zhao Y, Kabanov AV, and Bronich TK, Biodegradable hybrid polymer micelles for combination drug therapy in ovarian cancer, J Control Release 171.3 (2013): 339-348. Copyright 2013 Elsevier B.V.

size, long circulation times, and ability to circumvent renal excretion and extravasate at sites of enhanced vascular permeability. However, disintegration of the polymer micelles is a major drawback for their application in drug delivery. In order to overcome this limitation, we have proposed hydrophilic polyelectrolyte micelles with core composed of a network of cross-linked polyanion chains and PEG shell that can encapsulate CDDP with high capacity (up to 35 w/w%) [7, 8]. We have demonstrated significant improvement of drug safety and drug delivery using such CDDP-loaded cross-linked micelles. However, single drug therapy agents directed to individual targets frequently show limited efficacies. Hence, multi-component therapies and multi-targeted drug combinations are key to most cancer treatments [9]. Combination chemotherapy using sequential administration of paclitaxel (PTX) with a platinum-based regimen is currently the standard first-line therapy for ovarian cancer resulting in increased success rates in eradicating tumors and/or longer remission periods [10]. These clinical benefits of the combination therapy can be possibly maximized by controlled delivery of the desired drug ratio to the *in vivo* target. Combining drugs in one delivery carrier is well-suited strategy for controlling the pharmacokinetics and co-delivery of the desired drug ratio *in vivo*. The drug loading and structure of such carriers can be tuned to control the drug release rates, maximize the therapeutic potency and minimize drug-associated toxicities. Nanoscale delivery carriers such as liposomes, nanoparticles, polymeric micelles have been explored for co-delivery of anticancer drugs [11-13]. However, co-incorporation of drug molecules with different physicochemical properties, such as hydrophilic CDDP and hydrophobic PTX, has been challenging. As an attempt to address this challenge, we report a design of multi-compartment cross-linked micelles, also known as nanogels

(NG) based on hybrid triblock copolymers, poly(ethylene glycol)-*block*-poly(L-glutamic acid)-*block*-poly(L-phenylalanine) (PEG-*b*-PGlu-*b*-PPhe) for simultaneous loading and delivery of binary CDDP and PTX combination. Such NGs have 1) a hydrophobic core formed by PPhe chains, which serves as a reservoir for PTX solubilization, 2) an anionic layer, which incorporates CDDP through coordination with the carboxylic groups of PGlu, and 3) an outer PEG shell stabilized, which stabilizes NGs in aqueous dispersion. The crosslinks incorporated into PGlu block layer ensure that the PEG-*b*-PGlu-*b*-PPhe NGs remain stable until they encounter proteases, which degrade the NGs by cleaving the polypeptide chains of the block copolymers. This work demonstrates that such biodegradable hybrid NGs carrying CDDP and PTX drug combination exert superior antitumor efficacy in treatment of ovarian cancer in xenograft mouse tumor model.

## 2.2 Material and Methods

### 2.2.1 Materials

PEG-*b*-PGlu-*b*-PPhe block copolymers with different ratios of glutamic acid and phenylalanine units (90:7 and 90:25) were synthesized as described below. α-Amino-ω-methoxy poly(ethylene glycol) (mPEG-NH$_2$ , $M_w$ = 5,000 g mol$^{-1}$, $M_w$ / $M_n$ = 1.05) was purchased from Creative PEGWorks Inc., (NC, USA). CDDP was purchased from Acros Organics. L-glutamic acid *γ*-benzyl ester (BGlu), L-phenylalanine (Phe), 1,2-ethylenediamine, 1-(3-dimethylaminopropyl)-3-ethylcarbodiimide hydrochloride (EDC), paclitaxel, and other chemicals were purchased from Sigma-Aldrich (St Louis, MO) and were used without further purification. Fetal bovine serum (FBS), RPMI 1640 medium, penicillin, streptomycin, Trypsin–ethylenediaminetetraacetic acid (EDTA) (0.5% trypsin,

5.3 mM EDTA tetra-sodium) and other chemicals were purchased from Invitrogen (Carlsbad, CA, USA).

### 2.2.2 N-carboxyanhydrides (NCA) of BGlu and Phe

BGlu (0.020 mole) or Phe (0.026 mole) and anhydrous tetrahydrofuran (THF) were added into a dried glass reactor to form a suspension. Triphosgen (0.023mole) was separately dissolved in fresh anhydrous THF and injected drop wise into reaction mixture. Nitrogen was bubbled through the mixture during synthesis. The mixture was heated at about 40$^o$C with constant stirring till mixture became transparent. The solution was precipitated in n-hexane and then stored at -20$^o$C overnight in order to allow complete precipitation of $\gamma$-benzyl L-glutamate-N-carboxyanhydride (BGlu-NCA) or L-phenulalanine –N-carboxyanhydride (Phe-NCA). The white solids obtained were collected and purified further by repeated precipitation with n-hexane. The resulting NCA monomers were dried under vacuum for 24 h and characterized by the proton nuclear magnetic resonance ($^1H$-NMR).

### 2.2.3 PEG-b-PGlu-b-PPhe block copolymer

Monoaminomethoxypoly(ethylene glycol) (mPEG-NH$_2$) (0.02 mmol) was dissolved under stirring in 10 mL of anhydrous dimethylformamide (DMF) in nitrogen atmosphere at 40$^o$C. BGlu-NCA (2 mmol, the feed molar ratio of mPEG-NH$_2$ to BGlu-NCA was 1: 100) dissolved in 5 mL of anhydrous DMF was added dropwise and the solution was stirred for 24 hrs. The aliquot of the reaction mixture was precipitated using excess of diethyl ether, dried under vacuum, and the composition of PEG-PBGlu diblock copolymer was determined by $^1H$-NMR from the peak intensity ratios of the methylene protons of PEG and the phenyl protons of the $\gamma$-benzyl groups (400 MHz in CDCl$_3$: δ =

3.5 (s, 4H, -OCH$_2$CH$_2$-), 5.0 (m, 2H, benzyl), 7.3 (m, 5H, aryl)). The calculated amount of the monomer for the third block, Phe-NCA, dissolved in anhydrous DMF was then injected dropwise and mixture was stirred under a N$_2$ atmosphere at 40 °C for additional 24 hrs. The product (PEG-*b*-PBGlu-*b*-PPhe) was precipitated by diethyl ether, purified by repeated precipitation in diethyl ether and dried in a vacuum. The benzyl groups of PEG-*b*-PBGA-*b*-PPhe were removed in the presence of NaOH to obtain PEG-*b*-PGlu-*b*-PPhe. Polymer sample was dissolved in 10 mL of THF followed by addition of 5 mL of 1N NaOH. After stirring for 10 hrs at 40°C THF was removed at reduced pressure, the residual solution was neutralized by 1M HCl and dialyzed using a dialysis membrane (MWCO 3,500 Da) against distilled water for 24 hrs. After dialysis the product was dried, washed 2-3 times with ethanol followed by lyophilization. By varying the feed molar ratio of mPEG-NH$_2$ to Phe-NCA (1:10 and 1:30), two copolymers with targeted compositions PEG-*b*-PBGlu(100)-*b*-PPhe(10) and PEG-*b*-PBGlu(100)-*b*-PPhe(30) were synthesized. The concentration of carboxylate groups in the copolymer samples was estimated by potentiometric titration. Self-assembly behavior of PEG-*b*-PGlu-*b*-PPhe copolymers was examined using pyrene as a hydrophobic fluorescence probe [14].

### 2.2.4 Pyrene assay and fluorescence spectroscopy

Self-assembly studies of PEG-PGlu$_{90}$-PPhe$_{25}$ and PEG-PGlu$_{90}$-PPhe$_7$ using pyrene as fluorescent probe were performed using a spectrofluorometer system (Flourlog®, HORIBA Jobin Yvon Inc., NJ, USA). Known amounts of pyrene in acetone were added to empty vials, followed by acetone evaporation. Subsequently, the pyrene film was incubated with varying concentrations (ranging from 3.9 to 2000mg/L) of polymer overnight on shaker at room temperature. The pyrene concentration in the final solution

was 6 x 10-7 M (MW 202.25). Fluorescence spectra were recorded on a microplate reader (SpectraMax M5, MDS, CA) with samples in a 1.0 cm quartz cuvette. Emission spectra were recorded for PEG-PGlu90-PPhe25 and PEG-PGlu90-PPhe7 solutions in water (1mg/mL) from 250 to 350 nm using an excitation wavelength $\lambda$ex=265 nm.

### 2.2.5 Preparation of NGs

NGs were prepared by directly dissolving PEG-*b*-PGlu-*b*-PPhe copolymer in aqueous media at a concentration of about 1 mg/mL. EDC in water (0.2 eq with respect to the amount of carboxylate groups) was added dropwise to this solution and allowed to stir for additional 10 min at r.t.. An aqueous solution of cross-linker, 1,2-ethylenediamine (0.1 eq) was then added to the dispersion of micellar aggregate to achieve 20% of cross-linking degree. This degree represents the maximum theoretical amount of cross-linking that could take place, rather than the precise extent of amidation. The reaction mixture was allowed to stir overnight at r.t. Byproducts of the cross-linking reaction were removed by exhaustive dialysis of the reaction mixtures against distilled water.

### 2.2.6 Physicochemical methods of characterization and in vitro degradation of NGs

The $^1$H NMR spectra for the monomers and copolymers were acquired in CDCl$_3$ or D$_2$O at 25 °C using a Bruker 400 MHz spectrometer. Effective hydrodynamic diameters (D$_{eff}$) and $\zeta$-potential of NGs were determined by dynamic light scattering (DLS) using a Zetasizer Nano ZS (Malvern Instruments Ltd., Malvern, UK). All measurements were performed in automatic mode at 25°C. Software provided by the manufacturer was used to calculate the size, polydispersity indices (PDI), and $\zeta$-potential of NGs. All measurements were performed at least in triplicate to calculate mean values ± SD.

Morphology of the NGs was characterized by transmission electron microscopy (TEM) and atomic force microscopy (AFM) as previously described [24]. NGs (ca. 1 mg/mL) were incubated with cathepsin B from human liver (10 units/mL) in phosphate buffered saline (PBS, pH 6.5, 0.14 M NaCl) at $37^0$C for various time points (0, 12, 24 hrs) and analyzed by size exclusion chromatography (SEC) using an ÄKTA FPLC (Amersham Biosciences) system and Sepharose CL-6B column (300 mm × 10 mm; flow rate 0.5 mL/min; mobile phase PBS, r.t.).  Detection was performed at 280 nm.

2.2.7   *Drug loading*

A solution of PTX in ethanol (2 mg/mL) was added dropwise into the aqueous dispersion of NGs (1 mg/mL) and the mixture was stirred at r.t. overnight in an open-air system to allow slow evaporation of ethanol [15]. The residual ethanol was then removed at reduced pressure. The precipitate of unbound PTX was removed by centrifugation. The aqueous dispersion of PTX-loaded NGs were mixed with an aqueous solution of CDDP (1 mg/mL) at pH 9.0 at 0.5 molar ratio of CDDP to carboxylate groups followed by incubation at 37°C for 48 h. Unbound CDDP was removed by Ultracon filter units (MWCO 10,000 Da, Millipore). Pt content in NGs (Pt194/Pt195) was assayed on Nexion ion coupled plasma-mass spectrometer (NexION 300Q, PerkinElmer) calibrated with Pt (2-100 ng/ml) and Holmium as the internal standard. Samples were diluted in 0.1 N HCl. PTX levels were determined by high-performance liquid chromatography (HPLC) analysis under isocratic conditions using an Agilent 1200 HPLC system a diode array detector set at 227 nm. As stationary phase a Nucleosil C18 column was used (250 mm × 4.6 mm), a mobile phase of acetonitrile/water mixture (55/45, v/v) was applied at a flow rate of 1 mL/min.

### 2.2.8 Release studies

Drug release from the NGs was examined in PBS (pH 7.4), acetate buffered saline (ABS, pH 5.5, 0.14 M NaCl), and ABS in presence of cathepsin B (10 units/mL) by dialysis method using a membrane with 3,500 Da cutoff. The concentrations of PTX and Pt(II) released were determined by HPLC and inductively coupled plasma mass spectrometry (ICP-MS), respectively, and expressed as a percentage of the total PTX or Pt(II) available *vs.* time.

### 2.2.9 Cell culture and cytotoxicity assay

A2780 human ovarian carcinoma cells were provided by Dr. P. Rogers (Institute of Cancer Research, University of Bristol, UK). Cells were maintained in RPMI 1640 medium with 2 mM glutamine supplemented with 10% (v/v) FBS in the presence of penicillin and streptomycin (100 U/ml and 0.1 mg/ml, respectively) at 37°C in a humidified atmosphere containing 5% $CO_2$. Cells were harvested with trypsin-EDTA (Life Technologies) after 80% confluence. Cells seeded in 96-well plates (5,000 cells/well) 24 h prior the experiment were exposed to various doses (0-10 $\mu$g/mL on CDDP or PTX basis) of CDDP alone, polymeric NGs alone, CDDP-loaded NGs, PTX-loaded NGs and (CDDP+PTX)-loaded NGs for 72 h at 37 °C, followed by washing with PBS, and maintaining in RPMI 1640 medium with 10% FBS for additional 24 h. Cytotoxicity of drug-loaded NGs was assessed by a standard MTT assay [16] and the $IC_{50}$ values were calculated using GraphPad Prism software. Combination index (CI) analysis based on Chou and Talaly method [17] was performed using CompuSyn software for CDDP and PTX combinations, determining synergistic, additive, or antagonistic cytotoxic effects against A2780 breast cancer cells. Values of CI < 1

demonstrate synergism while CI = 1 and CI > 1 values represent additive and antagonistic effects of drug combination, respectively.

### 2.2.10 Animal studies

Upon arrival, animals were placed in a facility accredited by the Association for Assessment and Accreditation of Laboratory Animal Care. Food and reverse osmosis water were available ad libitum throughout the study. Treatments were administered by tail vein injection. Drug amount was calculated based on the average animal body weight. The University of Nebraska Medical Center Institutional Animal Care and Use Committee approved all animal protocols. A xenograft human ovarian carcinoma model was used as previously described [8, 18]. Briefly, A2780 cells ($5 \times 10^6$ cells/site) were subcutaneously transplanted into the flanks, one above each hind limb, of four-week-old female athymic (Ncr-nu/nu) mice (National Cancer Institute). When the tumors reached a size of about 200-400 $mm^3$ (12-15 days after transplantation) animals were randomized (5 treatment groups, n = 8) and treated with free CDDP or CDDP/NGs or PTX/NGs or (CDDP+PTX)/NGs at an equivalent dose of 4 mg/kg CDDP, or 1mg/kg PTX or (4 mg/kg CDDP+1 mg/kg PTX) or 5% dextrose solution. Treatments were administered via tail vein injections at 4-day intervals. Animal body weight and tumor volume were monitored every second day. Tumor volume ($V = 0.5 \times L \times W^2$) was estimated by measuring two orthogonal diameters (longer dimension: L, and smaller dimension: W) of the tumor using electronic calipers. Animals were sacrificed when tumor volume exceeded 3000 $mm^3$, greatest tumor dimension exceeded 20 mm, tumor became necrotic, or animal exhibited a body weight loss of more than 20%. Euthanasia was performed by $CO_2$ asphyxiation. All other animals were sacrificed by day 45.

### 2.2.11 Apoptosis and proliferation

Tumors from mice that received different treatments were excised at day 14 (2-3 mice per group). The tumors were dissected and fixed in 10% neutral buffered formalin. Then, the tissues were processed routinely into paraffin, sectioned at a thickness of 4 μm. Proliferating and apoptotic cells were detected using an antibody against Ki-67 and caspase-3, respectively. Visualization was done by incubation with DAB+ (brown, for Ki-67) and Permanent red (for caspase-3) (DAKO) for 2 min. After being rinsed with distilled water, the sections were counterstained with hematoxylin. For quantification of Ki-67 and caspase-3 expression, the area of positive cells was determined (Image J) in 5 random high power fields (20X magnification) and divided by the total area of cells for each field of slice.

### 2.2.12 Sample preparation and drug content measurement in tissue.

Known weights of thawed tissue, collected from the animals sacrificed at different days during treatment, were decomposed by wet-ashing in screw-capped vials with six volumes of concentrated nitric acid, overnight heating, and stirring at 65°C. An iridium internal standard was added prior to digestion. Total platinum concentrations were determined by ICP-MS using iridium correction. Calibration range for the assay was platinum 2–100 ng/mL with extrapolation to platinum 1000 ng/mL. Necessary dilutions were made when the platinum concentration exceeded the calibration range. Assay sensitivity was 0.8 ng of Pt/mL, with inter- and intraday assay variability not exceeding 5%. For PTX measurements, tissue sample (200 mg) was spiked with 50 uL diazepam (internal standard, I.S.) to achieve a final concentration about 25 ug/mL, then 2mL of *tert*-butyl methyl ether (TBME) was added and tissue was homogenized. Homogenized

samples were centrifuged at 3000g for 10 min, 1mL of supernatant TBME layer was collected and dried under air. Residue was reconstituted using 1mL of mobile phase and 20uL of it was injected into HPLC system. Samples of PTX was prepared by directly dissolving PTX and I.S. in mobile phase and measured in HPLC system to calculate recovery rate.

## 2.2.13 Blood chemistry and histopathology

Blood from the sacrificed animals was collected in EDTA tubes and analyzed for blood cell count and liver enzymes using Vetscan VS (Abaxis). Fixed tissues were processed, sectioned, inserted into tissue cassettes, dehydrated in 70% ethanol overnight, and paraffin embedded (UNMC Tissue Sciences Facility, Omaha, NE). Serial 5 μm sections were stained with either hematoxylin and eosin (H&E) or by immunohistochemistry (IHC). For histopathological diagnosis, H&E-stained slides were examined by light microscopy and photomicrographs were taken using a Nikon camera mounted on a Nikon Eclipse 600 microscope (both Nikon Instruments, Melville, NY) with Adobe Elements 3.0 software (Adobe Systems, San Jose, CA). For IHC detection of NGs in tissues, rabbit monoclonal antibody to PEG (anti-PEG methoxy group; Epitomics, Burlingame, CA) was used. Goat anti-rabbit secondary antibody conjugated with fluorescence label AF 488 was used for the detection followed by counterstaining with Mayer's hematoxylin. Stained slides were visualized using confocal imaging (Carl Zeiss LSM 510).

## 2.2.14 Statistical analysis

Statistical comparisons except animal studies were carried out using Student t-test. For the antitumor study and toxicity studies, group means for tumor volume and body

weights were evaluated using repeated measures analysis of variance with the Bonferroni post test. Survival was estimated using Kaplan–Meier analysis and compared using log-rank test. *P* values less than 0.05 were considered significant. Analysis of variance with Bonferroni test and Kaplan–Meier analysis with log-rank test were performed using GraphPad Prism 5 (GraphPad Software, Inc.).

## 2.3 Results and Discussion

### 2.3.1 Synthesis and characterization of PEG-b-PGlu-b-PPhe

The synthesis of the amphiphilic hybrid polypeptide-based triblock copolymers PEG-*b*-PGlu-*b*-PPhe is illustrated in Scheme 2.1.
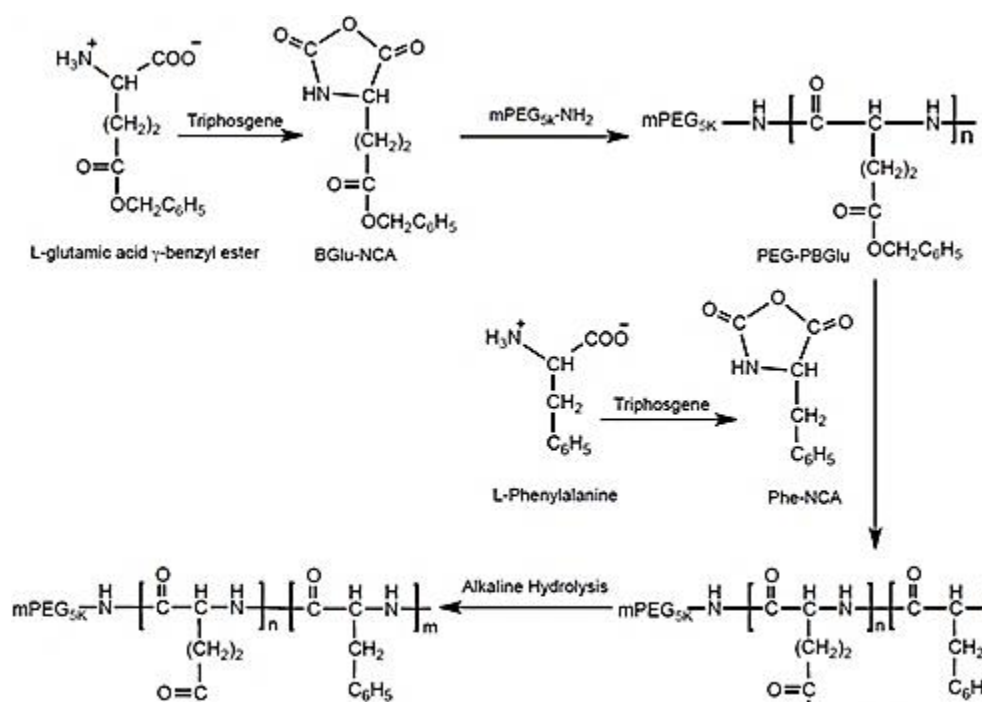


**Figure 2.1.** Scheme for the synthesis of PEG-*b*-PGlu-*b*-PPhe polymer via ring-opening NCA-based polymerization.

The copolymers were synthesized via sequential ring-opening polymerization of BGlu-NCA and Phe-NCA monomers using amino-terminated PEG ($M_w = 5,000$ g mol$^{-1}$) as macroinitiator in three stages. At first, PEG-*b*-PBGlu diblock copolymer was prepared.

The length of PBGlu block was set constant by using feed molar ratio of mPEG-NH$_2$ to BGlu-NCA at 1 : 100. The second step was polymerization of Phe-NCA initiated by PEG-*b*-PBGlu copolymer. The length of PPhe block was varied by adjusting the feed molar ratio of NCA monomers, BGlu-NCA : Phe-NCA (10:1 and 10:3). At the final step, the deprotection of the glutamate residues was carried out by alkali hydrolysis to obtain PEG-*b*-PGlu-*b*-PPhe. The chemical composition of two resulting triblock copolymers was determined by $^1H$-NMR analysis (Fig. 2.2) and further confirmed by Fourier transform infrared spectroscopy (FTIR) (data not shown).
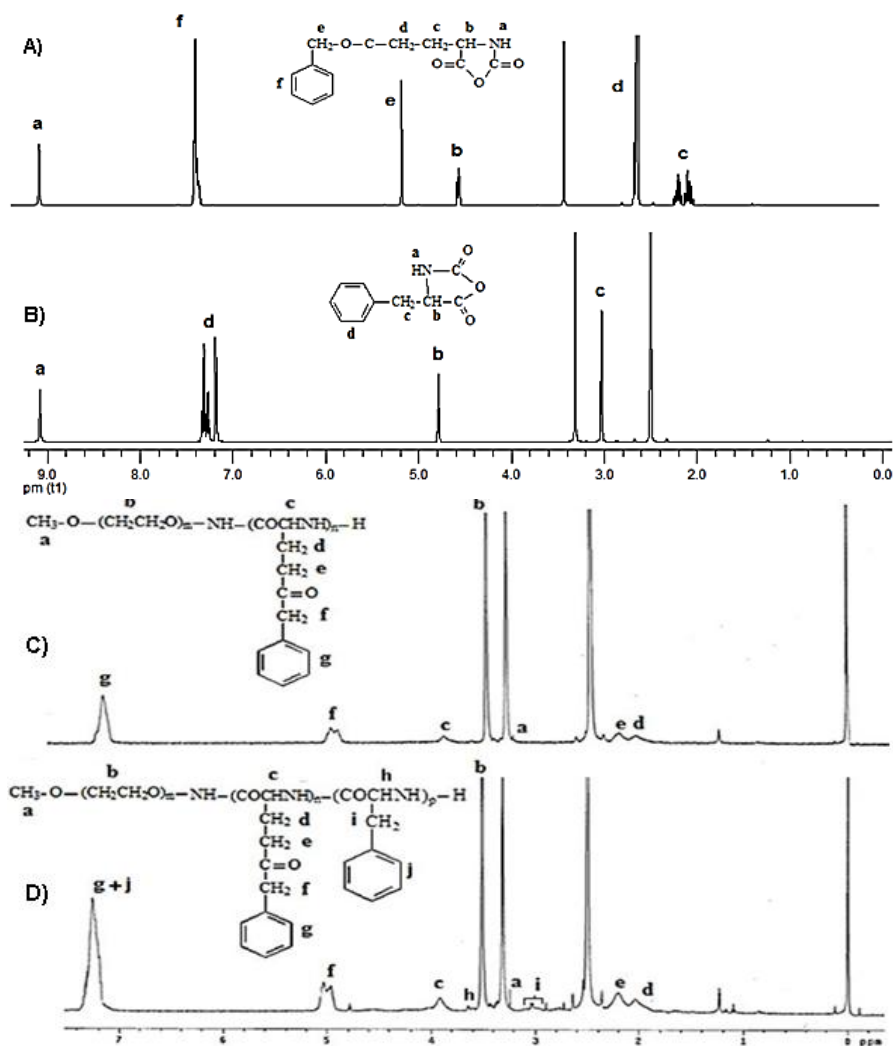
**Figure 2.2.** ^{1}H NMR spectra for A) BGlu-NCA, B) Phe-NCA, C) PEG-PBGlu and D) PEG-PBGlu-PPhe

Notes: peak assignments are as follows:

A) BGlu-NCA. ^{1}H-NMR (CDCl$_3$): δ ppm= 2.22 (2H, m, -CH$_2$-), 2.60 (2H, t, -CH$_2$-), 4.37 (1H, m, -CH-), 5.15 (2H, s, -CH$_2$-), 7.33 (5H, m, C$_6$H$_5$), 9.10 (1H, s, -NH-),

B) Phe-NCA. ^{1}H-NMR (CDCl$_3$): δ ppm= 3.01 (2H, s, -CH$_2$-), 4.90 (1H, m, -CH$_2$-); 7.20 (5H, m, C$_6$H$_5$), 9.10 (1H, s, -NH-).

C) PEG-PBGlu ^{1}H-NMR (DMSO-d$_6$): δ ppm= 1.95 (2H, broad s, -CH$_2$-) 2.25 (2H, broad s, -CH$_2$), 3.45 (4H, s, CH$_2$CH$_2$-), 5.06 (2H, m, -CH$_2$-); 7.24 (5H, m, C$_6$H$_5$).

D) PEG-PBGlu-PPhe ^{1}H-NMR (DMSO-d$_6$): δ ppm = 1.95 (2H, broad s, -CH$_2$-) 2.25 (2H, broad s, -CH$_2$-), 3.05 (2H, broad s, -CH2-), 3.45 (4H, s, CH$_2$CH$_2$-), 3.95 (1H, broad s, -CH-), 5.06 (2H, m, -CH$_2$-); 7.24 (10H, m, C$_6$H$_5$).

The polymerization degrees of PGlu and PPhe blocks are summarized in Table 2.1.

**Table 2.1.** Characteristics of the PEG-PGlu-PPhe triblock copolymer.

| Polymer | Feed molar ratio (mmol) | | | Repeating units ratio[*] | | | $M_w$[*] (g/mol) |
|---|---|---|---|---|---|---|---|
| | PEG | BGlu-NCA | Phe-NCA | PEG | PGlu | Phe | |
| PEG-PGlu$_{92}$-PPhe$_7$ | 0.02 | 2 | 0.2 | 114 | 92 | 7 | 19,700 |
| PEG-PGlu$_{90}$-PPhe$_{25}$ | 0.02 | 2 | 0.6 | 114 | 90 | 25 | 22,400 |

*Calculated from ^{1}H-NMR spectra.

Notably, PEG-*b*-PGlu-*b*-PPhe maintained the same degree of polymerization after complete removal of the benzyl protecting groups. These copolymers had a constant PEG block (114 repeating units), practically identical length of anionic PGlu block (about 90 repeating units), and differed in the length of PPhe blocks (7 and 25 repeating units). They are further denoted as PEG-PGlu$_{90}$-PPhe$_7$ and PEG-PGlu$_{90}$-PPhe$_{25}$, respectively.

2.3.2 *Synthesis and characterization of NGs*

We anticipated that incorporation of hydrophobic PPhe block into triblock copolymer confers amphiphilic properties and facilitate the formation of micellar aggregates in aqueous medium. Indeed, formation of small (intensity-average diameter of approximately 90 nm) particles with relatively narrow particle size distribution (PDI =

0.16) and net negative charge ($\xi$-potential = -22 mV) was detected in aqueous solutions of PEG-PGlu$_{90}$-PPhe$_{25}$ copolymer. In contrast, formation of large aggregates with a broad size distribution was observed only in relatively concentrated PEG-PGlu$_{90}$-PPhe$_{7}$ solutions. Differences in association behavior of PEG-PGlu-PPhe block copolymers were further confirmed by a fluorescence measurements using pyrene as a probe (Fig. 2.3).
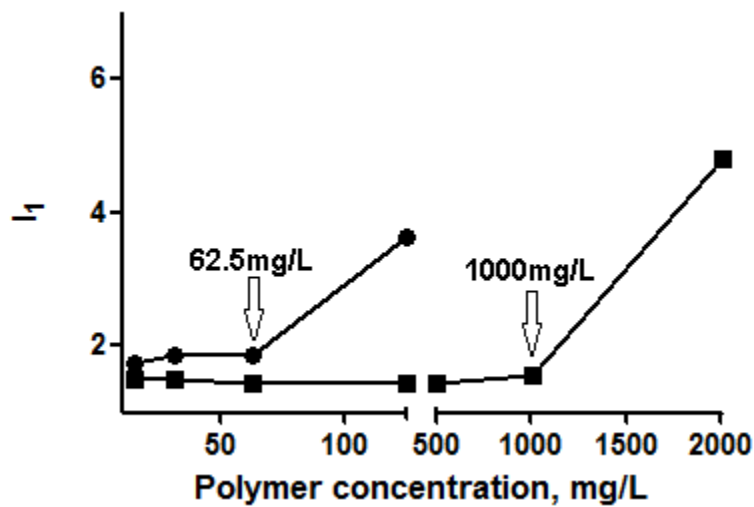


**Figure 2.3.** Plot of fluorescence intensity $I_1$ (from pyrene emission spectra) as a function of PEG-PGlu$_{90}$-PPhe$_{25}$ (●) and PEG-PGlu$_{90}$-PPhe$_{7}$ (■) concentration.

Using this approach, we determined that the critical micelle concentration (cmc) for PEG-PGlu$_{90}$-PPhe$_{25}$ was low (62.5 mg/L). In contrast the onset of aggregation of PEG-PGlu$_{90}$-PPhe$_{7}$ chains was detected at concentrations higher than 1000 mg/L. These data indicate that increase in the length of the hydrophobic PPhe block from 7 to 25 units is accompanied by an order of magnitude decrease in the cmc value. A similar trend in the dependency of cmc on the length of core-forming block was observed earlier for other amphiphilic block copolymers [19]. In dilute solution, hydrophobic and $\pi$-$\pi$ stacking interactions of the phenylalanine residues play a major role in driving self-assembly of Phe-based peptides like amyloid $\beta$ peptide [20] or synthetic polypeptides [21]. A red shift of the emission peak from the normal phenylalanine fluorescence maximum (around 280

nm) has been previously observed upon assembly in amyloid system [20]. In the present case, the fluorescence spectra obtained from 0.01% solutions of PEG-PGlu-PPhe copolymers displayed a peak at 320 nm that is attributable to $\pi$-$\pi$ stacking interactions of phenyl units; though the intensity of the fluorescence was lower for PEG-PGlu$_{90}$-PPhe$_7$ copolymer (Fig. 2.4).
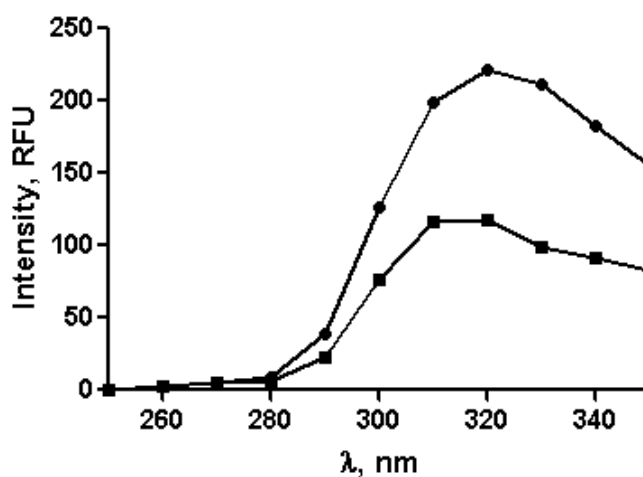


**Figure 2.4.** Emission spectra of A) PEG-PGlu$_{90}$-PPhe$_{25}$ ($\bullet$) and B) PEG-PGlu$_{90}$-PPhe$_7$ ($\blacksquare$) in water (1mg/mL, $\lambda_{ex}$=265 nm).

Notably, the fluorescence spectrum for PEG-PGlu$_{90}$-PPhe$_7$ was recorded below the cmc. It is possible that some loose pre-micelle aggregates of copolymer chains with short PPhe blocks might exist below experimentally determined cmc and the observed fluorescence characteristics may reflect the local association of aromatic units in such pre-aggregates. Interestingly, it was previously reported that peptide-PEG amphiphiles containing the hydrophobic sequence of four Phe residues conjugated to PEG of molar mass 5,000 g mol$^{-1}$ (PEG-PPhe$_4$ using our nomenclature) exhibit self-assembly behavior despite its relatively short peptide sequence with cmc value of 950 mg/L in water. It seems that insertion of ionic PGlu block into PEG-*b*-PGlu-*b*-PPhe triblock copolymer provides for additional negative contribution to micellization and increasing cmc. This may be

explained, on the one hand, by stabilization of the single polymer chains in solution, and, on the other hand, by destabilization of multimolecular NGs due to the strong electrostatic repulsion of PGlu chains in the micelle corona. Overall, the optimal hydrophilic-lipophilic balance (HLB) in terms of numbers of Phe groups with respect to PEG and PGlu chains is essential for the formation of multilayer NGs with well-defined and distinct domains: hydrophobic PPhe core, the intermediate ionic PGlu layer, and hydrophilic nonionic PEG outer shell.

The PEG-PGlu$_{90}$-PPhe$_{25}$ micelles were further utilized as ''core–shell'' templates for synthesis of NGs. The cross-linking was achieved via condensation reactions between the carboxylic groups of PGlu chains in intermediate layer and the amine groups of ethylenediamine in the presence of a water-soluble carbodiimide, EDC. The targeted extent of cross-linking (20%) was controlled by the molar ratio of cross-linker to carboxylic acid groups of the Glu residues. The NGs displayed an effective diameter of about 90 nm ($\xi$-potential = - 20 mV) and were uniform (monomodal, narrow size distribution) as determined by DLS. It is important to note that NGs had comparable sizes with the precursor PEG-PGlu$_{90}$-PPhe$_{25}$ micelles (90 ± 1.2 nm) indicating that the micelles retained their integrity and formation of cross-links was limited to intramicellar reactions. It is likely that the outer PEG shell of the micelles prevented the undesirable intermicellar reactions. The dimensions and morphology of NGs were further characterized by TEM and tapping-mode AFM in air. Based on AFM and TEM images PEG-PGlu$_{90}$-PPhe$_{25}$ NGs had a spherical morphology. As expected the number-average particle height ($H_{av}$) and diameter ($D_{av}$) values of dehydrated NGs were reduced compared to the hydrodynamic diameters $D_{eff}$ determined by DLS (Table 2.2). Upon adsorption on mica

surface NGs exhibited a high diameter versus height aspect ratios ($D_{av}/H_{av}$) suggesting substantial flattering of the particles. This observation was in agreement with the expected flexible character of the PEG-PGlu shell of the NGs. The electrostatic interactions of the negatively charged NGs with the positively charged amino-modified mica surface may induce additional flattering of NGs.

**Table 2.2.** Summary of characterization data for NGs by TEM, AFM, and DLS.

| Sample | TEM[a] | AFM[b] | | DLS[c] |
|--------|--------|--------|--------|--------|
| | $D_{av}$, nm | $D_{av}$, nm | $H_{av}$, nm | $D_{eff}$, nm |
| NG | 45 ± 3.3 | 47 ± 6.8 | 8.7 ± 3.7 | 90 ±1.2 |

[a] Number-average diameter ($D_{av}$), n = 27. A drop of the sample solution was allowed to settle on a Formvar precoated copper grid and the sample was allowed to air-dry.
[b] Number-average height (Hav) and diameter (Dav), n = 55. NGs were deposited from aqueous solutions at pH 6.5 onto APS mica surface and allowed to dry in vacuum.
[c] Intensity-average hydrodynamic diameter($D_{eff}$) for DLS was determined at pH 7.4, n= 5.
Data are expressed as mean ± SD.

Interestingly, the hybrid PEG-PGlu$_{90}$-PPhe$_{25}$ NGs were characterized by a significantly lower aspect ratio (ca. 6) compared to PEG-poly(methacrylic acid) (PEG-PMA) NGs containing entirely hydrophilic cross-linked PMA cores [22]. For example, PEG-PMA$_{133}$ and PEG-PMA$_{75}$ NGs were characterized by dimension aspect ratios of 13.3 and 15.0, respectively. The observed topological differences can be explained by the presence of relatively rigid hydrophobic PPhe cores in the PEG-PGlu$_{90}$-PPhe$_{25}$ NGs that rendered them more stiff and deceased their deformation at the substrate surface.

The pH-induced dimensional changes (nanogel-like behavior) of the NGs were evident from an increase in the micelle size and net negative charge (Fig. 2.5A).

A                                    B
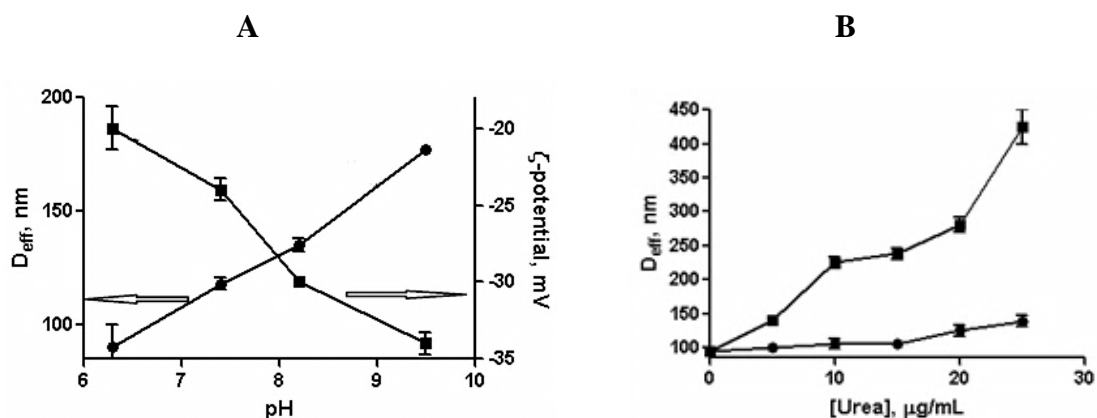


**Figure 2.5.** Swelling behavior (**A**) and stability (**B**) of NGs. (**A**) The effective diameter, $D_{eff}$ (●) and $\zeta$-potential (■) of NGs as a function of pH. (**B**) Changes in $D_{eff}$ of NGs (●) and non-crosslinked NGs (■) upon treatment with different concentrations of 8M urea.

Such behavior was indicative of ionization and swelling of the intermediate layer formed by the cross-linked PGlu chains in the shell of the NGs. The kinetic stability of NGs was further analyzed in the presence of urea (Fig. 2.5B). Urea, a small hydrophilic molecule, is widely used as protein denaturant due to its ability to form stronger attractive dispersion interactions with the protein side chains and backbone than does water. Therefore, it was expected that urea is able to destabilize PEG-PGlu$_{90}$-PPhe$_{25}$ NGs by weakening the hydrophobic interactions in PPhe core region as well as by disrupting hydrogen-bonding interactions between polypeptide chains. Indeed, for non-cross-linked NGs addition of 8 M urea led to significant increase in the size and PDI of the aggregates. In the meantime, only little changes in the average size of NGs were detected in the presence of urea (Fig. 2.4B). The observed limited swelling of PEG-PGlu$_{90}$-PPhe$_{25}$ NGs can be thus directly related to a restricted mobility of the PGlu chains in the shell and

provides additional evidence that the physical stability of NGs can be greatly enhanced via covalent crosslinking. Importantly, the cross-linking did not prevent the degradation of NGs by proteolytic enzymes. The enzymatic biodegradability of PEG-PGlu$_{90}$-PPhe$_{25}$ NGs was determined by incubating the NGs with cathepsin B followed by analysis of the reaction mixture using size exclusion chromatography (SEC) (Fig. 2.6).
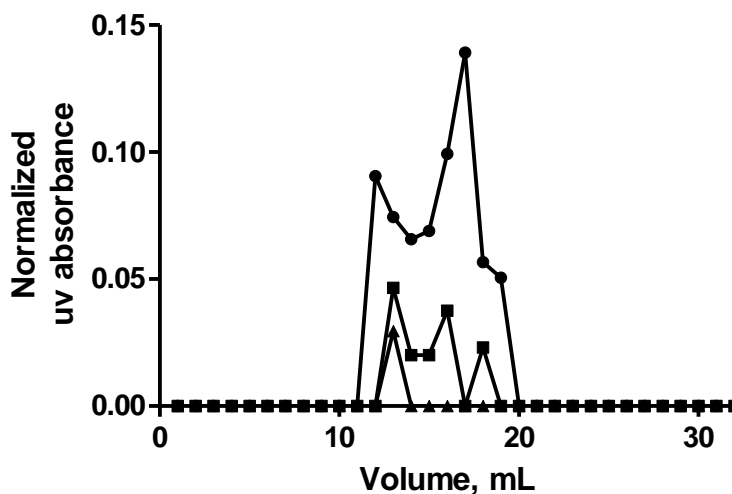


**Figure 2.6.** Degradation of NGs upon treatment with cathepsin B at 37$^0$C wherein aliquots were removed at 0 h (●), 12 h (■) and 24 h (▲) followed by its analysis using FPLC.

A gradual decrease in the UV absorption of the micelle peak was observed in SEC chromatograms over the incubation time, which almost disappeared after 24 hrs. Furthermore, decrease in light scattering intensity along with the drastic increase of PDI was detected by DLS of the NGs dispersions already after 12 hrs of incubation with cathepsin B suggesting structural disintegration of such NGs (Table 2.3).

**Table 2.3.** Physicochemical characteristics of NGs after incubation with cathepsin B (10 units/mL).

| Time (h) | NGs + cathepsin B[a] | |
|----------|------------------------|-----|
|          | D$_{eff}$, nm | PDI |
| 0 | 125±1.5 | 0.223 |

| | | |
|---|---|---|
| 12 | 181±2.2 | 0.424 |
| 24 | 738±9.0 | 0.619 |

[a] Effective diameter ($D_{eff}$) and polydispersity index (PDI) were determined in water (pH 6.1). Data are expressed as mean ± SD (n=3).

However, further studies will be necessary to characterize the degradation products and determine whether drug incorporation can alter the degradation pattern of the NGs. Overall, these results imply that the reinforcing cross-links within the shell of PEG-PGlu$_{90}$-PPhe$_{25}$ NGs can permanently suppress their dissociation. Resulting NGs can withstand environmental challenges and sink conditions encountered after systemic administration and, consequently, provide means for temporal control over drug disposition. On the other hand, enzymatic degradation of the polypeptide-based building blocks of NGs reduces the risk of polymer accumulation inside cells and can also facilitate specific intracellular drug release.

### 2.3.3   Drug loading and release from NGs.

PEG-PGlu$_{90}$-PPhe$_{25}$ NGs have a well-defined structure with a central hydrophobic core formed by PPhe chains, swollen intermediate layer of a cross-linked PGlu network and external PEG shell surrounding the core and intermediate layer.  Each of these three nanodomains contributes to the utility of NGs as drug nanocarriers. A PPhe core can serve as a cargo for water-insoluble drugs. An ionic intermediate layer can incorporate hydrophilic drug molecules through electrostatic or covalent bonding while PEG shell in addition to stabilizing NGs in dispersion also allows minimizing interactions of the NGs with blood components. Therefore, such NGs would provide unique opportunity to simultaneously incorporate and deliver multiple chemotherapeutic drugs with very different physical properties and modes of action inside a single polymeric carrier in

order to achieve a synergistic effect and enhance the efficacy of treatment. In the present study NGs with binary drug combination of hydrophilic CDDP and hydrophobic PTX were prepared. At first, PTX was solubilized into the PPhe cores of the NGs using micelle extraction method. According to this method, PTX dissolved in ethanol was added to the aqueous dispersion of NGs upon agitation followed by evaporation of organic solvent and removal of unbound PTX. Under these conditions PTX loading capacity (the net amount of drug loaded into a carrier) was about 9 w/w% weight as was quantified by HPLC. The size and $\zeta$-potential of the PTX-loaded NGs were comparable to those of empty NGs indicating that the PTX incorporation into PPhe cores did not affect the macroscopic characteristics of the pre-formed NGs. As the next step, CDDP was incubated with the aqueous dispersions of PTX-loaded NGs for 48 h at pH 9.0 [7]. Such conditions were chosen to maximize the swelling of PGlu cross-linked layer (Fig. 2.4A) and increase the accessibility of the bulk of the carboxylate groups to CDDP. As expected, the net negative charge and particle size of NGs decreased upon CDDP loading consistent with neutralization and condensation of PGlu segments by CDDP (Table 2.4).

**Table 2.4.** Physicochemical characteristics of NGs before and after drug loading.

| Sample | $D_{eff}$ (nm) | PDI | $\zeta$-potential (mV) | LC (w/w%)[b] |
|---|---|---|---|---|
| NGs | 90 ± 1.2 | 0.14 | -20.0 ± 1.2 | - |
| PTX/NG | 105 ± 2.8 | 0.23 | -19.1 ± 1.5 | 8.4 |
| CDDP/NG | 71 ± 3.3 | 0.19 | -3.7 ± 1.0 | 22.4 |
| (CDDP+PTX)/NG | 76 ± 4.0 | 0.24 | -5.7 ± 0.47 | 24.8[c] |

[a] Effective diameter ($D_{eff}$), polydispersity index (PDI) and $\zeta$-potential were determined in water (pH 6.5).

[b] Pt and PTX content were determined by ICP-MS and HPLC, respectively. Loading capacity (LC) is expressed as mass of incorporated drug per mass of drug loaded NGs (w/w).
[C] Total LC for combination of CDDP (15.4%) and PTX (9.4%).
Data are expressed as mean ± SD (n = 3).

15 w/w% loading was achieved with respect to CDDP while total loading values for binary drug combination was about 25% and corresponded to 10 : 1 molar ratio (CDDP : PTX) of drugs in the NGs. (CDDP+PTX)/NG maintained their spherical morphology as was confirmed by TEM (Fig. 2.7).
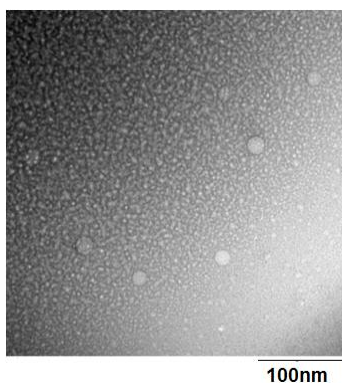


100nm

**Figure 2.7.** TEM image of (CDDP+PTX)/NG. Bar equals 100nm

Notably, (CDDP+PTX)-loaded NGs were stable in aqueous dispersions, exhibiting no aggregation or precipitation with loading capacity preserved for as long as month (Table 2.5).

**Table 2.5.** Physicochemical characteristics of empty and drug-loaded NGs after one month of storage in aqueous dispersion at $4^{o}$C.

| Sample | $D_{eff}$ (nm) | PDI | ζ-potential (mV) | LC (w/w%)[b] |
|---|---|---|---|---|
| NG | 95 ± 0.8 | 0.16 | -24.6 ± 3.2 | - |
| (CDDP+PTX)/NG | 77 ± 0.5 | 0.26 | -7.7 ± 1.8 | 21.2[C] |

[a] Effective diameter ($D_{eff}$), polydispersity index (PDI) and ζ-potential were determined in water (pH 6.5).
[b] Pt and PTX content were determined by ICP-MS and HPLC, respectively.
[C] Total LC for combination of CDDP (13.8%) and PTX (7.4%).

Interestingly, the loading capacity of NGs with respect to CDDP was decreased after loading of PTX as compared to single CDDP/NG formulation (15% vs. 23%). This

apparent difference in drug loading is not yet understood and needs to be investigated further. We hypothesize that the presence of hydrophobic solute in the core of the micelle affects the conformation of the polypeptide chains at the PPhe core - PGlu shell interface. Specifically, in more hydrophobic environment PGlu chains can transition from random coil to α-helical conformation leading to structural condensation in this region which may restrict space for the loading CDDP molecules. Validation of this hypothesis is of considerable interest and is ongoing in our laboratory.

The release of the drugs from NGs was studied by equilibrium dialysis at 37 °C at either pH 7.4 (PBS) or pH 5.5 (ABS), which reflect conditions encountered in plasma and in intracellular compartments (lysosomes), respectively. The kinetic profiles of drug release from (CDDP+PTX)/NGs are presented in Fig. 2.8. As seen from these data sustained but temporally distinct release of Pt(II) species and PTX was observed. Notably, PTX release was much faster than that of Pt(II), which is expected since PTX is physically entrapped into the PPhe core. In contrast, CDDP binds with PGlu chains through electrostatic and coordination interactions and its release usually proceeds via ligand exchange reactions with chloride or other biologically abundant anions, thus delaying its liberation from the NGs. Pt(II) release from the NGs was also a pH-dependent process. Indeed, Pt(II) species were liberated from the NGs faster at pH 5.5 than at pH 7.4 (Fig. 2.8B), probably, due to protonation of carboxylic groups of PGlu, which weakens the drug and micelle electrostatic coupling. For example, during 24 hrs (CDDP+PTX)/NGs released $16.7 \pm 5.5\%$ of loaded Pt(II) at pH 5.5 and only $8.8 \pm 3.6\%$ at pH 7.4, respectively.

A B C
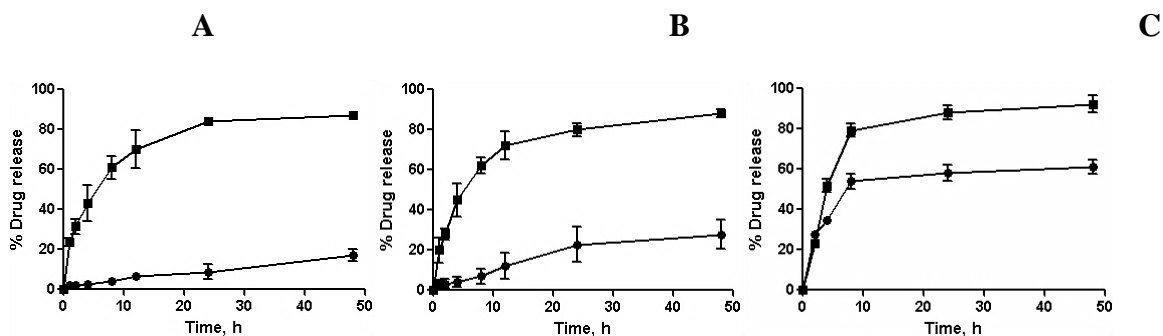


**Figure 2.8.** *In vitro* drug release profiles for Pt (●) and PTX (■) from NGs in (**A**) PBS, pH 7.4; (**B**) ABS, pH 5.5; and (**C**) ABS in presence of cathepsin B (10 units/mL) at 37°C. Data are expressed as mean ± SD (n=3).

Notably, pH changes practically did not affect the release of PTX. Also, noteworthy that Pt (II) release from (CDDP+PTX)/NG at the acidic pH was further accelerated in presence of cathepsin B in the media (Fig. 2.8C). Cathepsin B is a lysosomal thiol-dependent protease [23] and is also extracellularly present in pathological tissues such as tumors and sites of inflammation [24, 25]. These results indicate that degradation of NGs can further facilitate the drug release once located within targeted tissue and cells.

### 2.3.4 In vitro cytotoxicity of the drug-loaded NGs

The cytotoxicity of drug combination loaded into NGs was determined in human ovarian carcinoma A2780 cells using MTT assay. Calculated $IC_{50}$ values are summarized in Table 2.6.

**Table 2.6**. Comparison of $IC_{50}$ values for various drug-loaded NGs and free CDDP against A2780 cells as determined by the MTT assay.

| | $IC_{50}$ (µM) |
|---|---|
| Free CDDP | 1.5 |
| CDDP/NG | 3.9 |
| PTX/NG | 0.17 |
| (CDDP+PTX)/NG | 0.14* |
| CDDP/NG + PTX/NG | 6.3* |

*Calculated with respect to CDDP.

Importantly, NGs alone were nontoxic to the cells up to the concentration of 5 mg/mL. CDDP/NG displayed lower cytotoxic activity than free CDDP. Since unloaded NGs did not affect the cell survival in the entire range of concentrations the cytotoxic activity of CDDP/NG was mediated by the Pt(II) species slowly released from the NGs. However, we found that (CDDP+PTX)/NG were significantly more effective in killing A2780 ovarian cancer cells than CDDP/NG. The dose of CDDP in NGs was indeed reduced nearly by 30-fold when used in combination with PTX (at 10 : 1 CDDP/PTX molar ratio) to achieve the same cytotoxic effect produced by the CDDP loaded NGs. The CI value at $IC_{50}$ for this (CDDP+PTX)/NG combination was 0.078, indicating strong synergistic cytotoxicity against A2780 ovarian cancer cells. Notably, the combination of two separate micellar formulations (CDDP/NG +PTX/NG) applied at the same drug ratio elicited cytotoxicity comparable to that of the CDDP/NG formulation (Table 4) and displayed antagonistic CI value of 1.2 at $IC_{50}$. These data suggest that synchronized delivery of this drug combination in the same *cl*-micelle formulation may play an essential role in the cytotoxic activity.

## 2.3.5 Antitumor activity

Motivated by the enhanced *in vitro* efficacy of (CDDP+PTX)/NG formulation, we evaluated its antitumor efficacy *in vivo* in mice bearing A2780 human ovarian cancer xenografts. Free CDDP and CDDP/NG were injected 4 times at 4-day intervals at an equivalent dose of 4 mg-CDDP/kg determined as the maximum tolerated dose upon this treatment schedule [18]. Animals injected with (CDDP+PTX)/NG received 4mg/kg CDDP and 1 mg/kg PTX equivalents per dose. The changes in the relative tumor volume, body weight and animal lifespan are shown in Fig. 2.9.
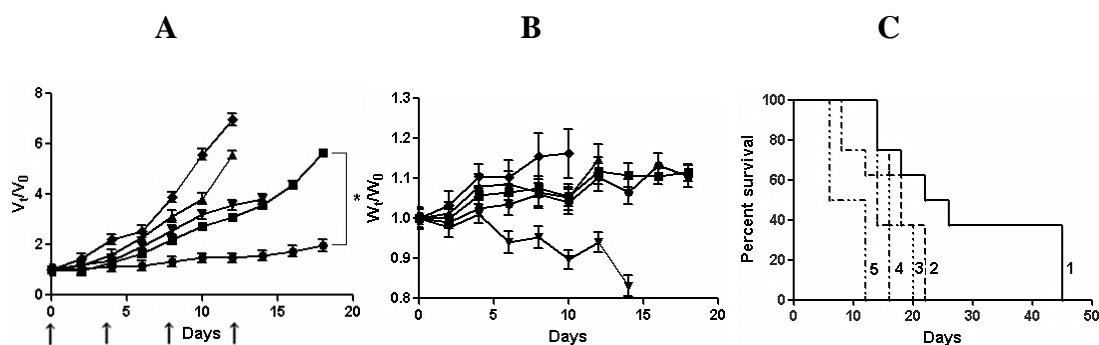
**Figure 2.9.** *In vivo* antitumor efficacy of (CDDP+PTX)/NG in A2780 human ovarian cancer xenograft-bearing female nude mice. Relative changes in (**A**) tumor volume and (**B**) body weight were measured following intravenous administration of (CDDP+PTX)/NG (●) or CDDP/NG (■) or PTX/NG (▲) or free CDDP (▼) or 5% dextrose (♦). Drug formulations were injected in100 μL at a dose of 4 mg CDDP or 1mg PTX equivalents/kg body weight 4 times at 4-day intervals as indicated by the arrows. Values indicated are means ± SEM (n = 8). (**C**) Kaplan–Meier analysis of overall survival in (CDDP+PTX)/NG group (1) or CDDP/*cl*-micelles group (2) or PTX/NG group (4) or free CDDP group (3) or control group (5). Tumor volume and body weight are normalized with respect to tumor volume or body weight at day 0. * $P<0.05$.

Tumor burden was significantly decreased by both free CDDP ($P<0.05$) and CDDP/NG ($P<0.05$) treatments compared to control (Fig. 2.9A). However, tumors in the animals treated with CDDP/NG remained relatively smaller than in animals treated with free CDDP between days 0 and 18. As a result, increased survival of the animals was observed in mice treated with CDDP/NG compared to CDDP alone (Fig. 2.9C). Notably, treatment with PTX-loaded NG did not have any substantial effect on the tumor growth and only minor increase in survival was observed over controls. In contrast, nearly complete inhibition of tumor growth was observed for the mice treated with (CDDP+PTX)/NG from day 0 to 14, which translated into significantly increased overall survival of the animals treated with (CDDP+PTX)/NG compared to either CDDP/NG ($P<0.05$) or CDDP alone ($P<0.05$) (Fig. 2.9A and C). On the second day post treatment animals injected with either (CDDP+PTX)/NG or CDDP/NG displayed significantly

higher levels of Pt in tumors compared to free CDDP treatment group ($P<0.05$) which may be attributed to the enhanced permeability and retention (EPR) effect (Fig. 2.10A) [26].

**A**                                                                         **B**
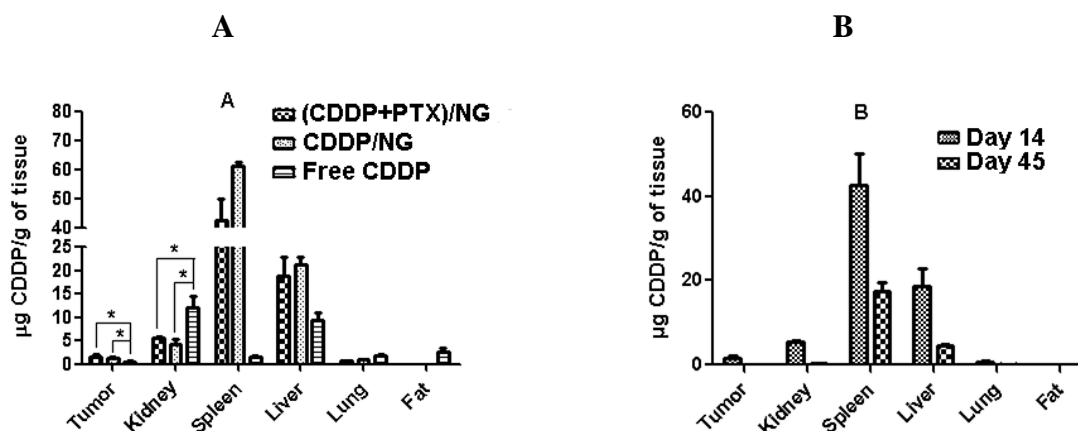


**Figure 2.10.** Tissue distribution of platinum in different treatment groups as determined ICP- MS. (**A**) Mice were sacrificed at day 14 of the treatment with (CDDP+PTX)/NG or CDDP/NG or free CDDP. (**B**) Significant reduction in the Pt levels in various organs of mice treated with (CDDP+PTX)/NG was confirmed by comparing Pt levels at day 14 and day 45. Values indicated are means ± SEM (n = 3), ＊$P<0.05$.

To elucidate the mechanism underlying the enhanced antitumor activity of (CDDP+PTX)/NG, the tumors were excised post-treatment (on $2^{nd}$ day after last injection) and processed for Ki-67-Caspase-3 assay to examine the effect of each treatment on induction of apoptosis (Fig. 2.11).
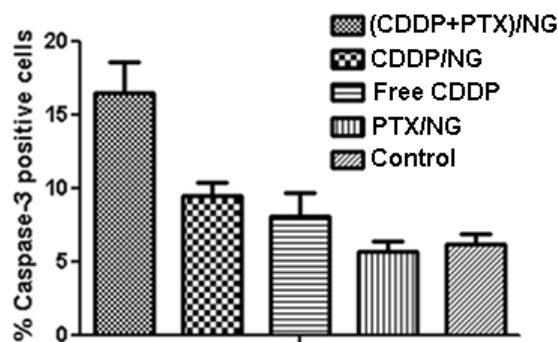
**Figure 2.11.** Ki-67-caspase-3 apoptosis assay. Quantification of caspase-3 positive cells in tumor tissue from mice from various groups. Data are presented as mean ± SD (n = 5 random microscopic fields for each tumor slice).

The number of caspase-3 positive cells were significantly higher in tumors from mice that received (CDDP+PTX)/NG compared to tumors in CDDP/NG *(P<0.05)* or PTX/NG *(P<0.05)* or free CDDP *(P<0.05)* (Fig. 2.11). This assay further corroborates the superior antitumor efficacy of binary drug combination NG formulation over single drug-loaded NGs or CDDP alone. Since the levels of Pt accumulation in tumors were comparable for the treatments with both single and binary drug formulations, we rationalize that an increase in therapeutic efficacy of (CDDP+PTX)/NG can be related to highly synergistic interactions between CDDP and PTX simultaneously delivered to the tumors. Indeed, the average weight ratio of the CDDP and PTX in the tumors of the animals treated with (CDDP+PTX)/NG was determined to be 4 : 1, the same as the drug loading ratio in NG, indicating the spatial-temporal synchronization of drug exposure. CDDP and PTX are highly suited for combination chemotherapy because they have distinct mechanisms of action. CDDP binds to DNA base pairs creating adducts, cross-links, and strand breaks that inhibit DNA replication. Unrepairable DNA damage often results in activation of the apoptotic pathway. Paclitaxel acts by binding to intracellular β-tubulin, which leads to microtubule stabilization, $G_2$–M arrest and apoptosis [27]. CDDP is thought to be relatively non-cell cycle specific in terms of its cell-killing effects and tends to synergize or have additive cytotoxicity with agents that alter mitosis (PTX) [28, 29]. Apart from the mechanism basis, synergistic effect greatly depends on drug dosages, combination ratios, cell lines and intervention schedules. Indeed, synergy between CDDP and PTX was reported to be highly schedule dependent [30, 31]. Profound synergistic effects were

observed when PTX was administered prior to CDDP [28, 30] while the sequence of CDDP before PTX had less antitumor activity *in vitro* [31], and induced more profound neutropenia *in vivo* [32]. One can speculate that the ability of (CDDP+PTX)/NG to supply drugs in a temporally controlled fashion by releasing PTX significantly faster than CDDP may contribute into observed improvement of antitumor efficacy of drug combination.

It should be emphasized that PTX and CDDP may also interact synergistically with respect to toxicity to the normal tissues as well. However, this was not the case in our studies. Fig. 2.9B shows that either single or binary drug loaded NG did not induce body weight loss while the same dose of the free CDDP produced a considerable body weight loss ($P < 0.05$), which indicated systemic toxicity of free CDDP. In the kidney, the primary target organ of CDDP toxicity [33, 34], single or binary drug loaded NGs showed significantly lower Pt levels than the free CDDP (Fig. 2.12A). Reduced Pt accumulation in kidney after (CDDP+PTX)/NG or CDDP/NG treatment ameliorated CDDP-induced nephrotoxicity as confirmed by tissue histopathology analysis.
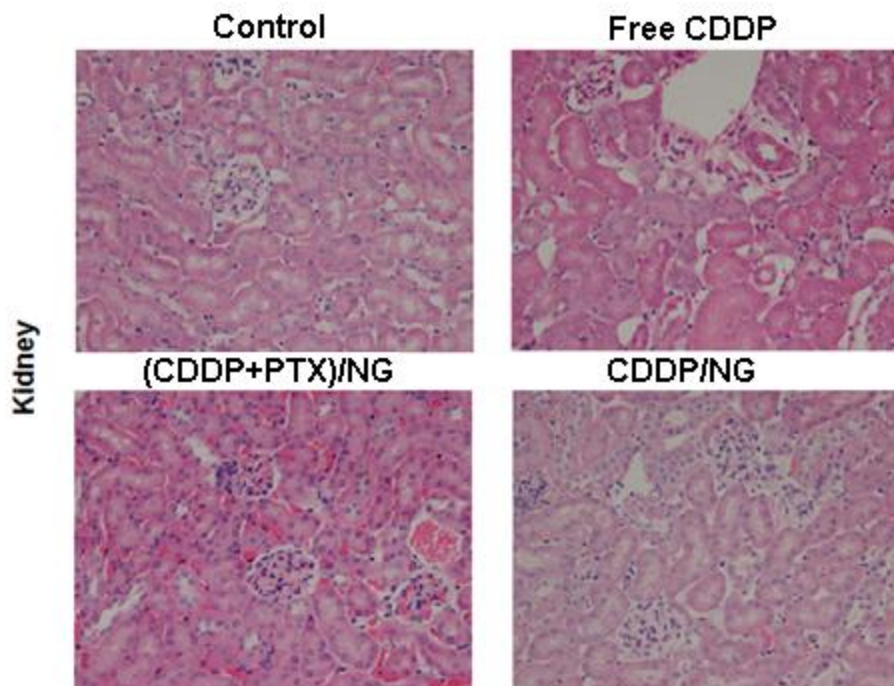
**Figure 2.12.** Light microscopy images (original magnification 100×) of hematoxylin and eosin-stained kidney sections of mice. Tissue samples were collected at day 14.

Light microscopic examination of H&E stained kidney sections from sacrificed animals indicated focal tubular basophilia with regeneration in kidneys from all animals treated with free CDDP, while no histopathological changes were observed in kidney from animals in the (CDDP+PTX)/NG-treated or CDDP/NG-treated groups compared with the control (Fig. 2.12). Reduced nephrotoxicity of (CDDP+PTX)/NG or CDDP/NG is likely due to its macromolecular size coupled with slow release of the drug, which leads to a lower renal tubular drug exposure. This is a significant result considering renal toxicity is the most severe, dose-limiting toxicity with CDDP treatment [35]. (CDDP+PTX)/NG showed very high Pt accumulation in spleen and liver (Fig. 2.10A), but this amount reduced significantly ($P<0.01$) with time (Fig. 2.10B). Despite much higher exposure of liver and spleen to CDDP in the (CDDP+PTX)/NG or CDDP/NG treatment, there was no

significant change in hepatic toxicity markers of blood chemistry (Table 2.7), indicating

no obvious toxicity to the liver.

**Table 2.7.** Clinical chemistry parameters at day 14 of the treatment.

|  | ALP | ALT |
|---|---|---|
| Control | <5 | $43 \pm 8$ |
| Free CDDP | <5 | $58 \pm 2$ |
| CDDP/NG | <5 | $45 \pm 9$ |
| PTX/NG | <5 | $66 \pm 17$ |
| (CDDP+PTX)/NG | <5 | $41 \pm 9$ |

Data were expressed as mean ± SD (n=3)
Values of ALP and ALT are expressed as U/L
**Abbreviations:** Alkaline phosphatase; ALP, alanine aminotransferase; ALT.

There was no evidence of liver or splenic toxicity by histopathology (data not shown). In

spleen, the NGs (either free or localized inside macrophages) were detected

predominantly in the red pulp with little to no staining in the lymphoid region (Fig. 2.13).

Free CDDP treatment has previously been reported to have a remarkable effect on

immunological function due to its ability to reduce lymphocytes in the thymus and the

spleen with changes in splenic white pulp being the most significant [36].
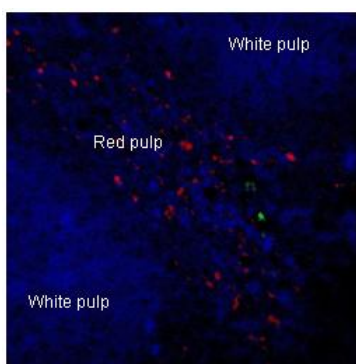


**Figure 2.13.** Confocal image of spleen section stained for NGs (green) and macrophages
(red). Spleen shows accumulation of NGs only in the red pulp region.

Absence of (CDDP+PTX)/NG in lymphoid regions of white pulp may thus limit free-

drug exposure to these follicles. Collectively, these results demonstrate that

biodegradable PEG-polypeptide hybrid NGs carrying CDDP and PTX drug combination

exerted superior antitumor efficacy, both in terms of tumor inhibition and survival, which could be attributed to the preferential simultaneous accumulation, and increased potency.

## 2.4 Conclusions

In the present investigation, NGs based on biodegradable and biocompatible amphiphilic PEG-*b*-PGlu-*b*-PPhe triblock copolymers were evaluated as potential carriers for co-delivery of chemotherapeutic drugs with various physicochemical properties and modes of action. These nanostructures were designed to have multicompartment morphology for drug loading and were cross-linked at an intermediate layer within the polymeric NGs to ensure their prolong stability upon systemic administration. Hydrophilic CDDP and hydrophobic PTX were loaded in such NGs with high efficiency, exhibited differential release profiles and synergistic cytotoxic effect against ovarian cancer cells. The binary drug combination simultaneously delivered using NGs exhibited superior antitumor efficacy over single drug *cl*-micelle analogues *in vivo* in synergistic manner. Altogether, this study demonstrates a fundamental possibility for simultaneous delivery of chemotherapeutics and molecular targeting agents via single well-defined and structurally tunable polymeric nanocarrier.

## 2.5. References:

[1] R.C. Bast, B. Hennessy, G.B. Mills, The biology of ovarian cancer: new opportunities for translation, Nat. Rev. Cancer, 9 (2009) 415-428.

[2] A. Kim, Y. Ueda, T. Naka, T. Enomoto, Therapeutic strategies in epithelial ovarian cancer, J. Exp. Clin. Cancer Res.: CR, 31 (2012) 14.

[3] B. Lippert, Cisplatin: chemistry and biochemistry of a leading anticancer drug, Wiley-VCH, 1999.

[4] R.S. Go, A.A. Adjei, Review of the comparative pharmacology and clinical activity of cisplatin and carboplatin, J. Clin. Oncol., 17 (1999) 409-409.

[5] N.J. Wheate, S. Walker, G.E. Craig, R. Oun, The status of platinum anticancer drugs in the clinic and in clinical trials, Dalton Trans., 39 (2010) 8113-8127.

[6] Y. Matsumura, K. Kataoka, Preclinical and clinical studies of anticancer agent-incorporating polymer micelles, Cancer Sci., 100 (2009) 572-579.

[7] H.S. Oberoi, F.C. Laquer, L.A. Marky, A.V. Kabanov, T.K. Bronich, Core cross-linked block ionomer micelles as pH-responsive carriers for cis-diamminedichloroplatinum (II), J. Control. Release, 153 (2011) 64-72.

[8] N.V. Nukolova, H.S. Oberoi, S.M. Cohen, A.V. Kabanov, T.K. Bronich, Folate-decorated nanogels for targeted therapy of ovarian cancer, Biomaterials, 32 (2011) 5417-5426.

[9] Y. Han, Z. He, A. Schulz, T.K. Bronich, R. Jordan, R. Luxenhofer, A.V. Kabanov, Synergistic combinations of multiple chemotherapeutic agents in high capacity poly (2-oxazoline) micelles, Mol. Pharm., 9 (2012) 2302-2313.

[10] J. Sandercock, M. Parmar, V. Torri, W. Qian, First-line treatment for advanced ovarian cancer: paclitaxel, platinum and the evidence, Br. J. Cancer, 87 (2002) 815-824.

[11] G. Batist, K.A. Gelmon, K.N. Chi, W.H. Miller, S.K. Chia, L.D. Mayer, C.E. Swenson, A.S. Janoff, A.C. Louie, Safety, pharmacokinetics, and efficacy of CPX-1 liposome injection in patients with advanced solid tumors, Clin. Cancer Res., 15 (2009) 692-700.

[12] H.-C. Shin, A.W. Alani, H. Cho, Y. Bae, J.M. Kolesar, G.S. Kwon, A 3-in-1 polymeric micelle nanocontainer for poorly water-soluble drugs, Mol. Pharm., 8 (2011) 1257-1265.

[13] N. Kolishetti, S. Dhar, P.M. Valencia, L.Q. Lin, R. Karnik, S.J. Lippard, R. Langer, O.C. Farokhzad, Engineering of self-assembled nanoparticle platform for precisely controlled combination drug therapy, Proc. Natl. Acad. Sci., 107 (2010) 17939-17944.

[14] K. Ananthapadmanabhan, E. Goddard, N. Turro, P. Kuo, Fluorescence probes for critical micelle concentration, Langmuir, 1 (1985) 352-355.

[15] D. Yang, S. Van, X. Jiang, L. Yu, Novel free paclitaxel-loaded poly(L-gamma-glutamylglutamine)-paclitaxel nanoparticles, Int. J. Nanomedicine, 6 (2011) 85-91.

[16] M. Ferrari, M.C. Fornasiero, A.M. Isetta, MTT colorimetric assay for testing macrophage cytotoxic activity in vitro, J Immunol. Methods, 131 (1990) 165-172.

[17] T.C. Chou, Drug combination studies and their synergy quantification using the Chou-Talalay method, Cancer Res., 70 (2010) 440-446.

[18] H.S. Oberoi, N.V. Nukolova, F.C. Laquer, L.Y. Poluektova, J. Huang, Y. Alnouti, M. Yokohira, L.L. Arnold, A.V. Kabanov, S.M. Cohen, Cisplatin-loaded core cross-linked micelles: comparative pharmacokinetics, antitumor activity, and toxicity in mice, Int. J. Nanomedicine, 7 (2012) 2557.

[19] I. Astafieva, K. Khougaz, A. Eisenberg, Micellization in block polyelectrolyte solutions. 2. fluorescence study of the critical micelle concentration as a function of soluble block length and salt concentration, Macromolecules, 28 (1995) 7127-7134.

[20] M.J. Krysmann, V. Castelletto, A. Kelarakis, I.W. Hamley, R.A. Hule, D.J. Pochan, Self-assembly and hydrogelation of an amyloid peptide fragment, Biochemistry, 47 (2008) 4597-4605.

[21] J. Sun, X. Chen, C. Deng, H. Yu, Z. Xie, X. Jing, Direct formation of giant vesicles from synthetic polypeptides, Langmuir, 23 (2007) 8308-8315.

[22] N.V. Nukolova, Z. Yang, J.O. Kim, A.V. Kabanov, T.K. Bronich, Polyelectrolyte nanogels decorated with monoclonal antibody for targeted drug delivery, React. Funct. Polym., 71 (2011) 315-323.

[23] H.H. Otto, T. Schirmeister, Cysteine proteases and their inhibitors, Chem. Rev., 97 (1997) 133-172.

[24] J.E. Koblinski, M. Ahram, B.F. Sloane, Unraveling the role of proteases in cancer, Clin. Chim. Acta., 291 (2000) 113-135.

[25] Y. Hashimoto, H. Kakegawa, Y. Narita, Y. Hachiya, T. Hayakawa, J. Kos, V. Turk, N. Katunuma, Significance of cathepsin B accumulation in synovial fluid of rheumatoid arthritis, Biochem. Biophys. Res. Commun., 283 (2001) 334-339.

[26] H. Maeda, J. Wu, T. Sawa, Y. Matsumura, K. Hori, Tumor vascular permeability and the EPR effect in macromolecular therapeutics: a review, J. Control. Release, 65 (2000) 271-284.

[27] R. Agarwal, S.B. Kaye, Ovarian cancer: strategies for overcoming resistance to chemotherapy, Nat. Rev. Cancer, 3 (2003) 502-516.

[28] A. Jekunen, R. Christen, D. Shalinsky, S. Howell, Synergistic interaction between cisplatin and taxol in human ovarian carcinoma cells in vitro, Br. J. Cancer, 69 (1994) 299.

[29] P. Engblom, V. Rantanen, J. Kulmala, H. Helenius, S. Grenman, Additive and supra-additive cytotoxicity of cisplatin-taxane combinations in ovarian carcinoma cell lines, Br. J. Cancer, 79 (1999) 286.

[30] C.G. Milross, L.J. Peters, N.R. Hunter, K.A. Mason, L. Milas, Sequence-dependent antitumor activity of paclitaxel (taxol) and cisplatin in vivo, Int. J. Cancer, 62 (1995) 599-604.

[31] U. Vanhoefer, A. Harstrick, H. Wilke, N. Schleucher, H. Walles, J. Schröder, S. Seeber, Schedule-dependent antagonism of paclitaxel and cisplatin in human gastric and ovarian carcinoma cell Lines in vitro, Eur. J. Cancer, 31 (1995) 92-97.

[32] E.K. Rowinsky, M. Gilbert, W. McGuire, D. Noe, L. Grochow, A. Forastiere, D. Ettinger, B. Lubejko, B. Clark, S. Sartorius, Sequences of taxol and cisplatin: a phase I and pharmacologic study, J. Clin. Oncol., 9 (1991) 1692-1703.

[33] H. Uchino, Y. Matsumura, T. Negishi, F. Koizumi, T. Hayashi, T. Honda, N. Nishiyama, K. Kataoka, S. Naito, T. Kakizoe, Cisplatin-incorporating polymeric micelles (NC-6004) can reduce nephrotoxicity and neurotoxicity of cisplatin in rats, Br. J. Cancer, 93 (2005) 678-687.

[34] Y. Mizumura, Y. Matsumura, T. Hamaguchi, N. Nishiyama, K. Kataoka, T. Kawaguchi, W.J.M. Hrushesky, F. Moriyasu, T. Kakizoe, Cisplatin-incorporated polymeric micelles eliminate nephrotoxicity, while maintaining antitumor activity, Cancer Sci., 92 (2001) 328-336.

[35] I. Arany, R.L. Safirstein, Cisplatin nephrotoxicity, in: Semin. Nephrol., 2003, pp. 460.

[36] Ž. Milićević, V. Slepčević, D. Nikolić, V. Živanović, N. Milićević, Effects of cis-Diamminedichloroplatinum II (Cisplatin) on the Splenic Tissue of Rats: A Histoquantitative Study, Exp. Mol. Pathol., 61 (1994) 77-81.

**CHAPTER III**

**TARGETED DELIVERY OF PLATINUM-TAXANE COMBINATION THERAPY IN OVARIAN CANCER**

## 3.1. Introduction

Combination chemotherapy is preferred over treatment with single agents to combat most cancers as it targets multiple cell-survival pathways at the same time and delays the onset of resistance. This helps in achieving long-term tumor remission and increases median survival [1]. Cisplatin (CDDP)-based therapy has been the standard treatment for ovarian cancer since its discovery. After paclitaxel (PTX) was shown to be effective in ovarian cancer, multiple clinical trials studied the overall efficacy of CDDP and PTX and found significant benefit over the pre-existing treatments. Since then, this combination has been the treatment of choice for both early stage as well as advanced cases of ovarian cancer [2, 3]. However, administration of two different agents comes with the inconvenience of repeated or extended duration of drug infusion in patients. Moreover, the most extensively used conventional formulation of paclitaxel, Taxol®, utilizes Cremophor EL (polyethoxylated castor oil) that has been linked to significant toxicities including allergic, hypersensitivity and anaphylactic reactions during infusion that require premedication and prolonged peripheral neuropathy. Combining such drugs in one delivery carrier is therefore a well-suited and convenient strategy for controlling the pharmacokinetics and co-delivery of the desired drug ratio *in vivo*, to maximize the therapeutic potency and minimize drug-associated toxicities.

Cross-linked nanogels have been found to be promising drug carriers to achieve this goal. Being mostly hydrophilic in nature, nanogels are highly biocompatible with a high loading capacity for guest molecules [4]. The nanogel structure can be readily adjusted to integrate features of different materials and, thus, offer advantages for combinatorial encapsulation of drugs with varying physicochemical properties. One of the widespread synthetic techniques for the synthesis of nanogels is the crosslinking of preformed core-shell self-assemblies such as polymer micelles that allows introducing a high degree of spatial organization into the nanogels [4, 5]. Cross-linking is known to impart control over the swelling behavior of the nanogels and thus helps in achieving controlled release of the incorporated cargo, which is an added advantage over the structural integrity imparted to the carrier system upon *in vivo* administration [4, 6]. The enhanced stability also makes the prolonged circulation of the nanogels possible, which in turn allows for increased drug accumulation at the target site [5-9].

We have previously described a biodegradable hybrid nanogel carrier system (NG) for the combination of CDDP and PTX for ovarian cancer therapy, which not only mitigated the toxicities associated with the use of free drugs but also improved treatment outcome [10]. However, our system relied solely on the enhanced permeation and retention (EPR) effect to facilitate the delivery of the drug combination to the tumor site [11]. Regardless of the importance and popularity of EPR effect-based drug delivery, this strategy has some limitations related to the inter- and intra-tumor heterogeneity, variations in the density as well as permeability of the tumor vasculature that can affect the accumulation of nanocarriers. One of the popular approaches to circumvent these problems is by surface-functionalization of the drug carrier with ligands that can target

receptors with differential expression on the cancer cell surface, which helps in increasing the mean residence time of the delivery system at the tumor site and improving target cell uptake [12-15]. One such receptor of interest is the folate receptor (FR). Malignant cells, due to their high rate of cell division, have an increased requirement of folic acid (FA), since it is essential component of cell metabolism and DNA synthesis and repair. To fulfill this higher need of FA, FR is known to be over-expressed in a large number of malignant tissues, including ovarian cancer, compared to normal tissues with the exception of the kidney and choroid plexus [16, 17]. Furthermore, this receptor becomes accessible via the plasma compartment only after the cells lose their polarity owing to malignant transformation which makes it a differential target for cancer tissue that is easily accessible for intravenously administered FA conjugated systems. Its natural ligand, FA, comes with the advantages of high binding affinity, stability and a simple chemical structure together with ease of availability, making it a suitable targeting ligand for ovarian cancer therapy. FA can thus be successfully conjugated to macromolecular systems without loss of binding affinity to its receptor [18]. Many different agents targeting the folate pathway are currently in clinical development [19]. To date, FA-targeted agents showed significant promise in phase II clinical trials but it has not been confirmed in phase III studies [20-22]. Accordingly, there is a need for further identification of new therapeutic combinations and refinement of patient selection. To this end, FA-conjugated imaging agents could be used for pre-selection of patients based on the expression of FR [23] and several methods have been already developed for this purpose [24, 25].

Our group has previously demonstrated a tumor-specific delivery and improved anti-cancer effect *in vivo* of CDDP-loaded NGs decorated with FA targeting groups [26]. In the current study, we designed FA-linked NGs incorporating platinum-taxane combination, and examined whether FR-targeted concurrent delivery of synergistic combination of CDDP and PTX can lead to enhanced therapeutic efficacy compared to nontargeted NG system.

## 3.2. Materials and Methods

### 3.2.1. Materials

α-Amino-ω-methoxy poly(ethylene glycol) (mPEG-NH$_2$, Mw = 5000 g mol$^{-1}$ , $M_w/M_n$ = 1.05) was purchased from Creative PEGWorks Inc., (NC, USA). Fmoc-NH-PEG-NH$_2$ ($M_w$ = 7500 g mol$^{-1}$, Mw/Mn = 1.04) was purchased from JenKem technology (TX, USA). CDDP was purchased from Acros Organics (NJ, USA). L-Glutamic acid γ-benzyl ester (BGlu), L-phenylalanine (Phe), 1,2-ethylenediamine (ED), 1-(3-dimethylaminopropyl)-3-ethylcarbodiimide hydrochloride (EDC), paclitaxel, folic acid and other chemicals were purchased from Sigma-Aldrich (MO, USA) and were used without further purification. Fetal bovine serum (FBS), RPMI 1640 medium, penicillin, streptomycin, Trypsin–ethylenediaminetetraacetic acid (EDTA) (0.5% trypsin, 5.3 mM EDTA tetra-sodium) and other chemicals were purchased from Invitrogen (CA, USA).

### 3.2.2. Preparation of polymeric NGs

Poly(ethylene glycol)-*b*-poly(L-glutamic acid)-*b*-poly(L-phenylalanine) block copolymer with 90:25 ratio of glutamic acid and phenylalanine units (PEG-PGlu$_{90}$-PPhe$_{25}$) was synthesized as previously described [10]. Details of the procedures used for polymer synthesis and characterization are described in the Chapter 2. NGs were prepared by

using previously described method [10] using PEG-PGlu$_{90}$-PPhe$_{25}$ micelles as templates for further cross-linking by ED and EDC ([EDC]/[ED] = 2; [COOH]/[EDC] = 5) at r.t., overnight. Byproducts of the cross-linking reaction were removed by exhaustive dialysis of the reaction mixtures against distilled water. To synthesize fluorescence (Alexa 594)-labeled NGs, solution of Alexa Fluor 594 hydrazide (0.25 µmol, equivalent to 1% of carboxylate groups in NGs) in DMF was added to aqueous dispersion of NGs and the mixture was incubated for 2 h in dark. Unbound dye was removed by filtration on Ultracon filter units (MWCO 10,000 Da, Millipore) at 3000 rpm for 15 min (3 washes) and then additionally purified using NAP-10 column (GE healthcare). Notably, the same stock of Alexa 594-labeled NGs was used to prepare FA-decorated NGs.

### 3.2.3. Synthesis of FA-decorated NGs and drug loading

FA targeting moieties were conjugated to drug-loaded NGs via PEG spacer having Fmoc protection group (Fmoc-NH-PEG-NH$_2$). Firstly, Fmoc-NH-PEG-NH$_2$ (0.013 mmol, 0.05 eq with respect to the amount of carboxylate groups and 1.5 eq with respect to required FA) was conjugated to the free carboxyl groups (0.25 mmol) of NGs via EDC (0.023 mmol) chemistry. Fmoc group was then removed by adding 5 µL of 30% piperidine/DMF (1.1 eq piperidine, 0.014 mmol) and incubating the reaction mixture for 10 min. Resulting constructs were purified using repeated ultrafiltration (MWCO 30,000, Millipore) at 3000 rpm for 15 min (3 washes). Size exclusion chromatography (ÄKTA Fast Protein Liquid Chromatography system) was used to determine the presence of residual PEG. PEG-NGs conjugates were analyzed by proton nuclear magnetic resonance spectroscopy ($^1$H NMR) using Varian INOVA 500 NMR spectrometer (Varian, Palo Alto, CA) operating at 500 MHz (1 mg/mL, D$_2$O, pH 7.0, 25 °C). The dispersion of PEG-

conjugated NGs was mixed with an aqueous solution of CDDP (1mg/mL) at pH 9.0 at a 0.5 molar ratio of CDDP (0.12 mmol) to carboxylate groups (0.24 mmol) of the NGs followed by incubation at 37 °C for 48 h. Unbound CDDP was removed by Ultracon filter units (MWCO 10,000 Da, Millipore) at 3000 rpm for 15 min. FA (0.025 mmol) dissolved in water was subsequently reacted with 1.5 eq EDC (0.037 mmol) at pH 7 for 2 h. This EDC-activated FA was then conjugated to amine terminus of the PEG linker. Amount of FA was selected based on the previously reported optimal density of FA on NGs (0.1-0.2 µmol/mg of polymer) to maintain good loading, stability and cell uptake [26]. The amount of conjugated FA was determined by UV spectrometry ($\epsilon_{363}$=6500 M$^{-1}$cm$^{-1}$) using non-modified PEG-conjugated NGs reference. Finally, PTX (0.01 mmol) was solubilized into the hydrophobic PPhe core of CDDP-loaded FA-modified NGs using an extraction method [27]. According to this method, a thin film of PTX (prepared by evaporation of a methanol solution of PTX) was incubated with aqueous dispersion of NGs (24 h, r.t.). Unincorporated PTX was removed by filtration with 0.8 µm syringe filters (Thermo Scientific). Similar procedures were used to prepare single drug NGs formulations. Pt content in NGs (Pt194/Pt195) was measured by the inductively coupled plasma-mass spectrometer (ICP-MS, NexION 300Q, ICP-MS spectrometer, PerkinElmer) calibrated with Pt (2-100 ng/ml) and Holmium as the internal standard. Samples were diluted in 1% $HNO_3$. PTX levels were determined by HPLC analysis under isocratic conditions using an Agilent 1200 HPLC system with a diode array detector set at 227 nm. As stationary phase a Nucleosil C18 column was used (250 mm × 4.6 mm), a mobile phase of acetonitrile/water mixture (55/45, v/v) was applied at a flow rate of 1 mL/min.

**3.2.4. Physicochemical characterization of the NGs and drug release study**

Intensity-mean Z-averaged particle diameter ($D_{eff}$) and $\zeta$-potential of NGs were determined using a Zetasizer NanoZS (Malvern Instruments Ltd.). All measurements were performed in automatic mode at $25^0C$. Software provided by the manufacturer was used to calculate size, polydispersity indices and $\zeta$-potential of NGs. All measurements were performed at least in triplicate to calculate the mean values $\pm$ SD. Drug release from NGs was examined in PBS (pH 7.4, 0.14M NaCl) by dialysis method using a membrane with 3500 Da cutoff. The concentrations of Pt and PTX released were determined by ICP-MS and HPLC, respectively, and expressed as a percentage of the total Pt or PTX available vs. time.

**3.2.5. Cell culture**

A2780 human ovarian carcinoma cells were provided by Dr. P. Rogers (Institute of Cancer Research, University of Bristol, UK). A2780 cells were transfected using F-Luc-GFP Lentivirus (Capital Biosciences, Rockville, MD) according to manufacturer's protocol to obtain A2780/Luc cell line. Cells were cultured in folate-depleted RPMI 1640 medium (FD-RPMI) with 2 mM glutamine, 10% (v/v) FBS, 100 U/ml penicillin and 0.1 mg/mL streptomycin at $37^0C$, 5% $CO_2$. This medium contains nearly physiological level of FA.

**3.2.6. Flow cytometry**

Cells (50,000 cells/well) grown in FD-RPMI media in 24-well plates for 2 days were exposed to Alexa 594-labeled NGs or FA-NG (0.20 µmol FA/mg of polymer) at $37^0C$ for up to 2 h, washed three times with PBS, trypsinized, centrifuged (1500 rpm, 5 min) and re-suspended in PBS (pH 7.4). The % gated cells were analyzed using Becton Dickinson

FACStarPlus flow cytometer and FACSDiva software (Version 8.0, Becton Dickinson, San Jose, CA). At least 5,000 events were acquired in linear mode, gated to exclude debris and dead cells, and visualized in logarithmic mode. For the competition assay, cells were co-incubated with Alexa 594-labeled FA-NGs in presence of free FA (25mM), and the experiment was carried out as described above.

### 3.2.7. In vitro cytotoxicity

A2780 cells seeded in 96-well plates (10,000 cells/well) 24 h before the experiment were exposed to various doses (0 -10 μg/ml on CDDP basis) of (CDDP+PTX)/NG or FA-(CDDP+PTX)/NG for 24 or 48 h in FD-RPMI at $37^0$C followed by washing with PBS, and maintaining in FD-RPMI medium with 10% FBS for additional 24 h. Cytotoxicity was determined by standard colorimetric MTT assay [28] and the $IC_{50}$ values were calculated using GraphPad Prism Software. Ratio of CDDP to PTX was c.a. 10:1 (mol/mol).

### 3.2.8. Animals and bioluminescence imaging procedure

Female six-week old nude mice (athymic nude-nu) were obtained from Charles River Laboratories and housed in AAALAC accredited facility. Food and reverse osmosis water were available ad libitum throughout the study. Animals were quarantined for 7 days prior to study initiation. All animal studies were conducted in accordance with the protocol approved by the University of Nebraska Medical Center Institutional Animal Care and Use Committee. Imaging was conducted with the *in vivo* imaging system IVIS-200 (Xenogen Corporation, Alameda, CA) composed of a cooled charge-coupled device camera connected to a light-tight black chamber. Animals were maintained on a FA deficient diet (Harlan diet TD.00434) for a week before tumor inoculation and during the

period of studies to achieve plasma folate levels in the physiologic range normally seen for humans [29]. Before *in vivo* imaging, animals were anesthetized with isoflurane (Henry Schein, Dublin, OH) and injected IP with D-luciferin (Perkin-Elmer, Waltham, MA) at the dose of 150 mg/kg (reconstituted in sterile PBS). Whole-body Imaging was performed 5 min after injection. Total bioluminescence signal in the regions of interest (ROIs) drawn around the whole abdomen region was quantified using Living Image software (version 2.50; Xenogen) and expressed as photons/s/cm$^2$/sr.

### 3.2.9. Animal studies

Peritoneal carcinomatosis was generated by IP injection of A2780/Luc cells ($\sim 1.75 \times 10^6$ cells). After development of tumors (3 days after injection) animals were randomized (8 treatment groups, n = 8) and treated with 5% dextrose (control) or free CDDP or (CDDP+PTX)/NG or combination of CDDP/NG and PTX/NG at the same drug ratio or FA-(CDDP)/NG or combination of FA-(CDDP)/NG and FA-(PTX)/NG or FA-(CDDP+PTX)/NG FA + FA-(CDDP+PTX)/NG at an equivalent dose of 4 mg/kg CDDP, or (4 mg/kg CDDP + 1 mg/kg PTX). Treatments were administered via tail vein injections at 4-day intervals. We used one additional group which received IP injection of FA-(CDDP+PTX)/NG. The treatment groups and the doses of each drug are presented in Table 3.1.

**Table 3.1** Treatment groups and drug doses used and the doses used in antitumor actificay studies.

| Treatment group | Route of administration | CDDP (mg/kg) | PTX (mg/kg) | Free FA (mg/kg) |
|---|---|---|---|---|
| Control | IV | - | - | - |
| Free CDDP | IV | 4 | - | - |
| (CDDP+PTX)/NG | IV | 4 | 1 | - |
| FA-(CDDP)/NG | IV | 4 | - | - |

| FA-(CDDP)/NG + FA-(PTX)/NG | IV | 4 | 1 | - |
|---|---|---|---|---|
| FA-(CDDP+PTX)/NG | IV | 4 | 1 | - |
| FA + FA-(CDDP+PTX)/NG | IV | 4 | 1 | 1 |
| FA-(CDDP+PTX)/NG | IP | 4 | 1 | - |

Animal body weight and tumor progression, as assessed by BLI, were monitored every fourth day. All images were acquired using identical BLI system settings. Tumors were allowed to grow until ascites developed or the mice showed signs of pain and/or distress, then the mice were euthanized via $CO_2$ asphyxiation. At necropsy, the abdominal cavity was carefully checked and the extent of tumor was determined.

### 3.2.10. Sample preparation and CDDP measurement in tissue

Known weights of thawed tissues (tumor, kidney, spleen, liver and lung), collected from the animals sacrificed at day 14 (2-3 mice per group) during treatment, were decomposed by wet-ashing in screw-capped vials with six volumes of concentrated nitric acid, overnight heating, and stirring at $65^0C$. An iridium internal standard was added prior to digestion. Total platinum concentrations were determined by ICP-MS using iridium correction. Calibration range for the assay was platinum 2–100 ng/mL with extrapolation to platinum 1000 ng/mL. Necessary dilutions were made when the platinum concentration exceeded the calibration range. Assay sensitivity was 0.8 ng of Pt/mL, with inter- and intraday assay variability not exceeding 5%.

### 3.2.11. Cancer antigen (CA)-125 assay and histopathology

Serum from the blood of sacrificed animals was collected and analyzed for CA-125 levels using CA-125 ELISA kit (Abcam, MA) according to the manufacturer's instructions. Formalin-fixed tissues were processed, sectioned, inserted into tissue cassettes, dehydrated in 70% ethanol overnight, and paraffin embedded (UNMC Tissue

Sciences Facility, Omaha, NE). Serial 5 μm sections were stained with hematoxylin and eosin (H&E). For histopathological diagnosis, H&E-stained slides were examined by light microscopy and photomicrographs were taken using a Nikon camera mounted on a Nikon Eclipse 600 microscope (both Nikon Instruments, Melville, NY) with Adobe Elements 3.0 software (Adobe Systems, San Jose, CA).

### 3.2.12. Statistical analysis

Statistical comparisons for in vitro studies were carried out using Students *t*-test. In animal studies, group means BL signal intensity and body weights were analyzed using one-way analysis of variance [30]. Survival was estimated using Kaplan–Meier analysis and compared using log-rank test. *P* values less than 0.05 were considered significant. Analysis of variance and Kaplan–Meier analysis tests were performed using GraphPad Prism 5 (GraphPad Software, Inc.).

### 3.3. Results and Discussion

### 3.3.1. Preparation and characterization of folate-targeted NGs

Triblock copolymer PEG-PGlu$_{90}$-PPhe$_{25}$ was utilized for the synthesis of multi-compartment biodegradable NG. We have previously demonstrated that the incorporation of Phe moieties into PEG-PGlu block copolymers facilitated self-assembly of block copolymers in an aqueous medium, which was ascribed to hydrophobic and π-π stacking interactions of the phenylalanine units, and was essential for solubilization of various hydrophobic compounds [10, 27]. As it was reported, the incorporation of aromatic units in the polymer chains forming the hydrophobic micellar core can considerably improve the stability, loading capacity and drug retention of taxane-loaded polymeric micelles [31-34]. These favorable properties were attributed to π-π stacking and hydrophobic

interactions between aromatic groups in the micelle's core, and those of the drug. Therefore, we believe that PPhe domains in our NG system may provide a suitable environment for encapsulation of PTX. NGs were prepared as previously described by template-assisted method involving self-assembly of these amphiphilic block copolymers into micelles, followed by chemical cross-linking of the polyion chains [10]. The cross-linking was achieved via condensation reactions between the carboxylic groups of PGlu segments and the amine groups of ethylenediamine in the presence of a water-soluble carbodiimide. The resulting NGs displayed an average diameter of about 90 nm ($\zeta$-potential = −20 mV) and were uniform (monomodal, narrow size distribution) as determined by dynamic light scattering (DLS). Such NGs have 1) a hydrophobic core formed by PPhe chains, which serves as a reservoir for PTX solubilization, 2) an anionic intermediate layer, which can incorporates CDDP through coordination with the carboxylic groups of PGlu, and 3) an outer PEG shell, which stabilizes NGs in aqueous dispersion. The crosslinks incorporated into PGlu block layer ensure that NGs remain stable until they encounter proteases, which degrade them by cleaving the polypeptide chains of the block copolymers [10]. NGs were further modified by FA via a PEG linker for delivering drug combination to FR-positive ovarian tumors. Scheme for the preparation of FA-targeted nanogels is presented in Figure 3.1.
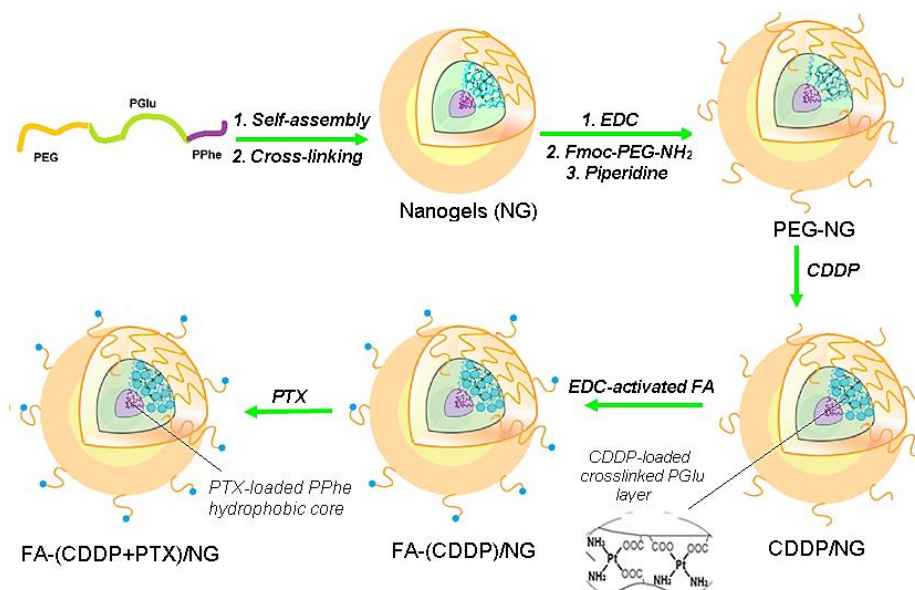
**Figure 3.1.** Scheme for the preparation of FA-decorated NGs.

To this end, EDC activated NGs were first reacted with Fmoc-NH-PEG-NH$_2$ (we chose PEG with a longer chain length, Mw = 7.5 kDa, to reduce steric interference with receptor binding) followed by deprotection of Fmoc groups. The deprotection was confirmed by disappearance of Fmoc signals in PEG-NGs $^1$H NMR spectrum (Fig. 3.2).
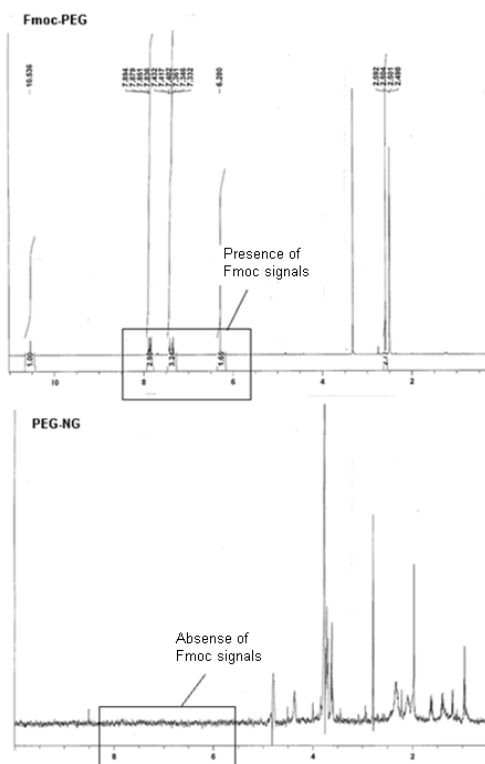


**Figure 3.2.** Confirmation of Fmoc deprotection by $^1$H-NMR

The hydrodynamic diameter of PEGylated NGs was 94 ± 3 nm, which is only slightly larger than that of precursor NGs (88 ± 2 nm). However, the ζ-potential of the PEG-modified NGs significantly increased to -11.1 ± 2.5 mV compared to -20.0 ± 1.2 mV for the unmodified NGs (Table 3.2), which can be indicative of consumption of the PGlu carboxylate groups that reacted with the PEG linkers as well as additional shielding of surface charge by tethered PEG chains. Finally, EDC-activated FA was reacted to amino groups on NG-attached PEG linkers. Conjugation using carbodiimide chemistry is known to produce inactive α- and active γ-isomers of folate. However, since multiple folate residues were linked to each nanogel, the resulting FA-NGs contained sufficient amounts of the active γ-derivative as shown in the cell association studies described below. After thorough purification, little to no residual PEG or FA was present in the final FA-NGs as was confirmed by size exclusion chromatography (Fig. 3.3).
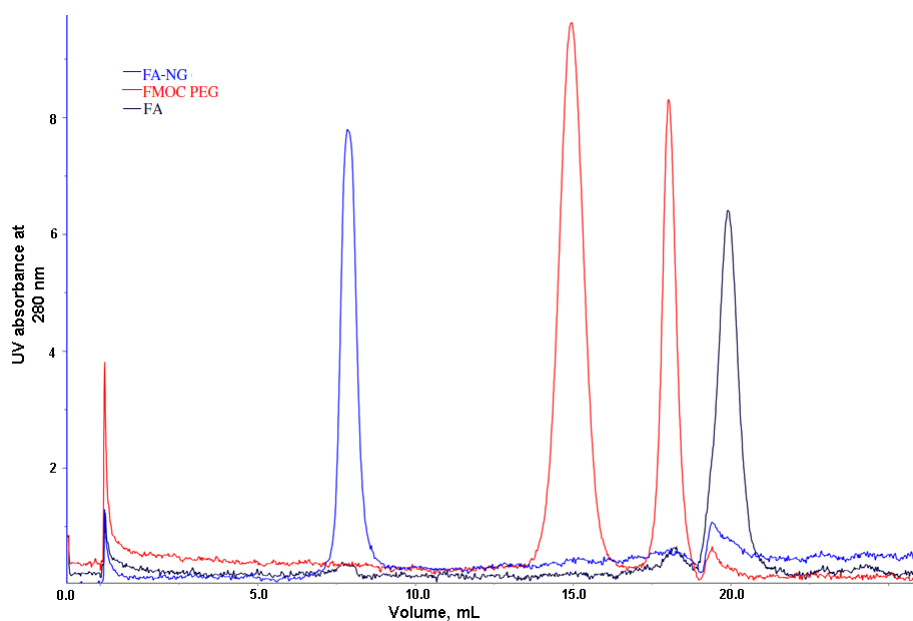


**Figure 3.3.** Estimation of residual content in FA-NG after its purification using FPLC. The particle size and ζ-potential of FA-NGs remained practically the same as those of the PEGylated NGs (Table 3.2).

**Table 3.2.** Physicochemical characteristics of empty NGs.

| Sample | $D_{eff}$ (nm)[a] | PDI[a] | $\zeta$-potential (mV)[a] |
|--------|-------------------|--------|---------------------------|
| NG | $88 \pm 2$ | 0.14 | $-20.0 \pm 1.2$ |
| PEG-NG | $94 \pm 3$ | 0.19 | $-11.5 \pm 2.5$ |
| FA-NG | $98 \pm 4$ | 0.20 | $-10.9 \pm 1.3$ |

[a] Effective diameter ($D_{eff}$), polydispersity index (PDI) and $\zeta$-potential were determined in water (pH 6.5). Data are expressed as mean $\pm$ SD (n = 3).

We have previously shown that the attachment of the FA groups should be carried out after NGs loading with CDDP to avoid inactivation of folate through CDDP binding with its carboxylic groups [26]. Therefore, in this study to prepare targeted NGs with binary drug combination (further abbreviated as FA-(CDDP+PTX)/NGs), CDDP was first loaded into PEGylated NGs followed by conjugation of FA ligands to PEG linkers. At the next step, PTX was solubilized into targeted CDDP/NGs using an extraction method. FA-(CDDP+PTX)/NG were small particles ($D_{eff}$ of approximately 95 nm) with unimodal particle size distribution (PDI = 0.24) and contained 0.2 μmol FA per mg of polymer. As expected, the net negative charge of drug-loaded NGs was further decreased ($\zeta$-potential = −5 mV) as a result of neutralization of PGlu segments upon CDDP binding. The average weight ratio of the CDDP and PTX incorporated into NGs was about 4 : 1, which has been previously shown to provide strong synergistic cytotoxic effects [10]. A similar procedure was used to prepare nontargeted (CDDP+PTX)/NGs from PEGylated NG precursors. Notably, the drug content and physicochemical characteristics of targeted FA-(CDDP+PTX)/NGs were quite similar to nontargeted NGs (Table 3.3). Moreover, FA-(CDDP+PTX)/NG were stable in aqueous dispersions, exhibiting no aggregation or

precipitation for a prolonged period of time (weeks) (Table 3.3). We have previously

showed that such NG system can retain drug cargo for longer period of time (weeks) [10]

**Table 3.3.** Physicochemical characteristics of drug-loaded NGs.

| Sample | $D_{eff}$ (nm)[a] | PDI[a] | $\zeta$-potential (mV)[a] | CDDP:PTX (wt/wt) |
|---|---|---|---|---|
| (CDDP+PTX)/NG | $86 \pm 2$ | 0.26 | $-7.0 \pm 0.7$ | 3.84:1 |
| FA-(CDDP+PTX)/NG | $95 \pm 3$ | 0.24 | $-5.5 \pm 1.0$ | 3.78:1 |
| FA-(CDDP+PTX)/NG [b] | $96 \pm 4$ | 0.25 | $-5.7 \pm 2.7$ | - |

[a] Effective diameter ($D_{eff}$), polydispersity index (PDI) and $\zeta$-potential were determined in water (pH 6.5). Data are expressed as mean $\pm$ SD (n = 3).
[b] Effective diameter, polydispersity index and $\zeta$-potential after one month of storage in aqueous dispersion at $4^0$C.

For both drugs there was very little difference in the release profiles between targeted

FA-(CDDP+PTX)/NG and nontargted (CDDP+PTX)/NG, which indicates that the

modification of nanogels with targeting groups had no influence on drug retention (Fig.

3.4). As it seen in Fig. 4, sustained but temporally distinct release of Pt [35] species and

PTX was observed. Notably, PTX release was much faster than that of Pt [35], which is

expected since PTX is physically entrapped into the PPhe core.
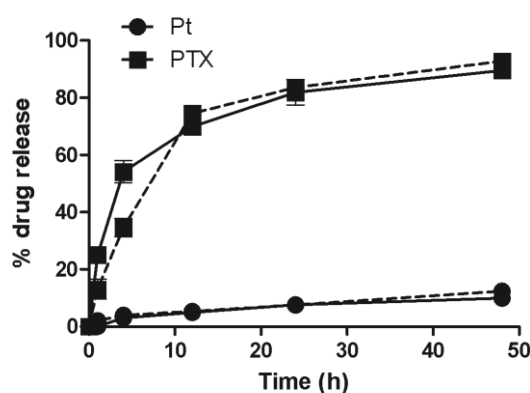


**Figure 3.4.** Drug release profiles from FA-(CDDP+PTX)/NG (solid line) and (CDDP+PTX)/NG (dotted line) for Pt (●) and PTX (■) in PBS buffer, pH 7.4. The data represent averaged values and standard deviations calculated based on three independent experiments.

### 3.3.2. Cellular association and in vitro cytotoxicity of FA-NGs

To demonstrate effect of attachment of FA on cellular association of NGs, we used FR+ human ovarian carcinoma A2780 cells and FR- A549 lung carcinoma cells [26]. Cultured cells were treated with fluorescence Alexa 594-labeled FA-NGs or NGs for 30 min at 37°C. Particle association with cells was determined by flow cytometry. As expected, the cellular association of FA-NGs with FR+ cells significantly ($P < 0.01$) exceeded that of the nontargeted NG (Fig. 3.5). On the other hand, no difference in association of targeted and nontargeted NGs was observed with A549 cells (Fig. 3.5).
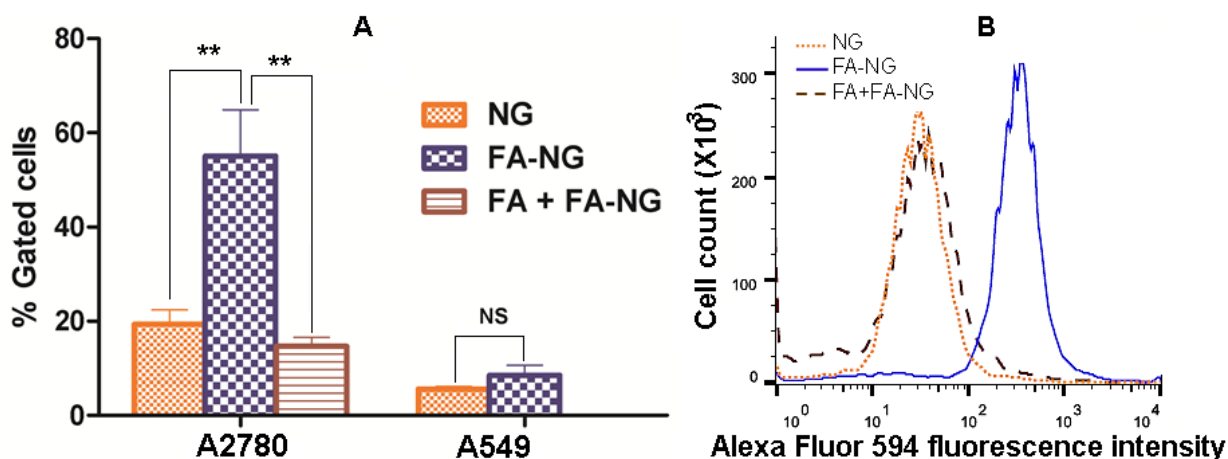


**Figure 3.5**. A) Cellular association of Alexa fluor 594-labeled NG, FA-NG and FA-NG in presence of free FA in FR+ A2780 and FR- A549 cell lines at 30 min. B) Inhibitory effect of free FA on the cellular association of FA-NG in FR+ A2780 as analyzed by flow cytometry. FA-NG = 0.5 mg/mL and 0.2 μmol FA/mg polymer. [FA-NG] = 0.5 mg/mL and 0.2 μmol folate/mg polymer. ** indicate significantly higher uptake of FA-NG vs. NG and FA-NG in presence of free FA. ** $P < 0.01$ and NS - not significant. Data are mean ± SD (n = 3).

To further elucidate whether the enhanced cellular association of FA-NGs depends on specific binding to FR on the cell surface, A2780 cells were treated with FA-NGs in the presence of excess free FA (25 mM). Flow cytometry analysis revealed that the cellular association of FA-NGs was suppressed to the level of the nontargeted NGs (Fig. 3.5).

This inhibition was also significant ($P < 0.05$) after 1 h of treatment in the FR+ A2780 cells (Fig. 3.6). These results validate that the conjugation of FA to the surface of NGs resulted in efficient and specific association with FR+ cells.
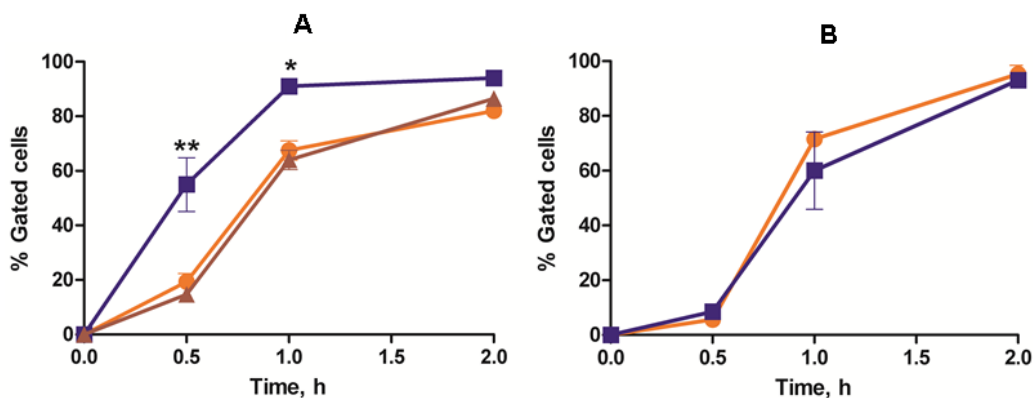


**Figure 3.6.** Cellular association of Alexa 594-labeled NG, FA-NG and FA-NG in presence of free FA with A) FR-positive A2780 and B) FR-negative A549 cell lines at different time points. [FA-NG] = 0.5 mg/mL and 0.2 µmol FA/mg polymer. * and ** indicate significantly higher cellular association of FA-NG vs. NG and FA-NG in presence of free FA. ** $P < 0.01$ and ** $P < 0.05$. Data are mean ± SD (n = 3).

It is worth noting that after two hours of treatment there was no significance between FR-targeted and nontargeted NGs uptake, which internalized efficiently (approx. 90% gated cells) in both cell types (Fig. 6), indicating that a long incubation time could enhance non-specific uptake of NGs. These differences in cellular association translated into cytotoxicity (Table 3.4). The cytotoxicity of FA-(CDDP+PTX)/NG against FR+ A2780 cells was increased by two fold compared to (CDDP+PTX)/NG ($IC_{50}$ expressed in CDDP equivalents: 1.4 ± 0.75 µM vs 3 ± 1.3 µM) at 24 h. Notably, the difference between targeted and nontargeted formulations was only apparent at lower time point and it becomes negligible at 48 h.

**Table 3.4**. Comparison of $IC_{50}$ values for targeted and nontargeted drug-loaded NGs against A2780 cells as determined by the MTT assay.

|  | IC$_{50}$ ($\mu$M)$^a$ | |
|---|---|---|
|  | 24 h | 48 h |
| (CDDP+PTX)/NG | 3.0 ±1.3 | 0.4 ± 0.1 |
| FA-[(CDDP+PTX)/NG] | 1.4 ± 0.7 | 0.3 ± 0.1 |

$^a$Calculated with respect to CDDP.

### 3.3.3. Antitumor activity in intrapertoneal xenograft model

Our previous studies have shown effective tumor inhibition by platinum-taxane-loaded NG system in subcutaneously growing ovarian tumor model. Herein, we tested the efficacy and the toxicity of FR-targeted combination therapy in peritoneal xenograft model that mimics the clinical manifestations in the advanced stage of the human ovarian carcinomatosis. The A2780/luc cells, injected into the peritoneum of female nude mice, grew rapidly *in vivo* and were able to trigger formation of tumor nodules throughout the abdominal peritoneum that were detectable by BLI as early as 3 days post inoculation. If mice were left untreated, the bioluminescene signal rapidly increased and mice ultimately developed ascites in 2-3 weeks. Treatments were initiated on 4$^{th}$ day post A2780/luc inoculation. IV administrations of each formulation were given 4 times at 4-day intervals at 4mg/kg CDDP and 1 mg/kg PTX equivalents per dose. CDDP (4 mg/kg) was also used as a control-free drug with the same dosing schedule. As shown in Fig. 4, all treatments were effective in delaying tumor progression in comparison with control group. Tumor growth inhibition ratio between treated versus control groups (T/C value) was calculated on day 16 after treatment initiation according to the formula: $T/C = (R_t - R_o)_{treated\ tumor}/ (R_t - R_o)_{control\ tumor}$, where $R_t$ and $R_o$ represent the mean bioluminescence intensity on the evaluation day and at the start of the treatment, respectively (Table 3.5). Consistent with our previous observations [10], platinum-taxane combination administered as single NG formulation, (CDDP+PTX)/NG, was found to be significantly more effective (T/C= 0.26)

than CDDP alone (T/C = 0.56, $P < 0.05$, Fig. 3.7). In contrast, the mice treated with a

cocktail of single drug NG formulations (CDDP/NG + PTX/NG) at the same drug ratio

had a similar impact on the tumor progression as free CDDP (Fig. 3.7). These data

reinforce our hypothesis that synchronized delivery of platinum-taxane combination

chemotherapy using NGs plays an essential role in its cytotoxic activity.

**Table 3.5.** *In vivo* antitumor efficacy of various formulations in ovarian cancer xenograft-bearing female nude mice.

| Treatment group | T/C | Median survival (days) |
|---|---|---|
| Control | - | 19 |
| Free CDDP | 0.56 | 23 |
| (CDDP+PTX)/NG | 0.26 | 31 |
| FA-(CDDP)/NG + FA-(PTX)/NG | 0.31 | 30 |
| FA-(CDDP+PTX)/NG | 0.09 | 41 |
| FA-(CDDP+PTX)/NG IP | 0.05 | 43 |
| FA + FA-(CDDP+PTX)/NG | 0.29 | 27 |

Note: T/C = $(R_t - R_o)$ treated tumor/ $(R_t - R_o)$ control tumor, where $R_t$ and $R_o$ represent the mean bioluminescence intensity on the evaluation day and at the start of the treatment, respectively.



**Figure 3.7.** *In vivo* antitumor efficacy of (CDDP+PTX)/NG] vs. CDDP/NG + PTX/NG in A2780/Luc human ovarian cancer xenograft-bearing female nude mice. (**A**)

Bioluminescence images of each 3 mice representative for 8 mice per experimental arm at the end of treatment (day 16). The colored scale bar indicates the intensities of bioluminescence in photons/s/cm$^2$/sr. (B) Comparison of tumor growth inhibition following IV administration of (CDDP+PTX)/NG (▲) or CDDP/NG + PTX/NG (Ж) or free CDDP (■) or control (●). Drug formulations were injected in100 μL at a dose of 4 mg CDDP or 1mg PTX equivalents/kg body weight 4 times at 4-day intervals as indicated by the arrows. Data presented in terms of relative bioluminescence units ($R_t/R_o$) to the day when treatment was initiated for individual animal. Values indicated are means ± SD    (n = 8), *$P$ < 0.05.    (C) Kaplan–Meier analysis of overall survival in (CDDP+PTX)/NG (1) or CDDP/NG + PTX/NG group (2) or free CDDP (3) or control group (4). * $P$<0.05.

Tumor growth in the mice treated with (CDDP+PTX)/NG was further suppressed when the same drug combination was administered in FA-decorated NGs. FA-(CDDP+PTX)/NG showed  significant tumor reduction as measured by BLI (T/C = 0.09) compared to nontargeted (CDDP+PTX)/NG group (T/C = 0.26, $P$ < 0.05) (Fig 3.8A and 3.8B). As a result, combination therapy with FA-(CDDP+PTX)/NG significantly increased the probability of survival compared to its nontargeted counterpart (Fig. 3.8C). The median survival times (post-tumor inoculation) for the FA-(CDDP+PTX)/NG and (CDDP+PTX)/NG groups were 41 and 31 days, respectively ($P$ < 0.01) (Table 3.5). Notably, the enhanced antitumor effect of FA-(CDDP+PTX)/NG was inhibited when it was administered with free FA (Fig 3.8A and 3.8B) suggesting that FA-decorated (CDDP+PTX)/NG display folate specificity and exhibit elevated activity through a mechanism involving *in vivo* FR. The peritoneal cavity is the principal site of disease in ovarian cancer. The concept of direct IP administration of chemotherapy, especially to treat microscopic residual disease after debulking surgery, has been evaluated in many clinical trials and has demonstrated an improvement in overall and disease-free survival [2, 36, 37]. A randomized phase III clinical trial showed IP administration of CDDP and PTX plus IV PTX improves survival when compared to standard of care with IV

combination of CDDP and PTX [2]. However, IP chemotherapy also led to significantly higher toxicities due to exposure of both cancer and healthy tissues to high concentrations of drugs. We, therefore, utilized our FA-(CDDP+PTX)/NG formulation to determine whether there are therapeutic advantages in providing targeted IP chemotherapy in ovarian cancer. As seen in Fig. 8B the BLI data shows a trend towards enhanced therapeutic efficacy of FA-(CDDP+PTX)/NG when administered IP (T/C = 0.05) compared to IV regimen (T/C = 0.09). Kaplan-Mayer survival analysis also demonstrated that mice given IP FA-(CDDP+PTX)/NG appear to have the best outcomes. However, the differences between groups were not statistically significant.
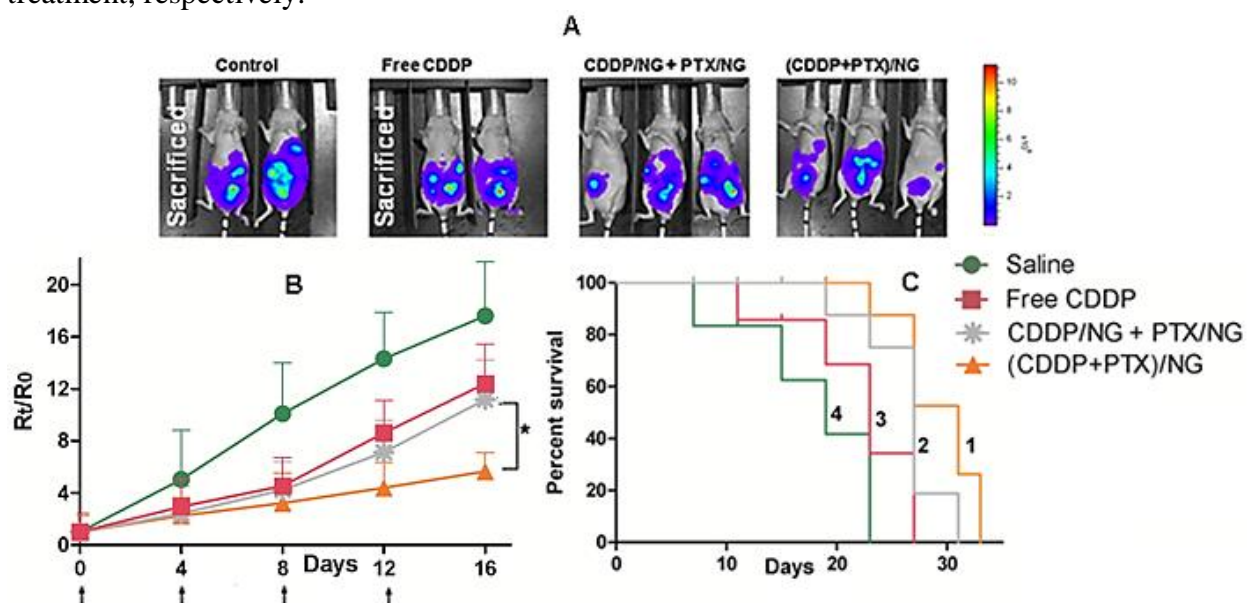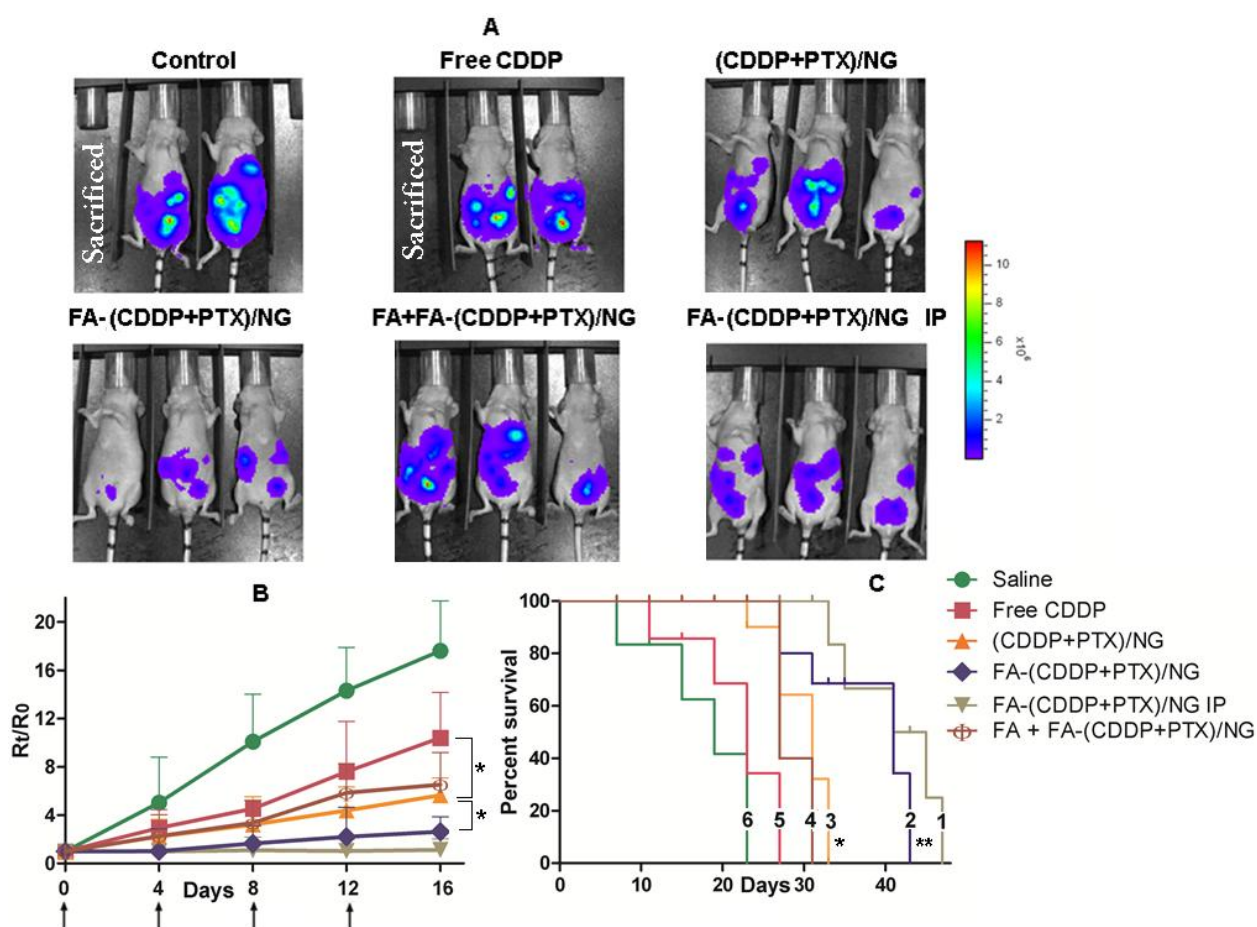


**Figure 3.8.** *In vivo* antitumor efficacy of FA-(CDDP+PTX)/NG in A2780/Luc human ovarian cancer xenograft-bearing female nude mice. (**A**) Bioluminescence images of each

3 mice representative for 8 mice per experimental arm after treatment (day 16). The colored scale bar indicates the intensities of bioluminescence in photons/s/cm$^2$/sr. **(B)** Comparison of tumor growth inhibition following IV administration of FA-(CDDP+PTX)/NG (♦) or (CDDP+PTX)/NG (▲) or mixture of 1 mg/kg FA and FA-(CDDP+PTX)/NG (ϕ) or free CDDP (■) or 5% dextrose (control) (●). We used one additional group which received IP injection of FA-(CDDP+PTX)/NG (▼). Drug formulations were injected in100 μL at a dose of 4 mg CDDP or 1mg PTX equivalents/kg body weight 4 times at 4-day intervals as indicated by the arrows. Data presented in terms of relative bioluminescence units (Rt/Ro) to the day when treatment was initiated for individual animal. Values indicated are means ± SD (n = 8), *$P < 0.05$. (**C**) Kaplan–Meier analysis of overall survival in FA-(CDDP+PTX)/NG IP group (1) or FA-(CDDP+PTX)/NG IV group (2) or (CDDP+PTX)/NG (3) or FA + FA-(CDDP+PTX)/NG (4) or free CDDP (5) or control group (6). Log-rank test was used to determine statistical difference between (CDDP+PTX)/NG and free CDDP groups, *$P < 0.05$, and between FA-(CDDP+PTX)/NG and (CDDP+PTX)/NG groups, **$P < 0.01$.

CA-125 also known as MUC16 is a protein that in humans is encoded by the MUC16 gene [38]. Around 90% of women with advanced ovarian cancer have elevated levels of CA-125 in their blood serum, making CA-125 a useful tool for detecting ovarian cancer after the onset of symptoms [39]. Monitoring CA-125 blood serum levels is also useful for determining how ovarian cancer is responding to treatment and for predicting a patient's prognosis after treatment [40]. It has frequently been used as an indicator of tumor progression in various ovarian cancer mouse xenograft models [41-43]. To further characterize tumor response to the treatments, we analyzed the serum CA-125 levels in mice on day 14 (second day after last injection). As shown in Fig. 3.9, levels of CA-125 were significantly low in the mice that received (CDDP+PTX)/NG compared to either control group ($P < 0.01$) or free CDDP group ($P < 0.05$). CA-125 levels were lowest in the mice that received FA-(CDDP+PTX)/NG either IV or IP. Notably, compared to nontargeted (CDDP+PTX)/NG group, IP treatment with FA-(CDDP+PTX)/NG resulted in significant decrease in serum CA-125 levels (P< 0.05) indicating its better therapeutic potential.
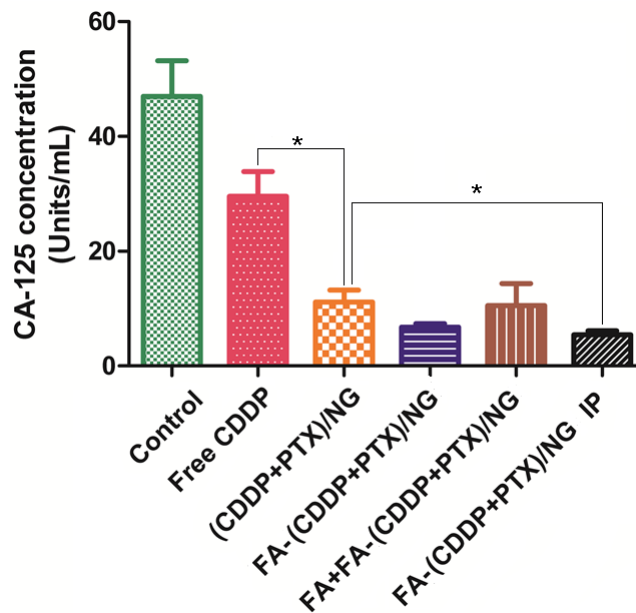
**Figure 3.9.** CA-125 ELISA assay. Quantification of serum CA-125 levels in mice from various treatment groups. Data are presented as mean ± SD (n = 3).

To compare the ability of the NGs-based carriers to deliver a cytotoxic payload to the tumor sites, we sacrificed 2-3 mice on day 14 and excised the tumors for CDDP content estimation. Both targeted and nontargeted drug-loaded NGs displayed enhanced tumor accumulation relative to administration of free drug supporting the well-known characteristic of nanoparticles to improve tumor drug delivery by the EPR effect (Fig. 3.10). However, FA-(CDDP+PTX)/NG induced a significantly higher Pt accumulation in the target site compared to nontargeted (CDDP+PTX)/NG ($P < 0.05$). This increase appeared to be due to FR-specific interaction of folated NGs with cancer cells because it was completely reversed by co-administration of free folate. We have previously showed that the average weight ratio of the CDDP and PTX in the tumors of the animals was same as the drug loading ratio in (CDDP+PTX)/NG, indicating the spatial–temporal synchronization of drug exposure. We expect the similar synchronized delivery of CDDP

and PTX is occurred using our current NG systems as well. Notably, while all drug-loaded NGs displayed considerable accumulation of Pt in the highly perfused organs such as liver and spleen, tumor was the only tissue where Pt content was significantly higher for FA-(CDDP+PTX)/NG (Fig. 3.10). FA-(CDDP+PTX)/NG treatment which was administered IP led to the maximum Pt retention in the tumors which may be a result of regional exposure to high drug concentrations at the tumor sites. This might be the reason for the observed enhanced tumor responsiveness with IP FA-(CDDP+PTX)/NG treatment. The binding of FA-(CDDP+PTX)/NG to and/or their uptake by FR+ cancer cells can retain them within the tumor for a longer period of time, prevent their rapid re-entering into systemic circulation and, thus, provide some benefits over passively targeted formulations. The introduction of FA moieties can also have an effect on pharmacokinetics and biodistribution of NGs and influence tumor uptake. Further detailed pharmacokinetic study may help to elucidate the relationship between the therapeutic effect of the FR-targeted NGs and distribution at the tumor and the whole body.
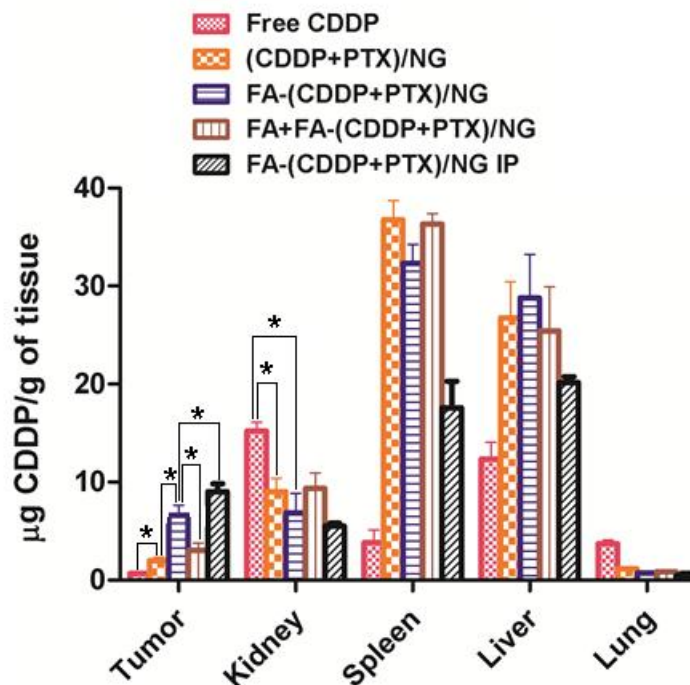
**Figure 3.10.** Tissue distribution of platinum in different treatment groups as determined by ICP-MS. Mice were sacrificed at day 14 of the treatment with FA-(CDDP+PTX)/NG IP or FA-(CDDP+PTX)/NG or FA+ FA-(CDDP+PTX)/NG or (CDDP+PTX)/NG or free CDDP. Data are presented as mean ± SD (n = 3). * $P < 0.05$.

To further determine whether concurrent targeted delivery of drug combination will have therapeutic benefits, we also compared the inhibition of tumor progression and survival between FA-(CDDP+PTX)/NG and a combination of targeted single drug formulations (FA-(CDDP)/NG + FA-(PTX)/NG) administered at the same drug ratio (Fig. 3.11 and 3.12). Our data showed significantly better tumor growth inhibition and survival for FA-(CDDP+PTX)/NG than FA-(CDDP)/NG + FA-(PTX)/NG. This confirms an advantage of delivering a platinum-taxane drug combination via single carrier to the same targeted cells simultaneously. We have not tested this strategy with other drug combinations. So at time we are not claiming that the same phenomena will hold true for other drug combinations.
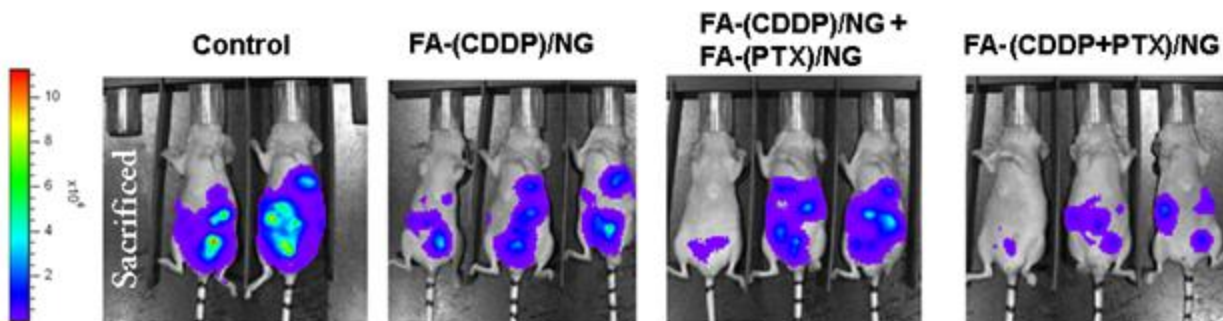
**Figure 3.11.** Bioluminescence images of each 3 mice representative for 8 mice per experimental arm at the end of treatment (day 16). The colored scale bar indicates the intensities of bioluminescence in photons/s/cm$^2$/sr.
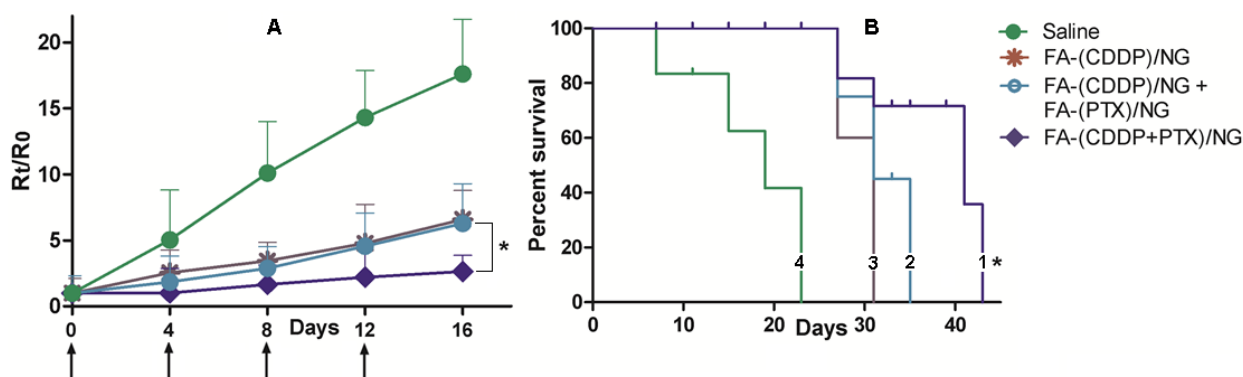


**Figure 3.12.** *In vivo* antitumor efficacy of FA-(CDDP+PTX)/NG vs. FA-(CDDP)/NG + FA-(PTX)/NG co-administration against A2780/Luc human ovarian cancer xenografts. (**A**) Comparison of tumor growth inhibition as indicated by relative radiance units over time following IV administration of FA-(CDDP+PTX)/NG (♦) or FA-CDDP/NG + FA-PTX/NG or FA-(CDDP)/NG (Ж) or control (●). Drug formulations were injected in 100 µL at a dose of 4 mg CDDP or 1 mg PTX equivalents/kg body weight 4 times at 4-day intervals as indicated by the arrows. Values indicated are means ± SD (n=8). (**C**) Kaplan–Meier analysis of overall survival in FA-(CDDP+PTX)/NG (1) or FA-(CDDP)/NG + FA-(PTX)/NG group (2) or FA-(CDDP)/NG (3) or control group (4). * $P < 0.05$. Log-rank test was used to determine statistical difference between FA-(CDDP+PTX)/NG and FA-(CDDP)/NG + FA-(PTX)/NG groups, *$P < 0.05$.

Importantly, the introduction of targeting FA moieties on the surface of NGs did not alter the favorable toxicity profile of (CDDP+PTX)/NG formulation. Neither targeted nor nontargeted NG-based binary drug combination caused a significant change in body weight, indicating that the treatments were well tolerated (Fig. 3.13). In contrast, the

same dose of free CDDP produced a considerable body weight loss (> 15%, $P < 0.05$), which indicated systemic toxicity of free CDDP (Fig. 3.13).
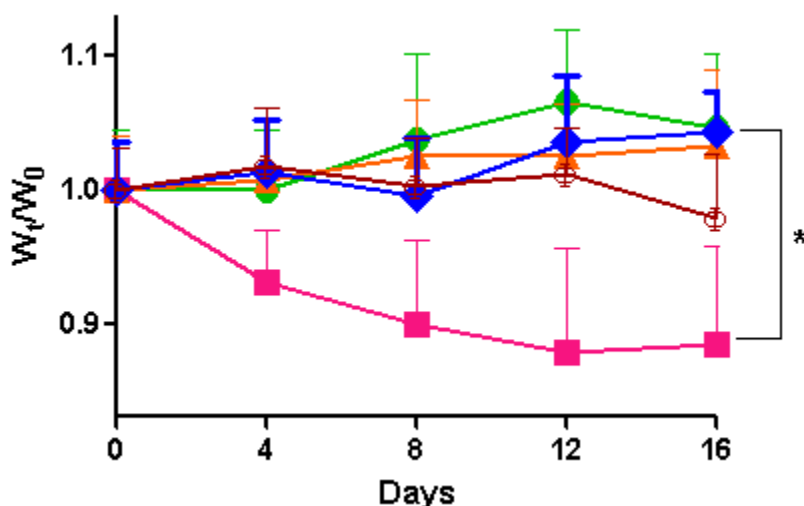


**Figure 3.13**. Relative changes in body weight were measured following intravenous administration of FA-(CDDP+PTX)/NG (♦) or (CDDP+PTX)/NG (▲) or FA + FA-(CDDP+PTX)/NG (ϕ) or free CDDP (■) or control (●).Values indicated are means ± SD (n=3). * *P*<0.05. Values indicated are means ± SD. * *P*<0.05.

In the kidney, the primary target organ of CDDP toxicity [44, 45], both targeted or nontargeted drug-loaded NGs showed significantly lower Pt levels than free CDDP (Fig. 10) which ameliorated CDDP-induced nephrotoxicity as confirmed by tissue histopathology analysis. Light microscopic examination of H&E stained kidney sections from sacrificed animals indicated focal tubular degeneration and regeneration in kidneys from all animals treated with free CDDP, while no histopathological changes were observed in kidney from animals in the FA-(CDDP+PTX)/NG-treated or (CDDP+PTX)/NG-treated groups compared with the control (Fig. 14). This is a significant result since a higher expression of FR in this organ may raise a concern of toxicity to this tissue [46]. We also observed focal acute inflammation in the lungs of animals treated with free CDDP while no such changes were detected in any of the NGs formulation (Fig. 3.14). Despite relatively higher exposure of liver and spleen to CDDP

in the FA-(CDDP+PTX)/NG or (CDDP+PTX)/NG treatment, there was no evidence of liver or splenic toxicity by histopathology (Fig. 3.15).
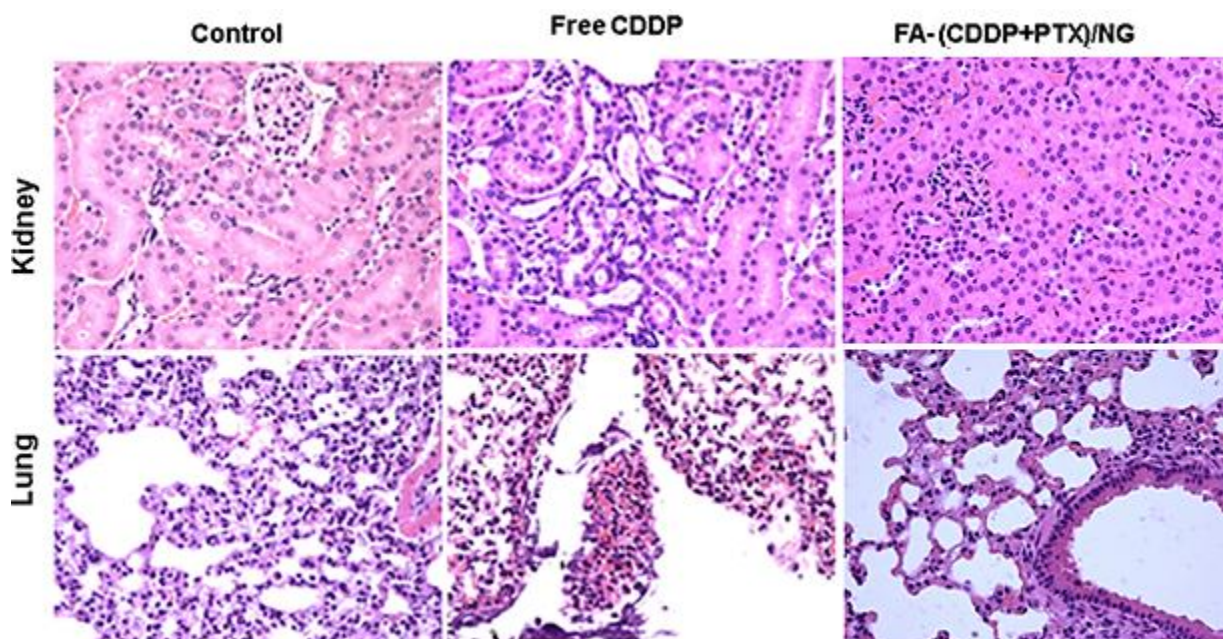


**Figure 3.14.** Light microscopy images (20X) of hematoxylin and eosin-stained kidney and lung sections of mice. Tissue samples were collected at day 14.
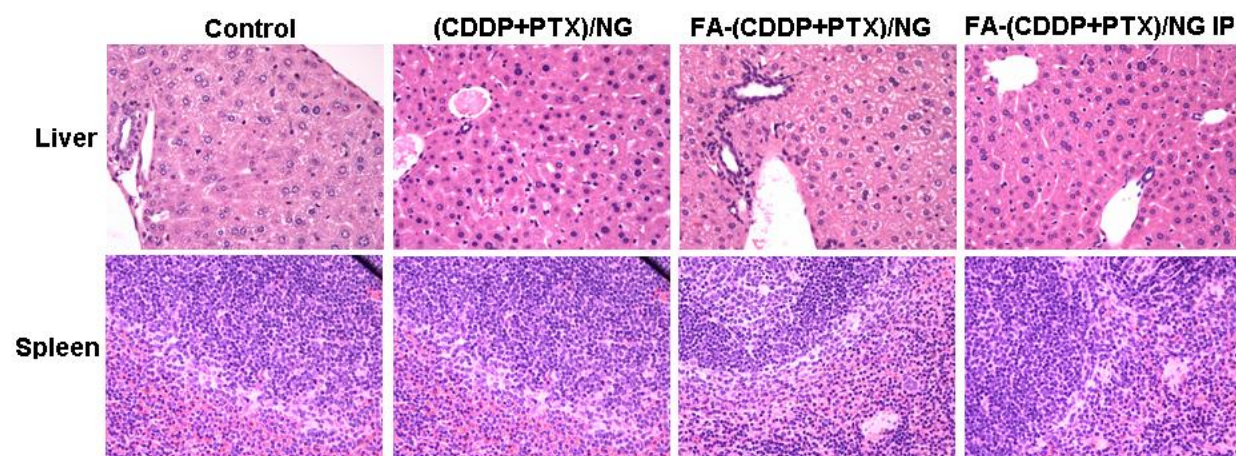


**Figure 3.15.** Light microscopy images (20X) of hematoxylin and eosin-stained kidney and lung sections of mice. Tissue samples were collected at day 14. Liver and spleen appear normal.

Mice which received FA-(CDDP+PTX)/NG IP also did not show any evidence of toxicity in any of the investigated organs. Indeed, the local delivery of FA-(CDDP+PTX)/NG into intraperitoneal cavity reduced nonspecific drug accumulation in normal tissues (spleen, liver, and kidney) (Fig. 3.10). Blood cell counting analysis on day 14 was conducted and normal cell counts were observed for red blood cells and platelets for all groups (Table 3.6) while there was significant reduction in the count of white blood cells (below normal range) in the mice which were treated with free CDDP.

**Table 3.6.** Blood cell counting analysis at day 14 (second day post-treatment).

| Sample | RBC ($10^{12}$/L) | PLT ($10^9$/L) |
|---|---|---|
| Control | $6.03 \pm 0.23$ | $312 \pm 32$ |
| Free CDDP | $4.66 \pm 0.10$ | $368 \pm 26$ |
| (CDDP+PTX)/NG | $4.13 \pm 0.31$ | $273 \pm 19$ |
| FA-(CDDP+PTX)/NG | $4.01 \pm 0.19$ | $350 \pm 42$ |
| FA-(CDDP+PTX)/NG IP | $3.60 \pm 0.14$ | $360 \pm 70$ |
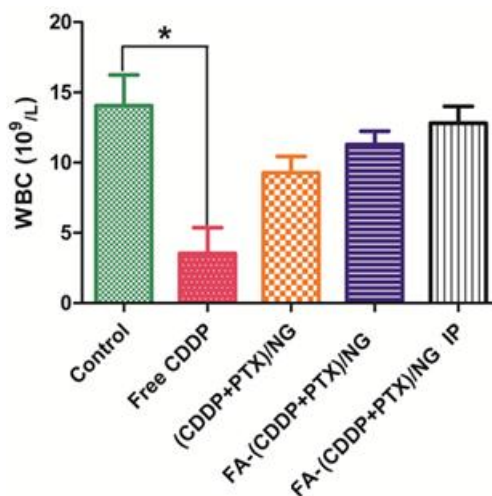


**Figure 3.16.** Blood cell counting analysis for WBC at day 14.

In contrast, mice treated with drugs loaded in NGs did not have any changes in white blood cells compared to control (Fig. 3.16).

Collectively, these *in vivo* data support the efficacy of this targeted platinum-taxane combination therapy in FR-expressing ovarian cancer model without toxicity-related consequences.

## 3.4. Conclusion

In this study, we demonstrated that folate-decorated NGs carrying CDDP and PTX drug combination exerted enhanced antitumor efficacy, both in terms of tumor growth inhibition and survival, compared to its nontargeted counterpart in rapidly growing murine model of FR-positive ovarian cancer. This better efficacy was only observed when CDDP and PTX are concurrently delivered to the tumor sites. Our data also indicate that IP administration of FA-(CDDP+PTX)/NG can be more effective in the context of targeted combination therapy without extending its cytotoxicity to the normal tissues. Localized chemotherapy has demonstrated survival advantages in advanced ovarian cancer patients and our NG-based drug delivery system can be a suitable candidate for further optimization and pre-clinical evaluation of intraperitoneal chemotherapy for ovarian cancer.

## 3.5. References

[1] J. Jia, F. Zhu, X. Ma, Z.W. Cao, Y.X. Li, Y.Z. Chen, Mechanisms of drug combinations: interaction and network perspectives, Nat Rev Drug Discov, 8 (2009) 111-128.

[2] D.K. Armstrong, B. Bundy, L. Wenzel, H.Q. Huang, R. Baergen, S. Lele, L.J. Copeland, J.L. Walker, R.A. Burger, Intraperitoneal cisplatin and paclitaxel in ovarian cancer, N Engl J Med, 354 (2006) 34-43.

[3] R. Agarwal, S.B. Kaye, Ovarian cancer: strategies for overcoming resistance to chemotherapy, Nat Rev Cancer, 3 (2003) 502-516.

[4] A.V. Kabanov, S.V. Vinogradov, Nanogels as pharmaceutical carriers: finite networks of infinite capabilities, Angew Chem Int Ed Engl, 48 (2009) 5418-5429.

[5] M. Talelli, M. Barz, C.J. Rijcken, F. Kiessling, W.E. Hennink, T. Lammers, Core-crosslinked polymeric micelles: Principles, preparation, biomedical applications and clinical translation, Nano Today, 10 (2015) 93-117.

[6] C.J. Rijcken, C.J. Snel, R.M. Schiffelers, C.F. van Nostrum, W.E. Hennink, Hydrolysable core-crosslinked thermosensitive polymeric micelles: synthesis, characterisation and in vivo studies, Biomaterials, 28 (2007) 5581-5593.

[7] J. Peng, T. Qi, J. Liao, B. Chu, Q. Yang, W. Li, Y. Qu, F. Luo, Z. Qian, Controlled release of cisplatin from pH-thermal dual responsive nanogels, Biomaterials, 34 (2013) 8726-8740.

[8] W. Jin, P. Xu, Y. Zhan, Y. Shen, E.A. Van Kirk, B. Alexander, W.J. Murdoch, L. Liu, D.D. Isaak, Degradable cisplatin-releasing core-shell nanogels from zwitterionic poly (β-aminoester)-graft-PEG for cancer chemotherapy, Drug Deliv, 14 (2007) 279-286.

[9] P. Liu, M. Gou, T. Yi, X. Qi, C. Xie, S. Zhou, H. Deng, Y. Wei, X. Zhao, The enhanced antitumor effects of biodegradable cationic heparin-polyethyleneimine nanogels delivering HSulf-1 gene combined with cisplatin on ovarian cancer, Int J Oncol, 41 (2012) 1504-1512.

[10] S.S. Desale, S.M. Cohen, Y. Zhao, A.V. Kabanov, T.K. Bronich, Biodegradable hybrid polymer micelles for combination drug therapy in ovarian cancer, J Control Release, 171 (2013) 339-348.

[11] J. Fang, H. Nakamura, H. Maeda, The EPR effect: unique features of tumor blood vessels for drug delivery, factors involved, and limitations and augmentation of the effect, Adv Drug Deliv Rev, 63 (2011) 136-151.

[12] B.S. Pattni, V.P. Torchilin, Targeted Drug Delivery Systems: Strategies and Challenges, in: Targeted Drug Delivery: Concepts and Design, Springer, 2015, pp. 3-38.

[13] F. Danhier, O. Feron, V. Préat, To exploit the tumor microenvironment: passive and active tumor targeting of nanocarriers for anti-cancer drug delivery, J Control Release, 148 (2010) 135-146.

[14] S. Hong, P.R. Leroueil, I.J. Majoros, B.G. Orr, J.R. Baker, M.M. Banaszak Holl, The binding avidity of a nanoparticle-based multivalent targeted drug delivery platform, Chem Biol, 14 (2007) 107-115.

[15] M. Talelli, C.J. Rijcken, S. Oliveira, R. van der Meel, P.M.v.B. en Henegouwen, T. Lammers, C.F. van Nostrum, G. Storm, W.E. Hennink, Reprint of" Nanobody—Shell functionalized thermosensitive core-crosslinked polymeric micelles for active drug targeting", Journal of Control Release, 153 (2011) 93-102.

[16] Y. Wang, R. Zhao, R.G. Russell, I.D. Goldman, Localization of the murine reduced folate carrier as assessed by immunohistochemical analysis, Biochim Biophys Acta, 1513 (2001) 49-54.

[17] S.K. Desmoulin, Z. Hou, A. Gangjee, L.H. Matherly, The human proton-coupled folate transporter: Biology and therapeutic applications to cancer, Cancer Biol Ther, 13 (2012) 1355-1373.

[18] Y. Lu, P.S. Low, Folate-mediated delivery of macromolecular anticancer therapeutic agents, Adv Drug Deliv Rev, 64 (2012) 342-352.

[19] I.B. Vergote, C. Marth, R.L. Coleman, Role of the folate receptor in ovarian cancer treatment: evidence, mechanism, and clinical implications, Cancer Metastasis Rev, 34 (2015) 41-52.

[20] R.W. Naumann, R.L. Coleman, R.A. Burger, E.A. Sausville, E. Kutarska, S.A. Ghamande, N.Y. Gabrail, S.E. DePasquale, E. Nowara, L. Gilbert, PRECEDENT: a randomized phase II trial comparing vintafolide (EC145) and pegylated liposomal doxorubicin (PLD) in combination versus PLD alone in patients with platinum-resistant ovarian cancer, J Clin Oncol, 31 (2013) 4400-4406.

[21] R. Morris, R. Joyrich, R. Naumann, N. Shah, A. Maurer, H. Strauss, J. Uszler, J. Symanowski, P. Ellis, W. Harb, Phase II study of treatment of advanced ovarian cancer with folate-receptor-targeted therapeutic (vintafolide) and companion SPECT-based imaging agent (99mTc-etarfolatide), Ann Oncol, 25 (2014) 852-858.

[22] I. Vergote, D. Armstrong, G. Scambia, K. Fujiwara, V. Gorbunova, C. Schweizer, S. Weil, A. Barnias, C. Poole, J. Sehouli, Phase 3 double-blind, placebo-controlled study of weekly farletuzumab with carboplatin/taxane in subjects with platinum-sensitive ovarian cancer in first relapse, Int J Gynecol Cancer, 23 (2013). Supplement 1.

[23] E.I. Sega, P.S. Low, Tumor detection using folate receptor-targeted imaging agents, Cancer Metastasis Rev, 27 (2008) 655-664.

[24] N. Parker, M.J. Turk, E. Westrick, J.D. Lewis, P.S. Low, C.P. Leamon, Folate receptor expression in carcinomas and normal tissues determined by a quantitative radioligand binding assay, Anal Biochem, 338 (2005) 284-293.

[25] R.E. Fisher, B.A. Siegel, S.L. Edell, N.M. Oyesiku, D.E. Morgenstern, R.A. Messmann, R.J. Amato, Exploratory study of 99mTc-EC20 imaging for identifying patients with folate receptor–positive solid tumors, J Nucl Med, 49 (2008) 899-906.

[26] N.V. Nukolova, H.S. Oberoi, S.M. Cohen, A.V. Kabanov, T.K. Bronich, Folate-decorated nanogels for targeted therapy of ovarian cancer, Biomaterials, 32 (2011) 5417-5426.

[27] S.S. Desale, S.M. Raja, J.O. Kim, B. Mohapatra, K.S. Soni, H. Luan, S.H. Williams, T.A. Bielecki, D. Feng, M. Storck, Polypeptide-based nanogels co-encapsulating a synergistic combination of doxorubicin with 17-AAG show potent anti-tumor activity in ErbB2-driven breast cancer models, J Control Release, 208 (2015) 59-66.

[28] M. Ferrari, M.C. Fornasiero, A.M. Isetta, MTT colorimetric assay for testing macrophage cytotoxic activity in vitro, J Immunol Methods, 131 (1990) 165-172.

[29] C.P. Leamon, J.A. Reddy, R. Dorton, A. Bloomfield, K. Emsweller, N. Parker, E. Westrick, Impact of high and low folate diets on tissue folate receptor levels and antitumor responses toward folate-drug conjugates, J Pharmacol Exp Ther, 327 (2008) 918-925.

[30] S.A. Ferreira, F.M. Gama, M. Vilanova, Polymeric nanogels as vaccine delivery systems, Nanomed Nanotechnol Biol Med, 9 (2013) 159-173.

[31] Y. Shi, M.J. van Steenbergen, E.A. Teunissen, L.s. Novo, S. Gradmann, M. Baldus, C.F. van Nostrum, W.E. Hennink, Π–Π stacking increases the stability and loading capacity of thermosensitive polymeric micelles for chemotherapeutic drugs, Biomacromolecules, 14 (2013) 1826-1837.

[32] Y. Shi, R. van der Meel, B. Theek, E. Oude Blenke, E.H. Pieters, M.H. Fens, J. Ehling, R.M. Schiffelers, G. Storm, C.F. van Nostrum, Complete Regression of Xenograft Tumors upon Targeted Delivery of Paclitaxel via Π–Π Stacking Stabilized Polymeric Micelles, ACS Nano, 9 (2015) 3740-3752.

[33] T. Hamaguchi, Y. Matsumura, M. Suzuki, K. Shimizu, R. Goda, I. Nakamura, I. Nakatomi, M. Yokoyama, K. Kataoka, T. Kakizoe, NK105, a paclitaxel-incorporating micellar nanoparticle formulation, can extend in vivo antitumour activity and reduce the neurotoxicity of paclitaxel, Br J Cancer, 92 (2005) 1240-1246.

[34] J. Logie, C.K. McLaughlin, R.Y. Tam, M.S. Shoichet, Innovative use of the taxol binding peptide overcomes key challenges of stable and high drug loading in polymeric nanomicelles, Chem Commun (Camb), 51 (2015) 12000-12003.

[35] N. Chida, Y. Hirasawa, T. Ohkawa, Y. Ishii, Y. Sudo, K. Tamura, S. Mutoh, Pharmacological profile of FR260330, a novel orally active inducible nitric oxide synthase inhibitor, Eur J Pharmacol, 509 (2005) 71-76.

[36] K. Jaaback, N. Johnson, Intraperitoneal chemotherapy for the initial management of primary epithelial ovarian cancer, Cochrane Libr, (2006).

[37] D.L. Chan, D.L. Morris, A. Rao, T.C. Chua, Intraperitoneal chemotherapy in ovarian cancer: a review of tolerance and efficacy, Cancer Manag Res, 4 (2012) 413.

[38] B.W. Yin, K.O. Lloyd, Molecular Cloning of the CA125 Ovarian Cancer Antigen identification as a new mucin, MUC16, Journal of Biological Chemistry, 276 (2001) 27371-27375.

[39] D. Gupta, C.G. Lis, Pretreatment serum albumin as a predictor of cancer survival: a systematic review of the epidemiological literature, Nutr J, 9 (2010) 10.1186.

[40] R.C. Bast Jr, T.L. Klug, E.S. John, E. Jenison, J.M. Niloff, H. Lazarus, R.S. Berkowitz, T. Leavitt, C.T. Griffiths, L. Parker, A radioimmunoassay using a monoclonal antibody to monitor the course of epithelial ovarian cancer, N Engl J Med, 309 (1983) 883-887.

[41] T.J. Shaw, M.K. Senterman, K. Dawson, C.A. Crane, B.C. Vanderhyden, Characterization of intraperitoneal, orthotopic, and metastatic xenograft models of human ovarian cancer, Mol Ther, 10 (2004) 1032-1042.

[42] M.F. Burbridge, L. Kraus-Berthier, M. Naze, A. Pierre, G. Atassi, N. Guilbaud, Biological and pharmacological characterisation of three models of human ovarian carcinoma established in nude mice: use of the CA125 tumour marker to predict antitumour activity, Int J Oncol, 15 (1999) 1155-1217.

[43] F. Kraeber-Bodéré, A. Mishra, P. Thédrez, A. Faivre-Chauvet, M. Bardiès, S. Imai, J. Le Boterff, J.-F. Chatal, Pharmacokinetics and biodistribution of samarium-153-labelled OC125 antibody coupled to CITCDTPA in a xenograft model of ovarian cancer, Eur J Nucl Med, 23 (1996) 560-567.

[44] H. Uchino, Y. Matsumura, T. Negishi, F. Koizumi, T. Hayashi, T. Honda, N. Nishiyama, K. Kataoka, S. Naito, T. Kakizoe, Cisplatin-incorporating polymeric micelles

(NC-6004) can reduce nephrotoxicity and neurotoxicity of cisplatin in rats, Br J Cancer, 93 (2005) 678-687.

[45] Y. Mizumura, Y. Matsumura, T. Hamaguchi, N. Nishiyama, K. Kataoka, T. Kawaguchi, W.J.M. Hrushesky, F. Moriyasu, T. Kakizoe, Cisplatin-incorporated polymeric micelles eliminate nephrotoxicity, while maintaining antitumor activity, Cancer Sci, 92 (2001) 328-336.

[46] P.S. Low, W.A. Henne, D.D. Doorneweerd, Discovery and development of folic-acid-based receptor targeting for imaging and therapy of cancer and inflammatory diseases, Acc Chem Res, 41 (2007) 120-129.

**CHAPTER IV**

**HSP90-INHIBITION ENHANCES THE LYSOSOMAL TARGETING AND EFFICACY OF ErbB2-TARGETED DRUG DELIVERY**

## 4.1. Introduction

Overexpression of surface receptors on cancer cells presents opportunities to achieve targeted delivery of cytotoxic agents linked directly to targeting ligands/antibodies or encapsulated within nanometer-sized drug delivery vehicles decorated with targeting ligands/antibodies [1]. The receptor tyrosine kinase family members, EGFR and ErbB2 are overexpressed in many types of cancers and have served as popular models for the development of targeted drug delivery modalities, including Antibody-Drug-Conjugates (ADCs) and nanoparticulate drug delivery systems. Trastuzumab-DM1 (Kadcyla®, Genentech, San Francisco) is an example of an ADC developed against ErbB2-overexpressing cancers in which the cytotoxic drug (Emtansine) is chemically conjugated to Trastuzumab (the humanized anti-ErbB2 monoclonal antibody) [2]. The success of these strategies is predictably dependent on robust endocytosis of the receptor-bound cargo and trafficking from early endosomes to the lysosomes, where the conjugate undergoes disintegration, resulting in the release of the cytotoxic drug into the cytosol. In normal cells, endocytosis and receptor trafficking is a highly regulated process mediated by several cellular factors. Receptors may be endocytosed via clathrin- or caveolin-mediated pathways, or via macropinocytosis. Following endocytosis, the receptors are either routed to the lysosomes or recycled back to the cell-surface, process regulated

among other factors by receptor ubiquitination (mediated by E3 ubiquitin ligases such as Cbl) or de-ubiquitination (mediated by AMSH or USP8) [3-8]. Ubiquitin-dependent sorting proteins, known as ESCRT (Endosomal Sorting Complex Required for Transport) proteins recognize the ubiquitinated receptor cargo and help sort them into inner vesicles of multivesicular bodies for transport to lysosomes [4, 5, 9, 10]. Various Rab-family GTPases, functioning at distinct vesicular trafficking stages, also play a critical role in directing the sorting of endocytosed cargo between recycling and lysosomal pathways. Cancer cell-specific alterations (mutations, overexpression) in receptors themselves or in the trafficking regulators can alter the balance between receptor-recycling and lysosomal trafficking [3, 11]. While the focus has been more in designing receptor-targeted drug delivery systems, the consequence of alterations in regulatory factors that affect the recycling vs. lysosomal trafficking behavior of targeted receptors and consequently the efficiency of drug delivery have received little attention. In this study, we illustrate the importance of receptor dynamics on targeted drug delivery, using ErbB2-overexpressing breast tumor targeting through anti-ErbB2 humanized monoclonal antibody Trastuzumab as a model.

The oncogenic receptor tyrosine kinase ErbB2, overexpressed in over 20% of breast cancers, has served as a major target for the development of targeted drug delivery strategies [12-15]. However, ErbB2 is thought to be either impaired in endocytosis or to rapidly recycle back to the cell-surface [16, 17], which can significantly dampen the efficacy of ErbB2-targeted drug delivery. Such altered trafficking dynamics is believed to be due to its constitutive association with HSP90 [18], [17-22] which can be anticipated to significantly dampen the efficacy of ErbB2-targeted drug delivery. We therefore

hypothesized that HSP90-inhibition will enhance ErbB2-targeted drug delivery by promoting the endocytic uptake of ErbB2-bound nanoencapsulated cargo and facilitating its re-routing from a recycling pathway to the lysosomes. Using Trastuzumab-conjugated nanogels (Trast-NG) encapsulating the DNA-damaging drug Doxorubicin (DOX) as a model chemotherapeutic, we demonstrate through both *in vitro* and *in vivo* studies that HSP90-inhibition can indeed lead to an enhancement of targeted delivery of DOX specifically into ErbB2-overexpressing breast cancer cells. As a consequence, a sub-therapeutic and non-toxic dose of the HSP90 inhibitor 17AAG markedly improves the efficacy of ErbB2-targetd nanogels *in vivo*.

## 4.2. Materials and methods:

### 4.2.1. Materials.

Trastuzumab was obtained from UNMC pharmacy. PEG-*b*-PMA diblock copolymer (Mw/Mn = 1.45) was purchased from Polymer Source Inc., Canada. The block lengths were 170 and 180 repeating units for PEG and PMA respectively. The concentration of carboxylate groups in the copolymer samples was estimated by potentiometric titration. FMOC-PEG-NHS was purchased from Creative PEGWorks, NC. Calcium chloride, Ethylenediamine, 1-(3-dimethylaminopropyl)-3-ethylcarbodiimide hydrochloride (EDC) *and* Ethylenediaminetetraacetic acid (EDTA) were obtained from Sigma-Aldrich (St Louis, MO). Doxorubicin hydrochloride was kindly provided by Dong-A Pharmaceutical Company, South Korea. Fetal bovine serum (FBS) (both dialyzed and heat inactivated), DMEM and RPMI 1640 media and Lysotracker$^{TM}$ (green) were purchased from Invitrogen Inc (Carlsbad, CA). Bovine serum albumin (BSA) and NUNC$^{TM}$ chambered glass coverslips for live cell imaging were purchased from Fisher Scientific (Waltham,

MA). MTT reagent (3-(4,5-Dimethylthiazol-2-yl)-2,5-diphenyltetrazolium bromide) was purchased from Research Products International (Prospect, IL). All other chemicals were of reagent grade and used without further purification. The following primary antibodies were used in this study: anti-human-ErbB2 mouse monoclonal (ErbB2) raised against the C-terminal amino acid residues (1242-1255), used for Western blotting studies, were purchased from BD Pharmingen™ (San Diego, CA); for flow cytometry and immunofluorescence studies, the goat anti-human-ErbB2 polyclonal antibody (AF1129) was from R&D Systems (Minneapolis, MN); the mouse monoclonal anti-phosphotyrosine (anti-pY; 4G10) was kindly provided by Dr. Brian Druker (Oregon Health & Science University, Portland, OR); the mouse monoclonal anti-Hsc70 antibody were from Santa Cruz Biotechnology Inc. (Santa Cruz, CA).

### 4.2.2. Synthesis of the NGs.

The general procedure for the synthesis of NGs has been described earlier [23, 24]. Briefly, PEG-$b$-PMA/Ca$^{2+}$ complexes were prepared by mixing an aqueous solution of PEG-$b$-PMA with a solution of CaCl$_2$ at a molar ratio of [Ca$^{2+}$] / [COO−] = 1.3. The chains were cross-linked overnight at room temperature (r.t.) using 1,2-ethylenediamine and EDC ([EDC]/[1,2-ethylenediamine] = 2; [COOH]/[EDC] = 5). The NGs were dialyzed (MWCO 3.5 kDa) extensively against a) 0.5% aqueous ammonia in the presence of EDTA and b) bi-distilled water.

### 4.2.3. Synthesis and characterization of mAb-modified DOX-loaded NGs.

MAb (Trast and mouse IgG) were attached to the NGs via streptavidin-biotin complex (Fig. 1). Details of conjugation procedure are as follows.

***PEGylation of streptavidin.*** Streptavidin was diluted with 50 mM sodium bicarbonate buffer till concentration becomes 1 mg/mL (total volume: 6 mL). Separately, Fmoc-PEG-NHS (Mw = 10 kDa, 1.5 mg, 1.5 eq with respect to streptavidin) was also diluted with same buffer. Solution of streptavidin was added dropwise to Fmoc-PEG-NHS solution. The mixture was incubated for 2 h followed by Fmoc group deprotection. Fmoc groups were removed by adding 0.5 µL of 20% piperidine/DMF (5 eq piperidine) and incubating the reaction mixture for 10 min. Resulting construct ($NH_2$-PEG-streptavidin) was purified using repeated ultrafiltration (MWCO 30,000, Millipore) at 3000 rpm for 15 min (3 washes) to remove unreacted PEG. Absence of free PEG was confirmed by size exclusion chromatography (SEC) using an ÄKTA FPLC (Amersham Biosciences) equipped with Sepharose CL-6B-based column.

***Insertion of $NH_2$-PEG-streptavidin into NGs***. Carboxylate groups of NG were activated with EDC (0.3 mg, 10 eq with respect to the amount of $NH_2$-PEG-streptavidin) followed by insertion of $NH_2$-PEG-streptavidin into NGs through the reaction between free $NH_2$ groups of PEG with EDC-activated carboxyl acid core of NGs. Mixture was allowed to react for 2 h followed by purification of streptavidin-NG conjugate using repeated ultrafiltration (MWCO 100,000, Millipore) at 4500 rpm for 30 min (3 washes) to remove unreacted PEG-Streptavidin. Absence of free PEG-Streptavidin was confirmed by SEC. Amount of streptavidin present in the streptavidin-NG conjugate was measured by Bradford method using BioRad assay kit (BioRad, Richmond, CA, USA) and bovine serum albumin as the standard.

***Preparation of mAb-NG via streptavidin biotin complex and drug loading.*** Streptavidin-NGs were further mixed with biotinylated mAb (ratio of streptavidin to biotin was 1:2).

The mixture was incubated for 2 h at r.t.. The mAb-NG was purified SEC. This purification procedure allowed removing all unbound mAb, while the unmodified NG and mAb-NGs were not separated. Amount of mAb present in the mAb-NG conjugate was measured by Bradford method using streptavidin-NG as control. mAb-NG/DOX was prepared by adding DOX to an aqueous dispersion of NGs at the feeding ratio of R= [DOX]/[COO$^-$] = 0.25, for 24 h at pH 7.0. Unbound DOX was separated by repeated ultrafiltration (MWCO 30,000, Millipore) at 3000 rpm for 15 min (3 washes).

### 4.2.4. Determination of particle size and zeta-potential.

Intensity-mean Z-averaged particle diameter ($D_{eff}$) and $\zeta$-potential of NG were determined using a Malvern Zetasizer (Malvern Instruments Ltd., Malvern, UK). All measurements were performed in automatic mode, at 25°C. Software provided by the manufacturer was used to calculate size, polydispersity indices and $\zeta$-potential of NGs. The values were calculated from the measurements performed at least in triplicate.

### 4.2.5. Cell culture conditions.

The ErbB2-overexpressing cell lines used in this study were SKBr-3, 21MT1 and BT-474. MCF-7 cells were used as a representative ErbB2-low cell line for comparison. All cell lines were maintained as previously described [19, 70]. The ErbB2-overexpressing breast cancer cell line 21MT-1 was established by Band et al [71] and has been previously described. BT-474 and MCF-7 cell lines were purchased from ATCC.

### 4.2.6. Confocal microscopy.

Cellular uptake and localization studies of Trast-NG were conducted using confocal microscope (Carl Zeiss LSM 510 Meta, Peabody, MA). SKBr-3 breast cancer cells ($1\times10^6$) were plated on glass coverslips. Trast-NG (without drug) were incubated with

ErbB2-overexpressing SKBr-3 cells for 1h. 17-AAG (100 nM) was added for the different times (2, 4 and 8h), after which the slides were washed and fixed in 4% parafolmaldehyde. Nanogels were visualized by staining the Fc-portion of the conjugated Trast on the NG using FITC-conjugated anti-Human antibody (green). ErbB2 was stained either using the goat anti-ErbB2 polyclonal antibody (AF1129) directed against the N-terminal extracellular domains of ErbB2 or a mouse monoclonal antibody directed against the C-terminal tail of ErbB2 (BD Pharmingen) followed by Alexa594-conjugated secondary antibody (anti-goat or anti-mouse respectively). The lysosomal marker LAMP-1 was stained using mouse anti-human LAMP-1 mAb, followed by Alexa-594-conjugated anti-mouse secondary.

### 4.2.7. Cell cycle analysis.

We evaluated the ability of 17-AAG to enhance the delivery of DOX encapsulated within the NG in 21MT-1 and MCF-7 cells by a cell cycle analysis [70]. Briefly, cells were seeded in 6-well plates and allowed to adhere for 24 h prior to drug treatment. Cells were then exposed to various concentrations of Trast-NG/DOX (1.7 – 13.3 μM Dox) for 6 hours, following which cells were either left alone (control) or treated with 100 nM 17-AAG for 18 hours. Cell cycle distribution was then evaluated by using standard protocol for FACS analysis of propidium iodide (PI)-stained cells.

### 4.2.8. Animal Studies.

All animal studies were conducted in accordance with an approved protocol by the University of Nebraska Medical Center Institutional Animal Care and Use Committee (IACUC). $10^7$ BT-474 cells (an ErbB2 overexpressing human breast cancer cell line) reconstituted in 50% Matrigel (BD Biosciences, California) in media were injected

directly into the mammary fat pad of 4-6 week old female Athymic NCr-nu/nu mice (NCI, Fredrick National Lab, Fredrick, MD). 17-β-Estradiol pellets (0.72mg/pellet; 60 day release; Innovative Research of America, Sarasota, Fl) were implanted subcutaneously on the lateral side of the neck of the mice, three days prior to the injection of the tumor cells.  The mice were stratified into treatment groups 14 days after tumor inoculation, when the average tumor size reached 100-200 mm$^3$.  Treatment groups included: 1) 5 % dextrose (Control); 2) Trast alone (3 mg/kg); 3) IgG-NG/DOX (6 mg/kg); 4) IgG-NG/DOX (6 mg/kg) + free 17AAG (1 mg/kg); 5) Trast-NG/DOX (6 mg/kg); 7) Trast-NG/DOX (6 mg/kg) + free 17AAG (1 mg/kg). Treatments were administered via tail vein injections at 4-day intervals. 17-AAG doses were given 2 h after NG formulation administration. Animal body weight and tumor volume were monitored every second day. Tumor volume ($V = 0.5$ x L x $W^2$) was estimated by measuring two orthogonal diameters (longer dimension: L, and smaller dimension: W) of the tumor using electronic calipers. Animals were sacrificed when tumor volume exceeded 3000 mm$^3$, greatest tumor dimension exceeded 20 mm, tumor became necrotic, or animal exhibited a body weight loss of more than 20%. All other animals were sacrificed by day 78.

### 4.2.9. Apoptosis and proliferation.

Tumors from mice that received different treatments were excised at day 14 (2–3 mice per group). The tumors were dissected and fixed in 10% neutral buffered formalin. Then, the tissues were processed routinely into paraffin, sectioned at a thickness of 4 μm. Proliferating and apoptotic cells were detected using an antibody against Ki-67 and caspase-3, respectively. Visualization was done by incubation with DAB + (brown, for

Ki-67) and Permanent red (for caspase-3) (DAKO) for 2 min. After rinsing with distilled water, the sections were counterstained with hematoxylin. For quantification of Ki-67 and caspase-3 expression, the area of positive cells was determined (Image J) in 5 random high power fields ($20\times$ magnification) and divided by the total area of cells for each field of slice.

### 4.2.10. Histopathology analysis.

Specific tissues (liver, spleen, heart kidney and lung) were fixed in buffered formalin and were sectioned, inserted into tissue cassettes, dehydrated in 70% ethanol overnight, and paraffin embedded (UNMC Tissue Sciences Facility, Omaha, NE). Serial 5 μm sections were stained with hematoxylin and eosin (H&E). For histopathological diagnosis, H&E-stained slides were examined by light microscopy.

### 4.2.11. Statistical analysis.

Statistical comparisons for evaluating biological effects for the various treatment groups were carried out using Student t-test using a type I error ($\alpha$) = 0.05 . For the antitumor study and toxicity studies, *in vivo*, group means for tumor volume and body weights were evaluated using repeated measures analysis of variance. Survival was estimated using Kaplan–Meier analysis and compared using log-rank test. *P* values less than 0.05 were considered significant. Analysis of variance and Kaplan–Meier analysis with log-rank test were performed using GraphPad Prism 5 (GraphPad Software, Inc.). Median survival time for the various groups and the associated Confidence Interval limits were derived by running PROC LIFETEST in SAS (Statistical Analysis System) software.

## 4.3. Results:

### 4.3.1. Preparation and characterization of Trast-NG.

Core-shell NG studied here were synthesized as previously described [23, 24] via self-assembly of doubly hydrophilic poly(ethylene glycol)-*b*-poly(methacrylic acid) (PEG-*b*-PMA) block copolymers in the presence of the condensing agent (CaCl$_2$) followed by chemical crosslinking of the polyion chains and removal of the condensing agent. The
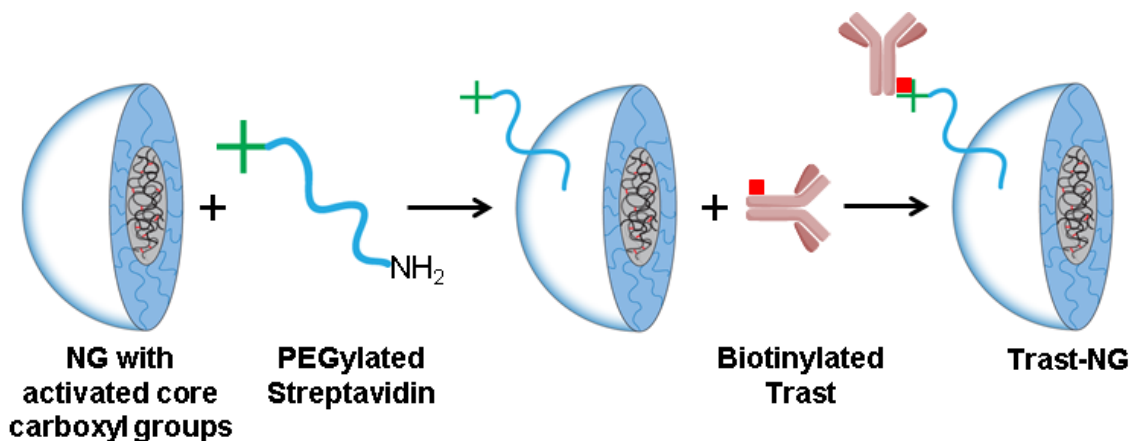


**Figure 4.1.** Scheme for the synthesis of Trast-NG conjugate via streptavidine-biotin

resulting NGs were of ca. 110 nm in diameter and had a net negative charge (ζ-potential = -22 mV). The core of such NGs comprised a swollen network of the cross-linked polyion chains bearing carboxylic groups and is surrounded by the shell of hydrophilic PEG chains. These (PEG-*b*-PMA)-based NGs can incorporate very large amounts (~30% wt.) of water-soluble drugs such as DOX through combination of electrostatic and Van der Waals interactions [24], The preparation of Trast-NG is depicted in Fig. 4.1 and detailed in the methods section. NGs were first functionalized with streptavidin by inserting an NH$_2$-PEG-streptavidin linker. Since 7.5 kDa PEG chains comprise NGs shells, we chose PEG with a longer chain length, M$_w$ = 10 kDa, to reduce potential steric interference with receptor binding. The average particle size of streptavidin-conjugated NGs was 137 ± 4 nm (polydispersity Index = 0.09, ζ-potential = -19.0 ± 2.3 mV), which

is only slightly larger than that of precursor NGs. Biotinylated Trast or control IgG was then coupled with streptavidin-modified NGs. Final product was purified using fast protein liquid chromatography (FPLC) (Fig. 4.2). FPLC chromatogram confirmed very high yield of reaction with little residual Trast or IgG (Fig. 4.2).
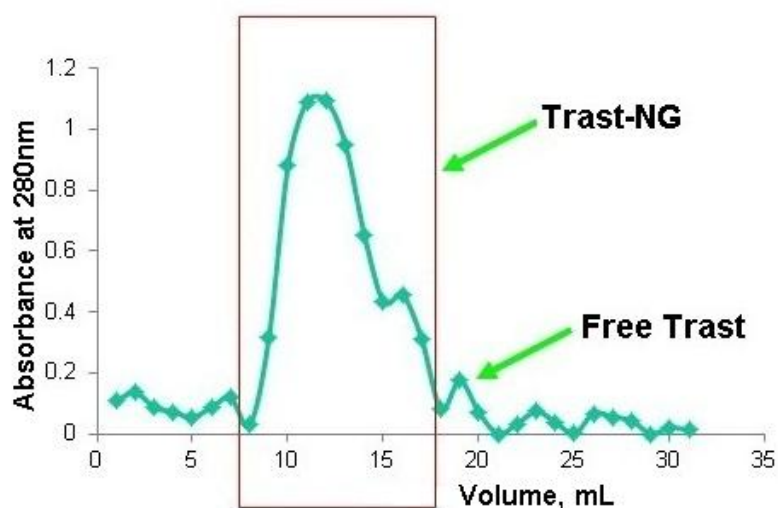


**Figure 4.2. Purification of Trast-NG by FPLC**

Purified Trast-NG had an average particle size of $173 \pm 3$ nm (polydispersity Index = 0.08, $\zeta$-potential = $-20.2 \pm 3.1$ mV), whereas the control IgG-NG had a size of $177 \pm 2$ nm (polydispersity Index = 0.07, $\zeta$-potential = $-19 \pm 2.2$ mV). After DOX loading, the average particle size of Trast-NG decreased to $154 \pm 4$ nm (polydispersity Index – 0.19, $\zeta$-potential = $-4.1 \pm 0.9$ mV), whereas the particle size of IgG-NG was $157 \pm 8$ (polydispersity Index = 0.24, $\zeta$-potential = $-2.7 \pm 1.3$ mV). Reduction in particle size and net negative charge of NGs after DOX loading was consistent with neutralization and condensation of PMA segments by DOX.

The conjugation of Trast to NG did not compromise its ability to specifically bind to ErbB2 receptors overexpressed on human breast adenocarcinoma SKBr-3 cells was

confirmed by flow cytometry (FACS) (Fig. 4.3A) and confocal immunofluorescence microscopy (Fig. 4.3B). By using two-color imaging, the latter analyses showed complete colocalization of ErbB2 staining with Trast (stained in red) with signals form the bound Trast-NG (stained in green) (Fig. 4.3B), demonstrating ErbB2-specific binding of the NG.
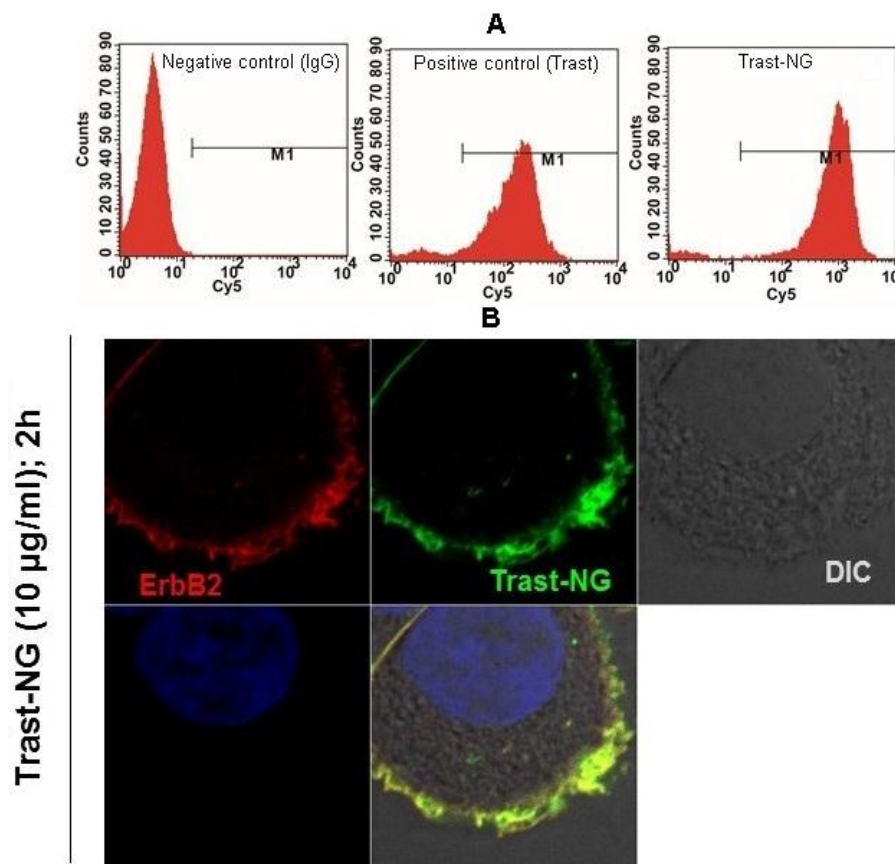


**Figure 4.3.** Trast-NG retains its ability to specifically bind to ErB2. A. ErbB2-overexpressing breast cancer cell line.  SKBr-3 was left untreated or treated with biotinylated Trast or Trast-NG on ice. The bound Trast or Trast-NG was detected using a Cy5-labeled anti-human secondary Ab alone.  Samples were subjected to FACS analysis. Untreated cells stained with the Cy5-labeled secondary Ab served as a negative control, whereas biotinylated Trast served as a positive control. B. Binding of Trast-NG to ErbB2-overexpressing breast cancer cells was confirmed by confocal microscopy. ErbB2-was visualized using a mouse monoclonal antibody directed against the C-terminal antigenic region of ErbB2 (BD Pharmingen), followed by Alexa594-conjugated

anti-mouse secondary antibody. The Trast-NG bound to the ErbB2 was detected using a FITC-conjugated goat anti-human secondary antibody to detect the Fc portion of the Trast-conjugated to the NG.

To further explore the specificity of Trast-NG towards ErbB2-overexpressing breast cancer cells, we compared the cancer cell growth inhibition induced by DOX encapsulated within untargeted NG vs. Trast-NG (Table 4.1). The ErbB2-overexpressing BT-474 and the ErbB2-low MCF-7 breast cancer cell lines were used as models for comparison of targeting specificity. The biological effects were assessed using MTT dye incorporation assay.

**Table 4.1 .** Comparison of $IC_{50}$ values for targeted Vs non-targeted DOX-loaded nanogels ErbB2 high and ErbB2 low cells as determined by the MTT assay.

| | $IC_{50}$ ($\mu$M) | |
|---|---|---|
| | BT-474 (ErbB2 +) | MCF-7 (ErbB2 -) |
| NG/DOX | $0.43 \pm 0.13$ | $0.29 \pm 0.1$ |
| Trast-NG/DOX | $0.07 \pm 0.08$ | $0.19 \pm 0.07$ |

The $IC_{50}$ value of DOX against ErbB2-overexpressing BT-474 cells was 6-fold lower using DOX-loaded Trast-NG (Trast-NG/DOX) compared to DOX-loaded NG (NG/DOX). On the other hand, no appreciable difference in the $IC_{50}$ against ErbB2-low MCF-7 cells was seen between Trast-NG/DOX and NG/DOX (Table 4.1). These experiments confirmed the ability of Trast-NG to deliver chemotherapeutic payloads to ErbB2-overexpressing breast cancer cells with high specificity.

## 4.3.2. Kinetics of endocytic uptake of Trast-NG into ErbB2-overexpressing breast cancer cells.

Next, we compared the kinetics of the endocytic uptake of Trast-NG into ErbB2-overexpressing cell line SKBr-3, using confocal immunofluorescence analysis in absence or presence of an HSP90 inhibitor. For this set of experiments, we used the empty Trast-

NG. Cells seeded on glass-coverslips were either left untreated or treated with 10 µg/mL of free Trast or the equivalent protein concentration of Trast-NG for 2, 4 or 8 hours in absence or presence of the HSP90 inhibitor 17-AAG (100 nM) followed by confocal imaging (Fig. 4.4). In the absence of 17AAG, Trast-NG (stained in green) was found at the cell surface throughout the 8h time course, with relatively little internalized pool, comparable to that seen with free Trast (Fig. 4.4, second vs. first column). In contrast, cells incubated with Trast-NG in the presence of 17-AAG demonstrated the rapid internalization of ErbB2 (stained in red) with notable internal staining at 2 h and nearly complete intracellular staining at 4h; as expected, ErbB2 levels decreased by 8h, reflecting the destabilization due to HSP90 inhibition (Fig. 4.4, last column).
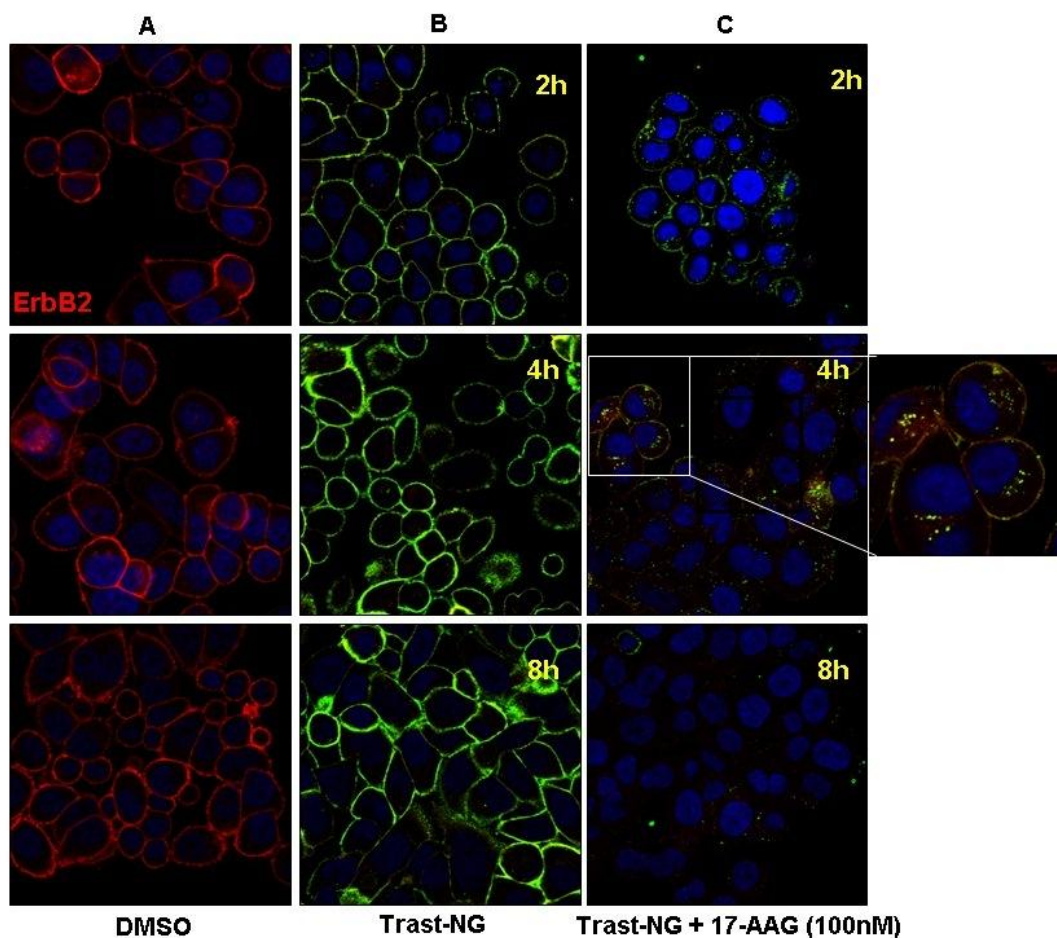
**Figure 4.4. The HSP90 inhibitor 17AAG promotes the internalization and lysosomal degradation of Trast-NG.** ErbB2-overexpressing SKBr3 cells were plated on glass coverslips and incubated with Trast-NG without any encapsulated drug for 1h to allow binding to the cell surface. 17-AAG (100 nM) was then added for the indicated time points, after which the slides were washed and fixed, stained as described in the legend for Fig. 4.3. The slides were analyzed by confocal immunofluorescence microscopy. The inset within panel C shows Trast-NG accumulating in punctate intracellular vesicles following 17-AAG treatment.

The loss of the green signal from Trast was concomitant with the loss of red signal from

ErbB2 (due to lysosomal degradation of both ErbB2 and Trast), suggesting that the

targeted NG cargo follows the endocytic itinerary of the ErbB2 receptor upon HSP90

inhibition [17-22]. To confirm if HSP90 inhibition indeed promoted the NG cargo

trafficking into the lysosomal compartment, which is desirable to facilitate the NG

disintegration and release of encapsulated drugs [17-22], we examined the colocalization of internalized NG (stained in green) with the lysosomal marker LAMP-1 (stained in red) in SKBr-3 cells. Confocal Immunofluorescence analysis (Fig 4.5) confirmed that the NG was indeed targeted to found in LAMP-1-positive compartments in the presence of 17AAG. These analyses demonstrate the strong positive impact of HSP90 inhibition to promote the internalization and lysosomal targeting of Trast-NG.
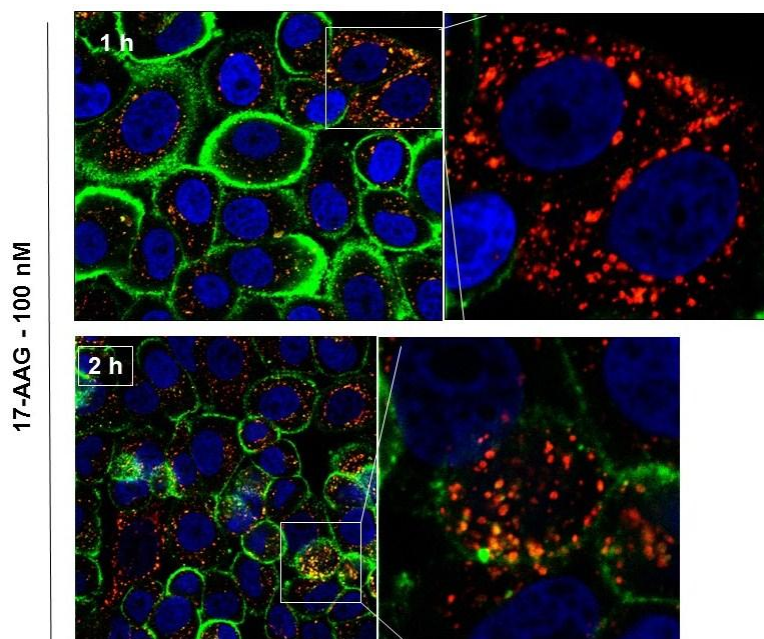


**Figure. 4.5**. SKBR-3 cells grown on glass coverslips were treated with Trast-NG followed by 17-AAG as described in the legend for Fig 3 A. The internalized Trast-NG (seen in green) was visualized as described in the legend for Fig 2. The lysosomal marker LAMP-1 (seen in red) was stained using mouse anti-human LAMP-1 mAb, followed by Alexa-594-conjugated anti-mouse secondary. Co-localization of Trast-NG with LAMP-1 can be seen as regions in yellow/orange.

**4.3.3. In vitro analysis of HSP90 inhibitor-facilitated delivery of DOX into ErbB2-overexpressing breast cancer cells.**

Having verified our central hypothesis that HSP90-inhibition facilitates the routing of Trast-NG (without drugs) into lysosomes, we evaluated the ability of 17-AAG to enhance the delivery of NG-encapsulated DOX. The ErbB2-overexpressing 21MT-1 cell or the ErbB2-low MCF7 cells (specificity control) were incubated with increasing concentrations of Trast-NG/DOX for 6 h, after which the cells were either left alone (control) or treated with 100 nM 17-AAG for 18 h to trigger the internalization and lysosomal routing of the targeted NG cargo. Biological effects were assessed by evaluating DOX-induced G2/M arrest using a FACS-based assay.
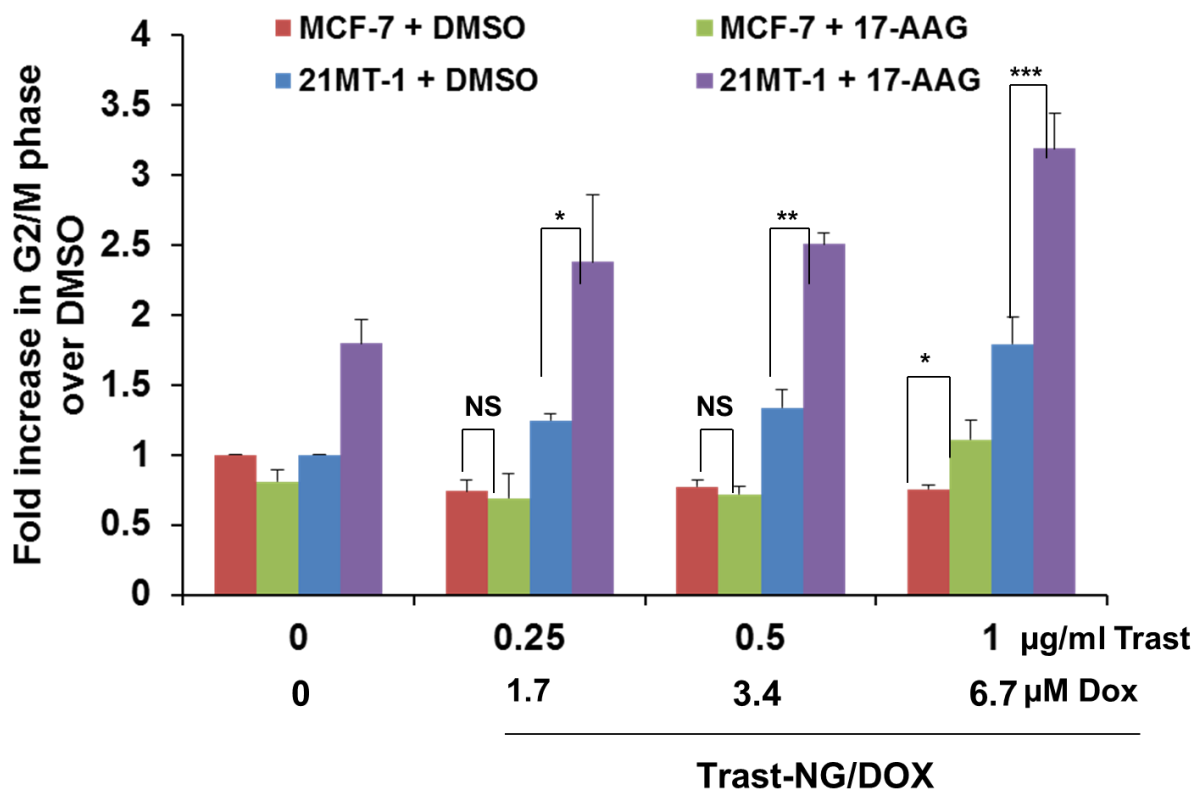


**Figure 4.6.** HSP90 inhibition potentiates the effect of Trast-NG/DOX on ErbB2-expressing breast cancer cells. The ErbB2-overexpressing 21MT-1 or ErbB2-low MCF-7 cells were plated in 6-well plates and triplicate wells were treated with the indicated concentrations of Trast-NG/DOX for 6h. Unbound Trast-NG/DOX was washed out and cells were cultured further in DOX-free media without or with 17-AAG (100 nM) for 18

h followed by the incubation with nanogel-free media. Cell cycle analysis was performed after 48 h of treatment. Shown are the fold increase in the % of cells in G2/M phase of the cell cycle for each treatment condition over DMSO control (the color coding is indicated inside the histogram). The number of asterisks indicates increasing significance (*, p<0.05; **, p<0.005; ***, p<0.0005); NS, not significant.

While Trast-NG/DOX treatment showed a dose-dependent increase in the % cells in G2M in ErbB2-overexpressing 21-MT1 cells, little effect was seen on ErbB2-low MCF7 cells, especially at lower concentrations (Fig. 4.6). Inclusion of 17AAG had no impact on the effect of lower concentrations of Trast-NG/DOX on the % of MCF7 cells in G2/M, but a statistically significant increase was noted in 21-MT1 cells treated with identical concentrations of Trast-NG/DOX (Fig. 4.6). Thus, inclusion of 17AAG markedly increased the biological impact of Trast-NG/DOX, relatively selectively against the ErbB2-overexpressing cell line.

## 4.3.4. Potentiation of the antitumor efficacy of Trast-NG/DOX by 17 AAG in an ErbB2-overexpressing breast cancer cell xenograft model in mice.

To examine if HSP90 inhibition potentiates the antitumor efficacy of Trast-NG/DOX *in vivo*, we treated mice bearing ErbB2-overexpressing breast cancer cell line (BT-474) xenografts with Trast-NGs carrying DOX with or without sequential treatment with 17AAG. *In vivo* experiments with BT-474 xenografts were conducted twice (with n= 10 mice/group). In the first set only tumor volume changes were measured, while in the second, the mice were also followed for survival analyses. For comparison, we also examined the impact of these treatments on xenografts of the ErbB2-low cell line MCF-7. Control treatments included: 1) 5 % dextrose solution (negative control); 2) Trast alone (positive control); 3) IgG-NG/DOX (non-targeted NG) and; 4) IgG-NG/DOX plus 17-AAG. A total of four treatments (intravenous injections) were given at 4-day

intervals at a NG dose equivalent to 6 mg of DOX/kg (determined as the maximum tolerated dose for this treatment schedule). The NG doses administered were equivalent to 6 mg/kg DOX and 3 mg/kg Trast per injection. In cohorts that included the 17-AAG treatment, this drug was administered at 1 mg/kg, 2 h after the Trast-NG/DOX or IgG-NG/DOX injection.

The changes in the relative tumor volume for mice bearing BT-474 (ErbB2-high) tumors are shown in Fig. 4.7A (data combines results from two independent experiments). To confirm the *in vivo* selectivity of the targeted NG to deliver DOX to ErbB2-overexpressing tumors, we also evaluated the effect of treatments with Trast-NG/DOX in comparison to the untargeted IgG-NG/DOX, on mice with MCF-7 (ErbB2-low) xenografts (Fig 4.8). Student's t-test was run on the tumor relative volume change data at day 16, comparing each treatment groups against 5% Dextrose control.
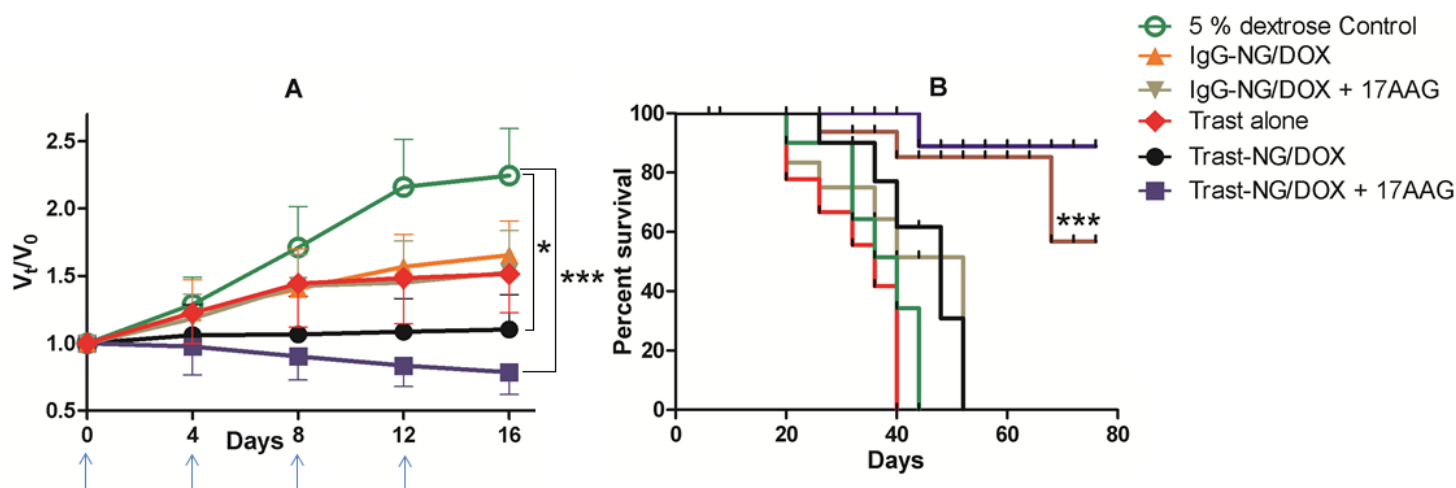


**Figure 4.7.** *In vivo* antitumor efficacy of Trast-NG/DOX and enhancement by concurrent administration of 17-AAG against ErbB2-overexpressing breast cancer xenografts. BT-474 xenografts were established by orthotopic injection of cells in mammary glands of female Nude mice, and the following treatments intravenous administered after tumors had grown between 200 and 300 mm$^3$ in volume: Trast-NG/DOX + 17-AAG (■) or Trast-NG/DOX (●) or IgG-NG/DOX + 17-AAG (▼) or IgG-NG/DOX (▲) or Trast

alone (♦) or Control.. Drug formulations were injected in100 µL at a dose of 6 mg DOX or 3 mg Trast equivalents/kg body weight 4 times at 4-day intervals as indicated by the arrows. 17-AAG at a dose of 1mg/kg was given 2 h after NG formulation administration. Changes in tumor volume (**A**) are presented as a fold-ratio compared baseline for each animal on day 0 of treatment.  Values represent mean ± SEM. Kaplan–Meier analysis of the overall survival is shown (**B**). * and ** indicates a statistically significant difference between the indicated groups. *** indicates a statistically significant difference between Trast-NG/DOX and Trast alone.

In mice carrying BT-474 xenografts, treatment with Trast-NG/DOX alone led to a statistically significant ($p < 0.05$) tumor growth inhibition when compared to the control groups (p-value = 0.0159) (Fig. 4.7A). Sequential treatment with 17AAG led to further enhancement of anti-tumor activity of the targeted nanoformulation, as compared to the Trast-NG/DOX alone group. Statistical analysis confirmed that the potentiation of the tumor inhibitory effect of Trast-NG/DOX by 17AAG was highly significant ($p = 0.0005$). Remarkably, the Trast-NG/DOX + 17AAG treatment led to an actual reduction in tumor volume (shrinkage) compared to the tumor volume at the beginning of the treatment and is clearly observed at later time points (Fig. 4.7A). However, the p-values ($p = 0.293$) between the Trast-NG/Dox vs. Trast-NG/DOX + 17-AAG did not appear to reflect statistically significant differences at the given time point.
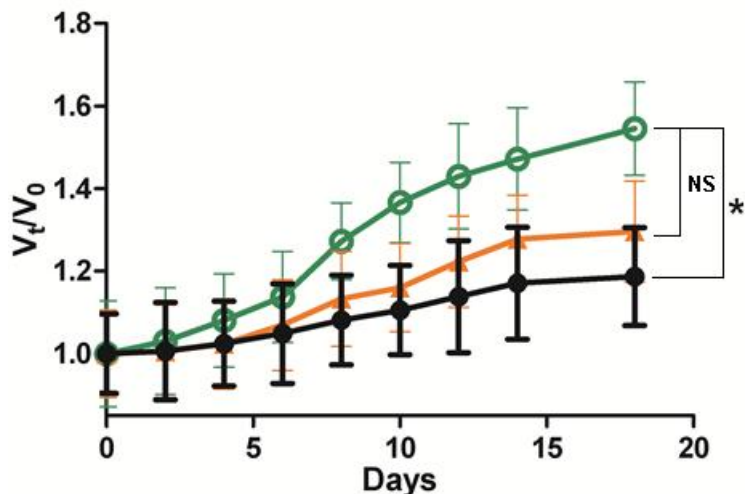
**Figure 4.8.** Relative changes in tumor volume after administration of ErbB2-targeted Trast-NG/DOX in ErbB2 - breast cancer mice model. Trast-NG/DOX (●) or IgG-NG/DOX (▲) or Control (Ø).

Compared to our results with the BT-474 xenograft model, mice bearing MCF-7 xenografts exhibited a small albeit statistically significant reduction in tumor volume upon treatment with Trast-NG/DOX ($p = 0.03$ vs. control); however, the difference in tumor volume between the IgG-NG/DOX and Trast-NG/DOX groups was not significant (p-value $= 0.397$) (Fig. 4.8). Comparative analysis of BT-474 vs. MCF-7 xenografts establish the advantage of Trast-based targeting against an ErbB2+ tumor, and clearly demonstrate the enhancement of the Trast-NG/DOX efficacy by sequential post-treatment with a small dose (which by itself has no measurable effect on tumor growth; not shown) of the HSP90 inhibitor 17AAG.

Kaplan-Meier analysis of survival was carried out among various treatment groups to assess the potential survival advantage of the treatment regimen combining 17AAG and DOX-loaded NGs in the BT-474 xenograft model. The median survival (in days), the associated Confidence Intervals and the p-values are shown in Table 4.2.

**Table 4.2:** Comparison of Median survival (in days), the associated Confidence Intervals and the p-values (with respect to 5% Dextrose control).

| Treatment Group | Median Survival (days) | Confidence Interval (days) (Lower limit – Upper limit) | p-values (vs. 5% Dextrose control | % Survival at censoring date (76 days) |
|---|---|---|---|---|
| Saline | 40 | 26 - NE | | 0 |
| Trast | 48 | 36 - NE | 0.1794 | 0 |
| IgG-NG/Dox | 52 | 26 - NE | 0.3221 | 0 |
| IgG-NG/Dox + 17-AAG | 40 | 32 - NE | 0.2827 | 0 |
| Trast-NG/Dox | NE | 68 - NE | 0.0032 | 56.8 |
| Trast-NG/Dox + 17-AAG | NE | NE - NE | <0.0001 | 88.8 |

NE - Estimate not reached

This analysis clearly shows that, at the end of the experiment (76 days; censoring date), the mice treated with Trast-NG/DOX + 17-AAG had a substantially longer survival (>88%) compared to the Trast-NG/DOX group (56.8%) (Fig. 4.7 B). No mice survived until the censoring date (0% survival) in all other treatment groups (5 % dextrose, Trast alone, IgG-NG/DOX and IgG-NG/DOX + 17-AAG) (Fig. 4.7 B). The data clearly indicates the superiority of Trast-NG/DOX treatment and suggests that combined treatment with HSP90 inhibitors can vastly improve survival times. Measurement of animal body weight during treatment with various regimens indicated that the treatment-related toxicities associated with the administration of Trast-NG/DOX or Trast-NG/DOX + 17-AAG were generally mild (<10%). In contrast, the

same dose of DOX or the free drug combination (DOX + 17-AAG) produced a considerable body weight loss (18-20%, $p < 0.05$) (Fig. 4.9).
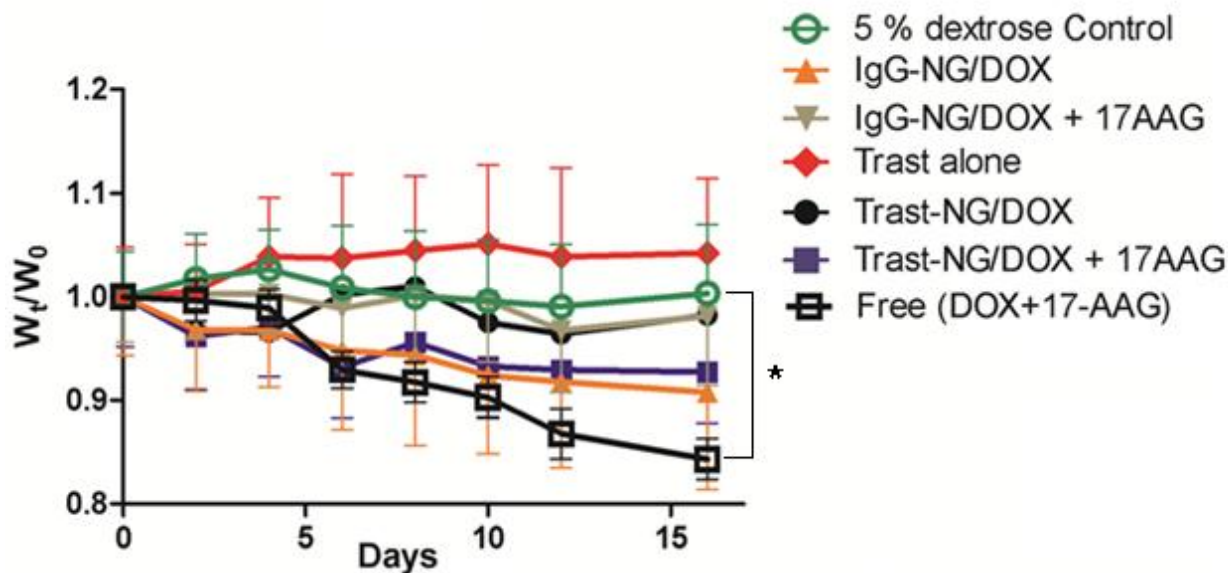


**Figure. 4.9**. Changes in body weight are presented as a fold-ratio compared baseline for each animal on day 0 of treatment. Values represent mean ± SEM.

.Light microscopic examination of the H&E-stained tissue sections of liver, lung, kidney, spleen and heart among the mice euthanized at the end of the experiment showed no histopathological changes in the organs of Trast-NG/DOX or Trast-NG/DOX + 17AAG treatment groups compared to the 5% dextrose control (data not shown), confirming the relatively low toxicities of the targeted NGs.

As further evidence of enhanced antitumor activity of Trast-NG/DOX or Trast-NG/DOX administered in combination with 17-AAG, we performed histopathological analyses of the tumors excised post-treatment (on 2nd day after last injection), using Ki-67 and Caspase-3 as markers for proliferation and apoptosis respectively.
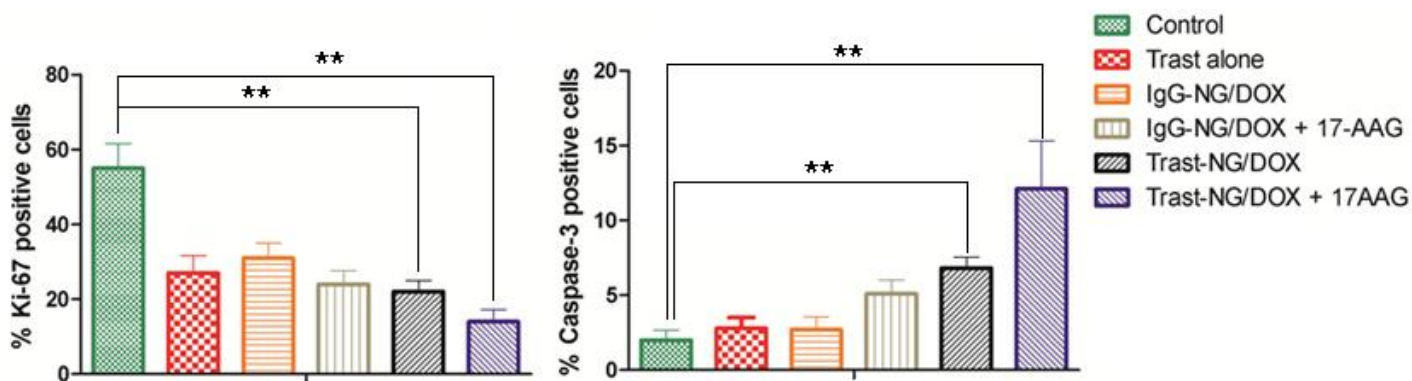
**Figure 4.10.** Administration of Trast-NG/DOX reduces the cell proliferation and promotes the apoptosis in BT-474 xenograft tumors and its activity is enhanced by 17AAG. Post-treatment tumor sections were stained for Ki-67 and caspase-3 and % Ki-67-positive (A) and % caspase-3-positive (B) cells in were calculated based on enumeration of at least 1000 cells. Tumors from three mice per group were analyzed. Data are presented as mean ± SD (n = 5 random microscopic fields for each tumor). The treatment groups are indicated.

As expected, treatment with Trast alone caused a significant reduction in Ki67+ cells (p = 0.0033) but little increase in caspase-3+ cells, consistent with the primarily cytostatic effects of Trast [25, 26](Fig. 4.10). Treatment with untargeted NG (IgG-NG/DOX) also reduced the percentage of Ki67+ cells (p = 0.0105) but with little impact on caspase-3+ cells (Fig. 4.10), consistent with a cytostatic mechanism of action of DOX [27, 28]. Notably, Trast-NG/DOX treatment led to a significant reduction in Ki67+ cells (p = 0.0023) and an increase in caspase-3+ cells (p = 0.0059), and combined treatment with 17AAG further increased the impact on both parameters (p = 0.0011 for Ki67+ cells and p = 0.0012 for caspase-3+ cells) (Fig. 4.10), indicating that the combination is superior and promotes substantial cytotoxicity in addition to a pronounced cytostatic effect. 17AAG also improved the pro-apoptotic efficacy of IgG-Trast/DOX but its impact on the anticancer activity of Trast-NG/DOX was substantially more pronounced, especially on caspase-3 activity

in tumors (Fig. 4.10). To mechanistically link the enhanced anti-tumor response of Trast-NG/DOX + 17-AAG combination with the effects of 17-AAG on ErbB2, we performed immunohistochemistry (IHC) and Western blot analyses of ErbB2 levels in tumors of mice treated with various regimens. Indeed, lower ErbB2 levels were seen in tumors of Trast-NG/DOX + 17-AAG treated mice (Fig. 4.11), correlating with the superior antitumor efficacy of a combination of HSP90 inhibitor and ErbB2-targeted drug-loaded NG strategy.
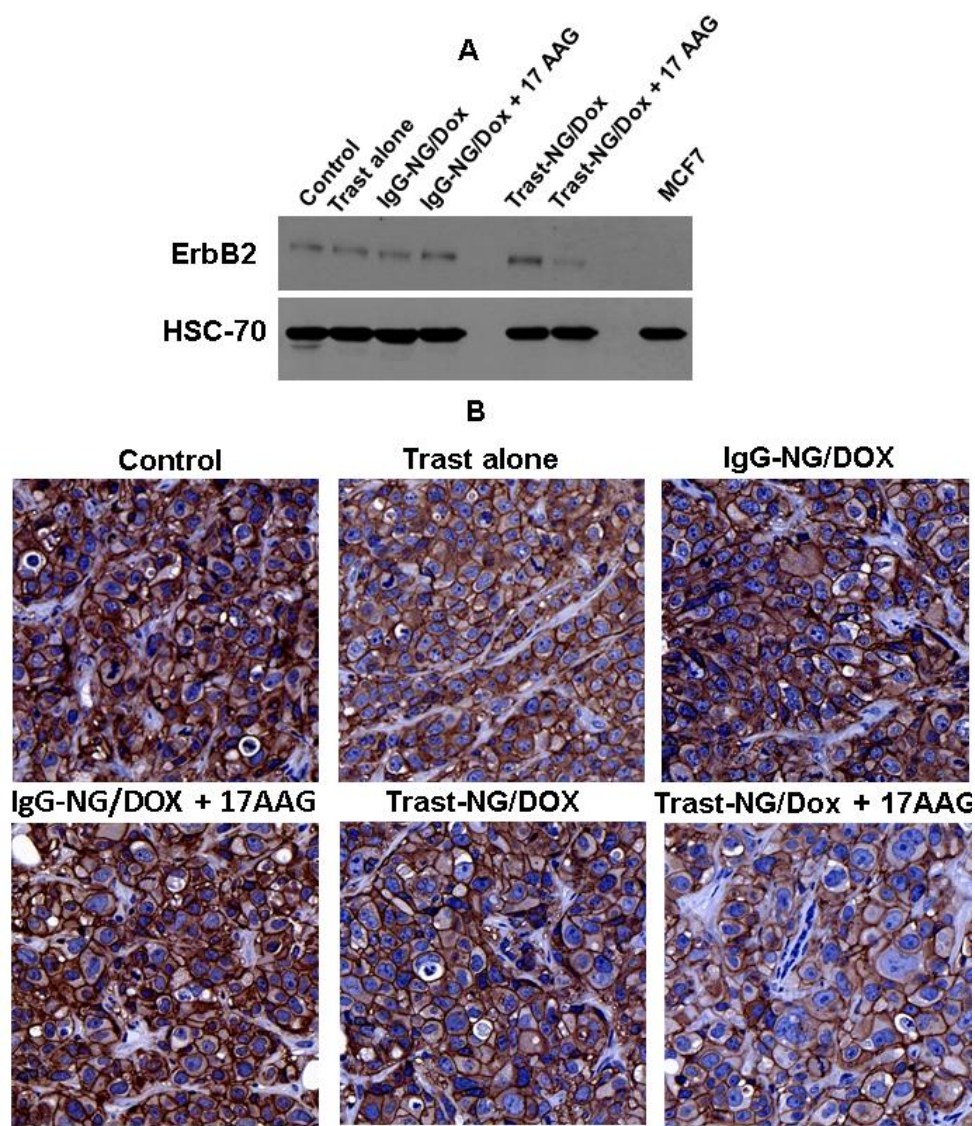
**Figure 4.11.** ErbB2 levels analyzed in the tumor sections using A) western blot and B) ErbB2-IHCs.

## 4.4. Discussion

Introduction of targeted cancer nanomedicines into clinical practice has provided substantial momentum for the development of similar approaches against a variety of cancers. Most nanosized therapeutic agents require internalization and traffic into acidic endocytic compartments to ensure the delivery of drug cargo into the appropriate subcellular target [29, 30]. While much consideration has been given to the polymer design and the nature of drug to ensure successful delivery, the importance of the endocytic traffic routes of cell surface receptors that provide the basis for targeting of nanocarriers has received little attention. Here, we develop a proof-of-principle strategy, using ErbB2 as a targeting receptor, to help facilitate the entry of a model nanogel-encapsulated therapeutic agent Doxorubicin into the lysosomes of breast cancer cells by tampering with the biological mechanism that retards the delivery of ErbB2 into lysosomes. Our studies demonstrate the feasibility of this novel approach in achieving superior *in vitro* targeting and *in vivo* anti-tumor efficacy in a xenograft breast cancer model. We suggest that this approach could significantly potentiate the efficacy of existing ErbB2-targeted nano-therapeutic agents against breast cancer. Furthermore, adaptation of this approach to facilitate the lysosomal delivery of other receptors currently used or considered for targeting cancer could substantially improve the efficacy of targeted cancer nanomedicines in general.

Our choice of ErbB2 receptor for our proof-of-principle studies was based on several key considerations: ErbB2 is the driver oncogene for over 20% of breast cancers and smaller subsets of many other malignancies [31-33]; ErbB2 is the target of an

clinically-approved Trastuzumab-emtansine conjugate, Kadcyla®, whose conjugated drug must be released to allow access to its cytosolic target [34]; ErbB2 is a prototype receptor that is biologically impaired in lysosomal entry [17, 18, 33]; studies by us and others have demonstrated that tampering with the function of a major biological partner of ErbB2 and key to its inability to enter the lysosome, the molecular chaperone HSP90, promotes rapid lysosomal sorting and eventual degradation of ErbB2 [17, 18, 33]. ErbB2 is constitutively associated with HSP90, and multiple lines of investigation have demonstrated that HSP90 function is required for ErbB2 stability and ErbB2-driven oncogenesis [35-37]. Availability of specific HSP90 inhibitors has allowed a dissection of the mechanisms of ErbB2 instability upon HSP90 inhibition, and have revealed roles for lysosomal degradation [17-22]. Careful cell biological studies have however revealed the lysosomal targeting of ErbB2 upon HSP90 inhibition to be a relatively early event, and one likely to be important for the rapid downregulation of ErbB2 from the surface of HSP90 inhibitor-treated cancer cells [17-22]. In contrast, lysosomal delivery of ErbB2 upon the treatment of ErbB2+ cancer cell lines with Trast is distinctly slower and incomplete [17, 19], apparently due to the maintenance of a recycling itinerary of Trast-bound ErbB2 [38]. Our previous studies demonstrated that low concentrations of an HSP90 inhibitor, 17AAG, could however promote Trast-induced lysosomal delivery of ErbB2 and produce synergistic anti-tumor killing *in vitro* [19]. Indeed, Trast + 17AAG exhibit enhanced antitumor activity *in vivo* [19]. However, 17AAG and other HSP90 inhibitors have been slower to be adopted clinically as they produce significant toxicity[39-44]. The focus of such studies has been on the using of maximally-tolerated doses of HSP90 inhibitors, even when these are combined with other therapeutic

agents[40-43, 45-49]. Our studies help establish a new paradigm in which HSP90 inhibitors at sub-therapeutic doses can substantially improve the efficacy of a nanoformulated therapeutic agent without significant added toxicity.

Our studies provide support for a potentially novel use of HSP90 inhibitors to facilitate the endolysosomal delivery of ADCs or antibody-conjugated drug nanocarriers (ANPs) that rely on targeting receptors that are HSP90 clients. A number of such targets have been identified, including the mutant EGFR in non-small cell lung cancer [50-53], a receptor we have shown to constitutively enter the endocytic recycling pathway [3, 53]. Similarly, glioblastoma-associated EGFR-vIII which lacks the normal EGFR's ability to undergo ligand-triggered lysosomal traffic [54]. Recent studies also suggest that overexpressed EGFR in gastric cancer cells is efficiently targeted by HSP90 inhibitors for degradation [55]. Thus, our approach using low doses of an HSP90 inhibitor is likely to be applicable to other malignancies as ADCs or ANPs against other HSP90-dependent receptors are developed for clinical use. While our studies relied on 17AAG as an HSP90 inhibitor, a number of other HSP90 inhibitors are being evaluated in clinical trials, including ones with oral bioavailability [42, 45, 46], and testing of such drugs in the context of ANPs is highly desirable. Since HSP90 inhibition eventually promotes the degradation of receptors such as ErbB2 [19, 35, 56, 57], the scheduling of the ANP and HSP90 inhibitor is likely to be of key importance. In our studies, we considered this issue upfront and demonstrated the ability of HSP90 inhibition to facilitate the internalization and lysosomal targeting of Trast-NG *in vitro* (Fig 3). Accordingly, our preclinical therapy was designed to administer the HSP90 inhibitor 17AAG 2h hours after the nano-therapy, allowing time for the latter to reach its target. It remains possible that further studies to

optimize the scheduling of the HSP90 inhibitor relative to the ANP will help improve the efficacy of regimens targeting ErbB2 or other HSP90 client receptors.

Our studies also provide evidence that sub-therapeutic doses of an HSP90 inhibitor (1 mg/Kg 17AAG in our studies, which has little efficacy against BT-474 xenografts; unpublished data), dramatically enhances tumor killing by DOX-loaded ErbB2-targeted NGs (Fig. 5A). Such a combination led to not just inhibition of xenograft tumor growth but in fact a significant shrinkage of tumor masses from their pre-treatment volume (Fig 5A). This was associated with a significant shift from a merely cytostatic to a significantly cytotoxic effect on tumors as demonstrated by Ki67 and caspase-3 staining of tumors among surviving mice at the end of therapy. Not surprisingly, combination with low dose 17AAG markedly improved the survival of tumor-bearing mice (Fig. 5B). We must point out that DOX was used in our proof-of-principle studies as the polymer design we have previously established allows efficient loading of this clinically-used chemotherapeutic agent [23]. However, DOX enhances cardiotoxicity associated with ErbB2-targeted antibody therapeutics, including Trastuzumab [58-60], and as such the approach will need modifications to incorporate more appropriate agents for ErbB2+ cancers. Such studies are currently ongoing in our laboratories. The current nanocarrier design should however be applicable to other tumors where a targeting antibody or other moiety is available.

Based on our studies, we suggest that the endocytic traffic itinerary of receptors selected for targeting of ADCs and ANPs should receive careful consideration. An understanding of mechanisms that may impair the endolysomal traffic of a targeted receptor (as with ErbB2) may help overcome an efficacy barrier on newer agents in

development and potentially improve the efficacy of agents already in the clinic. In this regard, the potential combination of HSP90 inhibitors that are already in clinical trials together with the ErbB2-targeted TDM-1 will be of considerable interest and is under study in our group. A recently FDA-approved ADC, Brentuximab-Vedotin, targets CD30 receptor in Hodgkin's lymphomas [61, 62] which requires lysosomal traffic for its efficacy [63], although the mechanisms of lysosomal trafficking of CD30-bound ADC remains unknown.

It is of interest that HSP90 is also thought to regulate the activity of Rab GTPase-dependent endocytic recycling by its association with a Rab Guanine Nucleotide Displacement Inhibitor (GDI) [64, 65], and HSP90 inhibitors could potentially help attenuate Rab-dependent recycling of transmembrane receptors that are not direct HSP90 clients to enhance ADC or ANP delivery inside the tumor cell. Other factors that may control trafficking of oncogenic cell-surface receptors such as the non-receptor tyrosine kinase c-Src, endocytic adaptor proteins, E3 ubiquitin ligases, deubiquitinating enzymes, RAB GTPases, ESCRT proteins and EHD family proteins [66, 67],[68, 69] may offer future opportunities to develop facilitators of ADC and ANP traffic to endolysomal compartments as approaches of therapeutic potentiation.

**4.5. Conclusion.** Our study demonstrates the potential of therapeutically exploiting the vulnerabilities in cancer cell-specific trafficking behavior of receptors used to selectively deliver nanoencapsulated therapeutic agents, and highlights the importance of identifying such vulnerabilities in targeting receptors in order to fully realize the potential of ADCs and targeted nanomedicines in cancer and other diseases.

## 4.6. References

1. Mehra NK, Mishra V, Jain NK. Receptor-based targeting of therapeutics. Ther Deliv 2013;4(3):369-94.

2. Mathew J, Perez EA. Trastuzumab emtansine in human epidermal growth factor receptor 2- positive breast cancer: a review. Curr Opin Oncol 2011;23(6):594-600.

3. Chung BM, Tom E, Zutshi N, Bielecki TA, Band V, Band H. Nexus of signaling and endocytosis in oncogenesis driven by non-small cell lung cancer-associated epidermal growth factor receptor mutants. World J Clin Oncol 2014;5(5):806.

4. Molfetta R, Quatrini L, Gasparrini F, Zitti B, Santoni A, Paolini R. Regulation of Fc receptor endocytic trafficking by ubiquitination. Front Immunol 2014;5.

5. Piper RC, Lehner PJ. Endosomal transport via ubiquitination. Trends Cell Biol 2011;21(11):647-55.

6. Sorkin A, Goh LK. Endocytosis and intracellular trafficking of ErbBs. Exp Cell Res 2009;315(4):683-96.

7. Marmor MD, Yarden Y. Role of protein ubiquitylation in regulating endocytosis of receptor tyrosine kinases. Oncogene 2004;23(11):2057-70.

8. Wright MH, Berlin I, Nash PD. Regulation of endocytic sorting by ESCRT–DUB-mediated deubiquitination. Cell Biochem Biophys 2011;60(1-2):39-46.

9. Tu C, Ahmad G, Mohapatra B, Bhattacharyya S, Ortega-Cava C, Chung BM, et al. ESCRT proteins: Double-edged regulators of cellular signaling. Bioarchitecture 2011;1(1):45-48.

10. Raiborg C, Stenmark H. The ESCRT machinery in endosomal sorting of ubiquitylated membrane proteins. Nature 2009;458(7237):445-52.

11. Mellman I, Yarden Y. Endocytosis and cancer. Cold Spring Harb Perspect Biol 2013;5(12):a016949.

12. Hendriks BS, Klinz SG, Reynolds JG, Espelin CW, Gaddy DF, Wickham TJ. Impact of tumor HER2/ERBB2 expression level on HER2-targeted liposomal doxorubicin-mediated drug delivery: multiple low-affinity interactions lead to a threshold effect. Mol Cancer Ther 2013;12(9):1816-28.

13. Yousefpour P, Atyabi F, Farahani EV, Sakhtianchi R, Dinarvand R. Polyanionic carbohydrate doxorubicin-dextran nanocomplex as a delivery system for anticancer drugs: in vitro analysis and evaluations. Int J Nanomedicine 2011;6:1487-96.

14. Inoue S, Ding H, Portilla-Arias J, Hu J, Konda B, Fujita M, et al. Polymalic Acid–Based Nanobiopolymer Provides Efficient Systemic Breast Cancer Treatment by Inhibiting both HER2/neu Receptor Synthesis and Activity. Cancer Res 2011;71(4):1454-64.

15. Miyano T, Wijagkanalan W, Kawakami S, Yamashita F, Hashida M. Anionic Amino Acid Dendrimer− Trastuzumab Conjugates for Specific Internalization in HER2-Positive Cancer Cells. Mol Pharm 2010;7(4):1318-27.

16. Baulida J, Kraus MH, Alimandi M, Di Fiore PP, Carpenter G. All ErbB receptors other than the epidermal growth factor receptor are endocytosis impaired. J Biol Chem 1996;271(9):5251-57.

17. Austin CD, De Mazière AM, Pisacane PI, van Dijk SM, Eigenbrot C, Sliwkowski MX, et al. Endocytosis and sorting of ErbB2 and the site of action of cancer therapeutics trastuzumab and geldanamycin. Mol Biol Cell 2004;15(12):5268-82.

18. Cortese K, Howes MT, Lundmark R, Tagliatti E, Bagnato P, Petrelli A, et al. The HSP90 inhibitor geldanamycin perturbs endosomal structure and drives recycling ErbB2 and transferrin to modified MVBs/lysosomal compartments. Mol Biol Cell 2013;24(2):129-44.

19. Raja SM, Clubb RJ, Bhattacharyya M, Dimri M, Cheng H, Pan W, et al. A combination of trastuzumab and 17-AAG induces enhanced ubiquitinylation and lysosomal pathway-dependent ErbB2 degradation and cytotoxicity in ErbB2-overexpressing breast cancer cells. Cancer Biol Ther 2008;7(10):1630-40.

20. Marx C, Held JM, Gibson BW, Benz CC. ErbB2 trafficking and degradation associated with K48 and K63 polyubiquitination. Cancer Res 2010;70(9):3709-17.

21. Bailey TA, Luan H, Tom E, Bielecki TA, Mohapatra B, Ahmad G, et al. A kinase inhibitor screen reveals protein kinase c-dependent endocytic recycling of erbb2 in breast cancer cells. J Biol Chem 2014;289(44):30443-58.

22. Lerdrup M, Hommelgaard AM, Grandal M, van Deurs B. Geldanamycin stimulates internalization of ErbB2 in a proteasome-dependent way. J Cell Sci 2006;119(1):85-95.

23. Kim JO, Nukolova NV, Oberoi HS, Kabanov AV, Bronich TK. Block ionomer complex micelles with cross-linked cores for drug delivery. Polym Sci Ser A 2009;51(6):708-18.

24. Kim JO, Kabanov AV, Bronich TK. Polymer micelles with cross-linked polyanion core for delivery of a cationic drug doxorubicin. J Control Release 2009;138(3):197-204.

25. Raja SM, Clubb RJ, Ortega-Cava C, Williams SH, Bailey TA, Duan L, et al. Anticancer activity of Celastrol in combination with ErbB2-targeted therapeutics for treatment of ErbB2-overexpressing breast cancers. Cancer Biol Ther 2011;11(2):263-76.

26. Band V, Zajchowski D, Swisshelm K, Trask D, Kulesa V, Cohen C, et al. Tumor progression in four mammary epithelial cell lines derived from the same patient. Cancer Res 1990;50(22):7351-57.

27. Baselga J, Albanell J, Molina MA, Arribas J. Mechanism of action of trastuzumab and scientific update. Semin Oncol 2001. Elsevier. p 4-11.

28. Albanell J, Codony J, Rovira A, Mellado B, Gascón P. Mechanism of action of anti-HER2 monoclonal antibodies: scientific update on trastuzumab and 2C4. New Trends in Cancer for the 21st Century: Springer; 2003. p 253-68.

29. Fornari FA, Jarvis WD, Grant S, Orr MS, Randolph JK, White FK, et al. Growth arrest and non-apoptotic cell death associated with the suppression of c-myc expression in MCF-7 breast tumor cells following acute exposure to doxorubicin. Biochem Pharmacol 1996;51(7):931-40.

30. Konopa J. G 2 block induced by DNA crosslinking agents and its possible consequences. Biochem Pharmacol 1988;37(12):2303-09.

31. Sahay G, Alakhova DY, Kabanov AV. Endocytosis of nanomedicines. J Control Release 2010;145(3):182-95.

32. Sahay G, Querbes W, Alabi C, Eltoukhy A, Sarkar S, Zurenko C, et al. Efficiency of siRNA delivery by lipid nanoparticles is limited by endocytic recycling. Nat Biotechnol 2013;31(7):653-58.

33. Perou CM, Sørlie T, Eisen MB, van de Rijn M, Jeffrey SS, Rees CA, et al. Molecular portraits of human breast tumours. Nature 2000;406(6797):747-52.

34. Sorlie T, Perou CM, Tibshirani R, Aas T, Geisler S, Johnsen H, et al. Gene expression patterns of breast carcinomas distinguish tumor subclasses with clinical implications. Proc Natl Acad Sci USA 2001;98(19):10869-74.

35. Roepstorff K, Grøvdal L, Grandal M, Lerdrup M, van Deurs B. Endocytic downregulation of ErbB receptors: mechanisms and relevance in cancer. Histochem Cell Biol 2008;129(5):563-78.

36. Phillips GDL, Li G, Dugger DL, Crocker LM, Parsons KL, Mai E, et al. Targeting HER2-positive breast cancer with trastuzumab-DM1, an antibody–cytotoxic drug conjugate. Cancer Res 2008;68(22):9280-90.

37. Zhou P, Fernandes N, Dodge IL, Reddi AL, Rao N, Safran H, et al. ErbB2 degradation mediated by the co-chaperone protein CHIP. J Biol Chem 2003;278(16):13829-37.

38. Xu W, Mimnaugh EG, Kim J-S, Trepel JB, Neckers LM. Hsp90, not Grp94, regulates the intracellular trafficking and stability of nascent ErbB2. Cell Stress Chaperones 2002;7(1):91.

39. Citri A, Kochupurakkal BS, Yarden Y. The achilles heel of ErbB-2/HER2: regulation by the Hsp90 chaperone machine and potential for pharmacological intervention. Cell Cycle 2004;3(1):50-59.

40. LoRusso PM, Weiss D, Guardino E, Girish S, Sliwkowski MX. Trastuzumab emtansine: a unique antibody-drug conjugate in development for human epidermal growth factor receptor 2–positive cancer. Clin Cancer Res 2011;17(20):6437-47.

41. Arteaga CL. Why is this effective HSP90 inhibitor not being developed in HER2+ breast cancer? Clin Cancer Res 2011;17(15):4919-21.

42. Modi S, Stopeck A, Linden H, Solit D, Chandarlapaty S, Rosen N, et al. HSP90 inhibition is effective in breast cancer: a phase II trial of tanespimycin (17-AAG) plus trastuzumab in patients with HER2-positive metastatic breast cancer progressing on trastuzumab. Clinl Cancer Res 2011;17(15):5132-39.

43. Johnson ML, Helena AY, Hart EM, Weitner BB, Rademaker AW, Patel JD, et al. Phase I/II Study of HSP90 Inhibitor AUY922 and Erlotinib for EGFR-Mutant Lung Cancer With Acquired Resistance to Epidermal Growth Factor Receptor Tyrosine Kinase Inhibitors. J Clin Oncol 2015:JCO. 2014.59. 7328.

44. Spreafico A, Delord J, De Mattos-Arruda L, Berge Y, Rodon J, Cottura E, et al. A first-in-human phase I, dose-escalation, multicentre study of HSP990 administered orally in adult patients with advanced solid malignancies. Br J Cancer 2015.

45. Modi S, Saura C, Henderson C, Lin NU, Mahtani R, Goddard J, et al. A multicenter trial evaluating retaspimycin HCL (IPI-504) plus trastuzumab in patients with advanced or metastatic HER2-positive breast cancer. Breast Cancer Res Treat 2013;139(1):107-13.

46. Pacey S, Banerj U, Judson I, Workman P. Hsp90 inhibitors in the clinic. Molecular Chaperones in Health and Disease: Springer; 2006. p 331-58.

47. Infante JR, Weiss GJ, Jones S, Tibes R, Bauer TM, Bendell JC, et al. Phase I dose-escalation studies of SNX-5422, an orally bioavailable heat shock protein 90 inhibitor, in patients with refractory solid tumours. Eur J Cancer 2014;50(17):2897-904.

48. Saif MW, Takimoto C, Mita M, Banerji U, Lamanna N, Castro J, et al. A phase 1, dose-escalation, pharmacokinetic and pharmacodynamic study of BIIB021 administered orally in patients with advanced solid tumors. Clin Cancer Res 2014;20(2):445-55.

49. Nowakowski GS, McCollum AK, Ames MM, Mandrekar SJ, Reid JM, Adjei AA, et al. A phase I trial of twice-weekly 17-allylamino-demethoxy-geldanamycin in patients with advanced cancer. Clin Cancer Res 2006;12(20):6087-93.

50. Heath EI, Hillman DW, Vaishampayan U, Sheng S, Sarkar F, Harper F, et al. A phase II trial of 17-allylamino-17-demethoxygeldanamycin in patients with hormone-refractory metastatic prostate cancer. Clin Cancer Res 2008;14(23):7940-46.

51. Oh WK, Galsky MD, Stadler WM, Srinivas S, Chu F, Bubley G, et al. Multicenter phase II trial of the heat shock protein 90 inhibitor, retaspimycin hydrochloride (IPI-504), in patients with castration-resistant prostate cancer. Urology 2011;78(3):626-30.

52. Garon EB, Finn RS, Hamidi H, Dering J, Pitts S, Kamranpour N, et al. The HSP90 inhibitor NVP-AUY922 potently inhibits non–small cell lung cancer growth. Mol Cancer Ther 2013;12(6):890-900.

53. Shimamura T, Lowell AM, Engelman JA, Shapiro GI. Epidermal growth factor receptors harboring kinase domain mutations associate with the heat shock protein 90 chaperone and are destabilized following exposure to geldanamycins. Cancer Res 2005;65(14):6401-08.

54. Yang J, Mani SA, Weinberg RA. Exploring a new twist on tumor metastasis. Cancer Res 2006;66(9):4549-52.

55. Chung BM, Raja SM, Clubb RJ, Tu C, George M, Band V, et al. Aberrant trafficking of NSCLC-associated EGFR mutants through the endocytic recycling pathway promotes interaction with Src@. BMC Cell Biol 2009;10(1):84.

56. Grandal MV, Zandi R, Pedersen MW, Willumsen BM, van Deurs B, Poulsen HS. EGFRvIII escapes down-regulation due to impaired internalization and sorting to lysosomes. Carcinogenesis 2007;28(7):1408-17.

57. Liu H, Lu J, Hua Y, Zhang P, Liang Z, Ruan L, et al. Targeting heat-shock protein 90 with ganetespib for molecularly targeted therapy of gastric cancer. Cell Death Dis 2015;6(1):e1595.

58. Solit DB, Zheng FF, Drobnjak M, Münster PN, Higgins B, Verbel D, et al. 17-Allylamino-17-demethoxygeldanamycin induces the degradation of androgen receptor and HER-2/neu and inhibits the growth of prostate cancer xenografts. Clin Cancer Res 2002;8(5):986-93.

59. Tikhomirov O, Carpenter G. Geldanamycin induces ErbB-2 degradation by proteolytic fragmentation. J Biol Chem 2000;275(34):26625-31.

60. Gianni L, Salvatorelli E, Minotti G. Anthracycline cardiotoxicity in breast cancer patients: synergism with trastuzumab and taxanes. Cardiovasc Toxicol 2007;7(2):67-71.

61. Feldman AM, Lorell BH, Reis SE. Trastuzumab in the Treatment of Metastatic Breast Cancer Anticancer Therapy Versus Cardiotoxicity. Circulation 2000;102(3):272-74.

62. Seidman A, Hudis C, Pierri MK, Shak S, Paton V, Ashby M, et al. Cardiac dysfunction in the trastuzumab clinical trials experience. J Clin Oncol 2002;20(5):1215-21.

63. van de Donk NW, Dhimolea E. Brentuximab vedotin. 2012. Taylor & Francis. p 458-65.

64. Muta H, Podack ER. CD30: from basic research to cancer therapy. Immunol Res 2013;57(1-3):151-58.

65. Sutherland MSK, Sanderson RJ, Gordon KA, Andreyka J, Cerveny CG, Yu C, et al. Lysosomal trafficking and cysteine protease metabolism confer target-specific cytotoxicity by peptide-linked anti-CD30-auristatin conjugates. J Biol Chem 2006;281(15):10540-47.

66. Sakisaka T, Meerlo T, Matteson J, Plutner H, Balch WE. Rab-αGDI activity is regulated by a Hsp90 chaperone complex. EMBO J 2002;21(22):6125-35.

67. Chen CY, Sakisaka T, Balch WE. Use of Hsp90 Inhibitors to Disrupt GDI-Dependent Rab Recycling. Methods Enzymol 2005;403:339-47.

68. Sandilands E, Frame MC. Endosomal trafficking of Src tyrosine kinase. Trends Cell Biol 2008;18(7):322-29.

69. Reiter E, Lefkowitz RJ. GRKs and β-arrestins: roles in receptor silencing, trafficking and signaling. Trends Endocrinol Metab 2006;17(4):159-65.

70. George M, Ying G, Rainey MA, Solomon A, Parikh PT, Gao Q, et al. Shared as well as distinct roles of EHD proteins revealed by biochemical and functional comparisons in mammalian cells and C. elegans. BMC Cell Biol 2007;8(1):3.

71. Naslavsky N, Caplan S. EHD proteins: key conductors of endocytic transport. Trends Cell Biol 2011;21(2):122-31.

**CHAPTER V**

**POLYPEPTIDE-BASED NANOGELS CO-ENCAPSULATING A SYNERGISTIC COMBINATION OF DOXORUBICIN WITH 17-AAG SHOW POTENT ANTI-TUMOR ACTIVITY IN ErbB2-DRIVEN BREAST CANCER MODELS[2]**

**5.1. Introduction:**

The receptor tyrosine kinase ErbB2 (also known as Her2/Neu) is overexpressed in 20-25 % of breast cancer patients [1-5]. Oncogenic ErbB2 signaling results in hyperproliferation of the cells, increases cell survival and promotes invasion and metastasis [6, 7]. The anti-ErbB2 monoclonal antibody, Trastuzumab (Herceptin™)[8], in combination with chemotherapy is currently used for treatment of ErbB2-overexpressing breast cancers, following surgical removal of the primary tumor [5, 8, 9]. However, many patients either do not respond to Trastuzumab-based therapies or relapse during the course of the treatment, necessitating the development of newer therapeutics [8]. ErbB2 depends on heat shock protein 90 (HSP90) association for stability and, among client proteins of the chaperone, ErbB2 is perhaps the most sensitive to HSP90 inhibition [10]. HSP90 inhibitors (such as the ansamycin antibiotic, Geldanamycin and related molecules like 17-AAG) have shown significant promise in pre-clinical models of ErbB2-driven breast cancer as well as initial phase I/II clinical trials [11-13]. The mechanism involves attenuation of oncogenic signaling via degradation of ErbB2 as well as other critical downstream signaling mediators in the pathway, which include phospho-Akt and c-Raf.

---

[2] Reproduced with permission from Desale SS, et al. "Polypeptide-based nanogels co-encapsulating a synergistic combination of doxorubicin with 17-AAG show potent anti-tumor activity in ErbB2-driven breast cancer models." J Control Release 208 (2015): 59-66.Copyright 2015 Elsevier B.V.

In a cancer cell, these signaling molecules are strongly dependent on HSP90 to maintain their stability [14-16]. Since numerous oncoproteins have been identified as HSP90 clients, inhibition of Hsp90 functions affects multiple oncogenic substrates simultaneously and represents an appealing molecular target for combination drug therapy [17]. In a recently completed phase II study of 17-AAG and trastuzumab, an overall clinical benefit (including stable disease) was seen in 57% of the patients with ErbB2-positive metastatic breast cancer progressing on trastuzumab [13]. It has also been reported that inhibition of Hsp90 with 17-AAG sensitizes different cancer cell lines to DNA damage response mediated cellular senescence [18]. It was shown that the 17AAG pre-treatment followed by doxorubicin (DOX) treatment exhibited senescence-like characteristics such as increased nucleus to cytoplasm ratio and cell cycle arrest in the pre-clinical evaluation [18-20]. These data suggest that combination chemotherapy using co-administration of 17-AAG with a DOX-based regimen can be a potential therapy for cancer especially ErbB2-positive breast cancer [18].

Combining drugs in one delivery carrier is a well-suited strategy for controlling the pharmacokinetics and co-delivery of the desired drug ratio in vivo [21, 22]. The drug loading and structure of such carriers can be tuned to control the drug release rates, maximize the therapeutic potency and minimize drug-associated toxicities. However, co-incorporation of drug molecules with different physicochemical properties, such as hydrophilic DOX and hydrophobic 17-AAG, has been challenging. We have recently described biodegradable polymeric nanogels (NGs) based on poly(ethylene glycol)-*b*-poly(L-glutamic acid) (PEG-*b*-PGlu) with pendant phenylalnine functionalities [23]. Such NGs have multiple hydrophobic domains formed by phenylalanine moieties within

the cross-linked PGlu polyion cores surrounded by a hydrophilic PEG shell. Herein, we explored these novel NGs for co-encapsulation of 17-AAG and DOX. The potency of this co-delivery system was evaluated in a panel of human breast cancer lines and in an ErbB2-driven orthotopic xenograft model. We demonstrate that NGs-based co-delivery of synergistic combination of 17-AAG and DOX exhibited superior antitumor efficacy compared to a combination of free drugs. The implications of our results may support a new platform for delivery of combinations of HSP90 inhibitors with cytotoxic agents for treatment of various types of cancers.

## 5.2. Materials and Methods

### 5.2.1 Materials

Poly(ethylene glycol)-*b*-poly(L-glutamic acid) (PEG-*b*-PGlu) diblock copolymer ($M_w/M_n$ = 1.38, MW 27,500) was purchased from Alamanda Polymers, Inc (Madison, AL, USA). The block lengths were 114 and 150 repeating units for PEG and PGlu, respectively. L-phenylalanine methyl ester (PME), calcium chloride, cystamine, 1-(3-dimethylaminopropyl)-3-ethylcarbodiimide hydrochloride (EDC) *and* ethylenediaminetetraacetic acid (EDTA) were obtained from Sigma-Aldrich (St Louis, MO). Doxorubicin hydrochloride was kindly provided by Dong-A Pharmaceutical Company, South Korea. Fetal bovine serum (FBS) (both dialyzed and heat inactivated), DMEM and RPMI 1640 media and Lysotracker$^{TM}$ (green) were purchased from Invitrogen Inc (Carlsbad, CA). Bovine serum albumin (BSA) and NUNC$^{TM}$ chambered glass coverslips for live cell imaging were purchased from Fisher Scientific (Waltham, MA). MTT reagent (3-(4,5-Dimethylthiazol-2-yl)-2,5-diphenyltetrazolium bromide) was purchased from Research Products International (Prospect, IL). All other chemicals were

of reagent grade and used without further purification. The following primary antibodies were used in this study: anti-human-ErbB2 mouse monoclonal (ErbB2) raised against the C-terminal amino acid residues (1242-1255), used for Western blotting studies, were purchased from BD Pharmingen™ (San Diego, CA); for flow cytometry and immunofluorescence studies, the goat anti-human-ErbB2 polyclonal antibody (AF1129) was from R&D Systems (Minneapolis, MN); the mouse monoclonal anti-phosphotyrosine (anti-pY; 4G10) was kindly provided by Dr. Brian Druker (Oregon Health & Science University, Portland, OR); the mouse monoclonal anti-Hsc70 antibody was from Santa Cruz Biotechnology Inc. (Santa Cruz, CA).

## 5.2.2 Synthesis of nanogels

The hydrophobic phenylalanine functionalities were introduced in PEG-*b*-PGA copolymer by polymer-analogous modification of the PGA segment with PME using carbodiimide chemistry as we previously described [23]. The degree of PME grafting in resulting PEG-*b*-PPGlu copolymer was 30% as determined by 1H-NMR analysis. Nanogels were prepared as described earlier [23] by using block ionomer complex PEG-*b*-PPGA/$Ca^{2+}$ at a molar ratio of $[Ca^{2+}]/[COO^-] = 1.5$ with further cross-linking by cystamine and EDC ($[EDC]/[cystamine] = 2$; $[COOH]/[EDC] = 5$) at r.t., overnight. Byproducts of the cross-linking reaction and metal ions were removed by exhaustive dialysis of the reaction mixtures, first against 0.5% aqueous ammonia with EDTA and then against distilled water.

## 5.2.3 Drug loading

Dox-encapsulated nanogels (DOX/NG) were prepared by adding Dox to an aqueous dispersion of NGs at the feeding ratio of R= $[DOX]/[COO^-] = 0.25$, for 24h at pH 7.0.

Unbound Dox was separated by centrifugal filtration on drug-pretreated Amicon YM-30 filters. 17-AAG was solubilized into the hydrophobic domains of NGs using an extraction method [24]. According to this method, a thin film of 17-AAG (prepared by evaporation of a methanol solution of 17-AAG) was incubated with aqueous dispersion of NGs or DOX/NG (24 h, r.t.). Unincorporated 17-AAG was removed by filtration. Dox was assayed by UV spectrophotometry ($\varepsilon_{488} = 11,500$ $M^{-1}$ $cm^{-1}$ in water) [25]. The amount of 17-AAG incorporated into NGs was quantified via reverse-phase HPLC using an Agilent Eclipse XDB C18 5 μm column (250 mm × 4.6mm) and Agilent 1200 HPLC system. Mobile phase was composed of 10 mM ammonium acetate containing 0.1% (v/v) acetic acid (pH 4.8) and 50% acetonitrile and was applied at a flow rate of 1 mL/min. Detection wavelength was 334 nm. Drug loading capacity was calculated as percent ratio of mass of incorporated drug to total mass of drug-loaded NGs without water.

### 5.2.4 Physicochemical characterization of the NGs.

The effective hydrodynamic diameter ($D_{eff}$) and ζ-potential of NGs were determined using a Malvern Zetasizer (Malvern Instruments Ltd., Malvern, UK). All measurements were performed in automatic mode at 25°C. Software provided by the manufacturer was used to calculate size, polydispersity indices and ζ-potential of NGs. All measurements were performed at least in triplicate to calculate the mean values ± SD.

### 5.2.5 Drug release studies.

Drug release from NGs was examined in PBS (pH 7.4, 0.14M NaCl) by dialysis method using a membrane with 3500 Da cutoff. The concentrations of 17-AAG and Dox released were determined by HPLC and UV spectrophotometry, respectively, and expressed as a percentage of the total 17-AAG or Dox available vs. time.

**5.2.6 Cell culture.**

The ErbB2-overexpressing cell lines used in this study were 21MT-1 and BT-474. MCF-7 cells were used as a representative ErbB2-low cell line for comparison. The ErbB2-overexpressing breast cancer cell line 21MT-1 was established by Band et al [26] and has been previously described. BT-474 and MCF-7 cell lines were obtained from the American Type Culture Collection (ATCC). All cell lines were maintained as previously described [27, 28].

**5.2.7 Confocal microscopy on live cells.**

Cellular uptake and localization studies of (DOX+17-AAG)/NG were conducted using live cell confocal microscope (Carl Zeiss LSM 510 Meta, Peabody, MA). 21MT-1 human breast cancer cells ($1\times10^6$/chamber) were grown in live cell chambers (Fischer Scientific, Waltham, MA) for two days ($37^o$C, 5% $CO_2$) and exposed to (DOX+17-AAG)/NG for 30 min followed by incubation with Lysotracker Green for 5 min. After exposure cells were washed with PBS and kept in complete media prior to visualization by live cell confocal imaging (Carl Zeiss LSM 510 Meta, Peabody, MA).

**5.2.8 ErbB2 degradation.**

ErbB2-overexpressing cells plated in 6-well plates were treated with free 17-AAG or the drug-loaded NG formulations, following which the samples were lysed using RIPA lysis buffer, supplemented with protease and phosphatase inhibitors. Analysis of the kinetics and dose-response of ErbB2 degradation induced by free 17-AAG or 17-AAG/NG formulations were done using SDS-PAGE/WB [27, 28].

**5.2.9 In vitro cytotoxicity studies.**

Cytotoxicity of drug-loaded NGs was assessed in 21MT-1, BT-474, and MCF-7 cells by a standard MTT assay [29]. Briefly, cells were seeded in 96-well plates (5,000 cells/well) and allowed to adhere for 24 h prior to the assay. Cells were exposed to various concentrations of free drugs (0 - 10 μg/mL Dox or 0 - 17.2 μM 17-AAG), drug-loaded NGs for 48 h at 37 °C. Cells were then washed with PBS and MTT indicator dye (25 μL, 5 mg/mL) was added to each well and the cells were incubated for 2 h at 37°C in the dark. A solution of 50% DMF-20% SDS (100 μL) was added to each well and kept overnight at 37 °C. Absorbance was read at 570 nm using a plate reader (SpectraMax M5, Molecular Devices Co., USA). Cell survival rates were calculated as normalized to control untreated wells. All measurements were taken eight times. Based on the results of the test, the $IC_{50}$ values and synergic effects of DOX and 17-AAG in these cells were calculated by using CampuSyn Software (Combosyn, USA). Combination index (CI) values less than 1 indicate synergism while CI values equal or more than 1 represent additive and antagonistic effects of drug combination, respectively.

**5.2.10 Animal Studies.**

All animal studies were conducted in accordance with an approved protocol by the University of Nebraska Medical Center Institutional Animal Care and Use Committee (IACUC). $10^7$ BT-474 cells (an ErbB2 overexpressing human breast cancer cell line) reconstituted in 50% Matrigel (BD Biosciences, California) in media were injected directly into the mammary fat pad of 4-6 week old female Athymic NCr-nu/nu mice (NCI, Fredrick National Lab, Fredrick, MD). 17-β-Estradiol pellets (0.72mg/pellet; 60 day release; Innovative Research of America, Sarasota, Fl) were implanted subcutaneously on the lateral side of the neck of the mice three days prior to the injection

of the tumor cells. The mice were randomized when the average tumor size reached 100-200 mm$^3$ (14 days after tumor inoculation) into treatment groups (n = 10), and treated with DOX/NG or 17-AAG/NG or (DOX+17-AAG)/NG or combination of free Dox and 17-AAG in the same ratio as in (DOX+17-AAG)/NG at an equivalent dose of 6 mg/kg DOX, or 1 mg/kg 17-AAG or (6 mg/kg DOX + 1 mg/kg 17-AAG) or 5% dextrose solution. 17-AAG was formulated in Chemophor-EL : propylene glycol : ethanol (2:3:5 by volume) mixture for injections as a component of the free drug combination. Treatments were administered via tail vein injections at 4-day intervals. Animal body weight and tumor volume were monitored every second day. Tumor volume (V = 0.5 x L x W$^2$) was estimated by measuring two orthogonal diameters (longer dimension: L, and smaller dimension: W) of the tumor using electronic calipers. The T/C values were determined from changes in average tumor volumes of drug-treated groups relative to control group. Animals were sacrificed when tumor volume exceeded 3000 mm$^3$, greatest tumor dimension exceeded 20 mm, tumor became necrotic, or animal exhibited a body weight loss of more than 20%. All other animals were sacrificed by day 23.

**5.2.11 Cell proliferation assay.**

Tumors from mice that received different treatments were excised at day 14 (3 mice per group). The tumors were dissected and fixed in 10% neutral buffered formalin. Then, the tissues were processed routinely into paraffin, sectioned at a thickness of 4 μm. Proliferation was detected using an antibody against Ki-67 (Biocare medical, CA) followed by visualization by incubation with DAB+ (brown, for Ki-67) for 2 min. After rinsing with distilled water, the sections were counterstained with hematoxylin. For quantification of Ki-67 expression, the number of Ki-67 positive cells was determined

(Image J) in 5 random high power fields (20X magnification) and divided by the total number of cells for each field of slice.

### 5.2.12 Histopathology analysis.

Specific tissues (liver, spleen, heart kidney and lung) were fixed in buffered formalin and were sectioned, inserted into tissue cassettes, dehydrated in 70% ethanol overnight, and paraffin embedded (UNMC Tissue Sciences Facility, Omaha, NE). Serial 5 μm sections were stained with hematoxylin and eosin (H&E). For histopathological diagnosis, H&E-stained slides were examined by light microscopy.

### 5.2.13 Statistical analysis.

Statistical comparisons for in vitro studies were carried out using Student t-test. For the antitumor study and toxicity studies, group means for tumor volume and body weights were evaluated using repeated measures analysis of variance. Survival was estimated using Kaplan–Meier analysis and compared using log-rank test. $P$ values less than 0.05 were considered significant. Analysis of variance and Kaplan–Meier analysis with log-rank test were performed using GraphPad Prism 5 (GraphPad Software, Inc.).

### 5.3. Results and Discussion

### 5.3.1 Preparation and characterization of nanogels co-encapsulating 17-AAG and Dox

PEG-b-PGlu diblock copolymer, in which about 30% of GA units were modified with hydrophobic phenylalanine moieties, were utilized for the synthesis of biodegradable NGs. NGs were prepared as previously described by template-assisted method involving condensation of these hydrophobically-modified block copolymers by $Ca^{2+}$ ions into polyion complex micelles, followed by chemical cross-linking of the

polyion chains in their cores [23]. A cleavable diamine crosslinker, cystamine, was used for synthesis of the NGs with targeted density of cross-links of 20% (based on the molar ratio of cross-linker to carboxylic acid groups of the Glu residues). The resulting core-shell NGs displayed an effective diameter of about 80 nm ($\zeta$-potential = −45 mV) and were uniform (monomodal, narrow size distribution) as determined by dynamic light scattering (DLS). We have previously shown that water-soluble anticancer drugs such as DOX or cisplatin can be encapsulated with high loading efficiency into NGs ionic cores through electrostatic or coordination interactions [23, 30]. In addition, it was demonstrated that hydrophobic domains formed by phenylalanine moieties within the ionic cores of NGs could solubilize hydrophobic molecules and, therefore, such hybrid NGs provide unique opportunities for combinational drug delivery especially for the drugs that possess different solubility.

It has been reported that HSP90 inhibitors including 17-AAG show additive or synergistic activities with agents commonly used to treat advanced malignancies [31-35]. Particularly, it was demonstrated that 17-AAG synergistically enhances the antiproliferative effect of DOX chemotherapy. The mechanism of synergy is thought to involve 17-AAG-mediated degradation of many of the proteins required for DNA-damage response (such as ATM/ATR or Chk1 kinase), the activities of which are dependent on HSP90 chaperoning function [36]. Additionally, in the case of ErbB2-driven cancers, given the ability of 17-AAG to attenuate hyperactive ErbB2 signaling (which is known to be involved in transcriptional upregulation of genes encoding DNA-damage repair enzymes) [37], it can potentially enhance the cytotoxic effect of DOX-induced DNA damage. Based on these considerations, we attempted to encapsulate both

hydrophilic DOX and hydrophobic 17-AAG into NGs with hydrophobically modified ionic cores.  At first, DOX was incubated with aqueous dispersion of NGs for 24 h at pH 7.0. As expected, the net negative charge and particle size of Dox-loaded NGs (Dox/NG) decreased upon DOX loading due to progressive neutralization and condensation of the PGA segments upon DOX binding to carboxylate groups (Table 5.1).

**Table 5.1.** Physicochemical characterization of NGs before and after drug loading[a]

| Formulation | $D_{eff}$ (nm) | PDI | ζ-potential (mV) | LC (% w/w)[b] | |
|---|---|---|---|---|---|
| | | | | Dox | 17-AAG |
| Empty NG | 82 ± 1 | 0.18 | -45.0 ± 5.2 | - | - |
| DOX/NG | 69 ± 2 | 0.20 | -19.1 ± 1.5 | 18.1 | - |
| 17-AAG/NG | 95 ± 1 | 0.17 | -25.7 ± 1.7 | - | 2.7 |
| (DOX+17-AAG)/NG | 63 ± 5 | 0.16 | -21.5 ± 0.47 | 18.1 | 3.1 |

[a] Effective diameter ($D_{eff}$), polydispersity index (PDI) and ζ-potential were determined  in water (pH 6.5).
[b] Dox and 17-AAG content were determined by UV and HPLC, respectively.
Loading capacity (LC) is expressed as mass of incorporated drug per mass of
drug-loaded nanogels (w/w).

Under these conditions DOX loading capacity of NGs was about 18% w/w as measured by UV-Vis spectroscopy. Binary drug formulation, (DOX+17-AAG)/NG, was prepared by solubilization of 17-AAG into DOX/NG using an extraction method. A similar procedure was used to prepare single 17-AAG/NG formulations. 17-AAG content was determined by HPLC. Comparable loading capacity values for 17-AAG were achieved for NGs with binary drug combination (3.1%) and for single 17-AAG/NG (2.7%). A total

loading capacity of NGs for the binary drug combination was about 21% w/w and corresponds to 6:1 DOX/17-AAG molar ratio. The physicochemical characteristics of drug-loaded NGs are presented in Table 1. The size and $\zeta$-potential of the (DOX+17-AAG)/NG were comparable to those of DOX/NG indicating that an inclusion of 17-AAG into the NG cores did not affect the macroscopic characteristics of DOX-loaded NGs. Importantly, single and binary drug formulations exhibited excellent stability in aqueous dispersions: no changes in sizes and loading capacities were observed for at least two months.

The release profile of the encapsulated drug from the nanocarrier is crucial for the synergy of the drugs [20]. Profound synergistic effects were observed when 17-AAG was administered prior to DOX while the sequence of DOX before 17-AAG had less cytotoxic activity in vitro [20, 34]. Figure 5.1 shows the cumulative release profiles of DOX and 17-AAG from the NGs at physiological pH and temperature.
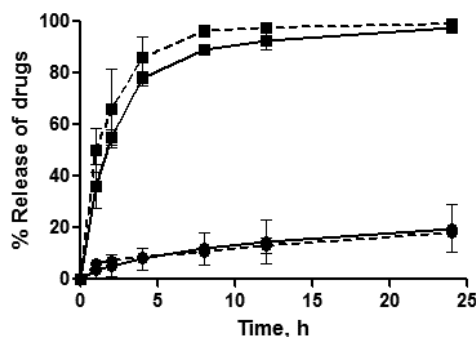


**Figure 5.1.** Drug release profiles from single drug-loaded NGs (solid line) and binary drug combination-loaded NGs (dotted line) for DOX (●) and 17-AAG (■) in PBS buffer, pH 7.4. The loading amount of DOX for each sample is 200 μg. The data represent averaged values and standard deviations calculated based on three independent experiments.

As seen from these data, sustained but temporally distinct release of DOX and 17-AAG was observed. For example, during 12 hrs (DOX+17-AAG)/NG released ~ 90% of

loaded 17-AAG and only ~ 17% of loaded DOX. Notably, 17-AAG release was much faster than that of DOX, which is expected since 17-AAG is physically entrapped into the hydrophobic domains in the cores of NGs. In contrast, DOX binds with PGlu chains through electrostatic and van der Waals interactions and its release usually proceeds via ion exchange reactions, thus delaying its liberation from the NGs. Furthermore, intermolecular interactions between the anthraquinone moiety of DOX and phenylalanine hydrophobic domains of NGs in combination with more compact cross-linked core [23] could account for the delayed and controlled release of DOX from the NGs. It is also interesting that the individual drug release rates practically did not change for binary drug formulations compared to the single drug-loaded NGs (Fig. 5.1).

*5.2.2 Intracellular uptake of drug-loaded NGs.*

NG-based drug-carriers (made of biodegradable materials) are designed to be internalized by cancer cells via the endocytic pathway and disintegrate under lysosomal pH and reducing environment, to release the anticancer drugs into the cytosol. It was important to confirm that the (DOX+17-AAG)/NG uptake into the cells was indeed a result of internalization of intact drug-loaded NGs and subsequent drug release. We therefore compared the kinetics of uptake of free DOX or DOX/NG into 21MT-1 cells, monitoring the intrinsic fluorescence of DOX, using a fluorescence microscope. Images were taken using a 10x and a 20x microscope lens.
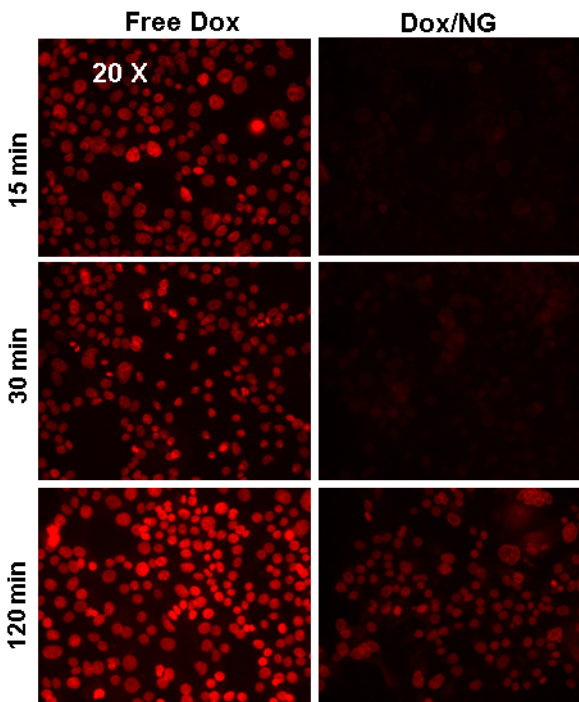
**Figure 5.2.** Comparison of kinetics of cellular DOX distribution in ErbB2 overexpressing 21MT-1 cells after treatment with Free DOX or DOX/NG. Cells, grown on glass coverslips, were exposed to free DOX or DOX/NG (10 µg/mL DOX equivalents) for the indicated time periods following which the cells were washed 3X in PBS and fixed using 4% PFA for 20 min. The cells on the coverslips were then imaged using a regular fluorescence microscope, using a 20X objective. Shown here is a comparison of the distribution of DOX-fluorescence (red) within the cells, as a function of time, when added in the free form vs the NG-formulation.

As shown in Fig. 5.2, the free DOX, which rapidly partitions across the plasma membrane, was found within the nuclei of cells as early as 15 min. On the other hand, the fluorescence of DOX followed by treatments with DOX/NG (at the same concentration of DOX) at early time points (15 and 30 min) was very weak and diffused throughout the cytoplasm; nuclear localization of DOX could only be seen at longer time points (120 min, Fig. 5.2). Confocal microscopy tracking the DOX uptake in live cells confirmed that the DOX/NG accumulated in Transferrin positive early endosomes within 15 min (seen as co-localized yellow punctate structures in Fig. 5.3A, merged panel) and trafficked into

lysosomes within 30 min (as seen by colocalization with Lysotracker dye in Fig. 3B, merged panel).
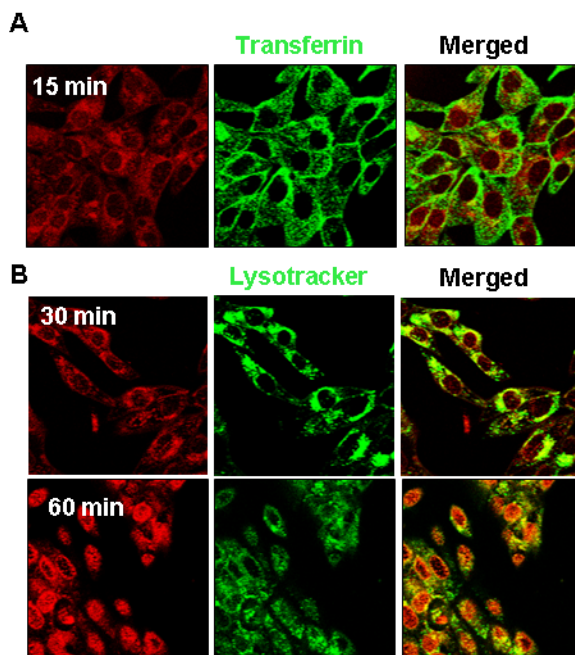


**Figure 5.3.** Confocal immunofluorescence analysis of cellular distribution of DOX/NG. 21MT-1 cells grown on coverslips were loaded with 10 µg/ml Alexa488-labeled transferrin (early endosomal marker) or Lysotracker Green (lysosomal marker; 100nM) for 10 min at $37^{0}$C. DOX/NG (10 µg/mL Dox equivalents) was then added and the uptake and intracellular distribution of DOX/NG (red) within Transferrin- or Lysotacker green-positive compartments, was followed using live cell imaging. Shown here the distribution of DOX fluorescence (red) within transferrin-positive (panel A) early endosomes after 15 min, and in lysosomal compartment (lysotracker green positive) after 30 min (panel B). Clear nuclear localization is seen after 60 min of incubation.

As seen in the low-resolution microscopy images shown in Fig. 5.3, after 30 min incubation most of the fluorescence from DOX was within the cytosol and not the nucleus. However, by 60 min, the DOX fluorescence was found in the nucleus, confirming diffusion of DOX from the lysosomes. Lysosomal trapping of drug-loaded NGs is expected to modulate the release of the drug as well as control the degradation of the carrier. We have previously shown that DOX release rate from NGs is higher at the

acidic pH, which is likely due to protonation of carboxylic groups of PGlu and abating the drug and micelle electrostatic coupling. Since intracellular endocytotic vesicles are acidic (pH≈4.0 to 6.0), the transport of the NGs in these compartments can potentially trigger a release of a bolus of drug from the carrier. Degradation of the PGlu-based NGs in the presence of lysosomal proteases such as cathepsin B or cleavage of reductively labile disulfide bonds in the NGs ionic cores can further facilitate the Dox release.

While the intrinsic fluorescence of DOX served as a method to follow the uptake of drug-loaded NGs and DOX-release, we followed ErbB2 degradation using a Western blot technique as a means to assess the release of 17-AAG and its ability to inhibit intracellular HSP90. The data shown in Fig. 5.4 clearly demonstrate that the encapsulated 17-AAG is released into the cytosol and can inhibit HSP90 leading to ErbB2-degradation.
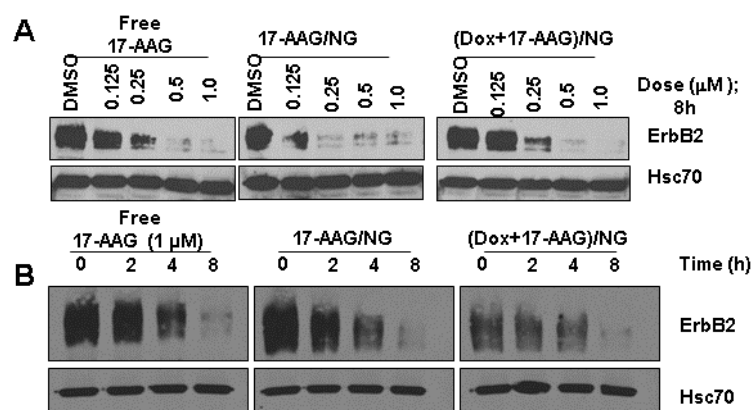


**Figure 5.4.** 17-AAG-loaded NGs can induce ErbB2-degradation in 21MT-1 cell lines as efficiently as free 17 AAG. Cells were treated with the indicated concentrations of free 17-AAG or the NG-formulations for 8h (Dose response experiment; panel **A**) or with fixed concentration (1 µM) of free 17-AAG or the NG-formulations for the indicated time periods (kinetics; panel **B**). Samples were lysed in Triton X-100 lysis buffer and 25 µg aliquot of total protein was analyzed by SDS-PAGE/WB. Shown here are changes in ErbB2-levels as a result of HSP90-inhibition. Hsc70 is shown as loading control.

As seen in Fig. 4A, 17AAG/NG or (DOX+17AAG)/NG induced ErbB2 degradation at the same level as the treatment with free 17-AAG in a dose-dependent manner. Notably, the kinetics of ErbB2 degradation were also comparable for NG-formulations and free 17-AAG (Fig. 5.4B).

Previous studies from our laboratory has shown that NGs with cross-linked ionic cores can be selectively endocytosed into cancer cells, which lack epithelial cell tight junctions, in contrast to normal epithelial cells that form tight junctions [38]. The internalization route appeared to be predominantly via the caveolar pathway. While the current studies report the ability of untargeted NGs to be internalized into ErbB2-overexpressing breast cancer cells, we anticipate that integration of targeting anti-ErbB2 antibody on to the surface of NGs could further facilitate selective delivery of their payload specifically into ErbB2-overexpressing breast cancer cells. In conjunction with passive targeting, ErbB2-targeted drug delivery should further reduce side effects of the chemotherapeutics. In contrast to the untargeted NGs, the ErbB2-specific uptake of the targeted NGs will be dictated by the ErbB2 endocytic pathway. However, one anticipated caveat is that the rate of Trastuzumab-induced ErbB2 internalization is very slow [28, 39]. Immunogold labeled electron microscopy has revealed that gold-labeled Trastuzumab can be detected within microvili-like protrusions and clathrin-coated pits at the cell surface as well as within recycling endosomes [39, 40]. We have shown that HSP90-inhibition induces ErbB2-ubiquitinylation, resulting in accelerated internalization, ubiquitin-dependent sorting into multivesicular bodies and subsequent lysosomal-degradation [28]. Accordingly, we hypothesize that the uptake of the chemotherapeutic payload being delivered via ErbB2-targeted NGs can be significantly enhanced by

concomitant treatment with HSP90-inhibitors, which can accelerate the internalization of the ErbB2-bound targeted drug cargo and routing them to the lysosomes leading to efficient drug-release and induction of cytotoxicity. These studies are ongoing in our laboratories and will be reported elsewhere.

## 5.2.3 In vitro cytotoxicity of DOX, 17-AAG or drug combination against ErbB2-high and ErbB2-low breast cancer cell lines.

DOX is among the most active cytotoxic agents for the treatment of breast cancer. DOX induces DNA damage, and many DNA-repair components are HSP90 client proteins [41]. To test a hypothesis that 17-AAG contentment leads to sensitization of cancer cells to cytotoxic effects of DOX, we determined the cytotoxicity of various drug formulations in a panel of breast cancer cell lines with differential ErbB2 expression using MTT cell cytotoxicity assay (Supplementary Fig. 1-3). Calculated $IC_{50}$ values (the concentration that inhibited cell growth by 50%) are summarized in Table 5.2.

**Table 5.2.** Comparison of $IC_{50}$ values for drug-loaded NGs and free drugs against various breast cancer cell lines as determined by the MTT assay.

| Formulation | $IC_{50}$ (µM) [with respect to Dox] | | |
|:---:|:---:|:---:|:---:|
| | BT-474 | 21MT-1 | MCF-7 |
| Free DOX | $0.60 \pm 0.08$ | $0.13 \pm 0.17$ | $0.65 \pm 0.13$ |
| Free 17-AAG | $0.011 \pm 0.003$ | $0.005 \pm 0.002$ | $0.09 \pm 0.04$ |
| Free DOX + 17-AAG[a] | $0.09 \pm 0.03$ $(CI^{b} = 0.055)$ | $0.007 \pm 0.002$ $(CI = 0.043)$ | $0.63 \pm 0.17$ $(CI = 0.85)$ |
| DOX/NG | $2.40 \pm 0.22$ | $0.47 \pm 0.20$ | $1.05 \pm 0.02$ |
| 17-AAG/NG | $0.022 \pm 0.002$ | $0.009 \pm 0.003$ | $0.14 \pm 0.04$ |

| | $0.13 \pm 0.05$ | $0.08 \pm 0.03*$ | $0.81 \pm 0.18$ |
|---|---|---|---|
| (DOX+17-AAG)/NG[a] | (CI = 0.043) | (CI = 0.060) | (CI = 0.93) |

[a] The molar ratio of DOX :17-AAG of 6:1 was used for the drug combination studies.
[b] CI values were calculated at $IC_{50}$.

We first confirmed that the DOX and 17-AAG combination at a 6:1 molar ratio (corresponding to the drug content encapsulated into NGs) was indeed synergistic in its cytotoxicity against high-level ErbB2-expressing BT-474 and 21MT-1 cell lines after concomitant treatment for 48 h. An approximately 6- and 18-fold reduction in the $IC_{50}$ for DOX was seen in BT-474 and 21MT-1 cells, respectively, after treatment with drug combination. Chou-Talalay analysis of the data clearly indicated a combination index below 1 (such as 0.055 for BT-474 and 0.043 for 21MT-1) confirming strong pharmacological synergy. Similarly, we found that (DOX+17-AAG)/NG combination was significantly more effective in killing ErbB2-overexpressing cells than single DOX/NG formulation and displayed very pronounced synergistic cytotoxicity. The corresponding CI values of (DOX+17-AAG)/NG combination at $IC_{50}$ were 0.043 and 0.06 for BT-474 and 21MT-1cells, respectively. On the other hand, no appreciable differences between the combination treatment and DOX alone (either free or loaded in NGs) were detected in similar experiments conducted on the ErbB2-low MCF-7 cells (Table 2), suggesting that 17-AAG plus DOX combination can induce synergistic anti-proliferative effects selectively in ErbB2-overexpressing breast cancer cells.

**5.2.4 Anti-tumor activity of (DOX+17-AAG)/NG in ErbB2-driven xenograft model.**

Motivated by the enhanced *in vitro* efficacy of (DOX+17-AAG)/NG formulation, we evaluated its antitumor efficacy *in vivo* in ErbB2-driven xenograft model. Intravenous administrations of each formulation were given 4 times at 4-day intervals at an equivalent

dose of 6 mg-DOX/kg. Animals injected with (DOX+17-AAG)/NG or free drug combination received 6mg/kg DOX and 1 mg/kg 17-AAG equivalents per dose. The changes in the relative tumor volume, body weight and animal lifespan are shown in Fig. 5.5A, 5.5B and 5.5C, respectively.
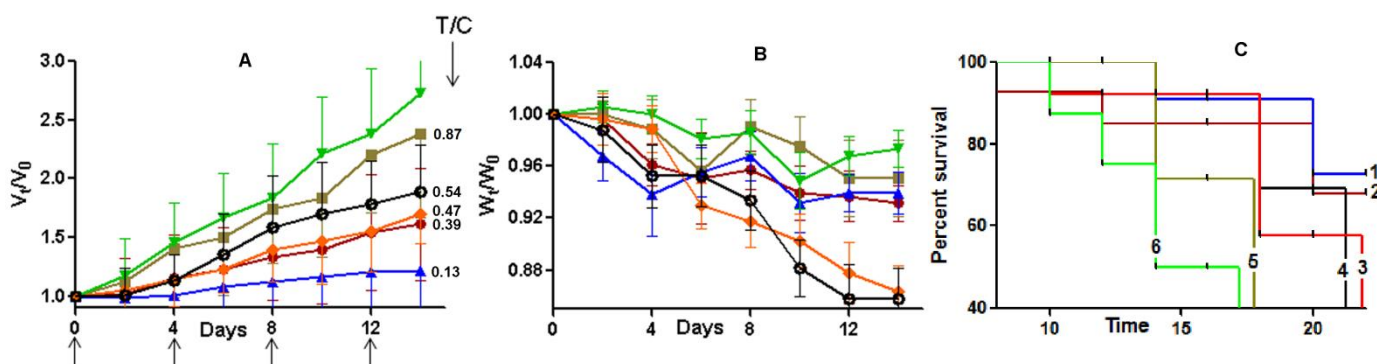


**Fig. 5.5.** In vivo antitumor efficacy of (DOX + 17-AAG)/NG in ErbB2+ - BT-474 breast cancer mice model. Relative changes in (A) tumor volume and (B) body weight were measured following intravenous administration of (DOX + 17-AAG)/NG (▲) or DOX/NG (●) or DOX + 17-AAG (♦) or Free DOX (Ø) or 17-AAG/NG (■) or 5% dextrose (▼). Drug formulations were injected in 100 μL at a dose of 6 mg DOX or 1mg 17-AAG equivalents/kg body weight 4 times at 4-day intervals as indicated by the arrows. Values indicated are means ± SEM (n = 10). (C) Kaplan–Meier analysis of overall survival in (DOX + 17-AAG)/NG group (1) or DOX/NG group (2) or DOX + 17-AAG group (3) or DOX alone (4) or 17-AAG/NG group (5) or control group (6). Tumor volume and body weight are normalized with respect to tumor volume or body weight at day 0. * *P*<0.05, ** *P*<0.01.

Tumor growth inhibition ratio between treated versus control groups (T/C value) was calculated on day 14 after treatment initiation according to the formula: $T/C = (V_t-V_o)_{treated\ tumor}/(V_t-V_o)_{control\ tumor}$, where $V_t$ and $V_o$ represent the mean tumor volume on the evaluation day and at the start of the experiment, respectively. Consistent with the *in vitro* findings, combination treatment with (DOX+17-AAG)/NG formulation resulted in a more significant tumor volume reduction (T/C = 0.13), which translated into increased overall survival of the animals compared to the animal groups treated with a combination of free drugs (DOX+17-AAG) at equivalent drug concentrations (*P*<0.05, Fig. 5.5A &

5.5C). Although not as prominent as (DOX+17-AAG)/NG formulation, tumor burden was also decreased by treatments with DOX alone (T/C = 0.54) or combination of free drugs (DOX+17-AAG, T/C = 0.47) or Dox/NG (T/C = 0.39) compared to control (Fig. 5.5A). Notably, survival of the animals treated with DOX/NG was higher than in animals treated with the combination of free drugs or DOX alone, which could be attributed to the pronounced systemic toxicity of (DOX+17-AAG) and DOX treatments (Fig. 5.5C). Figure 5.5B shows that animals treated with either single or binary drug-loaded NGs only lost ~5% body weight during the 2-week study period compared to control group while the same dose of Dox or the free drug combination (DOX+17-AAG) produced a considerable body weight loss (>15%, $P < 0.05$). These results indicate that DOX-loaded NGs have a much-improved therapeutic index when compared with free DOX. Notably, treatment with 17-AAG/NG did not have any substantial effect on the tumor growth (T/C = 0.87) and only minor increase in survival was observed over controls. To further corroborate the superior antitumor efficacy of binary drug combination in NGs, the tumors were excised post-treatment (on 10th day after last injection) and processed for staining of Ki-67 to examine the effect of treatment on cell proliferation.
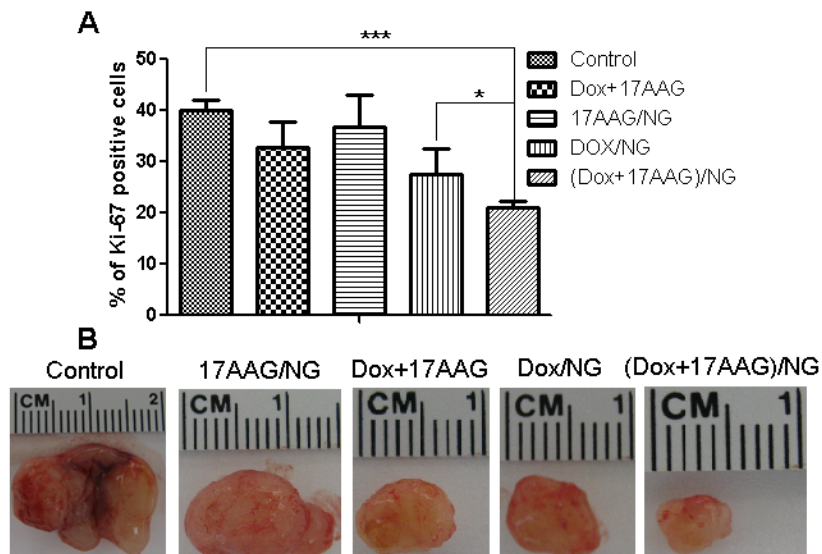
**Fig. 5.6:** Ki-67-caspase-3 apoptosis assay of excised tumors from mice treated with free drugs or NG-formulations. Panel **A** - Quantification of Ki-67 positive cells in tumor tissue from mice from various groups. Data are presented as mean ± SD (n = 5 random microscopic fields for each tumor slice). * $P<0.05$, *** $P<0.001$. Panel **B** shows a comparison of the tumor size for each treatment condition.

The number of Ki-67 positive cells were significantly lower in tumors from mice that received (DOX+17-AAG)/NG compared to tumors in control *(P<0.001)* or DOX+17-AAG *(P<0.01)* or DOX/NG *(P<0.05)* (Fig. 5.6A), which reflected the decrease in the size of the excised tumors (Fig. 6B). Light microscopic examination of H&E-stained tissue (liver, spleen, heart kidney and lung) sections from sacrificed animals (day 22) did not show any evidence of toxicity (data not shown). Collectively, these data provide *in vivo* evidence that biodegradable PEG-polypeptide NGs carrying DOX and 17-AAG drug combination exerted superior antitumor efficacy, both in terms of tumor inhibition and survival, which could be attributed to the preferential simultaneous accumulation, and increased potency.

**5.4 Conclusions**

Using an ErbB2-driven breast cancer model, we demonstrated the potential of PEG-polypeptide nanogels as novel nanocarriers for the delivery of synergistic combinations of chemotherapeutics with the HSP90 inhibitor, 17-AAG. Importantly, the binary drug combination of 17-AAG and DOX simultaneously delivered using NGs exhibited superior antitumor efficacy compared to a combination of free drugs and single drug NGs analogues. Inhibition of HSP90, which leads to degradation and down-regulation of several oncogenic client proteins, is a strategy being extensively explored as treatment for various types of cancers. HSP90 inhibitors, such as 17-AAG, which can synergize with various currently used anticancer agents has shown significant potential in initial phase II clinical trials, including in ErbB2-driven breast cancers. We have previously demonstrated the potential of 17-AAG to synergize with Trastuzumab and induce cytotoxicity in ErbB2-driven breast cancer models. Our studies with biodegradable and biocompatible polymeric NGs provide an alternative to the formulation issues that have impeded the development of 17-AAG. Moreover, these nanocarriers provide an opportunity to encapsulate multiple drugs with various physicochemical properties and modes of action. While doxorubicin was chosen as a model chemotherapeutic in this study, we anticipate that the multidrug loaded NGs represent an attractive platform for the development of potent combinations of HSP90 inhibitors with cytotoxic agents and, thus, further investigations of these NGs are warranted.

for excellent technical assistance.

## 5.5. References

[1] D.J. Slamon, W. Godolphin, L.A. Jones, J.A. Holt, S.G. Wong, D.E. Keith, W.J. Levin, S.G. Stuart, J. Udove, A. Ullrich, Studies of the HER-2/neu proto-oncogene in human breast and ovarian cancer, Science, 244 (1989) 707-712.
[2] C.M. Perou, T. Sørlie, M.B. Eisen, M. van de Rijn, S.S. Jeffrey, C.A. Rees, J.R. Pollack, D.T. Ross, H. Johnsen, L.A. Akslen, Molecular portraits of human breast tumours, Nature, 406 (2000) 747-752.
[3] T. Sørlie, R. Tibshirani, J. Parker, T. Hastie, J. Marron, A. Nobel, S. Deng, H. Johnsen, R. Pesich, S. Geisler, Repeated observation of breast tumor subtypes in independent gene expression data sets, Proc Natl Acad Sci U S, 100 (2003) 8418-8423.
[4] C. Sotiriou, S.-Y. Neo, L.M. McShane, E.L. Korn, P.M. Long, A. Jazaeri, P. Martiat, S.B. Fox, A.L. Harris, E.T. Liu, Breast cancer classification and prognosis based on gene expression profiles from a population-based study, Proc Natl Acad Sci U S, 100 (2003) 10393-10398.
[5] D.J. Slamon, B. Leyland-Jones, S. Shak, H. Fuchs, V. Paton, A. Bajamonde, T. Fleming, W. Eiermann, J. Wolter, M. Pegram, Use of chemotherapy plus a monoclonal antibody against HER2 for metastatic breast cancer that overexpresses HER2, N Engl J Med, 344 (2001) 783-792.
[6] D. Graus-Porta, R.R. Beerli, J.M. Daly, N.E. Hynes, ErbB-2, the preferred heterodimerization partner of all ErbB receptors, is a mediator of lateral signaling, EMBO J, 16 (1997) 1647-1655.
[7] M.M. Moasser, The oncogene HER2: its signaling and transforming functions and its role in human cancer pathogenesis, Oncogene, 26 (2007) 6469-6487.
[8] T.A. Bailey, H. Luan, R.J. Clubb, M. Naramura, V. Band, S.M. Raja, H. Band, Mechanisms of Trastuzumab resistance in ErbB2-driven breast cancer and newer opportunities to overcome therapy resistance, J Carcinog, 10 (2011) 28.
[9] C.A. Hudis, Trastuzumab—mechanism of action and use in clinical practice, N Engl J Med, 357 (2007) 39-51.
[10] E.G. Mimnaugh, C. Chavany, L. Neckers, Polyubiquitination and proteasomal degradation of the p185c-erbB-2 receptor protein-tyrosine kinase induced by geldanamycin, J Biol Chem, 271 (1996) 22796-22801.
[11] T.W. Schulte, L.M. Neckers, The benzoquinone ansamycin 17-allylamino-17-demethoxygeldanamycin binds to HSP90 and shares important biologic activities with geldanamycin, Cancer Chemother Pharmacol, 42 (1998) 273-279.
[12] L. Neckers, Heat shock protein 90 is a rational molecular target in breast cancer, Breast Dis, 15 (2002) 53-60.
[13] S. Modi, A. Stopeck, H. Linden, D. Solit, S. Chandarlapaty, N. Rosen, G. D'Andrea, M. Dickler, M.E. Moynahan, S. Sugarman, HSP90 inhibition is effective in breast cancer: a phase II trial of tanespimycin (17-AAG) plus trastuzumab in patients with HER2-positive metastatic breast cancer progressing on trastuzumab, Clin Cancer Res, 17 (2011) 5132-5139.
[14] W. Xu, E. Mimnaugh, M.F. Rosser, C. Nicchitta, M. Marcu, Y. Yarden, L. Neckers, Sensitivity of mature Erbb2 to geldanamycin is conferred by its kinase domain and is mediated by the chaperone protein Hsp90, J Biol Chem, 276 (2001) 3702-3708.
[15] A.D. Basso, D.B. Solit, P.N. Munster, N. Rosen, Ansamycin antibiotics inhibit Akt activation and cyclin D expression in breast cancer cells that overexpress HER2, Oncogene, 21 (2002) 1159.
[16] M.V. Powers, P. Workman, Targeting of multiple signalling pathways by heat shock protein 90 molecular chaperone inhibitors, Endocrine-Related Cancer, 13 (2006) S125-S135.
[17] J. Trepel, M. Mollapour, G. Giaccone, L. Neckers, Targeting the dynamic HSP90 complex in cancer, Nat Rev Cancer, 10 (2010) 537-549.

[18] P.N. Münster, A. Basso, D. Solit, L. Norton, N. Rosen, Modulation of Hsp90 Function by Ansamycins Sensitizes Breast Cancer Cells to Chemotherapy-induced Apoptosis in an RB-and Schedule-dependent Manner See The Biology Behind: EA Sausville, Combining Cytotoxics and 17-Allylamino, 17-Demethoxygeldanamycin: Sequence and Tumor Biology Matters. Clin Cancer Res, 7 (2001) 2228-2236.

[19] G. Georgakis, Y. Li, A. Younes, Preclinical evaluation of the HSP-90 inhibitor 17AAG in Hodgkin's and non-Hodgkin's lymphomas: Induction of apoptosis and potentiation of chemotherapy cytotoxicity, in: Proc Annu Meet Am Soc Clin Onco, 2005, pp. 6570.

[20] U. Sarangi, K.R. Paithankar, J.U. Kumar, V. Subramaniam, A.S. Sreedhar, 17AAG Treatment Accelerates Doxorubicin Induced cellular senescence: Hsp90 Interferes with enforced senescence of Tumor cells, Drug target insights, 6 (2012) 19.

[21] S.S. Desale, S.M. Cohen, Y. Zhao, A.V. Kabanov, T.K. Bronich, Biodegradable hybrid polymer micelles for combination drug therapy in ovarian cancer, J Control Release, 171 (2013) 339-348.

[22] M.E. Godsey, S. Suryaprakash, K.W. Leong, Materials innovation for co-delivery of diverse therapeutic cargos, RSC Adv, 3 (2013) 24794-24811.

[23] H.S.O. Jong Oh Kim, Swapnil Desale, Alexander V. Kabanov, and Tatiana K. Bronich, Polypeptide nanogels with hydrophobic moieties in the cross-linked ionic cores: synthesis, characterization and implications for anticancer drug delivery, J Drug Taget, (2013).

[24] Y. Han, Z. He, A. Schulz, T.K. Bronich, R. Jordan, R. Luxenhofer, A.V. Kabanov, Synergistic combinations of multiple chemotherapeutic agents in high capacity poly (2-oxazoline) micelles, Mol Pharm, 9 (2012) 2302-2313.

[25] C.C. Lee, E.R. Gillies, M.E. Fox, S.J. Guillaudeu, J.M. Fréchet, E.E. Dy, F.C. Szoka, A single dose of doxorubicin-functionalized bow-tie dendrimer cures mice bearing C-26 colon carcinomas, Proc Natl Acad Sci U S A, 103 (2006) 16649-16654.

[26] V. Band, D. Zajchowski, K. Swisshelm, D. Trask, V. Kulesa, C. Cohen, J. Connolly, R. Sager, Tumor progression in four mammary epithelial cell lines derived from the same patient, Cancer Res, 50 (1990) 7351-7357.

[27] S.M. Raja, R.J. Clubb, C. Ortega-Cava, S.H. Williams, T.A. Bailey, L. Duan, X. Zhao, A.L. Reddi, A.M. Nyong, A. Natarajan, Anticancer activity of Celastrol in combination with ErbB2-targeted therapeutics for treatment of ErbB2-overexpressing breast cancers, Cancer Biol Ther, 11 (2011) 263-276.

[28] S.M. Raja, R.J. Clubb, M. Bhattacharyya, M. Dimri, H. Cheng, W. Pan, C. Ortega-Cava, A. Lakku-Reddi, M. Naramura, V. Band, A combination of trastuzumab and 17-AAG induces enhanced ubiquitinylation and lysosomal pathway-dependent ErbB2 degradation and cytotoxicity in ErbB2-overexpressing breast cancer cells, Cancer Biol Ther, 7 (2008) 1630-1640.

[29] M. Ferrari, M.C. Fornasiero, A.M. Isetta, MTT colorimetric assay for testing macrophage cytotoxic activity in vitro, J Immunol Methods, 131 (1990) 165-172.

[30] N.V. Nukolova, H.S. Oberoi, S.M. Cohen, A.V. Kabanov, T.K. Bronich, Folate-decorated nanogels for targeted therapy of ovarian cancer, Biomaterials, 32 (2011) 5417-5426.

[31] M. Scaltriti, S. Dawood, J. Cortes, Molecular pathways: targeting hsp90—who benefits and who does not, Clin Cancer Res, 18 (2012) 4508-4513.

[32] C.S. Mitsiades, N.S. Mitsiades, C.J. McMullan, V. Poulaki, A.L. Kung, F.E. Davies, G. Morgan, M. Akiyama, R. Shringarpure, N.C. Munshi, Antimyeloma activity of heat shock protein-90 inhibition, Blood, 107 (2006) 1092-1100.

[33] O. Ayrault, M.D. Godeny, C. Dillon, F. Zindy, P. Fitzgerald, M.F. Roussel, H.M. Beere, Inhibition of Hsp90 via 17-DMAG induces apoptosis in a p53-dependent manner to prevent medulloblastoma, Proc Natl Acad Sci U S A, 106 (2009) 17037-17042.

[34] G.V. Georgakis, Y. Li, G.Z. Rassidakis, L.J. Medeiros, A. Younes, The HSP90 inhibitor 17-AAG synergizes with doxorubicin and U0126 in anaplastic large cell lymphoma irrespective of ALK expression, Exp Hematol, 34 (2006) 1670-1679.

[35] C. Lai, K. Park, D. Lee, A. Alberobello, M. Raffeld, M. Pierobon, E. Pin, E. Petricoin III, Y. Wang, G. Giaccone, HSP-90 inhibitor ganetespib is synergistic with doxorubicin in small cell lung cancer, Oncogene, 33 (2013) 4867-4876.

[36] S.J. Arlander, A.K. Eapen, B.T. Vroman, R.J. McDonald, D.O. Toft, L.M. Karnitz, Hsp90 inhibition depletes Chk1 and sensitizes tumor cells to replication stress, J Biol Chem, 278 (2003) 52572-52577.

[37] N.L. Spector, K.L. Blackwell, Understanding the mechanisms behind trastuzumab therapy for human epidermal growth factor receptor 2–positive breast cancer, J Clin Oncol, 27 (2009) 5838-5847.

[38] G. Sahay, D.Y. Alakhova, A.V. Kabanov, Endocytosis of nanomedicines, J Control Release, 145 (2010) 182-195.

[39] C.D. Austin, A.M. De Mazière, P.I. Pisacane, S.M. van Dijk, C. Eigenbrot, M.X. Sliwkowski, J. Klumperman, R.H. Scheller, Endocytosis and sorting of ErbB2 and the site of action of cancer therapeutics trastuzumab and geldanamycin, Mol Biol Cell, 15 (2004) 5268-5282.

[40] L.A. Maier, F.J. Xu, S. Hester, C.M. Boyer, S. McKenzie, A.M. Bruskin, Y. Argon, R.C. Bast, Requirements for the internalization of a murine monoclonal antibody directed against the HER-2/neu gene product c-erbB-2, Cancer Res, 51 (1991) 5361-5369.

[41] K.B. Kaplan, R. Li, A prescription for 'stress'–the role of Hsp90 in genome stability and cellular adaptation, Trends Cell Biol, 22 (2012) 576-583.

# CHAPTER VI

# SUMMARY

Combination chemotherapy is preferred over treatment with single agents to combat most cancers as it targets multiple cell-survival pathways at the same time and delays the onset of resistance. This helps in achieving long-term tumor remission and increases median survival. Cisplatin (CDDP)-based therapy has been the standard treatment for ovarian cancer since its discovery. After paclitaxel (PTX) was shown to be effective in ovarian cancer, multiple clinical trials studied the overall efficacy of CDDP and PTX and found significant benefit over the pre-existing treatments. Since then, this combination has been the treatment of choice for both early stage as well as advanced cases of ovarian cancer. However, administration of two different agents comes with the inconvenience of repeated or extended duration of drug infusion in patients. Moreover, the most extensively used conventional formulation of paclitaxel, Taxol®, utilizes Cremophor EL (polyethoxylated castor oil) that has been linked to significant toxicities including allergic, hypersensitivity and anaphylactic reactions during infusion that require premedication and prolonged peripheral neuropathy. Combining such drugs in one delivery carrier is therefore a well-suited and convenient strategy for controlling the pharmacokinetics and co-delivery of the desired drug ratio in vivo, to maximize the therapeutic potency and minimize drug-associated toxicities.

Cross-linked nanogels have been found to be promising drug carriers to achieve this goal. Being mostly hydrophilic in nature, nanogels are highly biocompatible with a high loading capacity for guest molecules. The nanogel structure can be readily adjusted to

integrate features of different materials and, thus, offer advantages for combinatorial encapsulation of drugs with varying physicochemical properties. One of the widespread synthetic techniques for the synthesis of nanogels is the crosslinking of preformed core-shell self-assemblies such as polymer micelles that allows introducing a high degree of spatial organization into the nanogels. Cross-linking is known to impart control over the swelling behavior of the nanogels and thus helps in achieving controlled release of the incorporated cargo, which is an added advantage over the structural integrity imparted to the carrier system upon in vivo administration. The enhanced stability also makes the prolonged circulation of the nanogels possible, which in turn allows for increased drug accumulation at the target site by enhanced permeability and retention effect (EPR). We report in **Chapter II** design of multi-compartment cross-linked nanogels based on hybrid triblock copolymers, poly(ethylene glycol)-block-poly(L-glutamic acid)-block-poly(L-phenylalanine) (PEG-b-PGlu-b-PPhe) for simultaneous loading and delivery of binary CDDP and PTX combination. Such nanogels have 1) a hydrophobic core formed by PPhe chains, which serves as a reservoir for PTX solubilization, 2) an anionic layer, which incorporates CDDP through coordination with the carboxylic groups of PGlu, and 3) an outer PEG shell stabilized, which stabilizes micelles in aqueous dispersion. The crosslinks incorporated into PGlu block layer ensure that the PEG-b-PGlu-b-PPhe micelles remain stable until they encounter proteases, which degrade the micelles by cleaving the polypeptide chains of the block copolymers. This work demonstrates that such biodegradable hybrid micelles carrying CDDP and PTX drug combination exert superior antitumor efficacy in treatment of ovarian cancer in xenograft mouse tumor model.

Regardless of the importance and popularity of EPR effect-based drug delivery, this strategy has some limitations related to the inter- and intra-tumor heterogeneity, variations in the density as well as permeability of the tumor vasculature that can affect the accumulation of nanocarriers. One of the popular approaches to circumvent these problems is by surface-functionalization of the drug carrier with ligands that can target receptors with differential expression on the cancer cell surface, which helps in increasing the mean residence time of the delivery system at the tumor site and improving target cell uptake. One such receptor of interest is the folate receptor (FR). Malignant cells, due to their high rate of cell division, have an increased requirement of folic acid (FA), since it is essential component of cell metabolism and DNA synthesis and repair. To fulfill this higher need of FA, FR is known to be over-expressed in a large number of malignant tissues, including ovarian cancer, compared to normal tissues with the exception of the kidney and choroid plexus. Furthermore, this receptor becomes accessible via the plasma compartment only after the cells lose their polarity owing to malignant transformation which makes it a differential target for cancer tissue that is easily accessible for intravenously administered FA conjugated systems. Its natural ligand, FA, comes with the advantages of high binding affinity, stability and a simple chemical structure together with ease of availability, making it a suitable targeting ligand for ovarian cancer therapy. FA can thus be successfully conjugated to macromolecular systems without loss of binding affinity to its receptor. Many different agents targeting the folate pathway are currently in clinical development. To date, FA-targeted agents showed significant promise in phase II clinical trials but it has not been confirmed in phase III studies. Accordingly, there is a need for further identification of new therapeutic

combinations and refinement of patient selection. To this end, FA-conjugated imaging agents could be used for pre-selection of patients based on the expression of FR and several methods have been already developed for this purpose.

Our group has previously demonstrated a tumor-specific delivery and improved anti-cancer effect in vivo of CDDP-loaded nanogels decorated with FA targeting groups. In our **Chapter III**, we designed FA-linked nanogels incorporating platinum-taxane combination, and examined whether FR-targeted concurrent delivery of synergistic combination of CDDP and PTX can lead to enhanced therapeutic efficacy compared to nontargeted NG system.

The oncogenic receptor tyrosine kinase ErbB2, overexpressed in over 20% of breast cancers, has served as a major target for the development of targeted drug delivery strategies. However, ErbB2 is thought to be either impaired in endocytosis or to rapidly recycle back to the cell-surface, which can significantly dampen the efficacy of ErbB2-targeted drug delivery. Such altered trafficking dynamics is believed to be due to its constitutive association with HSP90 which can be anticipated to significantly dampen the efficacy of ErbB2-targeted drug delivery. We therefore hypothesized that HSP90-inhibition will enhance ErbB2-targeted drug delivery by promoting the endocytic uptake of ErbB2-bound nano-encapsulated cargo and facilitating its re-routing from a recycling pathway to the lysosomes. Using Trastuzumab-conjugated NGs (Trast-NG) encapsulating the DNA-damaging drug Doxorubicin (DOX) as a model chemotherapeutic, we demonstrate in **Chapter IV** through both in vitro and in vivo studies that HSP90-inhibition can indeed lead to an enhancement of targeted delivery of DOX specifically into ErbB2-overexpressing breast cancer cells. As a consequence, a sub-therapeutic and

non-toxic dose of the HSP90 inhibitor 17AAG markedly improves the efficacy of ErbB2-targetd nanogels in vivo. In a follow up study, we attempted to co-encapsulate DOX and 17-AAG since combining drugs in one delivery carrier is a well-suited strategy for controlling the pharmacokinetics and co-delivery of the desired drug ratio in vivo. However, co-incorporation of drug molecules with different physicochemical properties, such as hydrophilic DOX and hydrophobic 17-AAG, has been challenging. In **Chapter V**, we have described biodegradable polymeric nanogels (NGs) based on poly(ethylene glycol)-b-poly(L-glutamic acid) (PEG-b-PGA) with pendant phenylalnine functionalities. Such NGs have multiple hydrophobic domains formed by phenylalanine moieties within the cross-linked PGA polyion cores surrounded by a hydrophilic PEG shell.  Herein, we explored these novel NGs for co-encapsulation of 17-AAG and DOX. The potency of this co-delivery system was evaluated in a panel of human breast cancer lines and in an ErbB2-driven orthotopic xenograft model. We demonstrate that NGs-based co-delivery of synergistic combination of 17-AAG and DOX exhibited superior antitumor efficacy compared to a combination of free drugs in ErbB2-positive breast cancer cells. The implications of our results may support a new platform for delivery of combinations of HSP90 inhibitors with cytotoxic agents for treatment of various types of cancers.

## LIMITATIONS AND FUTURE DIRECTIONS

The data reported in chapter II showed the preclinical evaluation of platinum-taxane-loaded nanogels. Our work demonstrated that such biodegradable hybrid nanogels carrying CDDP and PTX drug combination exert superior antitumor efficacy in treatment of ovarian cancer in xenograft mouse tumor model. However, our system relied solely on the EPR effect to facilitate the delivery of the drug combination to the tumor site. No matter what the importance and popularity of EPR effect-based drug delivery is, this strategy has some limitations related to the inter- and intra-tumor heterogeneity, variations in the density as well as permeability of the tumor vasculature that can affect the accumulation of nanocarriers. One of the popular approaches to circumvent these problems is by surface-functionalization of the drug carrier with ligands that can target receptors with differential expression on the cancer cell surface, which helps in increasing the mean residence time of the delivery system at the tumor site and improving target cell uptake. In our Chapter III, we designed FA-linked nanogels incorporating platinum-taxane combination, and examined whether FR-targeted concurrent delivery of synergistic combination of CDDP and PTX can lead to enhanced therapeutic efficacy compared to nontargeted NG system. Many recent studies have shown that the particulate system with the size less than 50 nm has profound effect on its tumor accumulation. Although we were able to generate particles with the size less than 100 nm, it wasn't small enough for the very effective tumor accumulation as per recent reports. Another limitation of current triblock copolymer-based nanogels system is loading same drug combination at different ratios. Although our current drug ratio is very synergetic, we are also exploring the different block length ratios which would allow us to have system with

different ratios of same drug combination. Current and future studies planned in our group include design and fabrication of sub-100 nm particulate system. One such a system under investigation is based on diblock copolymers of PEG and poly(L-leucin). This copolymer assembles into a uniform micellar aggregates in aqueous solutions. The resulting micelles have size of less than 50 nm. It also allows for loading to highly synergistic combination of hydrophobic drug molecules including paclitaxel.

The binding of FA-(CDDP + PTX)/NG to and/or their uptake by FR+ cancer cells can retain them within the tumor for a longer period of time, prevent their rapid re-entering into systemic circulation and, thus, provide some benefits over passively targeted formulations. The introduction of FA moieties can also have an effect on pharmacokinetics and biodistribution of NGs and influence tumor uptake. Our future efforts include detailed pharmacokinetic study which may help to elucidate the relationship between the therapeutic effect of the FR-targeted NGs and distribution at the tumor and the whole body. FA targeting achieved desirable tumor inhibition in our present study but its distribution in other organs especially kidney (main site of platinum toxicity) which still remains a concern. Selecting an alternative targeting moiety with a better selectivity to tumor target is therefore desirable. We also would like to try our treatment regimen on the cisplatin-resistant cell line to see if targeted combination therapy can induce a therapeutic response in them.

Current clinical therapy for ErbB2-positive breast cancer includes the administration of Trastuzumab monoclonal antibody (Herceptin™). This therapy suffers from several limitations. Firstly, its long-term clinical use is questionable because tumor cells acquire resistance to the therapy and secondly, ErbB2 is either impaired in endocytosis or rapidly

recycles back to the cell surface. In chapter IV, our studies demonstrated, both *in vitro* and *in vivo*, that HSP90 inhibition facilitates the uptake and delivery of trastuzumab-based ErbB2-targeted nanoparticle therapy carrying a model chemotherapeutic agent, Doxorubicin, specifically into ErbB2-overexpressing breast cancer cells. These novel findings highlight the importance of considering oncogene-specific alterations in receptor dynamics towards the design of targeted drug delivery strategies. We suggest that combination of ADCs or ANPs with therapeutic agents that enhance receptor endocytosis and lysosomal routing can provide a novel strategy with significantly higher therapeutic benefit. Based on our studies, we suggest that the endocytic traffic itinerary of receptors selected for targeting of ADCs and ANPs should receive careful consideration. An understanding of mechanisms that may impair the endolysomal traffic of a targeted receptor (as with ErbB2) may help overcome an efficacy barrier on newer agents in development and potentially improve the efficacy of agents already in the clinic. In this regard, the potential combination of HSP90 inhibitors that are already in clinical trials together with the ErbB2-targeted TDM-1 will be of considerable interest and is under study in our group. It is of interest that HSP90 is also thought to regulate the activity of Rab GTPase-dependent endocytic recycling by its association with a Rab Guanine Nucleotide Displacement Inhibitor (GDI), and HSP90 inhibitors could potentially help attenuate Rab-dependent recycling of transmembrane receptors that are not direct HSP90 clients to enhance ADC or ANP delivery inside the tumor cell. Other factors that may control trafficking of oncogenic cell-surface receptors such as the non-receptor tyrosine kinase c-Src, endocytic adaptor proteins, E3 ubiquitin ligases, deubiquitinating enzymes, RAB GTPases, ESCRT proteins and EHD family proteins may offer future opportunities

to develop facilitators of ADC and ANP traffic to endolysomal compartments as approaches of therapeutic potentiation.

Our studies also provide evidence that sub-therapeutic doses of an HSP90 inhibitor (1 mg/Kg 17AAG in our studies, which has little efficacy against BT-474 xenografts; unpublished data), dramatically enhances tumor killing by DOX-loaded ErbB2-targeted NGs. Such a combination led to not just inhibition of xenograft tumor growth but in fact a significant shrinkage of tumor masses from their pre-treatment volume. This was associated with a significant shift from a merely cytostatic to a significantly cytotoxic effect on tumors as demonstrated by Ki67 and caspase-3 staining of tumors among surviving mice at the end of therapy. Not surprisingly, combination with low dose 17AAG markedly improved the survival of tumor-bearing mice. We must point out that DOX was used in our proof-of-principle studies as the polymer design we have previously established allows efficient loading of this clinically-used chemotherapeutic agent. However, DOX enhances cardiotoxicity associated with ErbB2-targeted antibody therapeutics, including Trastuzumab, and as such the approach will need modifications to incorporate more appropriate agents for ErbB2+ cancers. Such studies are currently ongoing in our laboratories. The current nanocarrier design should however be applicable to other tumors where a targeting antibody or other moiety is available. We have tested the efficacy of our regimen on the Trast-sensitive cell lines. Our ongoing efforts are to test the efficacy of our regimen on trast-resistant cell lines and also choose a transgenic mouse model to test our treatment regimen.